

Application of high-resolution peripheral quantitative computed tomography in a clinical setting

Citation for published version (APA):

Bevers, M. S. A. M. (2024). *Application of high-resolution peripheral quantitative computed tomography in a clinical setting*. [Doctoral Thesis, Maastricht University]. Maastricht University. <https://doi.org/10.26481/dis.20240315mb>

Document status and date:

Published: 01/01/2024

DOI:

[10.26481/dis.20240315mb](https://doi.org/10.26481/dis.20240315mb)

Document Version:

Publisher's PDF, also known as Version of record

Please check the document version of this publication:

- A submitted manuscript is the version of the article upon submission and before peer-review. There can be important differences between the submitted version and the official published version of record. People interested in the research are advised to contact the author for the final version of the publication, or visit the DOI to the publisher's website.
- The final author version and the galley proof are versions of the publication after peer review.
- The final published version features the final layout of the paper including the volume, issue and page numbers.

[Link to publication](#)

General rights

Copyright and moral rights for the publications made accessible in the public portal are retained by the authors and/or other copyright owners and it is a condition of accessing publications that users recognise and abide by the legal requirements associated with these rights.

- Users may download and print one copy of any publication from the public portal for the purpose of private study or research.
- You may not further distribute the material or use it for any profit-making activity or commercial gain
- You may freely distribute the URL identifying the publication in the public portal.

If the publication is distributed under the terms of Article 25fa of the Dutch Copyright Act, indicated by the "Taverne" license above, please follow below link for the End User Agreement:

www.umlib.nl/taverne-license

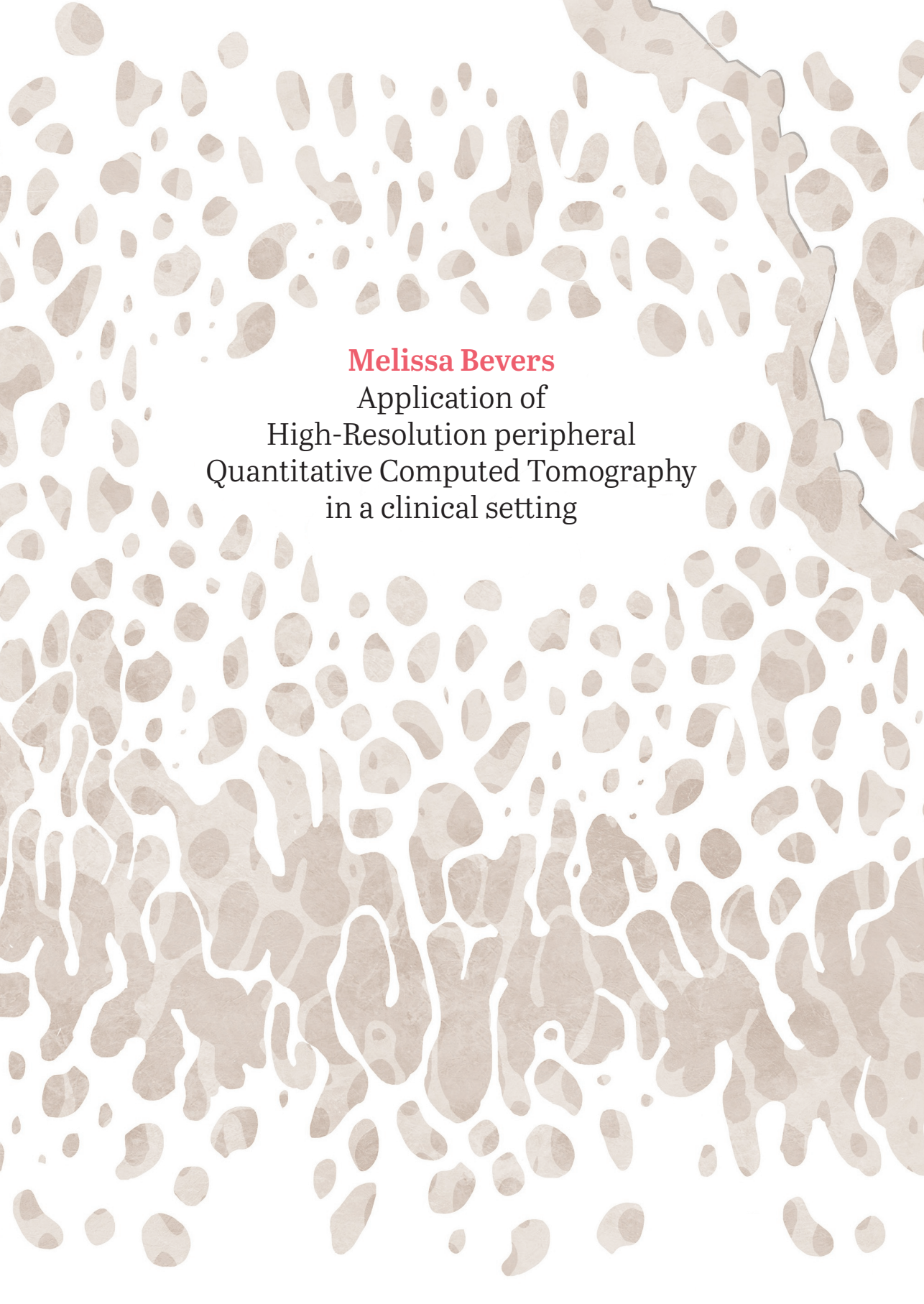
Take down policy

If you believe that this document breaches copyright please contact us at:

repository@maastrichtuniversity.nl

providing details and we will investigate your claim.

Download date: 28 Apr. 2024



Melissa Bevers
Application of
High-Resolution peripheral
Quantitative Computed Tomography
in a clinical setting

Application of High-Resolution peripheral Quantitative Computed Tomography in a clinical setting

Melissa Bevers

Copyright © M.S.A.M. Bevers, 2024

All rights preserved. No part of this thesis may be reproduced in any form or by any means without written permission from the author or, when appropriate, from the publisher of the publication.

Cover design: Simone Golob || sgiv.nl
Layout: ProefschriftMaken || proefschriftmaken.nl
Production: ProefschriftMaken || proefschriftmaken.nl
ISBN: 978-94-6469-814-5

Dissemination of this thesis was financially supported by Maastricht University, SCANCO Medical, and Anna Foundation|NOREF.

Application of High-Resolution peripheral Quantitative Computed Tomography in a clinical setting

PROEFSCHRIFT

ter verkrijging van de graad van doctor aan de Universiteit Maastricht,
op gezag van de Rector Magnificus, Prof. dr. P. Habibović,
volgens het besluit van het College van Decanen,
in het openbaar te verdedigen
op 15 maart 2024 om 13.00 uur

door

Melissa Sophia Anna Maria Bevers
Geboren op 27 december 1995 te Helmond

Promotor

Prof. dr. J.P. van den Bergh

Copromotoren

Dr. C.E. Wyers (VieCuri Medisch Centrum Venlo)

Dr. ir. B. van Rietbergen (Technische Universiteit Eindhoven)

Beoordelingscommissie

Prof. dr. P.C. Willems (*voorzitter*)

Prof. dr. A.E. Boonen

Dr. ir. J.J.A. de Jong

Prof. dr. G.H. van Lenthe (Katholieke Universiteit Leuven)

Prof. dr. E.H.G. Oei (Erasmus MC Rotterdam)

CONTENTS

| | |
|---|-----|
| List of abbreviations | 6 |
| List of HR-pQCT parameters | 8 |
| Chapter 1. General introduction | 11 |
| PART 1. Bone microarchitecture and strength from HR-pQCT in disease and with treatment | 31 |
| Chapter 2. Bone microarchitecture and strength in adults with osteogenesis imperfecta using HR-pQCT: normative comparison and challenges | 33 |
| Chapter 3. Microarchitecture of heterotopic ossification in fibrodysplasia ossificans progressiva: an HR-pQCT case series | 61 |
| Chapter 4. Effect of denosumab compared with risedronate on bone strength in patients initiating or continuing glucocorticoid treatment | 81 |
| Chapter 5. Bone microarchitecture and strength changes during teriparatide and zoledronic acid treatment in a patient with pregnancy and lactation-associated osteoporosis with multiple vertebral fractures | 103 |
| PART 2. HR-pQCT for distal radius and scaphoid fractures | 123 |
| Chapter 6. The contribution of lower-mineralized tissue to the healing of conservatively-treated distal radius fractures assessed using HR-pQCT | 125 |
| Chapter 7. The feasibility of high-resolution peripheral quantitative computed tomography (HR-pQCT) in patients with suspected scaphoid fractures | 149 |
| Chapter 8. Improved detection of scaphoid fractures with high-resolution peripheral quantitative CT compared with conventional CT | 169 |
| Chapter 9. Association between bone shape and the presence of a fracture in patients with a clinically suspected scaphoid fracture | 187 |
| Chapter 10. Assessment of the healing of conservatively-treated scaphoid fractures using HR-pQCT | 207 |
| Chapter 11. General discussion | 231 |
| Chapter 12. Summary | 257 |
| Samenvatting | 261 |
| Addendum Impact paragraph | 269 |
| Dankwoord | 273 |
| Curriculum vitae | 278 |
| List of publications | 279 |

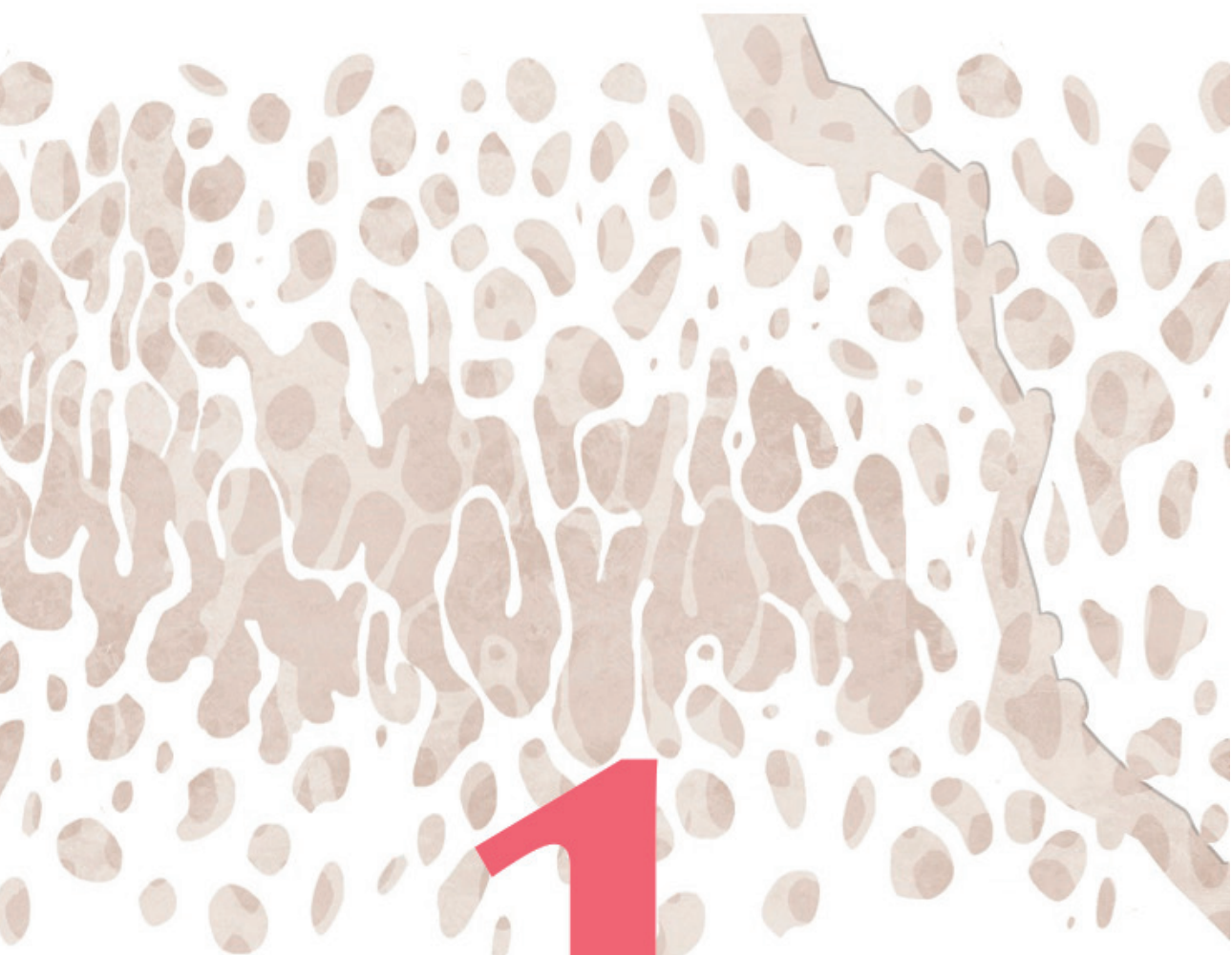
LIST OF ABBREVIATIONS

| | |
|----------------|--|
| (μ)CT | (micro-) computed tomography |
| (μ)MRI | (micro-) magnetic resonance imaging |
| (μ)FE | (micro-) finite element analysis |
| [18]NaF PET-CT | fluorine-18-labeled sodium fluoride positron emission tomography-computed tomography |
| (95%-) CI | (95%-) confidence interval |
| aBMD | areal bone mineral density |
| AIC | Akaike information criterion |
| AOM | anti-osteoporosis treatment |
| AUC | area under the receiver operator characteristic curve |
| AUTO | automatically obtained periosteal contours |
| BL | baseline |
| BMD | (volumetric) bone mineral density |
| BP | bisphosphonate |
| BS | bone scintigraphy |
| CTX | collagen type I C-terminal telopeptide |
| DICOM | digital imaging and communications in medicine |
| DXA | dual-energy X-ray absorptiometry |
| ED | emergency department |
| EMM | estimated marginal means |
| FDR | false discovery rate |
| FOP | fibrodysplasia ossificans progressiva |
| GC | glucocorticoid |
| GC-C | patients continuing glucocorticoid treatment |
| GC-I | patients initiating glucocorticoid treatment |
| GIOP | glucocorticoid-induced osteoporosis |
| HO | heterotopic ossification |
| HR-pQCT | high-resolution peripheral quantitative computed tomography |
| ICP | iterative closest point |
| IQR | interquartile range |
| J | Youden's Index |
| LMM | linear mixed effects model |
| LSC | least-significant change |
| M_{dual} | dual-threshold micro-finite element model |
| M_{single} | single-threshold micro-finite element model |
| METC | Medical ethics committee (Dutch: medisch ethische toetsingscommissie) |
| NPV | negative predictive value |

| | |
|-------|--|
| NSAID | non-steroidal anti-inflammatory drug |
| OI | osteogenesis imperfecta |
| P1NP | procollagen type I N-terminal propeptide |
| PCA | principal component analysis |
| Pctl | percentile |
| PLO | pregnancy- and lactation-associated osteoporosis |
| PMI | polar moment of inertia |
| PMOP | postmenopausal osteoporosis |
| PPV | positive predictive value |
| pQCT | peripheral quantitative computed tomography |
| QCT | quantitative computed tomography |
| RCT | randomized controlled trial |
| RMSE | root-mean squared error |
| ROC | receiver operating characteristic |
| sAUTO | periosteal contours after manual adjustment of automatically obtained contours |
| SD | standard deviation |
| SSM | statistical shape model |
| TPTD | teriparatide |
| W | Kendall <i>W</i> statistic or coefficient of concordance |
| WMO | medical research involving human subjects act (Dutch: Wet medisch-wetenschappelijk onderzoek met mensen) |
| ZA | zoledronic acid |

LIST OF HR-pQCT PARAMETERS

| | |
|---|---|
| BMD | bone mineral density of the total bone region [mg HA/cm ³] |
| BV/TV | bone volume fraction of the total bone region [- or %] |
| BV/TV ₂₀₀ | BV/TV based on a threshold of 200 HA/cm ³ for bone segmentation [- or %] |
| BV/TV ₃₂₀ | BV/TV based on a threshold of 320 HA/cm ³ for bone segmentation [- or %] |
| BV ₂₀₀ /BV ₃₂₀ | ratio of BV/TV ₂₀₀ over BV/TV ₃₂₀ , reflecting the contribution of lower-mineralized tissue to bone volume fraction [-] |
| Ct.Ar | cortical bone area [mm ²] |
| Ct.BMD | cortical bone mineral density [mg HA/cm ³] |
| Ct.Po | cortical porosity [- or %] |
| Ct.Po.Dm | cortical pore diameter [mm] |
| Ct.Th | cortical thickness [mm] |
| FL | failure load [N or kN] |
| S | stiffness [kN/mm] |
| <i>S_{dual}</i> | stiffness obtained using a dual-threshold approach [kN/mm] |
| <i>S_{dual1}</i> | <i>S_{dual}</i> using a Young's Modulus of 1 GPa for the lower-mineralized tissue [kN/mm] |
| <i>S_{dual5}</i> | <i>S_{dual}</i> using a Young's Modulus of 5 GPa for the lower-mineralized tissue [kN/mm] |
| <i>S_{dual10}</i> | <i>S_{dual}</i> using a Young's Modulus of 10 GPa for the lower-mineralized tissue [kN/mm] |
| <i>S_{single}</i> | stiffness obtained using a single-threshold approach [kN/mm] |
| <i>S_{dual}</i> / <i>S_{single}</i> | ratio of <i>S_{dual}</i> over <i>S_{single}</i> , reflecting the contribution of lower-mineralized tissue to stiffness [-] |
| <i>S_{dual1}</i> / <i>S_{single}</i> | ratio of <i>S_{dual1}</i> over <i>S_{single}</i> [-] |
| <i>S_{dual5}</i> / <i>S_{single}</i> | ratio of <i>S_{dual5}</i> over <i>S_{single}</i> [-] |
| <i>S_{dual10}</i> / <i>S_{single}</i> | ratio of <i>S_{dual10}</i> over <i>S_{single}</i> [-] |
| Tb.Ar | trabecular bone area [mm ²] |
| Tb.BMD | trabecular bone mineral density [mg Ha/cm ³] |
| Tb.BV/TV | trabecular bone volume fraction [- or %] |
| Tb.1/N.SD | trabecular heterogeneity [mm] |
| Tb.N | trabecular number [mm ⁻¹] |
| Tb.Th | trabecular thickness [mm] |
| Tb.Sp | trabecular separation [mm] |
| TMD | tissue mineral density of the total bone region [mg HA/cm ³] |
| Tt.Ar | total bone area [mm ²] |
| Tt.BMD | total bone mineral density [mg HA/cm ³] |



1

Chapter 1

General introduction

The skeletal system forms the internal framework of the human body of which the bones constitute the largest and a highly complex component. The skeleton supports and shapes the body, contributes to movement, and protects organs and tissues, such as the brain, spinal cord, and organs in the thoracic cavity. To enable these functions, the bones of the skeleton need to have a quality that can bear the experienced loading conditions, which vary with anatomic location and function. The quality of a bone may be defined as “the totality of features and characteristics that influence a bone’s ability to resist fracture” [1] and includes among others the material properties of a bone and the spatial arrangement of the bone material, *i.e.* structural properties [1]. The structural properties are controlled by the metabolic activity and interaction of the cells within the bone: osteoblasts, osteocytes, and osteoclasts [2].

BONE STRUCTURE AND FUNCTION

The structure of a bone is a complex hierarchical arrangement (**Figure 1**, [3]). At the meter and millimeter level, bones have a certain geometry (*i.e.* size, shape, and mass) and comprise a cortical and trabecular compartment. The cortical compartment consists of cortical bone that forms the dense outer shell of a bone, the cortex [3]. The trabecular compartment consists of trabecular bone that forms a highly open, porous, honeycomb-like structure inside the bone [3]. At the micrometer level, the cortical bone consists of osteons, which are densely packed cylindrical structures of concentric bone layers that surround a central canal with small blood vessels and nerve fibers [3,4]. The trabecular bone consists of single trabeculae, which are interspersed in the bone marrow in a highly connected network [3]. At this length scale, the structural properties of the cortical and trabecular bone can be described by among others thickness and porosity (cortex) and shape, thickness, connectivity, and orientation (trabeculae). At smaller sub-micrometer levels, the structure of a bone can be described by layers of bone that are formed by bundles of assembled mineralized collagen fibrils [3,4]. The structural properties at each length scale contribute to the mechanical properties of a bone and thereby to its quality [3-5].

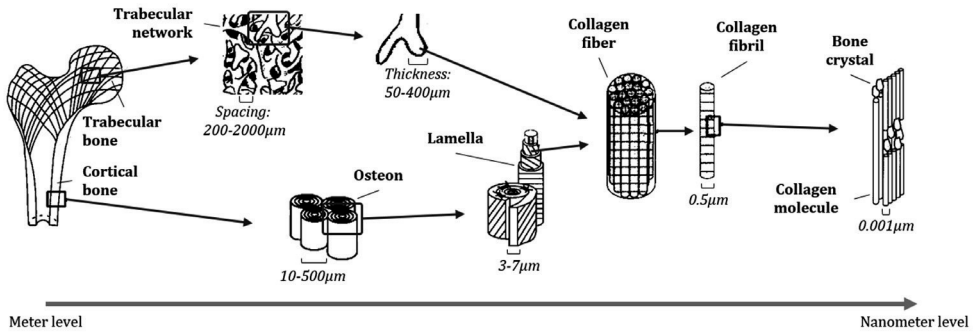


Figure 1. Hierarchical arrangement of bone. Adapted from Med Eng Phys 20(2), Rho JY *et al.*, Mechanical properties and the hierarchical structure of bone, p93, Copyright (2023), with permission from Elsevier [3].

Correspondingly, the structure of a bone is optimized to bear the experienced loads and provide the required combination of stiffness, resistance, flexibility, and deforming capacity, which depend on function and anatomic location of the bone. Vertebrae for example have a variable cross-sectional area, bone mineral density (BMD), and trabecular volume fraction and connectivity along the vertebral column [6,7], which provides the needed resistance to the specific loading conditions experienced at each vertebral level. Additionally, they largely consist of trabecular bone, which makes them light but strong structures [8,9]. The trabeculae within vertebrae are mainly oriented in superior-inferior direction, which enables bearing the compressive stresses experienced particularly in this direction [5,10]. Long bones, in contrast, predominantly consist of cortical bone at the shaft, which gradually changes to largely trabecular bone towards the joint [9,11]. Together with variations in shape, cross-sectional area, and bone mass distribution along the length of a long bone, it provides the required rigidity and stiffness at the shaft, load transfer capacity at the joint, and resistance to the specific loading conditions experienced at each level of a long bone [5,9,12]. The structural properties of a bone can also adapt to changing loading conditions in order to preserve the required load bearing capacity. This possibility to adapt to loads is reflected by for example the changes in bone size, shape, and mass with impact sports at anatomic locations that are specific for the loading conditions related to a sport [13].

The bone structure can be disturbed by disease and treatment, which can reduce the resistance to fractures and thereby increase fracture risk. This disturbance can occur at each length scale, which is reflected by for example the definition of osteoporosis as “a disease characterized by low bone mass and microarchitectural deterioration of bone tissue, leading to enhanced bone fragility and a consequent increase in fracture risk” [14]. It implies that the assessment of bone structure from meter to micrometer level has clinical relevance.

ASSESSMENT OF BONE STRUCTURE

Bone structure can be assessed using various clinically available techniques (**Figure 2**). Dual-energy X-ray absorptiometry (DXA) is a clinically widely available imaging modality for the evaluation of bone density. It is X-ray based and thus visualizes a bone based on differences in the attenuation of X-ray beams between bones and the surrounding soft tissues [15]. DXA is generally used for the two-dimensional quantification of bone mass of the lumbar spine and hip, in terms of areal BMD (aBMD), to diagnose osteoporosis, to estimate fracture risk, and to initiate and monitor treatment with anti-osteoporosis medication (AOM) [16]. Other clinically available imaging modalities can evaluate bone mass three-dimensionally (*i.e.* volumetric BMD), such as quantitative computed tomography (QCT; also X-ray based) and magnetic resonance imaging (MRI; based on tissue-dependent magnetic susceptibility) [17-20]. Assessment of the structure of the cortical and trabecular bone is restricted by the spatial resolution of the imaging modalities, considering the size of for example individual trabeculae (average thickness of $\sim 50\text{-}400\ \mu\text{m}$ and spacing of $\sim 200\text{-}2000\ \mu\text{m}$ [17-19]). Correspondingly, DXA can only indirectly quantify bone microarchitecture using texture- or pattern-based parameters (pixel size in the order of magnitude of 1 mm) [17,21], and QCT and MRI can at best estimate bone microarchitecture (slice thicknesses of $\sim 0.5\text{-}10\ \text{mm}$ and $\sim 0.5\text{-}1.5\ \text{mm}$, respectively) [17-20,22]. In contrast, the evaluation of bone specimens using histology or high-resolution *ex-vivo* imaging modalities such as micro-CT (μCT) and micro-MRI (μMRI) enables direct measurement of bone microarchitecture [17-19,23-25]. This approach requires invasive biopsies to obtain bone specimens, which are not standardly indicated in clinical practice for most diseases [23,24]. Alternatively, remnants from bone surgery can be used for such evaluation.

Developments in CT and MRI provide perspectives for direct, *in-vivo*, and noninvasive assessment of bone microarchitecture (**Figure 2**). For example, flat-panel CT uses an area of X-ray detectors instead of a row of detectors in conventional CT, which has been reported to provide sufficient spatial resolution for the quantification of trabecular microarchitecture (isotropic voxel size of $150\ \mu\text{m}$) [26,27]. As another example, cone-beam CT uses X-ray sources that emit cone-shaped beams instead of fan-shaped beams in conventional CT, which has been found promising in the quantification of bone microarchitecture in musculoskeletal applications (isotropic voxel size of $75\ \mu\text{m}$) [28]. More recently, photon-counting CT uses a type of X-ray detectors that enables direct rather than indirect conversion of X-ray photons to measurable electric signals, which may provide spatial resolutions of $70\text{-}280\ \mu\text{m}$ in whole-body systems that are currently being developed [29]. A final CT-advancement is high-resolution peripheral QCT (HR-pQCT, isotropic voxel size of $61\ \mu\text{m}$ or $82\ \mu\text{m}$), which has been

introduced in 2005 and developed as a standalone system dedicated to the assessment of the microarchitecture of peripheral bones in a research setting [30]. Developments in MRI relate to new image sequences and increased magnetic field strengths, which provides spatial resolutions in the order of magnitude of trabecular structures for the measurement of bone microarchitecture (isotropic voxel sizes up to $\sim 160 \mu\text{m}$) [22].

Of these developments, HR-pQCT has the best spatial resolution for the *in-vivo* assessment of bone microarchitecture and has thus far been the most widely available and studied modality for this assessment. This thesis therefore focuses on the use of HR-pQCT.

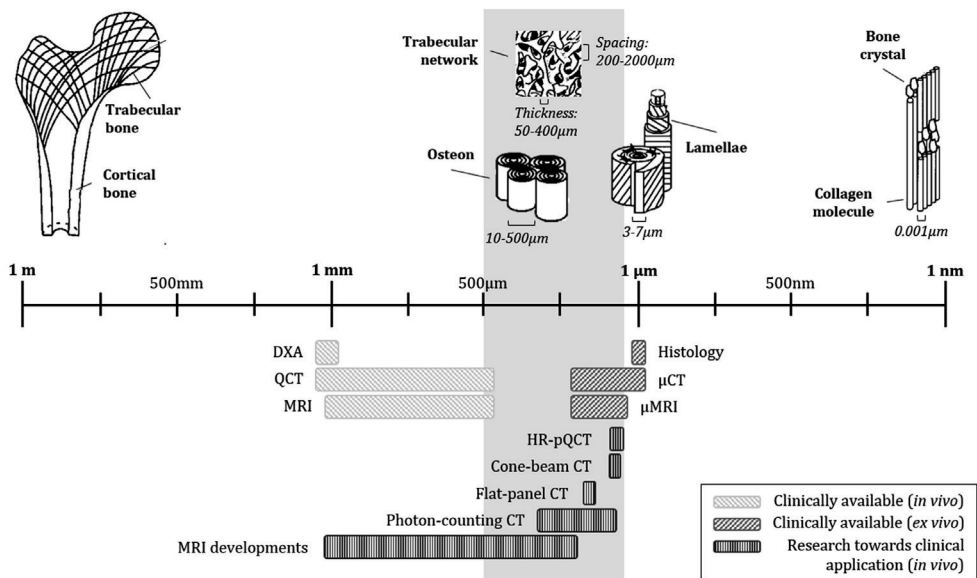


Figure 2. Overview of *in-vivo* and *ex-vivo* techniques for the assessment of bone structure. The length scales at which the techniques can evaluate bone structure are based on pixel sizes (DXA), slice thicknesses (histology, QCT, MRI, MRI developments) and spatial resolutions and isotropic voxel sizes (other techniques) from [18-20,22,25-31]. The grey bar shows the length scale needed to assess cortical and trabecular microarchitecture.

HIGH-RESOLUTION PERIPHERAL QUANTITATIVE COMPUTED TOMOGRAPHY

Two versions of HR-pQCT are in use, which are mainly located in research settings (**Table 1, Figure 3**). The first-generation HR-pQCT system has an isotropic voxel size of $82 \mu\text{m}$, while the second-generation system has an isotropic voxel size of $60.7 \mu\text{m}$. The standard clinical protocol involves acquisition of a scan of one stack of 9 mm (first-generation HR-pQCT) or 10 mm (second-generation HR-pQCT) of

the distal radius and distal tibia [31]. The standard scan region is located at a fixed distance from the reference line positioned at the distal endplate of the radius and tibia [31]. The effective radiation dose of a standard one-stack HR-pQCT scan is 3-5 μ Sv, which is approximately 0.1-0.2% of the average annual effective background radiation dose per capita in the Netherlands (2.8 mSv) [32]. The dose is comparable to that of DXA examinations (0.1-30 μ Sv) and lower than that of QCT examinations of the lumbar spine and hip (0.06-3.0 mSv) [19,33]. From the scans, the distal radius and tibia are segmented, after which cross-sectional area, volumetric BMD, and trabecular and cortical microarchitecture can be quantified. Most parameters can be directly measured from the scans, but several parameters need to be derived on first-generation HR-pQCT scans due to the spatial resolution of this generation system [31]. Additionally, bone strength can be estimated from the scans by means of finite element (FE-) analysis [31]. Typically, micro-FE (μ FE-) analysis is performed, which involves generation of a μ FE-model from an HR-pQCT scan by conversion of each bone voxel of a scan to a μ FE-element. Correspondingly, a μ FE-model contains detailed macro- and microstructural information of a bone. The elements are assigned material properties that mimic bone, after which a loading condition is applied to the model to calculate bone stiffness and to estimate failure load [31]. Both the scanner and the provided analysis software have been validated, and reproducibility studies have been performed [29,34-39]. Additionally, cross-sectional studies have been performed on age-, gender-, and ethnicity-related differences in bone microarchitecture and on the prevalence of bone fragility and osteoporosis [40,41]. Furthermore, normative datasets are available for first-generation [42-49] and second-generation [50-52] HR-pQCT systems.

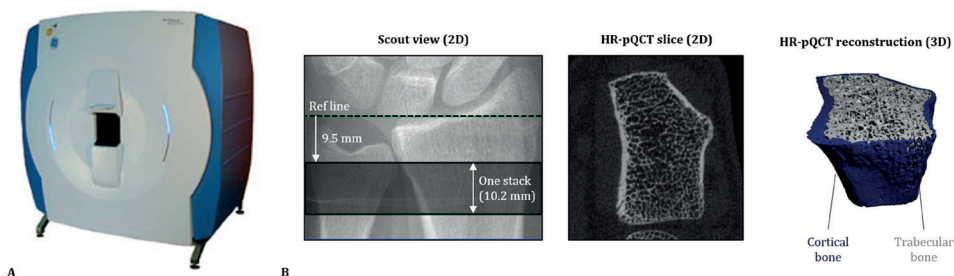


Figure 3. A) Second-generation HR-pQCT scanner; B) Example of a scout view of the distal radius to determine HR-pQCT scan region (left) with corresponding two-dimensional (2D) HR-pQCT slice and three-dimensional (3D) HR-pQCT reconstruction.

Table 1. Characteristics of the standard clinical scan protocol and analysis for first- and second-generation HR-pQCT systems (SCANCO Medical AG, Switzerland). Based on [31].

| | First-generation HR-pQCT | Second-generation HR-pQCT |
|---|---------------------------------|--|
| Standard clinical scan protocol | | |
| Scan diameter x height [mm] | 126 x 9.02 (one stack) | 140 x 10.2 (one stack) |
| Offset distance [mm] | 9.5 (radius), 22.5 (tibia) | 9.5 (radius), 22.5 (tibia) <i>or</i> 9.0 (radius), 22.0 (tibia) |
| Number of slices [-] | 110 | 168 |
| Isotropic voxel size [μm] | 82.0 | 60.7 |
| Acquisition time [min] | 2.8 | 2.0 |
| Effective radiation dose [μSv] | <3 | <5 |
| Standard quantitative analysis | | |
| <i>Total, trabecular, cortical bone:</i> | | |
| Cross-sectional area [mm^2] | Directly measured | Directly measured |
| Volumetric BMD [$\text{mg HA}/\text{cm}^3$] | Directly measured | Directly measured |
| <i>Cortical microarchitecture:</i> | | |
| Thickness [Ct.Th; mm] | Derived from volume and surface | Directly measured ¹ |
| Porosity [Ct.Po; %] | Directly measured ² | Directly measured ² |
| <i>Trabecular microarchitecture:</i> | | |
| Volume fraction [Tb.BV/TV; %] | Derived from trabecular BMD | Directly measured ³ |
| Number [Tb.N; mm^{-1}] | Directly measured ⁴ | Directly measured ⁴ |
| Thickness [Tb.Th; mm] | Derived from Tb.BV/TV and Tb.N | Directly measured ¹ |
| Separation [Tb.Sp; mm] | Derived from Tb.BV/TV and Tb.N | Directly measured ¹ |
| Heterogeneity [Tb.1/N.SD; mm] | Directly measured ⁴ | Directly measured ⁴ |

¹Measured using distance transformation; ²Measured using threshold-based pore segmentation; ³Measured using voxel counting; ⁴Measured using ridge extraction.

CLINICAL RESEARCH USING HR-pQCT

Although HR-pQCT has originally been developed for use in research settings, its use is gradually expanding towards clinical application. Several clinical applications are further discussed in this thesis.

Bone microarchitecture and strength assessment

(Rare) disorders that affect bone

HR-pQCT is increasingly being used to study bone microarchitecture and strength in secondary osteoporosis and other (rare) diseases that affect bone. There are various forms of secondary osteoporosis, which are caused by (genetic) diseases, nutritional deficiencies, treatments, or any of multiple other factors [53]. They thereby differ in pathophysiology from primary osteoporosis, which is caused by aging and hormonal changes. Consequently, skeletal effects may differ, and fractures can occur at relatively normal DXA-based aBMD [53]. HR-pQCT then provides more detailed information

on the structural bone defects than DXA. HR-pQCT has thus far been used to study among others various endocrine-related and autoimmune diseases, such as type 2 diabetes, chronic kidney disease, and hyperparathyroidism [40,41]. Based on this ability to evaluate bone microarchitecture and strength in diseased conditions *in-vivo* and noninvasively using HR-pQCT, clinical experts in rare bone diseases in the Netherlands proposed to use HR-pQCT in a clinical setting to gain new insights into bone microarchitecture and strength in patients with osteogenesis imperfecta (OI) and fibrodysplasia ossificans progressiva (FOP).

OI is a rare and heterogeneous connective tissue disorder, caused by genetic mutations related to the synthesis, structure, or post-processing of procollagen type I (a component of bone) [54]. The genetic variability is large, resulting in a large diversity in phenotypic manifestation and disease severity among individuals [55]. Nevertheless, primary characteristics are an increased bone fragility and osteoporosis due to defects in bone material and structure, which result in an increased fracture risk [55-57]. Data on the structural defects of bone in OI are scarce. Most data are DXA-based aBMD, which is generally low in OI [58]. However, aBMD does not always provide an accurate representation of the actual volumetric BMD in OI due to the two-dimensional nature of DXA combined with the occurrence of short and deformed bones in OI [58-60]. Additionally, it may, as a single parameter, not fully describe the complexity and heterogeneity of OI. HR-pQCT has recently been used to investigate bone microarchitecture in adults with OI as compared to non-OI populations [61-63], but the small sample sizes in these studies may not have fully captured the heterogeneity in OI. Furthermore, difficulties may potentially be faced when using HR-pQCT in OI, which were not addressed in these studies. Specifically, short extremities and bone deformities such as bending could challenge patient positioning and potentially influence scan region. However, extremity length was not taken into account in the previous HR-pQCT studies in adults with OI, and the effects of bone deformities on scan region were not discussed. Also, trabecular void spaces have been noted on HR-pQCT in OI [62], but their influence on HR-pQCT parameters has not been described. Evaluation of the feasibility of using HR-pQCT in OI is limited to a small study in nine children with OI [64].

FOP is a rare and genetic disease, characterized by the progressive formation of heterotopic ossifications (HOs) in ligaments, tendons, and muscles [65]. Data on mature HO in FOP are scarce. Based on macroscopic data from few studies, it has been suggested that HO has a normal modeling and remodeling and a cortical and trabecular organization [66]. Detailed evaluation of HO is limited in FOP as bone biopsies and other invasive procedures are contraindicated in this condition because they may trigger the formation of HO and thereby aggravate the disease [67]. HR-

pQCT may possibly alleviate this difficulty as it enables noninvasive assessment of bone microarchitecture, but it has, to our knowledge, not previously been used in FOP. Consequently, quantitative data on the microarchitecture of mature HO remain limited, and the feasibility of using HR-pQCT for this purpose is undescribed.

Anti-osteoporosis medication in secondary osteoporosis

HR-pQCT is also being used to study the effects of AOM-treatment on bone microarchitecture and strength [40,41,68], enabling study of the separate effects on cortical and trabecular bone. Most studies thus far have been conducted in postmenopausal women with primary osteoporosis or osteopenia (*i.e.* bone loss due to aging and hormonal changes) [68]. However, AOMs are also prescribed in patient populations with secondary forms of osteoporosis to whom the effects of AOM-treatment cannot be necessarily extrapolated due to differences in pathophysiology and possible influences of the underlying cause of the bone loss in these forms [53]. In this thesis, the use of HR-pQCT to study the effects of AOM-treatment is discussed in two forms of secondary osteoporosis, being glucocorticoid-induced osteoporosis (GIOP) and pregnancy- and lactation-associated osteoporosis (PLO).

GIOP is among the most prevalent forms of secondary osteoporosis and is induced by glucocorticoids (GCs). GCs are anti-inflammatory drugs prescribed for a wide range of medical conditions [69-71], and thus the patient population suffering from GIOP is diverse [72]. GIOP management can include pharmacological treatment, for which one of several AOMs can be prescribed [73]. Given the diverse patient population, the availability of multiple options for AOM-treatment is desired. Recently, it was found in a randomized controlled trial in GC-users that denosumab resulted in larger increases in aBMD than risedronate, which is an existing treatment option in GIOP [74,75]. The effects of both AOMs on bone microarchitecture and strength were not investigated. These effects have been studied using HR-pQCT in postmenopausal women [76-78], but they cannot necessarily be extrapolated to GIOP due to differences in the pathophysiology of the bone loss between GIOP and postmenopausal osteoporosis [72]. Correspondingly, the effects of denosumab and risedronate on bone microarchitecture and strength in individuals on GC-treatment remain to be elucidated.

PLO is a rare form of secondary osteoporosis, characterized by vertebral compression fractures and back pain during pregnancy and early postpartum [79]. Pregnancy and lactation are associated with physiological reductions in aBMD, volumetric BMD, and bone microarchitecture due to hormone-mediated adaptations in the maternal bone and mineral metabolism to meet the nutritional demands for fetal and neonatal growth [80-82]. They recover post-lactating spontaneously in most women without

long-term adverse consequences [82]. In PLO, the bone loss is more pronounced, and volumetric BMD and microarchitecture may be more impaired than in healthy controls and healthy lactating women [83,84]. The pathophysiology of PLO is only partly known, various factors may play a role, and underlying diseases cannot be excluded due to lacking data on bone quality before pregnancy in most women with PLO [79,85]. Correspondingly, disease management requires an individualized approach [79]. A clinical expert on rare bone diseases contacted us about a severe presentation of PLO and proposed to use HR-pQCT to monitor bone microarchitecture and strength during AOM-treatment in this woman.

Assessment of distal radius and scaphoid fractures

More recently, the use of HR-pQCT has also been explored in distal radius fracture healing [86,87], bone damage in finger joints in arthritis conditions [88], and knee joint changes due to disease or surgery [89]. In this thesis, the application to fractures of the forearm is discussed, specifically to fractures of the distal radius and scaphoid bone.

Distal radius fracture healing

Distal radius fractures are among the most common fractures in elderly [90,91] and often treated using cast immobilization in this age group [92]. Dutch guidelines prescribe to consider cast treatment for 3-5 weeks depending on fracture displacement and reduction, but they are based on limited evidence from clinical trials [93]. In previous HR-pQCT studies from our research group on the healing process of conservatively-treated distal radius fractures in elderly women, large visual changes around the fracture region were observed early during healing, which were suggested to reflect the formation and concomitant and subsequent remodeling of woven bone [86]. In the same studies, the stiffness of the fractured radii, computed using μ FE-analysis, increased significantly compared to baseline later during healing and continued to increase until months after cast removal [86,87]. The contribution of the lower-mineralized woven bone to the biomechanical recovery of distal radius fractures has not been quantified, and previous HR-pQCT studies are inconclusive about the differences in the stiffness of fractured distal radii during healing computed using μ FE-models that either include or exclude lower-mineralized tissue [86,94]. Lower-mineralized tissue may however play a role that is not quantified when using a single series of μ FE-models given the reported difference in the clinical and biomechanical perspective of fracture union. The use of multiple series of μ FE-models that include tissue of different mineralization densities may enable quantification of the contribution of lower-mineralized tissue to stiffness during fracture healing.

Scaphoid fracture diagnosis and healing

Fractures of the scaphoid bone, a small bone in the carpus with a unique vascularization and anatomy, are the most common carpal bone fractures [95,96]. Inadequate or delayed treatment can cause mal- or nonunion, which can lead to degenerative changes and osteoarthritis with consequent impaired mobility and functionality of the wrist [97,98]. Early and accurate diagnosis and adequate healing monitoring are therefore important but remain challenging. Clinical signs generally lack specificity, and initial radiography misses 30-40% of scaphoid fractures [99]. Therefore, current clinical practice in our medical center involves cast immobilization followed by a re-examination 10-14 days later when a scaphoid fracture is suspected based on clinical examination, also when initial radiographs are negative. Better sensitivity and specificity are obtained with bone scintigraphy, CT, and MRI, but definitely ruling in a scaphoid fracture remains difficult [99]. Consequently, there is no consensus on a gold standard imaging protocol to diagnose scaphoid fractures [100], and it cannot be excluded that scaphoid fractures remain occult with current imaging modalities [99]. The successful application of HR-pQCT to distal radius fractures and inflamed finger joints provides perspectives for application to the scaphoid bone. To our knowledge, HR-pQCT has been used to image the scaphoid bone *in vivo* in only one study thus far [101]. That study did not report on motion artefacts and scan quality, while a three-times larger scan region (and thus three-times longer scan time) is needed than with a standard HR-pQCT scan to cover the entire scaphoid bone. Therefore, the feasibility of using HR-pQCT to image the scaphoid bone remains largely unexplored and its potential to diagnose scaphoid fractures and monitor their healing to be elucidated.

Alternatively, it has been proposed to develop clinical decision rules to estimate the probability of a scaphoid fracture at presentation in the hospital [99]. Several clinical prediction rules have been explored, which combined various patient characteristics [102-104]. The shape of the scaphoid bone could possibly also be a factor in scaphoid fracture susceptibility after a fall on the outstretched hand given its anatomic location and curved shape [105-106], but the association between the shape of the scaphoid bone and the presence of a scaphoid fracture is unknown.

OBJECTIVES AND OUTLINE

The objective of this thesis is to study the use of HR-pQCT for the assessment of bone microarchitecture and strength in (rare) bone-affecting disorders, the response to AOM-treatment, and distal radius and scaphoid fractures. The first part of this thesis (**Chapters 2-5**) focuses on the use of HR-pQCT to evaluate bone microarchitecture and strength in rare conditions and in secondary osteoporosis in response to AOM-

treatment. Specifically, in **Chapter 2**, bone microarchitecture and strength are studied in a large cohort of adults with OI using HR-pQCT and an extremity-length dependent scan protocol, including a broader assessment of scan acquisition and scan analysis in this cohort. In **Chapter 3**, the explorative use of HR-pQCT in adults with FOP is studied. In **Chapter 4**, the effects of denosumab compared to risedronate are studied using HR-pQCT in adults initiating or continuing GC-treatment, and in **Chapter 5**, the effects of AOM-treatment are studied using HR-pQCT in a severe presentation of PLO. The second part of this thesis (**Chapters 6-10**) focuses on the use of HR-pQCT to evaluate distal radius fracture healing and scaphoid fracture diagnosis and healing. In **Chapter 6**, the contribution of lower-mineralized tissue to the stiffness of conservatively-treated distal radius fractures during healing is studied using a dual-density segmentation approach and multiple series of μ FE-models. In **Chapters 7-10**, the novel application of HR-pQCT to scaphoid fractures is studied: first, the feasibility of HR-pQCT imaging of the scaphoid bone is explored in **Chapter 7**, followed by a comparison of the diagnostic performance of HR-pQCT with conventional CT in **Chapter 8**, an exploration of the association between the shape of the scaphoid bone and the presence of a scaphoid fracture in **Chapter 9**, and an assessment of the healing of scaphoid fractures in **Chapter 10**. **Chapter 11** comprises a discussion of the main findings of this thesis and a conclusion and future perspectives, and **Chapter 12** summarizes the findings of this thesis.

REFERENCES

- [1] Bouxsein ML. Bone quality: where do we go from here? *Osteoporos Int.* 2003;14(5):118-27.
- [2] Seeman E, Delmas PD. Bone quality—the material and structural basis of bone strength and fragility. *N Engl J Med.* 2006;354(21):2250-61.
- [3] Rho JY, Kuhn-Spearing L, Zioupos P. Mechanical properties and the hierarchical structure of bone. *Med Eng Phys.* 1998;20(2):92-102.
- [4] Weiner S, Wagner HD. The material bone: structure-mechanical function relations. *Annu Rev Mater Sci.* 1998;28(1):271-98.
- [5] Cole JH, van der Meulen MC. Whole bone mechanics and bone quality. *Clin Orthop Relat Res.* 2011;469(8):2139-49.
- [6] Grote H, Amling M, Vogel M, Hahn M, Pösl M, Delling G. Intervertebral variation in trabecular microarchitecture throughout the normal spine in relation to age. *Bone.* 1995;16(3):301-8.
- [7] Oxland TR. Fundamental biomechanics of the spine—what we have learned in the past 25 years and future directions. *J Biomech.* 2016;49(6):817-32.
- [8] Eastell R, Mosekilde L, Hodgson SF, Riggs BL. Proportion of human vertebral body bone that is cancellous. *J Bone Miner Res.* 1990;5(12):1237-41.
- [9] Seeman E. Bone quality: the material and structural basis of bone strength. *J Bone Miner Metab.* 2008;26(1):1-8.
- [10] Galante J, Rostoker W, Ray R. Physical properties of trabecular bone. *Calcif Tissue Res.* 1970;5:236-46.
- [11] Schlenker R, VonSeggen W. The distribution of cortical and trabecular bone mass along the lengths of the radius and ulna and the implications for in vivo bone mass measurements. *Calcif Tissue Res.* 1976;20(1):41-52.
- [12] Zebaze RM, Jones A, Welsh F, Knackstedt M, Seeman E. Femoral neck shape and the spatial distribution of its mineral mass varies with its size: clinical and biomechanical implications. *Bone.* 2005;37(2):243-52.
- [13] Tenforde AS, Fredericson M. Influence of sports participation on bone health in the young athlete: a review of the literature. *PM&R.* 2011;3(9):861-7.
- [14] World Health Organization. Assessment of fracture risk and its application to screening for postmenopausal osteoporosis: report of a WHO study group. World Health Organization. 1994.
- [15] Suetens P. Radiography. Fundamental of medical imaging. Second edition. Cambridge, United Kingdom: Cambridge University Press; 2009.
- [16] Blake GM, Fogelman I. The role of DXA bone density scans in the diagnosis and treatment of osteoporosis. *Postgrad Med J.* 2007;83(982):509-17.
- [17] Bauer JS, Link TM. Advances in osteoporosis imaging. *Eur J Radiol.* 2009;71(3):440-9.
- [18] Genant H, Engelke K, Prevrhal S. Advanced CT bone imaging in osteoporosis. *Rheumatology.* 2008;47(suppl_4):iv9-iv16.
- [19] Griffith JF, Genant HK. Bone mass and architecture determination: state of the art. *Best Pract Res Clin Endocrinol Metab.* 2008;22(5):737-64.
- [20] Engelke K, Adams JE, Armbrrecht G, et al. Clinical use of quantitative computed tomography and peripheral quantitative computed tomography in the management of osteoporosis in adults: the 2007 ISCD Official Positions. *J Clin Densitom.* 2008;11(1):123-162.
- [21] Bousson V, Bergot C, Sutter B, Levitz P, Cortet B. Trabecular bone score (TBS): available knowledge, clinical relevance, and future prospects. *Osteoporos Int.* 2012;23(5):1489-501.
- [22] Chang G, Boone S, Martel D, et al. MRI assessment of bone structure and microarchitecture. *J Magn Reson Imaging.* 2017;46(2):323-37.

- [23] Compston J, Skingle L, Dempster DW. Bone histomorphometry. Vitamin D: Elsevier; 2018. p. 959-73.
- [24] Kulak CAM, Dempster DW. Bone histomorphometry: a concise review for endocrinologists and clinicians. *Arq Bras Endocrinol Metabol.* 2010;54:87-98.
- [25] Carbonare LD, Giannini S. Bone microarchitecture as an important determinant of bone strength. *J Endocrinol Invest.* 2004;27(1):99-105.
- [26] Reichardt B, Sarwar A, Bartling SH, et al. Musculoskeletal applications of flat-panel volume CT. *Skeletal Radiol.* 2008;37(12):1069-76.
- [27] Mulder L, van Rietbergen B, Noordhoek NJ, Ito K. Determination of vertebral and femoral trabecular morphology and stiffness using a flat-panel C-arm-based CT approach. *Bone.* 2012;50(1):200-8.
- [28] Mys K, Stockmans F, Vereecke E, van Lenthe GH. Quantification of bone microstructure in the wrist using cone-beam computed tomography. *Bone.* 2018;114:206-14.
- [29] Willeminck MJ, Persson M, Pourmorteza A, Pelc NJ, Fleischmann D. Photon-counting CT: technical principles and clinical prospects. *Radiology.* 2018;289(2):293-312.
- [30] Boutroy S, Bouxsein ML, Munoz F, Delmas PD. In vivo assessment of trabecular bone microarchitecture by high-resolution peripheral quantitative computed tomography. *J Clin Endocrinol Metab.* 2005;90(12):6508-15.
- [31] Whittier DE, Boyd SK, Burghardt AJ, et al. Guidelines for the assessment of bone density and microarchitecture in vivo using high-resolution peripheral quantitative computed tomography. *Osteoporos Int.* 2020;31(9):1607-27.
- [32] Blootstelling aan ioniserende straling samengevat [Dutch]. <https://www.rivm.nl/straling-en-radioactiviteit/blootstelling-en-gezondheidsrisico/blootstelling-aan-ioniserende-straling-samengevat>.
- [33] Damilakis J, Adams JE, Guglielmi G, Link TM. Radiation exposure in X-ray-based imaging techniques used in osteoporosis. *Eur Radiol.* 2010;20(11):2707-14.
- [34] Burghardt AJ, Buie HR, Laib A, Majumdar S, Boyd SK. Reproducibility of direct quantitative measures of cortical bone microarchitecture of the distal radius and tibia by HR-pQCT. *Bone.* 2010;47(3):519-28.
- [35] Chiba K, Okazaki N, Kurogi A, et al. Precision of second-generation high-resolution peripheral quantitative computed tomography: intra-and intertester reproducibilities and factors involved in the reproducibility of cortical porosity. *J Clin Densitom.* 2018;21(2):295-302.
- [36] MacNeil JA, Boyd SK. Improved reproducibility of high-resolution peripheral quantitative computed tomography for measurement of bone quality. *Med Eng Phys.* 2008;30(6):792-9.
- [37] Zhou B, Wang J, Yu YE, et al. High-resolution peripheral quantitative computed tomography (HR-pQCT) can assess microstructural and biomechanical properties of both human distal radius and tibia: Ex vivo computational and experimental validations. *Bone.* 2016;86:58-67.
- [38] Arias-Moreno AJ, Hosseini H, Bevers M, Ito K, Zysset P, van Rietbergen B. Validation of distal radius failure load predictions by homogenized-and micro-finite element analyses based on second-generation high-resolution peripheral quantitative CT images. *Osteoporos Int.* 2019;30(7):1433-43.
- [39] Pistoia W, van Rietbergen B, Lochmüller E-M, Lill C, Eckstein F, Rügsegger P. Image-based micro-finite-element modeling for improved distal radius strength diagnosis: moving from “bench” to “bedside”. *J Clin Densitom.* 2004;7(2):153-60.
- [40] Nishiyama KK, Shane E. Clinical imaging of bone microarchitecture with HR-pQCT. *Curr Osteoporos Rep.* 2013;11(2):147-55.

- [41] Geusens P, Chapurlat R, Schett G, et al. High-resolution in vivo imaging of bone and joints: a window to microarchitecture. *Nat Rev Rheumatol.* 2014;10(5):304-13.
- [42] Macdonald HM, Nishiyama KK, Kang J, Hanley DA, Boyd SK. Age-related patterns of trabecular and cortical bone loss differ between sexes and skeletal sites: a population-based HR-pQCT study. *J Bone Miner Res.* 2011;26(1):50-62.
- [43] Hansen S, Shambhogue V, Folkestad L, Nielsen MME, Brixen K. Bone microarchitecture and estimated strength in 499 adult Danish women and men: a cross-sectional, population-based high-resolution peripheral quantitative computed tomographic study on peak bone structure. *Calcif Tissue Int.* 2014;94(3):269-81.
- [44] Burt LA, Macdonald HM, Hanley DA, Boyd SK. Bone microarchitecture and strength of the radius and tibia in a reference population of young adults: an HR-pQCT study. *Arch Osteoporos.* 2014;9(1):1-9.
- [45] Hung V, Zhu T, Cheung W-H, et al. Age-related differences in volumetric bone mineral density, microarchitecture, and bone strength of distal radius and tibia in Chinese women: a high-resolution pQCT reference database study. *Osteoporos Int.* 2015;26(6):1691-703.
- [46] Alvarenga J, Fuller H, Pasoto S, Pereira R. Age-related reference curves of volumetric bone density, structure, and biomechanical parameters adjusted for weight and height in a population of healthy women: an HR-pQCT study. *Osteoporos Int.* 2017;28(4):1335-46.
- [47] Burt LA, Liang Z, Sajobi TT, Hanley DA, Boyd SK. Sex-and site-specific normative data curves for HR-pQCT. *J Bone Miner Res.* 2016;31(11):2041-7.
- [48] Gabel L, Macdonald HM, Nettlefold LA, McKay HA. Sex-, ethnic-, and age-specific centile curves for pQCT-and HR-pQCT-derived measures of bone structure and strength in adolescents and young adults. *J Bone Miner Res.* 2018;33(6):987-1000.
- [49] Zhu TY, Yip BH, Hung VW, et al. Normative standards for HRpQCT parameters in Chinese men and women. *J Bone Miner Res.* 2018;33(10):1889-99.
- [50] Yu F, Xu Y, Hou Y, et al. Age-, site-, and sex-specific normative centile curves for HR-pQCT-derived microarchitectural and bone strength parameters in a Chinese mainland population. *J Bone Miner Res.* 2020;35(11):2159-70.
- [51] Whittier DE, Burt LA, Hanley DA, Boyd SK. Sex-and site-specific reference data for bone microarchitecture in adults measured using second-generation HR-pQCT. *J Bone Miner Res.* 2020;35(11):2151-8.
- [52] Warden S, Liu Z, Fuchs R, van Rietbergen B, Moe S. Reference data and calculators for second-generation HR-pQCT measures of the radius and tibia at anatomically standardized regions in White adults. *Osteoporos Int.* 2022;33(4):791-806.
- [53] Mirza F, Canalis E. Secondary osteoporosis: pathophysiology and management. *Eur J Endocrinol.* 2015;173(3):R131.
- [54] Forlino A, Marini JC. Osteogenesis imperfecta. *Lancet.* 2016;387(10028):1657-71.
- [55] Van Dijk F, Sillence D. Osteogenesis imperfecta: clinical diagnosis, nomenclature and severity assessment. *Am J Med Genet. Part A.* 2014;164(6):1470-81.
- [56] Nijhuis WH, Eastwood DM, Allgrove J, et al. Current concepts in osteogenesis imperfecta: bone structure, biomechanics and medical management. *J Child Orthop.* 2019;13(1):1-11.
- [57] Folkestad L, Hald JD, Ersbøll AK, et al. Fracture rates and fracture sites in patients with osteogenesis imperfecta: a nationwide register-based cohort study. *J Bone Miner Res.* 2017;32(1):125-34.
- [58] Fratzl-Zelman N, Misof BM, Klaushofer K, Roschger P. Bone mass and mineralization in osteogenesis imperfecta. *Wien Med Wochenschr.* 2015;165(13-14):271-7.

- [59] Rauch F, Tuttlewski B, Schonau E. The bone behind a low areal bone mineral density: peripheral quantitative computed tomographic analysis in a woman with osteogenesis imperfecta. *J Musculoskelet Neuronal Interact.* 2002;2(4):306-8.
- [60] Gatti D, Colapietro F, Fracassi E, et al. The volumetric bone density and cortical thickness in adult patients affected by osteogenesis imperfecta. *J Clin Densitom.* 2003;6(2):173-7.
- [61] Folkestad L, Hald JD, Hansen S, et al. Bone geometry, density, and microarchitecture in the distal radius and tibia in adults with osteogenesis imperfecta type I assessed by high-resolution pQCT. *J Bone Miner Res.* 2012;27(6):1405-12.
- [62] Kocijan R, Muschitz C, Haschka J, et al. Bone structure assessed by HR-pQCT, TBS and DXL in adult patients with different types of osteogenesis imperfecta. *Osteoporos Int.* 2015;26(10):2431-40.
- [63] Rolvien T, Stürznickel J, Schmidt FN, et al. Comparison of bone microarchitecture between adult osteogenesis imperfecta and early-onset osteoporosis. *Calcif Tissue Int.* 2018;103(5):512-21.
- [64] Fennimore DJ, Digby M, Paggiosi M, et al. High-resolution peripheral quantitative computed tomography in children with osteogenesis imperfecta. *Pediatr Radiol.* 2020;50(12):1781-7.
- [65] Kaplan FS, Glaser DL, Shore EM, et al. The phenotype of fibrodysplasia ossificans progressiva. *Clin Rev Bone Miner Metab.* 2005;3:183-188.
- [66] Kaplan FS, Strear CM, Zasloff MA. Radiographic and scintigraphic features of modeling and remodeling in the heterotopic skeleton of patients who have fibrodysplasia ossificans progressiva. *Clin Orthop Relat Res.* 1994(304):238-47.
- [67] Kitterman JA, Kantanie S, Rocke DM, Kaplan FS. Iatrogenic harm caused by diagnostic errors in fibrodysplasia ossificans progressiva. *Pediatrics.* 2005;116(5):e654-e61.
- [68] Lespessailles E, Hambli R, Ferrari S. Osteoporosis drug effects on cortical and trabecular bone microstructure: a review of HR-pQCT analyses. *BoneKEy Rep.* 2016;5.
- [69] Fardet L, Petersen I, Nazareth I. Prevalence of long-term oral glucocorticoid prescriptions in the UK over the past 20 years. *Rheumatology.* 2011;50(11):1982-90.
- [70] Overman RA, Yeh JY, Deal CL. Prevalence of oral glucocorticoid usage in the United States: a general population perspective. *Arthritis Care Res.* 2013;65(2):294-8.
- [71] Laugesen K, Jørgensen JOL, Sørensen HT, Petersen I. Systemic glucocorticoid use in Denmark: a population-based prevalence study. *BMJ Open.* 2017;7(5):e015237.
- [72] Adami G, Saag K. Glucocorticoid-induced osteoporosis: 2019 concise clinical review. *Osteoporos Int.* 2019;30(6):1145-56.
- [73] Lekamwasam S, Adachi JD, Agnusdei D, et al. A framework for the development of guidelines for the management of glucocorticoid-induced osteoporosis. *Osteoporos Int.* 2012;23:2257-76.
- [74] Saag KG, Pannacciulli N, Geusens P, et al. Denosumab versus risedronate in glucocorticoid-induced osteoporosis: final results of a twenty-four-month randomized, double-blind, double-dummy trial. *Arthritis Rheumatol.* 2019;71(7):1174-84.
- [75] Saag KG, Wagman RB, Geusens P, et al. Denosumab versus risedronate in glucocorticoid-induced osteoporosis: a multicentre, randomised, double-blind, active-controlled, double-dummy, non-inferiority study. *Lancet Diabetes Endocrinol.* 2018;6(6):445-54.
- [76] Seeman E, Delmas PD, Hanley DA, et al. Microarchitectural deterioration of cortical and trabecular bone: differing effects of denosumab and alendronate. *J Bone Miner Res.* 2010;25(8):1886-94.
- [77] Tsai JN, Uihlein AV, Burnett-Bowie SAM, et al. Comparative effects of teriparatide, denosumab, and combination therapy on peripheral compartmental bone density, microarchitecture, and estimated strength: the DATA-HRpQCT Study. *J Bone Miner Res.* 2015;30(1):39-45.
- [78] Bala Y, Chapurlat R, Cheung AM, et al. Risedronate slows or partly reverses cortical and trabecular microarchitectural deterioration in postmenopausal women. *J Bone Miner Res.* 2014;29(2):380-8.

- [79] Kovacs C, Ralston S. Presentation and management of osteoporosis presenting in association with pregnancy or lactation. *Osteoporos Int.* 2015;26(9):2223-41.
- [80] Brembeck P, Lorentzon M, Ohlsson C, Winkvist A, Augustin H. Changes in cortical volumetric bone mineral density and thickness, and trabecular thickness in lactating women postpartum. *J Clin Endocrinol Metab.* 2015;100(2):535-43.
- [81] Ó Breasail M, Prentice A, Ward K. Pregnancy-Related Bone Mineral and Microarchitecture Changes in Women Aged 30 to 45 Years. *J Bone Miner Res.* 2020;35(7):1253-62.
- [82] Kovacs CS. Maternal mineral and bone metabolism during pregnancy, lactation, and post-weaning recovery. *Physiol Rev.* 2016.
- [83] Scioscia MF, Vidal M, Sarli M, et al. Severe Bone Microarchitecture Impairment in Women With Pregnancy and Lactation-Associated Osteoporosis. *J Endocr Soc.* 2021;5(5):bvab031.
- [84] Butscheidt S, Tsourdi E, Rolvien T, et al. Relevant genetic variants are common in women with pregnancy and lactation-associated osteoporosis (PLO) and predispose to more severe clinical manifestations. *Bone.* 2021;147:115911.
- [85] Winter EM, Ireland A, Butterfield NC, et al. Pregnancy and lactation, a challenge for the skeleton. *Endocr Connect.* 2020;9(6):R143-R57.
- [86] de Jong JJ, Willems PC, Arts JJ, et al. Assessment of the healing process in distal radius fractures by high resolution peripheral quantitative computed tomography. *Bone.* 2014;64:65-74.
- [87] de Jong JJ, Heyer FL, Arts JJ, et al. Fracture repair in the distal radius in postmenopausal women: a follow-up 2 years Postfracture using HRpQCT. *J Bone Miner Res.* 2016;31(5):1114-22.
- [88] Nagaraj S, Finzel S, Stok KS, Barnabe C, collaboration S. High-resolution peripheral quantitative computed tomography imaging in the assessment of periarticular bone of metacarpophalangeal and wrist joints. *J Rheumatol.* 2016;43(10):1921-34.
- [89] Kroker A, Zhu Y, Manske SL, Barber R, Mohtadi N, Boyd SK. Quantitative in vivo assessment of bone microarchitecture in the human knee using HR-pQCT. *Bone.* 2017;97:43-8.
- [90] Baron JA, Karagas M, Barrett J, et al. Basic epidemiology of fractures of the upper and lower limb among Americans over 65 years of age. *Epidemiology.* 1996;7(6):612-8.
- [91] Karl JW, Olson PR, Rosenwasser MP. The epidemiology of upper extremity fractures in the United States, 2009. *J Orthop Trauma.* 2015;29(8):e242-e4.
- [92] Chung KC, Shauver MJ, Birkmeyer JD. Trends in the United States in the treatment of distal radial fractures in the elderly. *J Bone Joint Surg Am.* 2009;91(8):1868.
- [93] NVvH DNVvH. Distale radiusfracturen. Duur immobilisatie bij distale radiusfracturen2021.
- [94] Spanswick P, Whittier D, Kwong C, Korley R, Boyd S, Schneider P. Restoration of Stiffness During Fracture Healing at the Distal Radius, Using HR-pQCT and Finite Element Methods. *J Clin Densitom.* 2021;24(3):422-432.
- [95] Van Onselen E, Karim R, Hage JJ, Ritt M. Prevalence and distribution of hand fractures. *J Hand Surg.* 2003;28(5):491-5.
- [96] Duckworth AD, Jenkins PJ, Aitken SA, Clement ND, McQueen MM. Scaphoid fracture epidemiology. *J Trauma Acute Care Surg.* 2012;72(2):E41-E5.
- [97] Hackney LA, Dodds SD. Assessment of scaphoid fracture healing. *Curr Rev Musculoskelet Med.* 2011;4:16-22.
- [98] Mack G, Bosse M, Gelberman RH, Yu E. The natural history of scaphoid non-union. *J Bone Joint Surg Am.* 1984;66(4):504-9.
- [99] Duckworth A, Ring D, McQueen M. Assessment of the suspected fracture of the scaphoid. *J Bone Joint Surg Br.* 2011;93(6):713-9.
- [100] Groves AM, Kayani I, Syed R, et al. An international survey of hospital practice in the imaging of acute scaphoid trauma. *Am J Roentgenol.* 2006;187(6):1453-6.

- [101] Reina N, Cavaignac E, Trousdale WH, Laffosse JM, Braga J. Laterality and grip strength influence hand bone micro-architecture in modern humans, an HR p QCT study. *J Anat.* 2017;230(6):796-804.
- [102] Parvizi J, Wayman J, Kelly P, Moran CG. Combining the clinical signs improves diagnosis of scaphoid fractures: a prospective study with follow-up. *J Hand Surg Eur Vol.* 1998;23B:324-327.
- [103] Rhemrev SJ, Beeres FJP, Van Leerdam RH, Hogervorst M, Ring D. Clinical prediction rule for suspected scaphoid fractures: A Prospective Cohort Study. *Injury.* 2010;41:1026-1030.
- [104] Duckworth AD, Buijze GA, Moran M, et al. Predictors of fracture following suspected injury to the scaphoid. *J Bone Joint Surg Br.* 2012;94B:961-968.
- [105] Weber ER, Chao EY. An experimental approach to the mechanism of scaphoid waist fractures. *J Hand Surg Am.* 1978;3:142-148.
- [106] Majima M, Horii E, Matsuki H, Hirata H, Genda E. Load transmission through the wrist in the extended position. *J Hand Surg Am.* 2008;33:182-188.

PART 1

Bone microarchitecture and
strength from HR-pQCT in disease
and with treatment



2

Chapter 2

Bone microarchitecture and strength in adults with osteogenesis imperfecta using HR-pQCT: normative comparison and challenges

Melissa S.A.M. Bevers, Arjan G.J. Harsevoort, Koert Gooijer, Caroline E. Wyers, Hans Feenstra, Bert van Rietbergen, Martijn F. Boomsma, Joop P. van den Bergh, Guus J.M. Janus

Accepted for publication in J. Bone Miner. Res. (revised version)

ABSTRACT

Data on bone microarchitecture in osteogenesis imperfecta (OI) are scarce. The aim of this cross-sectional study was to assess bone microarchitecture and strength in a large cohort of adults with OI using high-resolution peripheral quantitative CT (HR-pQCT) and to evaluate the use of HR-pQCT in this cohort. Second-generation HR-pQCT scans were obtained at the distal radius and tibia using an extremity-length dependent scan protocol in 118 men and women (≥ 18 years) with Sillence OI type I, III, or IV. HR-pQCT parameters were compared with a normative dataset from literature and expressed as Z -scores. In total, 102 radius and 105 tibia scans of sufficient quality could be obtained, of which 91 radius and 91 tibia scans had no deviated axial angle as compared to scans of 13 young women (radius: 5.1-21.9°; tibia: 0-10.8°). At the radius, Z -scores for trabecular BMD, number, and separation were -1.6 ± 1.3 , -2.5 ± 1.4 , and -2.7 (IQR: 2.7), respectively. Z -scores for bone stiffness and failure load were -1.4 ± 1.5 and -1.1 ± 1.2 , respectively. Mean Z -scores for trabecular thickness and cortical parameters were normal. Z -scores for trabecular BMD, stiffness, failure load, and cortical area and thickness were significantly lower at the tibia. In scans with a deviated axial angle, the proportion of Z -scores < -4 or > 4 was significantly higher for trabecular BMD and separation (radius) or for most total and trabecular parameters (tibia). Local microarchitectural inhomogeneities were observed; most often void volumes in the trabecular compartment. To conclude, especially trabecular bone microarchitecture and bone strength were reduced in adults with OI as compared to normative data. Most HR-pQCT scans could be obtained without difficulties, although ten percent of the scans may have a deviated axial angle in OI. Furthermore, standard HR-pQCT analyses may not always give reliable results in OI due to microarchitectural inhomogeneities.

INTRODUCTION

Osteogenesis imperfecta (OI) is a rare and largely heterogeneous connective tissue disorder. It is caused by genetic mutations related to the structure or processing of procollagen type I [1], thereby affecting quantity or quality of collagen type I [1]. Many causative genetic mutations have been discovered today, resulting in a large genetic heterogeneity [2,3]. Consequently, clinical phenotype and disease severity are heterogeneous among individuals with OI. Clinical phenotype can include a broad range of skeletal and extra-skeletal characteristics [4], but primary characteristics are an increased bone fragility due to defects in the bone material and structure with a consequent increased fracture risk [4-6]. Characteristics that occur in some but not all individuals with OI are among others short stature, bone deformities, blue sclerae, and dentinogenesis imperfecta [4].

Data on the defects in bone structure in OI are scarce. Available data are mostly areal bone mineral density (aBMD) from dual-energy X-ray absorptiometry (DXA). aBMD is generally low in individuals with OI [7], but it can be interfered by bone size and deformity [7,8]. Volumetric BMD, as assessed using peripheral quantitative computed tomography (pQCT), has been reported to be reduced, normal, or elevated in OI depending on skeletal site [8,9]. Bone microarchitecture in OI has been less well studied. Several histomorphometry studies on iliac crests biopsies of children and adults with OI suggested thinner cortices and lower trabecular bone volumes with less and thinner trabeculae in OI as compared to healthy controls [10-13]. More recently, several studies have used high-resolution pQCT (HR-pQCT) to non-invasively assess bone microarchitecture in adults with OI and reported an impairment of especially trabecular bone microarchitecture as compared to healthy controls [14-16]. These histomorphometry and HR-pQCT studies were generally limited in sample size [11-16] and mostly included individuals with mild to moderate OI (Sillence type I and IV) [10-12,14,16]. Consequently, the interindividual heterogeneity of OI may not have been fully captured in these studies.

Additionally, difficulties may arise when using HR-pQCT in OI, which have not been fully addressed in previous HR-pQCT studies in OI. For example, the short stature and bone deformities, *e.g.* bending, in OI could challenge the positioning for scan acquisition and may potentially influence scan region and thereby HR-pQCT parameters. Specifically, short extremities can lead to relatively proximal scan regions when the standard HR-pQCT scan acquisition protocol is used, which could influence HR-pQCT parameters due to the changes in bone structure along the length of the standardly scanned radius and tibia [17,18]. Yet, extremity length was not taken into account in previous HR-pQCT studies that compared OI with healthy controls [14-

16]. Bone deformities were also not addressed, while they may hamper the acquisition of scans that are axially aligned with the bone. Another potential difficulty are empty trabecular volumes, which have been noted in OI previously but which influence on HR-pQCT parameters was not discussed [15,19]. Besides that, previous HR-pQCT studies in OI were limited to first-generation HR-pQCT and did not include micro-finite element (μ FE-) analysis to estimate bone strength [14-16]. The aims of our study were 1) to assess bone microarchitecture and strength in a large cohort of adults with OI (Sillence OI types I, III, and IV [20]) using second-generation HR-pQCT and an extremity-length dependent scan protocol, and 2) to evaluate potential challenges in the acquisition and analysis of HR-pQCT scans in this cohort related to short stature, bone deformities, and microarchitectural inhomogeneities.

METHODS

Study population

Between September 2021 and July 2022, adults with clinically confirmed OI (≥ 18 years old) and treatment at the Expertise Center for Osteogenesis Imperfecta of medical center Isala, Zwolle (The Netherlands) were screened for participation in this cross-sectional study. Exclusion criteria were limited mobility that would impede proper and comfortable positioning for scan acquisition based on a pre-screening from available radiographs, a recent fracture at both distal radii and tibiae (< 2 years), a malignancy in recent medical history (< 2 years), a severe kidney disease (eGFR < 30 ml/min) or other metabolic diseases that affect bone, treatment with glucocorticoids < 3 months ago, pregnancy, and cognitive impairment or inability to understand the conditions of the study as judged by the principal investigator. Individuals that met these criteria and agreed to participate provided written informed consent. The study was approved by an independent Medical Ethics Committee (Isala Hospital Zwolle; NL76107.075.21).

Clinical characteristics

Clinical data were available at the OI Expertise Center as part of standard clinical practice. The data that were extracted for this study were clinical OI type based on the Sillence classification [20]; causative genetic mutation; level of mobility based on a modified version of the Bleck classification [21,22]; medical history of fracture based on detailed anamnestic evaluation; results of DXA examinations < 3 years of study initiation; bisphosphonate (BP) use classified as current use, recent use (< 3 years of study initiation), non-recent use (> 3 years of study initiation), and never use; serum 25-OH vitamin D level; and the bone markers collagen type I C-terminal telopeptide (CTX) and procollagen type I N-terminal propeptide (P1NP).

HR-pQCT imaging

Scan acquisition

HR-pQCT scans were taken at the distal radius and tibia (XtremeCT II, Scanco Medical AG, Switzerland) at VieCuri Medical Center (Venlo, The Netherlands). The non-dominant site was scanned unless prior recent fracture (< 2 years), surgery, or metal implants. During scan acquisition, the participants were seated in the standard chair used for HR-pQCT imaging. In case a wheelchair-dependent participant was not able to transfer to the standard chair, the wheelchair was used. Standard motion restraining holders were used to immobilize the forearm (radius scan) and lower leg (tibia scan). The scans were taken using an extremity-length dependent scan protocol to take into account short extremities in OI [23]. Using this protocol, a reference line was placed at the medial edge of the distal endplate of the radius (radius scan) or at the rim of the distal endplate of the tibia (tibia scan), and the center of the HR-pQCT scan was positioned proximally from this line at a distance equal to 4.0% of the radius length and 7.3% of the tibia length, respectively. Each scan acquisition took approximately 2 minutes and had an effective radiation dose of approximately 5 μ Sv. After acquisition, the quality of the scan was assessed by the operator based on a single low-resolution preview slice. In case of motion artefacts on this preview slice, the scan was repeated once. The scans were reconstructed with a voxel size of 61 μ m.

Evaluation of BMD, microarchitecture, and strength

The scans were analyzed conform standard protocol. First, scan quality was graded based on the reconstructed slices by one investigator (MB) according to the standard five-point grading system [24]. Scans of grade 4-5 were excluded from further analysis. From the scans of sufficient quality (grade 1-3), the distal radius and tibia were automatically contoured using software provided by the manufacturer. The periosteal contours were visually inspected and manually adjusted when deviating from bone margins. The endosteal contours were not inspected. Subsequently, the contoured radii and tibiae were evaluated using standard analysis software, which included quantification of total, trabecular, and cortical cross-sectional area and BMD, and cortical and trabecular microarchitecture [25]. Additionally, micro-finite element (μ FE-) analysis was performed to estimate bone stiffness and failure load (FL) in compression [26,27]. The evaluated parameters were compared with age- and gender-matched controls from a recently published normative dataset [26], obtained using the same scan and analysis protocol as in our study.

Evaluation of deviated scanned regions

To objectively detect deviations in scanned bone regions due to for example bending, changed anatomic alignment after fracture, and factors related to positioning for scan acquisition, we developed an algorithm that defined the line between the centroid of the

periosteal bone contour on the first and last slice of an HR-pQCT scan (**Figure 1A**). The smallest angle between this line and the axial scan direction was then computed and compared to the same angle of HR-pQCT scans of a control group of 13 young women obtained using the same scanner and scan protocol. The angle, referred to as ‘axial angle’, was considered to be deviated when it was lower than the 25th percentile - 1.5 x interquartile range (IQR) or higher than the 75th percentile + 1.5 x IQR of the angle in the control group. This equaled an axial scan angle outside the range of 5.1-21.9° for the radius scans and an axial scan angle > 10.8° for the tibia scans (**Figure 1B**).

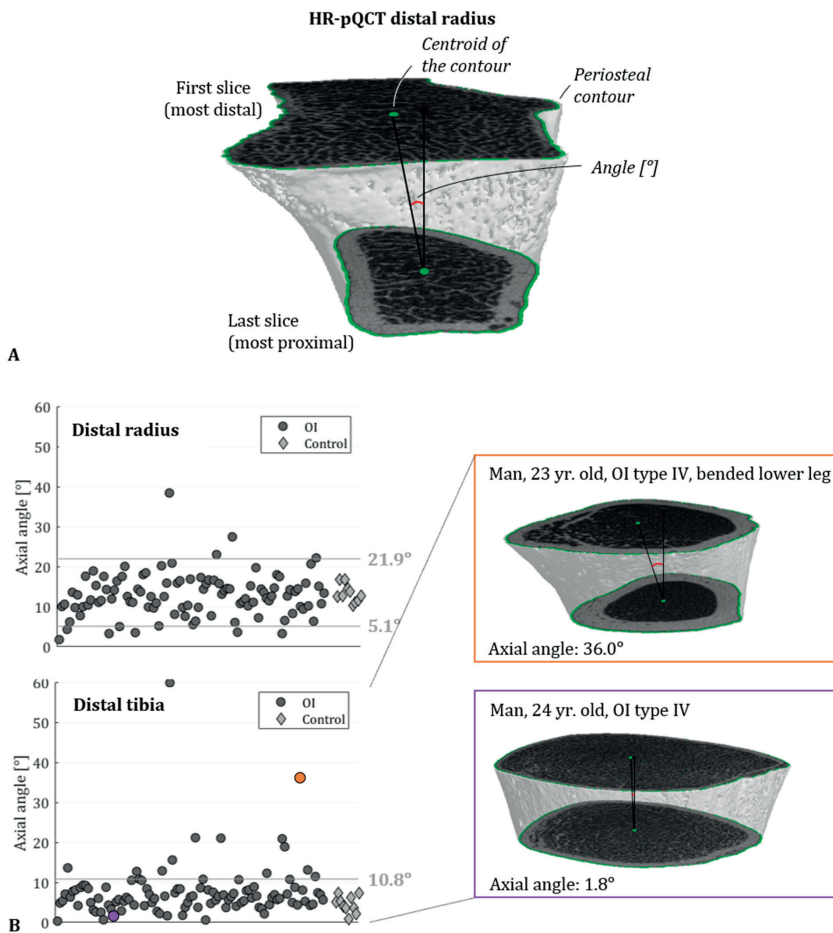


Figure 1. A) Axial angle of an HR-pQCT scan, defined as the angle between the axial scan direction and the line that connects the centroid of the periosteal contour on the first and last slice of an HR-pQCT scan. B) The axial angle of the radius (top) and tibia (bottom) scans. The grey lines indicate the 25th percentile - 1.5x the interquartile range and the 75th percentile + 1.5x the interquartile range of the angle in the control group of 13 healthy young women. The two three-dimensional visualizations depict an HR-pQCT scan of the distal tibia with an axial angle outside (top; orange) or within (bottom; purple) the range defined by the grey lines.

Statistical analysis

The comparison of the HR-pQCT parameters with the normative data was expressed as *Z*-scores; *i.e.* the number of standard deviations difference from the median value of age- and gender-matched controls from the normative dataset [26]. A negative *Z*-score indicated a value below the median of age- and gender-matched controls and *vice versa* for all HR-pQCT parameters except for trabecular separation (Tb.Sp), cortical porosity (Ct.Po), and cortical pore diameter (Ct.Po.Dm). For these three parameters, a negative *Z*-score indicated a value above the age- and gender-matched median and *vice versa*.

Participant characteristics and *Z*-scores for the HR-pQCT parameters were analyzed for all participants together and for subgroups of participants with mild OI (Sillence type I) or moderate to severe OI (Sillence types IV and III, respectively). Sillence OI types III and IV were pooled for the subgroup analysis due to the small sample size of especially OI type III. Absolute and categorized *Z*-scores for the HR-pQCT parameters were analyzed separately for the scans with and without deviated axial angle. For both the entire group and the two subgroups, the distribution of numerical variables was assessed visually (Q-Q plot) and quantitatively (Shapiro-Wilk test). In case of a normal distribution and a sample size of > 20 , a numerical variable was described as mean \pm standard deviation. In case of a non-normal distribution or a sample size < 20 , a numerical variable was described as median (IQR). Differences in absolute *Z*-scores for HR-pQCT parameters between the distal radius and tibia were evaluated using Independent Samples *T* Tests or Mann-Whitney U Tests, depending on the normality of the *Z*-scores and the sample sizes. Additionally, participant characteristics and categorized *Z*-scores for the HR-pQCT parameters were compared between the scans with and without deviated axial angle. For this comparison, Independent-Samples Mann-Whitney U Tests were used to assess the difference in numerical variables between the two groups of scans, and two-sided Fisher's Exact Tests were used to assess the association of categorical variables with the deviation of the axial angle (yes *vs.* no deviation). The significance level was set at $\alpha = 0.05$. All analyses were performed in SPSS (SPSS 26.0, IBM Corp., Armonk, NY, USA).

RESULTS

Participant characteristics

A total of 222 adults with OI were screened for study participation of whom 127 patients were eligible for study participation and gave written informed consent (**Figure 2; Study participants**). The other 95 adults were not eligible for study participation (N = 26) or were not willing to participate nor responded (N = 69). Out of the 127 participants that provided informed consent, 118 visited the hospital for HR-pQCT measurements. Out of the 118 participants, 89 had OI type I (75.4%), 7 had OI type III (5.9%), and 22 had type IV (18.6%) (**Table 1**). Causative genetic mutation was known in 107 out of the 118 participants, of whom 77 had the causative mutation in collagen type I alpha 1 (72.0%) and 24 in collagen type I alpha 2 (22.4%). The proportion of causative collagen type I alpha 1 mutations was 85.0% in OI type I and 33.3% in OI types III and IV. The entire group consisted of 57 men (48.3%) and 61 women (51.7%). The proportion of men was 43.8% in OI type I and 62.1% in OI types III and IV. Median age was 41.8 (IQR: 25.1) years in the entire group and similar in the two subgroups. The Z-score for aBMD was < -1 in 58 out of 108 participants (53.7%) with available data on total hip aBMD and in 88 out of 112 participants (78.6%) with available data on lumbar spine aBMD. Data on BP use were available of 116 out of the 118 participants, of whom 31.0% currently used BPs and similar proportions non-recently (> 3 years of study initiation) or never. Out of the 118 participants, 57.6% of the participants were community walkers without mobility aids (*e.g.* walking cane or frame, wheelchair, mobility scooter); 11.0% were non-walkers (modified Bleck scale 1: 1 with OI type I; 12 with OI type III or IV).

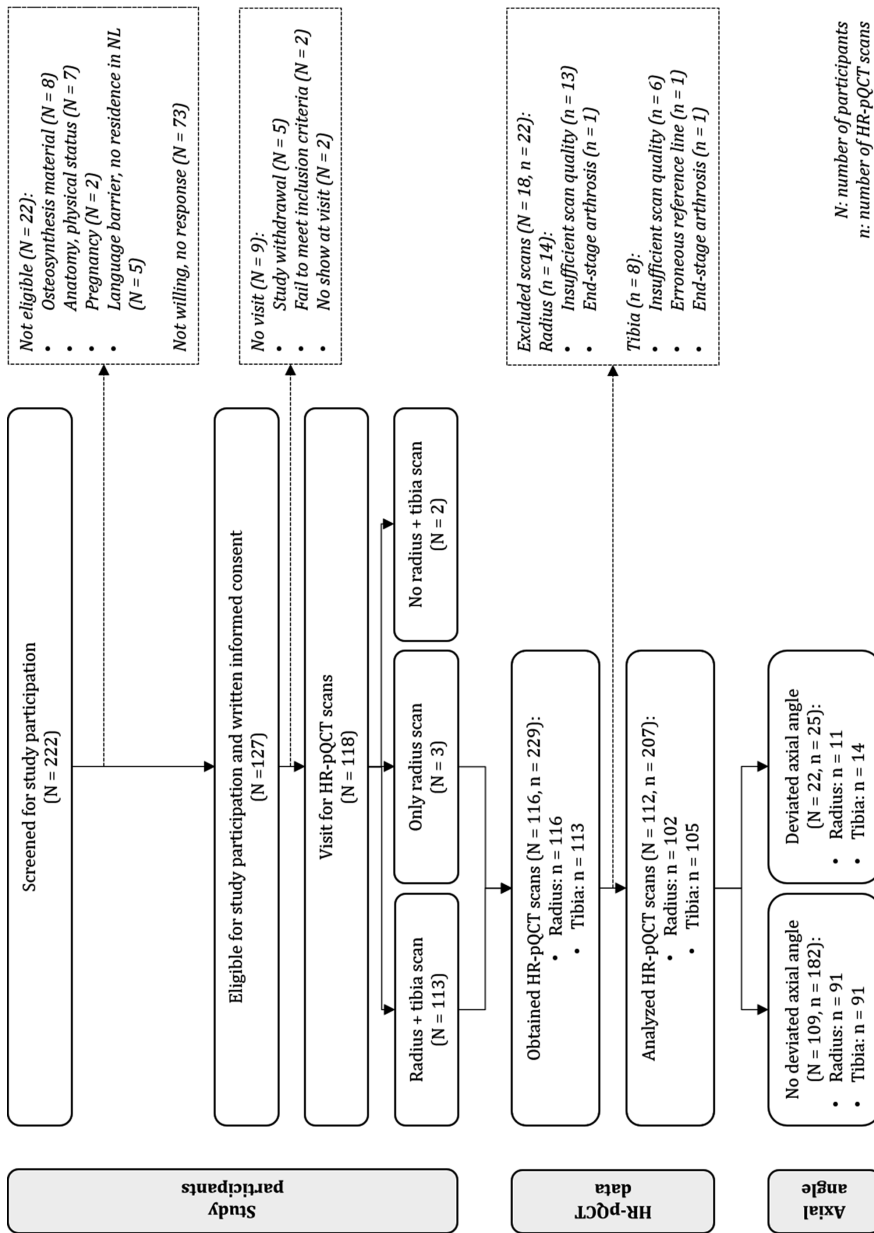


Figure 2. Study participants and HR-pQCT scans obtained and analyzed for this study.

Table 1. Characteristics of the study participants.

| | Sillence type I (N = 89) | Sillence types III, IV (N = 29) | Total (N = 118) |
|--|-----------------------------|------------------------------------|--------------------|
| Gender [men] | 39 (43.8) | 18 (62.1) | 57 (48.3) |
| Age [years] | 44.0 (28.7) | 40.4 ± 13.4 | 41.8 (25.1) |
| Number of fractures [-] | 17.0 (21.0) | 20.0 (37.0) | 18.5 (24.0) |
| Mutated gene ¹ | | | |
| COL-1A1 | 68 (85.0) | 9 (33.3) | 77 (72.0) |
| COL-1A2 | 10 (12.5) | 14 (51.9) | 24 (22.4) |
| Other | 2 (2.5) | 4 (14.8) | 6 (5.6) |
| DXA total hip aBMD Z-score [-] ² | -1.1 ± 0.8 | -1.3 ± 1.7 | -1.1 ± 1.1 |
| Z-score < -1 | 44 (52.4) | 14 (58.3) | 58 (53.7) |
| Z-score < -2.5 | 3 (3.6) | 5 (20.8) | 8 (7.4) |
| DXA lumbar spine aBMD Z-score [-] ³ | -2.0 ± 1.3 | -2.2 ± 2.3 | -2.1 ± 1.6 |
| Z-score < -1 | 66 (75.9) | 22 (88.0) | 88 (78.6) |
| Z-score < -2.5 | 32 (36.8) | 10 (40.0) | 42 (37.5) |
| Bisphosphonate use ⁴ | | | |
| Current | 28 (31.8) | 8 (28.6) | 36 (31.0) |
| Recent (< 3 yrs.) | 11 (12.5) | 1 (3.6) | 12 (10.3) |
| Non-recent (> 3 yrs.) | 23 (26.1) | 10 (35.7) | 33 (28.4) |
| Never | 26 (29.5) | 9 (32.1) | 35 (30.2) |
| 25(OH)D-level [nmol/L] | 81.8 ± 33.9 | 76.7 ± 41.0 | 80.6 ± 35.6 |
| < 50 nmol/L | 17 (19.1) | 9 (31.0) | 26 (22.0) |
| P1NP [ug/L] ⁴ | 27.1 (21.8) | 40.2 (28.7) | 30.5 (23.7) |
| Z-score [-] ⁵ | -0.9 (1.2) | -0.5 (2.1) | -0.7 (1.3) |
| CTX [pg/mL] ⁶ | 164.5 (122.0) | 294.4 ± 155.1 | 182.0 (157.0) |
| Z-score [-] ⁵ | -0.7 (1.0) | -0.2 ± 0.9 | -0.7 (1.0) |
| Modified Bleck scale [-] | | | |
| 1 Non-walker >2 yrs. old | 1 (1.1) | 12 (41.4) | 13 (11.0) |
| 2 Therapy walker (with crutches or canes) | 1 (1.1) | 0 (0.0) | 1 (0.8) |
| 3 Therapy walker (no crutches or canes) | 1 (1.1) | 1 (3.4) | 2 (1.7) |
| 4 Household walker (with crutches or canes) | 2 (2.2) | 0 (0.0) | 2 (1.7) |
| 5 Household walker (no crutches or canes) | 1 (1.1) | 0 (0.0) | 1 (0.8) |
| 6 Neighborhood walker (with crutches or canes) | 3 (3.4) | 1 (3.4) | 4 (3.4) |
| 7 Neighborhood walker (no crutches or canes) | 23 (25.8) | 1 (3.4) | 24 (20.3) |
| 8 Community walker (with crutches or canes) | 1 (1.1) | 2 (6.9) | 3 (2.5) |
| 9 Community walker (no crutches or canes) | 56 (62.9) | 12 (41.4) | 68 (57.6) |

Continuous data are reported as mean ± std or median (interquartile range), categorical data as number (percentage).

¹N = 107; ²N = 108; ³N = 112; ⁴N = 116; ⁵N = 114; ⁶N = 117

COL-1A1, collagen type I alpha 1. COL-1A2, collagen type I alpha 2. DXA, dual-energy X-ray absorptiometry. aBMD, areal bone mineral density. 25(OH)D, 25-hydroxyvitamin D. P1NP, procollagen type I N-terminal propeptide. CTX, collagen type I C-terminal telopeptide.

HR-pQCT measurements

Scan acquisition and quality

HR-pQCT scans could be obtained in 116 out of the 118 participants (**Figure 2; Study participants**). In 113 participants, an HR-pQCT scan could be taken of both the distal radius and tibia. In three participants (OI types III and IV), an HR-pQCT scan could be obtained of the distal radius but not of the distal tibia due to short and deformed lower extremities, limited mobility, osteosynthesis material, and/or discomfort with positioning. In two other participants (both OI type III), no scan of the distal radius nor distal tibia could be obtained for the same reason. Most HR-pQCT scans could be performed using the standard chair for scan acquisition, but two participants (both OI type III) had either the radius or tibia scan in their wheelchair and two other participants (OI types III and IV) had unsuccessful attempts for scan acquisition in the wheelchair. In ten participants, the positioning different from the standard procedure to enable scan acquisition (*e.g.* bent posture in the standard chair, no full knee extension for the tibia scan, back support of the standard chair horizontally) or required other adjustments (*e.g.* no foot sole in the leg holder, use of the arm holder for the tibia scan, use of pillows to increase seating height or comfort).

Consequently, there was a total of 229 evaluable HR-pQCT scans from 116 participants (**Figure 2; HR-pQCT data**). Of these scans, 22 scans from 18 participants were excluded due to insufficient scan quality (radius + tibia scan in 2 participants, radius scan in 11 participants, tibia scan in 4 participants), end-stage arthrosis of the scanned region (radius + tibia scan in 1 participant), or an erroneously placed reference line (tibia scan in 1 participant). Consequently, 207 HR-pQCT scans from 112 participants were available for quantitative analysis.

Axial scan angle

The median axial angle of the 102 radius scans was 12.6° (IQR: 6.0°; **Figure 1B**), and a deviated angle was found in 11 of the scans (10.8%; **Figure 2; Axial scan angle**). The other 91 radius scans had no deviated axial angle. The deviation of the axial angle of the radius scans was not associated with OI type (deviated angle: 8 type I, 72.7%; non-deviated angle: 68 type I, 74.7%; $p = 1.000$) nor with non-walker (modified Bleck 1) *vs.* walker (modified Bleck 2-9) (2 non-walkers, 18.2% compared to 7, 7.7%; $p = 0.250$). The total number of fractures in medical history was significantly higher in participants with a deviated axial angle of the distal radius scan (27 (IQR: 18)) than in those without a deviated axial angle of the radius scan (15 (IQR: 22); $p = 0.034$).

The median axial angle of the 105 tibia scans was 6.3° (IQR: 4.2°; **Figure 1B**), and a deviated angle was found in 14 of the scans (13.3%; **Figure 2; Axial scan angle**). The other 91 tibia scans had no deviated axial angle. The deviation of the axial angle

of the tibia scans was significantly associated with OI type (deviated angle: 8 type I, 57.1%; non-deviated angle: 76 type I, 83.5%; $p = 0.033$) and non-walker *vs.* walker (4 non-walkers, 28.6% compared to 2, 2.2%; $p = 0.003$). The total number of fractures in medical history was not different between the participants with or without deviated axial angle of the tibia scan (28 (IQR: 14) and 15 (IQR: 22), respectively; $p = 0.073$).

Comparison with normative data

In the 91 radius scans and 91 tibia scans without a deviated axial angle, especially the total and trabecular parameters differed from normative values (**Table 2, Figure 3**). At the distal radius, total BMD (Tt.BMD), stiffness, and FL were low as compared to normative data. More reduced were trabecular BMD (Tb.BMD), trabecular bone volume fraction (Tb.BV/TV), and trabecular number (Tb.N), while Tb.Sp was considerably higher than normative data. Trabecular thickness (Tb.Th), cortical BMD (Ct.BMD), and cortical microarchitectural parameters differed less from normative data, as was the case for total bone area (Tt.Ar), trabecular bone area (Tb.Ar), and cortical bone area (Ct.Ar). The Z -scores were similar in the subgroup of OI type I and the subgroup of OI types III and IV for most HR-pQCT parameters.

A similar pattern with generally larger differences from normative data was seen at the distal tibia (**Table 2, Figure 3**). The Z -scores at the distal tibia were significantly lower than at the distal radius for Tt.BMD, stiffness, FL (all $p < 0.0001$), Tb.BMD ($p = 0.003$), Tb.BV/TV ($p = 0.012$), Ct.Ar, and Ct.Th (both $p < 0.0001$) and significantly higher for Tb.Ar ($p = 0.016$) in the entire group and in the subgroup of OI type I but not in the subgroup of OI types III and IV. The Z -scores were lower in the subgroup of OI types I than in the subgroup of OI types III and IV for most HR-pQCT parameters.

Consistent with these findings, larger proportions of participants had Z -scores < -1 or > 1 for total and trabecular parameters than for cortical parameters, although there was considerable heterogeneity in Z -scores among participants (**Figure 4A**). Again, larger proportions had Z -scores < -1 or > 1 at the distal tibia than at the distal radius, particularly for HR-pQCT parameters of total and trabecular bone.

Table 2. Z-scores for HR-pQCT parameters at the distal radius and distal tibia from scans without a deviated axial angle.

| | Distal radius | | | Distal tibia | | |
|------------------------|-----------------------------|---------------------------------------|-------------------|-----------------------------|---------------------------------------|-------------------|
| | Sillence type I (n = 68) | Sillence types III, IV (n = 23) | Total (n = 91) | Sillence type I (n = 76) | Sillence types III, IV (n = 15) | Total (n = 91) |
| Total bone | | | | | | |
| Tt.Ar | -0.7 ± 1.0 | -0.7 ± 1.4 | -0.7 ± 1.1 | -0.5 ± 1.4 | -0.3 (2.4) | -0.5 ± 1.4 |
| Tt.BMD | -1.2 ± 1.5 | -0.6 ± 2.4 | -1.0 ± 1.8 | -2.1 ± 1.1* | -0.7 (2.4) | -1.9 ± 1.3* |
| Stiffness | -1.5 ± 1.3 | -0.9 ± 1.9 | -1.4 ± 1.5 | -2.4 ± 1.0* | -0.8 (1.8) | -2.1 ± 1.2* |
| FL | -1.3 ± 0.9 | -0.7 ± 1.6 | -1.1 ± 1.2 | -2.1 (0.8)* | -0.9 (1.6) | -2.0 (0.7)* |
| Trabecular bone | | | | | | |
| Tb.Ar | -0.5 ± 1.0 | -0.6 ± 1.4 | -0.6 ± 1.1 | -0.1 ± 1.2* | -0.4 (2.6) | -0.1 ± 1.2* |
| Tb.BMD | -1.8 ± 1.1 | -1.1 ± 1.7 | -1.6 ± 1.3 | -2.5 ± 1.2* | -0.8 (1.6) | -2.2 ± 1.3* |
| Tb.BV/TV | -1.7 ± 1.1 | -1.2 ± 1.7 | -1.6 ± 1.3 | -2.3 ± 1.0* | -1.0 (1.6) | -2.0 ± 1.2* |
| Tb.N | -2.6 ± 1.2 | -2.2 ± 1.9 | -2.5 ± 1.4 | -2.9 ± 1.3 | -2.2 (1.3) | -2.8 ± 1.3 |
| Tb.Th | 0.7 ± 1.4 | 1.0 ± 1.6 | 0.8 ± 1.5 | 0.9 ± 1.6 | 1.5 (2.8) | 1.0 ± 1.6 |
| Tb.Sp | -2.9 (2.6) | -1.8 (2.3) | -2.7 (2.7) | -3.6 (3.4) | -1.9 (2.4) | -3.1 (2.9) |
| Cortical bone | | | | | | |
| Ct.Ar | -0.9 ± 1.3 | -0.3 ± 1.7 | -0.8 ± 1.4 | -1.7 ± 1.1* | -0.6 (1.6) | -1.6 ± 1.1* |
| Ct.BMD | 0.2 ± 1.4 | 0.2 ± 1.4 | 0.2 ± 1.4 | 0.0 ± 2.0 | -1.4 (1.9)* | -0.1 ± 1.9 |
| Ct.Th | -0.6 ± 1.4 | 0.1 ± 2.0 | -0.4 ± 1.6 | -1.4 ± 1.3* | -0.4 (1.4) | -1.2 ± 1.3* |
| Ct.Po | 0.6 ± 1.0 | 0.3 ± 1.1 | 0.5 ± 1.0 | 0.4 ± 1.5 | 0.0 (1.3) | 0.3 ± 1.5 |
| Ct.Po.Dm | 0.4 ± 1.1 | -0.2 ± 1.3 | 0.2 ± 1.2 | 0.3 (1.3) | -0.3 (1.6) | 0.3 (1.4) |

Data are reported as mean ± standard deviation or median (interquartile range).

*Significant difference in Z-score between the distal radius and distal tibia in the respective (sub)group ($p < 0.05$).

Tt.Ar, total bone area. Tt.BMD, total bone mineral density. FL, failure load. Tb.Ar, trabecular bone area. Tb.BMD, trabecular bone mineral density. Tb.BV/TV, trabecular bone volume fraction. Tb.N, trabecular number. Tb.Th, trabecular thickness. Tb.Sp, trabecular separation. Ct.Ar, cortical bone area. Ct.BMD, cortical bone mineral density. Ct.Th, cortical thickness. Ct.Po, cortical porosity. Ct.Po.Dm, cortical pore diameter.

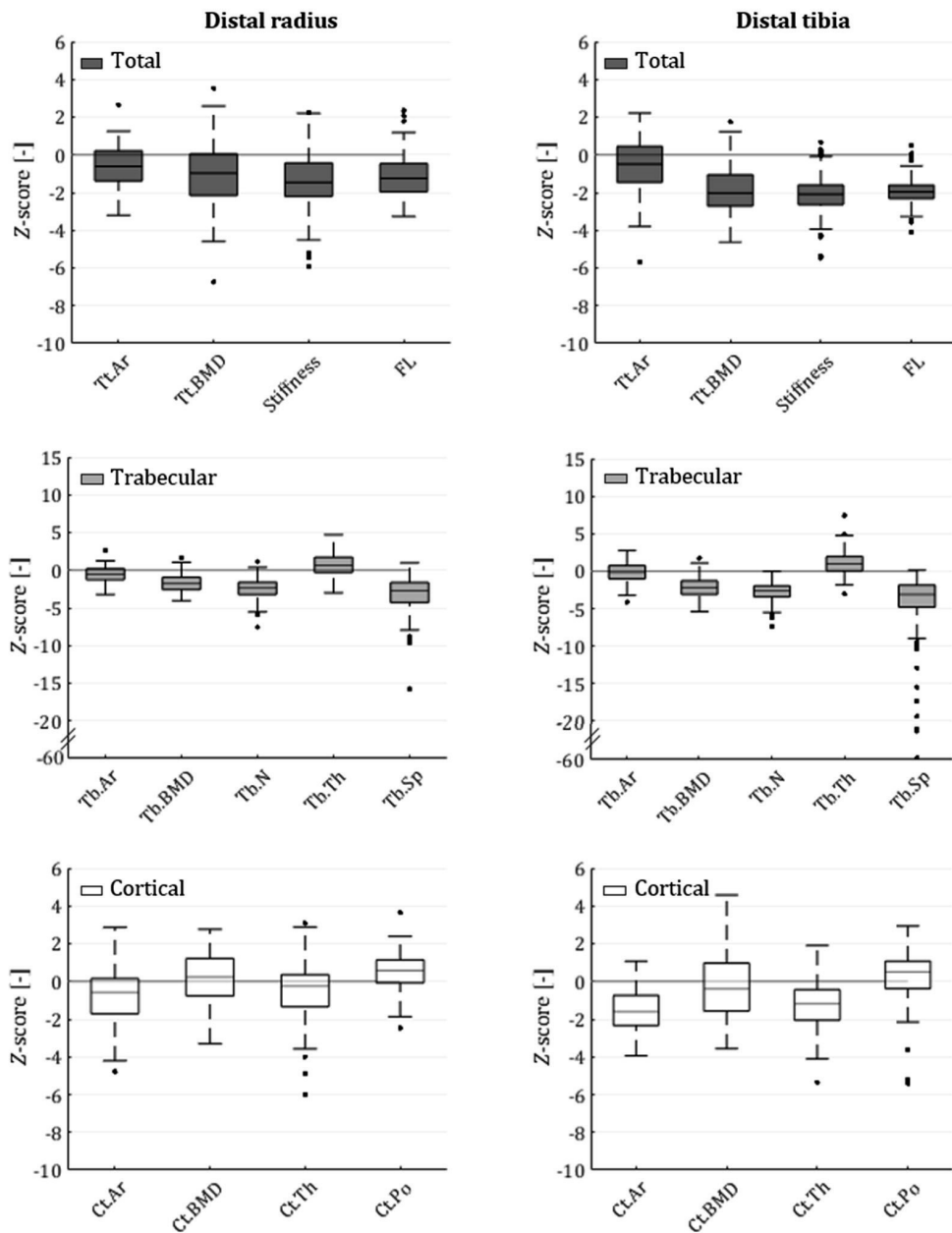


Figure 3. The distribution of Z-scores for HR-pQCT parameters of total, trabecular, and cortical bone at the distal radius (left) and at the distal tibia (right) of scans without deviated axial angle.

HR-pQCT analysis and interpretation

Impact of a deviated axial scan angle

The proportion of participants with a Z-score < -4 or > 4 was significantly higher for HR-pQCT parameters of total and trabecular bone in scans with a deviated axial angle than in scans without deviated axial angle (**Figure 4, Table 3**). There were no significant associations between the deviation of the axial angle and Z-scores for the HR-pQCT parameters within *vs.* outside the range of ± 1 , except for Tb.Ar at the distal tibia. For this parameter, the proportion of participants with a Z-score outside the range of ± 1 was higher in scans with a deviated axial angle than in scans without a deviated axial angle. There were significant associations between the deviation of the axial angle and Z-scores within *vs.* outside the range of ± 4 . At the distal radius, the association was significant for Z-scores for Tb.BMD, Tb.BV/TV, and Tb.Sp. At the distal tibia, the association was significant for Z-scores for the same parameters and additionally for Tt.Ar, stiffness, FL, Tb.Ar, and Tb.N. For these parameters, the proportion of participants with a Z-score outside the range of ± 4 was higher in the scans with a deviated axial angle than in the scans without a deviated axial angle. There were no significant associations with Z-scores for cortical parameters.

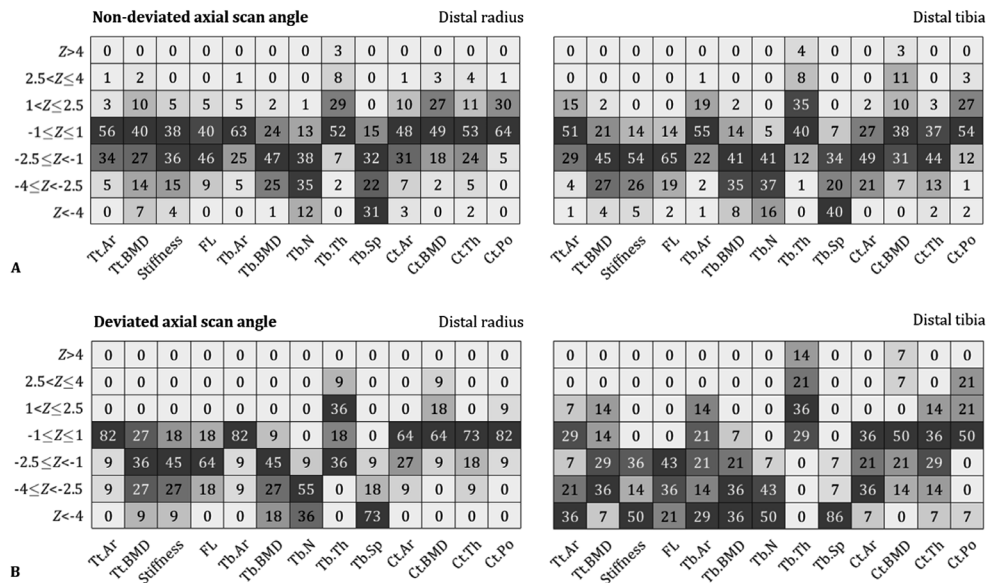


Figure 4. Percentage of participations with Z-scores for HR-pQCT parameters of different categories at the distal radius (left) and distal tibia (right) of scans **A**) without deviated axial angle, and **B**) with deviated axial angle. The color coding is scaled per parameter from light (low percentage) to dark (high percentage) gray values.

Table 3. Proportion of Z-scores for HR-pQCT parameters at the distal radius and distal tibia from scans with and without deviated axial angle.

| | Distal radius | | | | Distal tibia | | | | | | | |
|------------------------|-------------------------------|-----------------------------------|---------------------|-------------------------------|-----------------------------------|--------------|-------------------------------|-----------------------------------|--------------|-----------|-----------|--------------|
| | Z-score > 1 or < -1 | | Z-score > 4 or < -4 | | Z-score > 1 or < -1 | | Z-score > 4 or < -4 | | | | | |
| | Deviated axial angle (n = 11) | Non-deviated axial angle (n = 91) | p-Value | Deviated axial angle (n = 11) | Non-deviated axial angle (n = 91) | p-Value | Deviated axial angle (n = 14) | Non-deviated axial angle (n = 91) | p-Value | | | |
| Total bone | | | | | | | | | | | | |
| Tt.Ar | 2 (18.2) | 40 (44.0) | 0.119 | 0 (0.0) | 0 (0.0) | - | 10 (71.4) | 45 (49.5) | 0.157 | 5 (35.7) | 1 (1.1) | 0.000 |
| Tt.BMD | 8 (72.7) | 55 (60.4) | 0.525 | 1 (9.1) | 6 (6.6) | 0.562 | 12 (85.7) | 72 (79.1) | 0.731 | 1 (7.1) | 4 (4.4) | 0.518 |
| Stiffness | 9 (81.8) | 56 (61.5) | 0.320 | 1 (9.1) | 4 (4.4) | 0.442 | 14 (100.0) | 78 (85.7) | 0.208 | 7 (50.0) | 5 (5.5) | 0.000 |
| FL | 9 (81.8) | 55 (60.4) | 0.204 | 0 (0.0) | 0 (0.0) | - | 14 (100.0) | 78 (85.7) | 0.208 | 3 (21.4) | 2 (2.2) | 0.016 |
| Trabecular bone | | | | | | | | | | | | |
| Tb.Ar | 2 (18.2) | 34 (37.4) | 0.320 | 0 (0.0) | 0 (0.0) | - | 11 (78.6) | 41 (45.1) | 0.023 | 4 (28.6) | 1 (1.1) | 0.001 |
| Tb.BMD | 10 (90.9) | 69 (75.8) | 0.448 | 2 (18.2) | 1 (1.1) | 0.030 | 13 (92.9) | 78 (85.7) | 0.687 | 5 (35.7) | 7 (7.7) | 0.009 |
| Tb.BV/TV | 10 (90.9) | 68 (74.7) | 0.451 | 2 (18.2) | 1 (1.1) | 0.030 | 13 (92.9) | 77 (84.6) | 0.687 | 3 (21.4) | 3 (3.3) | 0.030 |
| Tb.N | 11 (100.0) | 79 (86.8) | 0.353 | 4 (36.4) | 11 (12.1) | 0.054 | 14 (100.0) | 86 (94.5) | 1.000 | 7 (50.0) | 15 (16.5) | 0.009 |
| Tb.Th | 9 (81.8) | 44 (48.4) | 0.054 | 0 (0.0) | 3 (3.3) | 1.000 | 10 (71.4) | 55 (60.4) | 0.560 | 2 (14.3) | 4 (4.4) | 0.181 |
| Tb.Sp | 11 (100.0) | 77 (84.6) | 0.353 | 8 (72.7) | 28 (30.8) | 0.015 | 14 (100.0) | 85 (93.4) | 1.000 | 12 (85.7) | 36 (39.6) | 0.001 |
| Cortical bone | | | | | | | | | | | | |
| Ct.Ar | 4 (36.4) | 47 (51.6) | 0.525 | 0 (0.0) | 3 (3.3) | 1.000 | 9 (64.3) | 66 (72.5) | 0.536 | 1 (7.1) | 0 (0.0) | 0.133 |
| Ct.BMD | 4 (36.4) | 46 (50.5) | 0.526 | 0 (0.0) | 0 (0.0) | - | 7 (50.0) | 56 (61.5) | 0.559 | 1 (7.1) | 3 (3.3) | 0.441 |
| Ct.Th | 3 (27.3) | 43 (47.3) | 0.337 | 0 (0.0) | 2 (2.2) | 1.000 | 9 (64.3) | 57 (62.6) | 1.000 | 1 (7.1) | 2 (2.2) | 0.352 |
| Ct.Po | 2 (18.2) | 33 (36.3) | 0.323 | 0 (0.0) | 0 (0.0) | - | 7 (50.0) | 42 (46.2) | 1.000 | 1 (7.1) | 2 (2.2) | 0.352 |
| Ct.Po.Dm | 3 (27.3) | 34 (37.4) | 0.742 | 0 (0.0) | 0 (0.0) | - | 9 (64.3) | 37 (40.7) | 0.147 | 0 (0.0) | 1 (1.1) | 1.000 |

Data are reported as number (percentage). The p-values indicate the significance of the association between the deviation of the axial scan angle (yes vs. no) and the proportion of participants with a Z-score within vs. outside the range of ± 1 or ± 4 . $p < 0.05$ is depicted in bold.

Tt.Ar, total bone area. Tt.BMD, total bone mineral density. FL, failure load. Tb.Ar, trabecular bone area. Tb.BMD, trabecular bone mineral density. Tb.BV/TV, trabecular bone volume fraction. Tb.N, trabecular number. Tb.Th, trabecular thickness. Tb.Sp, trabecular separation. Ct.Ar, cortical bone area. Ct.BMD, cortical bone mineral density. Ct.Th, cortical thickness. Ct.Po, cortical porosity. Ct.Po.Dm, cortical pore diameter.

Microarchitectural heterogeneity

Based on a visual assessment of the scans, the trabecular and cortical bone appeared heterogeneously distributed within the bone compartments. The most often observed inhomogeneity in the trabecular compartment were void volumes (**Figure 5A**). They were variable in size, number, and location but often occurred as one centrally located volume with increased prominence in proximal direction. The void volumes appeared to be more often seen, to be relatively larger, and to be more clearly demarcated at the distal tibia than at the distal radius. They appeared to correspond with (highly) negative Z -scores for Tb.N and Tb.Sp (*i.e.* low Tb.N and high Tb.Sp). Other trabecular inhomogeneities included local sclerotic spots and locally thickened trabeculae (**Figure 5B**), which also appeared to occur more often at the distal tibia than at the distal radius. In pronounced cases, these sclerotic regions were accompanied by horizontal lines on the two-dimensional preview image (**Figure 5B; middle**). Sclerotic regions and thickened trabeculae could co-occur with a high Tb.Th, but high Tb.Th values also occurred in the absence of sclerotic spots (**Figure 5B; right**). In the cortical compartment, periosteal surfaces of the cortex could be coarse, and porosity and mineralization density could be locally increased and decreased, respectively (**Figure 5C; left**). Also the cortical inhomogeneities appeared to occur more often at the tibia than at the radius. The locally increased cortical porosity could but did not always co-occur with high values for Ct.Po (*i.e.* negative Z -scores). Mineralization densities below the density threshold for segmentation resulted in no inclusion in the cortical analysis (**Figure 5C; right**). Besides that, the trabecular and cortical inhomogeneities could appear as 'secondary cortices' (**Figure 6; top row**), which were included in either the cortical or trabecular analysis depending on their appearance and relative size and on their evolution over the scanned region (**Figure 6; bottom row**).

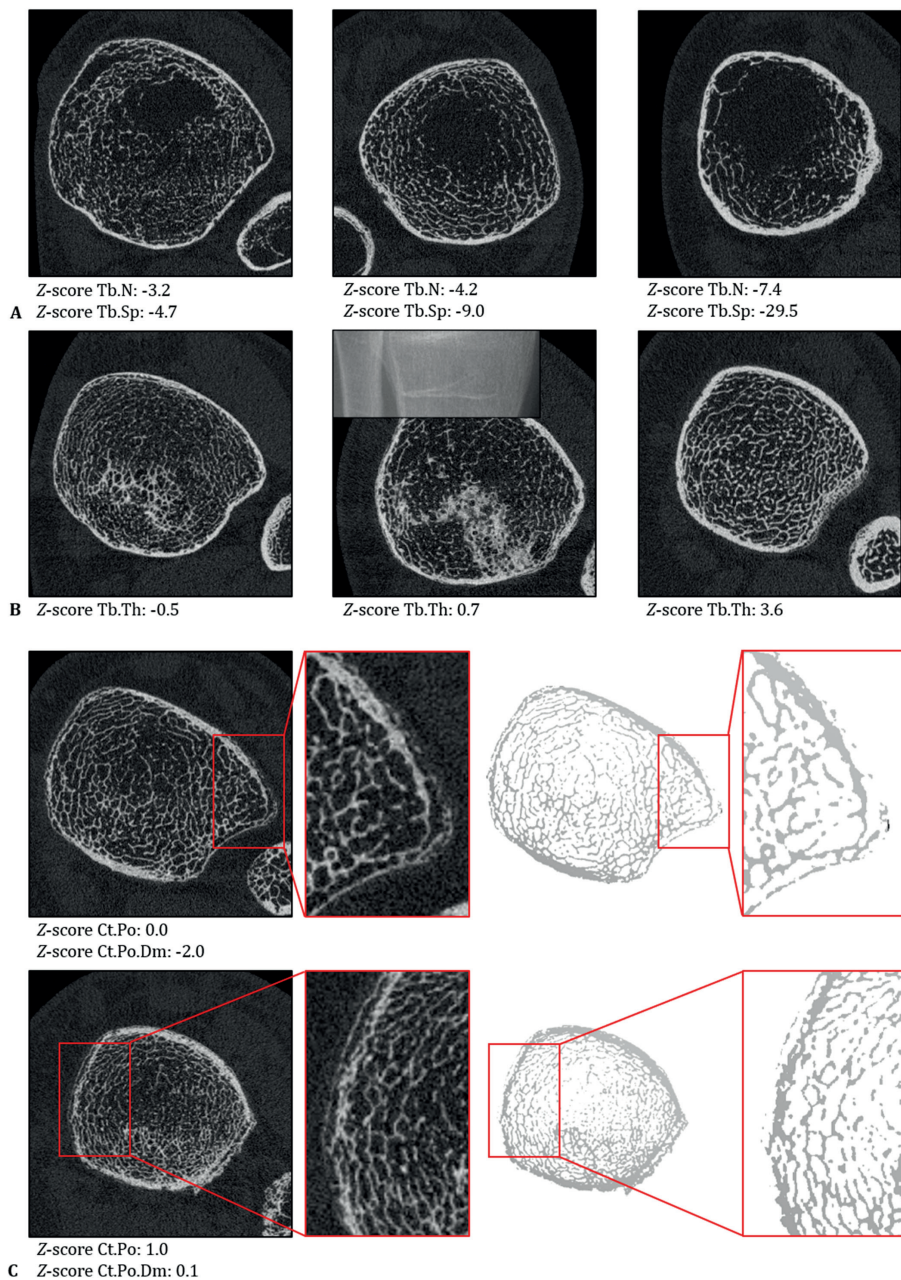


Figure 5. Examples of HR-pQCT slices showing **A**) trabecular void volumes with corresponding Z-scores for trabecular number (Tb.N) and trabecular separation (Tb.Sp); **B**) local sclerotic regions and thickened trabeculae (left, middle) with corresponding Z-score for trabecular thickness (Tb.Th) and corresponding two-dimensional preview image with horizontal lines (middle) or a high Z-score for Tb.Th in the absence of local sclerotic regions (right); and **C**) cortical heterogeneities near the periosteal surface with corresponding Z-scores for cortical porosity (Ct.Po) and cortical pore diameter (Ct.Po.Dm), which were not fully included in the HR-pQCT analyses after segmentation (right).

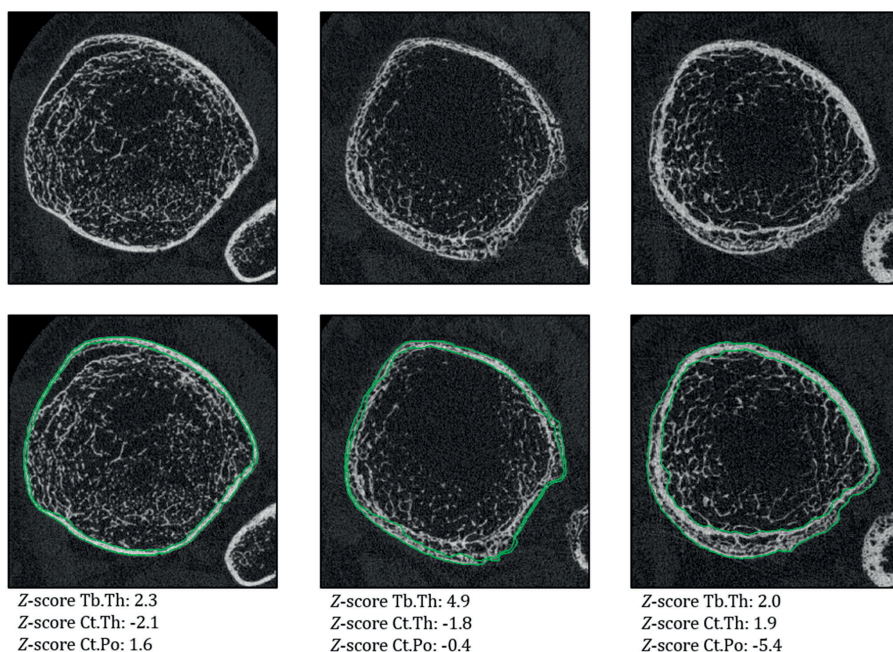


Figure 6. Local inhomogeneities near the endosteal surface could appear as ‘secondary cortices’ (top row). They were included in either the trabecular analysis (left, middle) or cortical analysis (right) as defined by the endosteal contour (green; bottom row) with corresponding Z-scores for trabecular thickness (Tb.Th), cortical thickness (Ct.Th), and cortical porosity (Ct.Po).

DISCUSSION

The aim of this study was to assess bone microarchitecture and strength in a large cohort of adults with OI types I, III, and IV using second-generation HR-pQCT and an extremity-length dependent scan protocol. Additionally, we evaluated potential challenges in the acquisition and analysis of HR-pQCT scans in this cohort related to short stature, bone deformities, and microarchitectural inhomogeneities. The most striking findings were a reduced total and trabecular BMD, stiffness, and failure load, and a highly reduced trabecular number and highly increased trabecular separation as compared to age- and gender-matched controls from normative data. Trabecular thickness, cortical BMD, and cortical microarchitectural parameters differed less from normative data at the group level. At the individual level, there was considerable heterogeneity in the extent of the difference in HR-pQCT parameters from normative data. Besides that, the cortical and trabecular bone appeared to be heterogeneously distributed within the bone compartments with local inhomogeneities. Most often observed were trabecular void volumes, which appeared to correspond with (highly)

negative Z -scores for trabecular number and separation. HR-pQCT scans could be obtained in most participants without problems; however, 11% of the radius scans and 13% of the tibia scans had a deviated axial scan angle, which was associated with a significantly higher proportion of Z -scores < -4 or > 4 for trabecular BMD and separation (radius) or for all total and trabecular parameters except total BMD and trabecular thickness (tibia).

Our findings on bone area, BMD, and microarchitecture are in line with previous research. We found that Z -scores were generally lower for trabecular BMD and microarchitectural parameters than for cortical BMD and microarchitectural parameters. This difference in impairment between the trabecular and cortical bone was also reflected by the lower Z -scores for lumbar spine aBMD than total hip aBMD from DXA. Consistent with these findings, previous HR-pQCT studies reported a significantly lower trabecular BMD and number and significantly higher trabecular separation in adults with OI than in healthy controls and few or no significant differences between OI and non-OI groups for cortical parameters [14-16]. The impairment of the trabecular bone in our study was reflected by low Z -scores for trabecular number but not for trabecular thickness. This difference between trabecular number and thickness is in line with previous HR-pQCT studies in adults with OI [14-16], whereas previous histomorphometry studies reported a significantly reduced trabecular thickness in iliac crests biopsies of children and adults with OI [10-13]. In contrast to BMD and microarchitecture, trabecular and cortical cross-sectional area were similarly reduced (radius) or cortical cross-sectional area was more reduced than trabecular cross-sectional area (tibia). This is also consistent with previous (HR-) pQCT studies [9,14,16].

We additionally evaluated bone stiffness and failure load from the HR-pQCT scans using μ FE-analysis. Stiffness and failure load were reduced as compared to normative data, and up to 5% of the participants had a Z -score < -4 for these parameters. In line with our findings, previous studies in adults with OI reported significantly reduced values for other parameters that reflect bone strength based on structural properties of bone [9,14,28]. By using μ FE-analysis, we used more detailed structural properties to estimate bone strength than previous studies. However, we used the default values for the material properties of bone in our μ FE-models, while the bone material properties are most likely also affected in OI [5,29]. Consequently, our estimates of bone strength probably overestimate the actual bone strength in OI, and it is unknown to what extent they reflect the actual strength. Nevertheless, our findings demonstrate that bone strength in OI is already reduced due to structural defects in the bone (specifically BMD, microarchitecture, and cross-sectional area). Notably, Z -scores for stiffness and failure load as well as several other parameters were significantly lower

at the weight-bearing distal tibia than at the non-weight-bearing distal radius in OI type I but not in OI types III and IV. The relatively large proportion of non-walkers in OI types III and IV (41%) could possibly contribute to the similar impairment of the distal radius and tibia in this subgroup due to a reduced mechanical loading of the lower extremities and a possibly increased use and loading of the upper extremities as compared to normative groups. It does however not explain the difference in Z -scores between the distal radius and tibia in OI type I. Further research is therefore needed to study this site-specific variation.

Strikingly, the Z -scores for especially trabecular number and separation were low and could reach the level that they may not be reliable. For example, a Z -score < -4 for trabecular number and separation was found in 12% and 31% of the participants at the distal radius and in 16% and 40% at the distal tibia. Given that the statistical probability of a Z -score of -4 is 0.003%, these extreme Z -scores probably reflect the observed void volumes in the trabecular compartment. We commonly observed such trabecular voids, which could occupy a large part of the trabecular compartment. Recently, trabecular void volumes were quantified in an HR-pQCT study in a non-OI population [30]. It is yet unknown whether the prevalence and size of these volumes is different in the OI-population, which requires further study. Furthermore, the extreme Z -scores we found for trabecular number and separation suggest that trabecular void volumes need to be excluded from the HR-pQCT analyses in OI in future research to obtain more reliable information on trabecular microarchitecture. Finally, it would be of clinical interest to investigate the effects of anti-osteoporosis medications, particularly anabolic medications, on the presence and size of the void volumes and on the remaining part of the trabecular compartment.

Other microarchitectural inhomogeneities that we observed did not result in similarly extreme values for HR-pQCT parameters but may nevertheless influence the interpretation of this parameter because the calculation of the HR-pQCT parameters assumes a reasonable homogeneity of the cortical and trabecular bone. The interpretation could be further challenged by the potential influence of trabecular and cortical inhomogeneities on the endosteal contouring and thereby on the definition of the cortical and trabecular compartment. Other inhomogeneities were not included in the analyses when their density was below the density threshold for segmentation (*e.g.* locally increased periosteal porosity) or were not evaluated using standard analyses (*e.g.* coarse periosteal surfaces). In contrast, the calculation of bone stiffness and failure load using μ FE-analysis is not influenced by any microarchitectural inhomogeneity. Yet, to get a more complete impression of the microarchitectural heterogeneity in OI, advanced HR-pQCT analyses would be valuable. Specifically, the heterogeneity of the trabecular network can be quantified, but this parameter was not reported in

the normative dataset [26]. Additionally, evaluation of the variation of HR-pQCT parameters of cortical and trabecular microarchitecture can give insights into the microarchitectural heterogeneity in the cortical and trabecular compartment, and the use of multiple density thresholds for segmentation would enable quantification of lower-mineralized bone. However, normative data of such advanced analyses are not yet available. Besides that, algorithms may be developed to quantify local sclerotic regions in the trabecular bone or coarse periosteal surfaces.

Another aspect that requires attention when using HR-pQCT in OI is the acquisition of scans that are axially aligned with the bone. We found that 11% of the radius scans and 13% of the tibia scans had a deviated axial angle as compared to scans from 13 young women used as reference. These deviations could possibly be related to bone deformities (*e.g.* bending and changes in bone alignment after fracture) and difficulties with scan acquisition (*e.g.* no full knee extension for the tibia scan), also given the significant association with the total number of fractures in medical history (radius), OI type (tibia), and walking/non-walking (tibia). In the scans with a deviated axial angle, the proportion of participants with Z -scores < -4 or > 4 was significantly larger than in scans without a deviated axial angle for trabecular BMD and separation (radius scans) or for all total and trabecular parameters except total BMD and trabecular thickness (tibia scans). It implies that a deviated axial angle may have impact when using HR-pQCT in participants with OI. However, our approach to detect deviations in scan regions was not validated, and our definition of a deviated axial angle was based on a comparison with only a small control group. Further research is therefore needed to evaluate the occurrence of deviated scan regions in OI and the effects of such deviations on HR-pQCT parameters before more firm conclusions can be drawn. Nonetheless, only 15 out of the 95 adults (16%) that did not provide informed consent were considered not eligible for study participation due to OI-related factors (osteosynthesis material in the region of interest, bone anatomy or physical or mobility restrictions), and HR-pQCT scans could be taken without difficulties in most participating adults. It indicates that HR-pQCT can generally be used in OI although the feasibility can be limited in severe OI.

Our study has several strengths. First, we used a larger cohort than previous HR-pQCT studies and included individuals with Sillence OI types I, III, and IV [14-16,31], which may have provided a more complete impression of bone microarchitecture and strength in OI as well as on the interindividual heterogeneity in these properties. Additionally, the size of our cohort allowed for the exclusion of scans with a deviated axial angle to reduce possible interference of such deviation with HR-pQCT parameters. Second, we compared the HR-pQCT parameters with normative data, which enables comparison at the individual level. It also enables comparison of the distal radius

and tibia, whereas absolute HR-pQCT values cannot be compared between the two skeletal sites. Third, we used an extremity-length dependent scan protocol. The use of this protocol may have likely increased the accuracy of the normative comparison, in particular in patients with short stature. Most previous HR-pQCT studies in adults with OI did not use such protocol [14-16], which may have contributed to the finding of low cortical thickness in adults with mild OI but not in adults with moderate to severe OI and significantly shorter stature [15]. An extremity-length dependent scan protocol has recently been used in a clinical trial in OI, but published data of that trial thus far analyzed the precision of HR-pQCT parameters in a multicenter setting and the use of homogenized FE-models from HR-pQCT data in OI to estimate bone strength and did not compare OI and non-OI study groups [20,32,33]. However, given the subjectivity of measuring extremity length, further research is needed to determine whether use of the extremity-length dependent protocol in OI leads to differences in HR-pQCT parameters from the standard HR-pQCT protocol.

Several limitations of our study should also be addressed. First, participants were recruited from one medical center. It may create single-center bias although the center is a national Expertise center for adults with OI in the Netherlands. Second, race and ethnicity were not collected for this study. The normative dataset included only data from White individuals [26], and thus comparison may not be accurate for individuals with other genetic backgrounds due to differences in bone microarchitecture and strength [34]. However, other normative datasets for second-generation extremity-length dependent HR-pQCT are not available in literature. Third, as mentioned above, our detection of deviated scan regions may not have been accurate: we defined the deviation of a scan region by the axial angle of a scan and based the definition of a deviated axial scan angle on the axial angle of scans of a control group that was small and included only young women. Our approach should therefore be validated before being considered for use to evaluate HR-pQCT scans in adults with OI. Fourth, 41% of the participants currently or recently used BPs and 70% had ever used BPs, while BP-treatment influences HR-pQCT parameters [35]. Finally, it was beyond the scope of our study to evaluate associations of HR-pQCT parameters with genetic and clinical characteristics to get further insights into the variability of the disease manifestation and severity among patients. Nevertheless, our results give valuable insights into bone microarchitecture and strength in OI, which may provide guidance for future study and advice on anti-osteoporotic treatments, e.g. osteoanabolic treatment, in adults with OI.

To conclude, BMD, microarchitecture, and strength were reduced in adults with OI as compared to age- and gender-matched controls from normative data. Particularly the trabecular bone was affected, represented by a low trabecular number and high

trabecular separation. Most HR-pQCT scans could be obtained without difficulties, although ten percent of the scans may have a deviated axial angle. This is likely related to deformities in the bone region of interest in OI and potentially influences HR-pQCT parameters. Furthermore, HR-pQCT parameters may be difficult to interpret or reach the level that they may be unreliable due to microarchitectural inhomogeneities, particularly trabecular void volumes, and they may not capture all observed microarchitectural inhomogeneities. Nevertheless, HR-pQCT can provide insights into bone microarchitecture and strength at the individual level in OI.

ACKNOWLEDGEMENTS

We thank Marije Reitsma (Isala Hospital, Zwolle, The Netherlands) for the study administration.

REFERENCES

- [1] Forlino A, Marini JC. Osteogenesis imperfecta. *Lancet*. 2016;387(10028):1657-1671.
- [2] Dalgleish R. The human collagen mutation database 1998. *Nucleic Acids Res*. 1998;26(1):253-255.
- [3] Fokkema IFAC, Taschner PEM, Schaafsma GCP, Celli J, Laros JFJ, den Dunnen JT. LOVD v. 2.0: the next generation in gene variant databases. *Hum Mutat*. 2011;32(5):557-563.
- [4] Van Dijk FS, Sillence DO. Osteogenesis imperfecta: clinical diagnosis, nomenclature and severity assessment. *Am J Med Genet A*. 2014;164(6):1470-1481.
- [5] Nijhuis WH, Eastwood DM, Allgrove J, et al. Current concepts in osteogenesis imperfecta: bone structure, biomechanics and medical management. *J Child Orthop*. 2019;13(1):1-11.
- [6] Folkestad L, Hald JD, Ersbøll AK, et al. Fracture rates and fracture sites in patients with osteogenesis imperfecta: a nationwide register-based cohort study. *J Bone Miner Res*. 2017;32(1):125-134.
- [7] Fratzl-Zelman N, Misof BM, Klaushofer K, Roschger P. Bone mass and mineralization in osteogenesis imperfecta. *Wien Med Wochenschr*. 2015;165(13-14), 271-7.
- [8] Rauch F, Tuttlewski B, Schönau E. The bone behind a low areal bone mineral density: peripheral quantitative computed tomographic analysis in a woman with osteogenesis imperfecta. *J Musculoskelet Neuronal Interact*. 2002;2(4):306-308.
- [9] Gatti D, Colapietro F, Fracassi E, et al. The volumetric bone density and cortical thickness in adult patients affected by osteogenesis imperfecta. *J Clin Densitom*. 2003;6(2):173-177.
- [10] Baron R, Gertner JM, Lang R, Vignery A. Increased Bone Turnover with Decreased Bone Formation by Osteoblasts in Children with Osteogenesis Imperfecta Tarda. *Pediatr Res*. 1983;17:204-207.
- [11] Ste-Marie LG, Charhon SA, Edouard C, Chapuy MC, Meunier PJ. Iliac bone histomorphometry in adults and children with osteogenesis imperfecta. *J Clin Pathol*. 1984;37:1081-1089.
- [12] McCarthy EF, Earnest K, Rossiter K, Shapiro J. Bone Histomorphometry in Adults with Type IA Osteogenesis Imperfecta. *Clin Orthop Relat Res*. 1997;336:254-262.
- [13] Rauch F, Travers R, Parfitt AM, Glorieux FH. Static and dynamic bone histomorphometry in children with osteogenesis imperfecta. *Bone*. 2000;26(6):581-589.
- [14] Folkestad L, Hald JD, Hansen S, et al. Bone geometry, density, and microarchitecture in the distal radius and tibia in adults with osteogenesis imperfecta type I assessed by high-resolution pQCT. *J Bone Miner Res*. 2012;27(6):1405-1412.
- [15] Kocijan R, Muschitz C, Haschka J, et al. Bone structure assessed by HR-pQCT, TBS and DXL in adult patients with different types of osteogenesis imperfecta. *Osteoporos Int*. 2015;26:2431-2440.
- [16] Rolvien T, Stürznickel J, Schmidt FN, et al. Comparison of bone microarchitecture between adult osteogenesis imperfecta and early-onset osteoporosis. *Calcif Tissue Int*. 2018;103:512-521.
- [17] Boyd SK. Site-specific variation of bone microarchitecture in the distal radius and tibia. *J Clin Densitom*. 2008;11(3):424-430.
- [18] Schlenker R, VonSeggen W. The distribution of cortical and trabecular bone mass along the lengths of the radius and ulna and the implications for in vivo bone mass measurements. *Calcif Tissue Res*. 1976;20(1):41-52.
- [19] Simon M, Indermaur M, Schenk D, Hosseinitabatabaei S, Willie BM, Zysset P. Fabric-elasticity relationships of tibial trabecular bone are similar in osteogenesis imperfecta and healthy individuals. *Bone*. 2022;155:116282.
- [20] Sillence D, Senn A, Danks DM. Genetic heterogeneity in osteogenesis imperfecta. *J Med Genet*. 1979;16(2):101-116.

- [21] Bleck EE. Nonoperative treatment of osteogenesis imperfecta: orthotic and mobility management. *Clin Orthop Relat Res.* 1981;159:111-122.
- [22] Engelbert RH, Uiterwaal CS, Gulmans VA, Pruijs H, Helders PJ. Osteogenesis imperfecta in childhood: prognosis for walking. *J Pediatr.* 2000;137(3):397-402.
- [23] Bonaretti S, Majumdar S, Lang TF, Khosla S, Burghardt AJ. The comparability of HR-pQCT bone measurements is improved by scanning anatomically standardized regions. *Osteoporos Int.* 2017;28:2115-2128.
- [24] Pialat JB, Burghardt AJ, Sode M, Link TM, Majumdar S. Visual grading of motion induced image degradation in high resolution peripheral computed tomography: impact of image quality on measures of bone density and microarchitecture. *Bone.* 2012;50(1):111-118.
- [25] Whittier DE, Boyd SK, Burghardt AJ, et al. Guidelines for the assessment of bone density and microarchitecture in vivo using high-resolution peripheral quantitative computed tomography. *Osteoporos Int.* 2020;31:1607-1627.
- [26] Warden SJ, Liu Z, Fuchs RK, van Rietbergen B, Moe SM. Reference data and calculators for second-generation HR-pQCT measures of the radius and tibia at anatomically standardized regions in White adults. *Osteoporos Int.* 2022;33:791-806.
- [27] Pistoia W, Van Rietbergen B, Lochmüller EM, Lill CA, Eckstein F, Rügsegger P. Estimation of distal radius failure load with micro-finite element analysis models based on three-dimensional peripheral quantitative computed tomography images. *Bone.* 2002;30(6):842-848.
- [28] Kocijan R, Muschitz C, Fratzl-Zelman N, et al. Femoral geometric parameters and BMD measurements by DXA in adult patients with different types of osteogenesis imperfecta. *Skeletal Radiol.* 2013;42:187-194.
- [29] Bishop N. Bone material properties in osteogenesis imperfecta. *J Bone Miner Res.* 2016;31(4):699-708.
- [30] Whittier DE, Burt LA, Boyd SK. A new approach for quantifying localized bone loss by measuring void spaces. *Bone.* 2021;143:115785.
- [31] Hald JD, Folkestad L, Harsløf T, et al. Skeletal phenotypes in adult patients with osteogenesis imperfecta—correlations with COL1A1/COL1A2 genotype and collagen structure. *Osteoporos Int.* 2016;27:3331-3341.
- [32] Mikolajewicz N, Zimmermann EA, Rummler M, et al. Multisite longitudinal calibration of HR-pQCT scanners and precision in osteogenesis imperfecta. *Bone.* 2021;147:115880.
- [33] Hosseinibatabaei S, Mikolajewicz N, Zimmermann EA, et al. 3D Image Registration Marginally Improves the Precision of HR-pQCT Measurements Compared to Cross-Sectional-Area Registration in Adults With Osteogenesis Imperfecta. *J Bone Miner Res.* 2022;7(5):908-924.
- [34] Durdin R, Parsons CM, Dennison E, Harvey NC, Cooper C, Ward K. Ethnic differences in bone microarchitecture. *Curr Osteoporos Rep.* 2020;18:803-810.
- [35] Lespessailles E, Hambli R, Ferrari S. Osteoporosis drug effects on cortical and trabecular bone microstructure: a review of HR-pQCT analyses. *Bonekey Rep.* 2016;5:836.



3

Chapter 3

Microarchitecture of heterotopic ossification in fibrodysplasia ossificans progressiva: an HR-pQCT case series

Melissa S.A.M. Bevers[†], Esmée Botman[†], Caroline E. Wyers, Bert van Rietbergen,
Bernd P. Teunissen, Pieter G. Raijmakers, J. Coen Netelenbos, Joop P. van den Bergh,
Elisabeth M.W. Eekhoff

[†] These authors have contributed equally to this work and share first authorship

ABSTRACT

It is challenging to study heterotopic ossification (HO) in patients with fibrodysplasia ossificans progressiva (FOP) due to the contraindication of invasive techniques (*i.e.*, bone biopsies), which can trigger flare-ups. The aim of this case study was to assess mature HO at the microarchitectural level non-invasively with high-resolution peripheral quantitative computed tomography (HR-pQCT). Depending on the patient's mobility, HR-pQCT scans were acquired of peripherally located HO and standard distal radius and tibia regions in two FOP patients, a 33-year-old woman and a 23-year-old man, with the classical mutation (p.R206H). HO was located around the halluces, the ankles, and in the Achilles tendon. Standard HR-pQCT analyses were performed of the distal radius, tibia, and HO to quantify bone mineral density (BMD) and bone microarchitecture. Micro-finite element analysis was used to estimate failure load (FL). The outcomes were compared between HO and neighboring skeletal bone and with an age- and gender-matched normative dataset from literature. The bone parameters of the radius were within the interquartile range (IQR) of normative data. In contrast, in the tibiae of both patients, total and trabecular BMD were below the IQR, as were trabecular bone volume fraction, number, and thickness, cortical thickness, and FL. Trabecular separation and heterogeneity were above the IQR. Isolated HO in the Achilles tendon had a lower total, trabecular, and cortical BMD, trabecular bone volume fraction, and cortical thickness than the normative tibia data. Trabecular microarchitecture was within the IQR, and FL was approximately 10% higher than that of the neighboring tibia after accounting for areal differences. Other scanned HO could only be qualitatively assessed, which revealed coalescence with the neighboring skeletal bone, development of a neo-cortex, and partial replacement of the original skeletal cortex with trabeculae. To conclude, isolated HO seemed microarchitecturally more comparable to reference tibia data than the peripheral skeleton of the FOP patients. HO and skeleton also appear to be able to become one entity when contiguous.

INTRODUCTION

Fibrodysplasia ossificans progressiva (FOP) is a rare genetic disease that is characterized by the formation of heterotopic ossification (HO) in ligaments, tendons, and muscles [1-3]. The formation of HO is often preceded by a clinical flare-up whose clinical signs are, among others, pain, redness, and swelling [3,4]. The histology of these flare-ups developing into HO has previously been studied through biopsies that were obtained for other purposes, mainly to exclude malignancies in non-diagnosed FOP patients [5,6]. It is thought that, in the early stage of this HO development, the infiltration of inflammatory cells, such as lymphocytes, mast cells, and macrophages, causes cell death of the affected connective tissue. Proliferation of fibroblasts is thought to play a crucial role in the successive HO stage [7]. Finally, the fibroproliferative tissue develops into cartilage before it develops into endochondral bone [5,6,8].

Less is known about mature HO. The few histological and radiological case reports suggest HO to follow a normal endochondral process, with deposition of bone matrix that visually appears indistinguishable from skeletal bone matrix with similar bone modeling and remodeling [9-11]. When mature, HO seems to consist of both compact and lamellar bone structures and apparently normal bone marrow [12,13]. In FOP patients with the classic mutation (p.R206H), the skeletal bone is also assumed to develop normally despite developmental anomalies such as the frequently present shortened toes and the less frequently present short femoral neck and fusion of cervical facet joints [3]. These case reports are mainly qualitative as a quantitative comparison of mature HO and skeletal bone remains difficult. Furthermore, histological examinations of mature human FOP HO are limited due to a contraindication of invasive techniques, such as bone biopsies, in FOP patients as these techniques can trigger a flare-up and consequently aggravate the disease [4,14].

High-resolution peripheral quantitative computed tomography (HR-pQCT) may possibly alleviate the difficulty in investigating mature HO. This high-resolution imaging modality allows non-invasive and quantitative assessment of peripheral bones at the microarchitectural level, including quantification of geometry, density, and microarchitecture of the cortical and trabecular bone compartments and of the biomechanical properties of bone. Until now, HR-pQCT has mainly been used to study the distal radius and tibia [15], and to our knowledge, it has not yet been applied to FOP patients. Therefore, the aim of this case study was to assess mature HO with HR-pQCT and to compare with neighboring skeletal bone. To evaluate whether the skeletal bone of FOP patients is representative, the FOP skeletal bone and HO were also compared with an age- and gender-matched reference. It was hypothesized that mature HO contains less and thinner trabeculae and a thinner cortex compared to

neighboring skeletal bone because it is often non-functional and non-weight bearing. The skeletal bone was expected to show differences with an age- and gender-matched reference because of reduced mobility related to the disease.

METHODS

The patients

Two FOP patients with the classical mutation (R206H), treated at the FOP Expertise Center of Amsterdam, underwent HR-pQCT imaging for this case study. Patient 1 is a 33-year-old woman who is ambulant: she can cover short distances, but she is not able to walk longer distances and to run. She is known with peripheral HO around both first metatarsals and in the left Achilles tendon. The peripheral HO has been present for over 20 years, and the patient has not noticed any flare-up or changes of this HO in the past 5 years. She has not been taking any glucocorticoids in the past 12 months but is on chronic non-steroidal anti-inflammatory drug (NSAID) treatment because of chronic pain due to HO at several sites. Patient 2 is a 23-year-old man. Peripheral HO is located around both first metatarsals and both ankles, all formed after a surgical correction of the hallux valgus early in childhood. The HO has been present for over 15 years, and the patient has not noticed any flare-up or changes of this HO in the past 5 years. He is wheelchair dependent when covering longer distances. He has not been using glucocorticoids and NSAIDs in the past 12 months. The peripheral HO in the patients was identified by physical examination and images acquired earlier by computed tomography (CT) and [18F] sodium fluoride (NaF) positron emission tomography (PET)-CT. They resembled mature bone as defined by a density > 200 HU on CT and were not metabolically active as assessed by peak standardized uptake values on [18F]NaF PET-CT [16]. Both patients have been participating in the LUMINA-1 clinical trial with Activin A blocking antibody Garetosmab for 3 and 4 months, respectively, at the time of HR-pQCT scanning. The HR-pQCT scans were not obtained as part of this double-blind placebo-controlled study. The patients signed the informed consent form to publish their data anonymously, and this form was approved by the Medical Ethics Review Committee of Amsterdam UMC (Amsterdam, the Netherlands).

HR-pQCT imaging protocol

If the mobility of the patients allowed proper and comfortable positioning, HR-pQCT scans were obtained using the second-generation HR-pQCT scanner (XtremeCT II, Scanco Medical AG, Switzerland) with standard clinical settings defined by the manufacturer (X-ray tube voltage of 68 kV, intensity of 1460 μ A, and integration time of 43 ms). For the distal radius and tibia, one 10.2-mm stack was scanned at

the standard location according to the standard protocol, starting 9.5 and 22.5 mm proximally from the radial and tibial endplate, respectively, and extending proximally. For the peripherally located HO, customized 30.6-mm regions (three consecutive stacks of 10.2 mm each) were scanned to ensure full capturing of the HO. The scout view, as part of the standard HR-pQCT procedure, was used to confirm a full capturing. To scan the HO in the halluces and ankles, the patients were carefully positioned with the hip and knee in flexion and the foot in plantar flexion. During acquisition of all scans, the lower arm or lower leg was placed in a standard motion restraining holder, and foam was added to the holder when necessary to ensure the patient's comfort. Quality of the scans was graded by the operator during scan acquisition by inspection of a single low-resolution slice of each stack using the clinically used grading system provided by the manufacturer [17]. A scan was repeated when the quality of at least one stack had a grade > 3 out of 5. Acquisition of one stack takes 2 min, resulting in a total acquisition time of 2 min for each radius and tibia scan and 6 min for each HO scan. Effective radiation dose is approximately 5 μ Sv per stack, leading to an effective dose of approximately 5 μ Sv per radius and tibia scan and of approximately 15 μ Sv per HO scan. The scans were reconstructed with an isotropic voxel size of 61 μ m, resulting in 168 consecutive slices per radius and tibia scan and in 504 consecutive slices per HO scan.

Evaluation of the HR-pQCT scans

The peripherally located HO were visually assessed by a musculoskeletal radiologist (BT) affiliated to the FOP Expertise Center; the isolated HO in the Achilles tendon of patient 1 was also quantitatively evaluated as were the distal radius and tibia. For the quantitative analysis, the isolated HO was manually segmented, and the distal radius and tibia were segmented using an automatic contouring algorithm provided by the manufacturer of the scanner. Thereafter, standard methods were used to quantify bone geometry, density, and microarchitecture of the segmented HO and distal radius and tibia. Geometric parameters included total, trabecular, and cortical area [Tt.Ar, Tb.Ar, and Ct.Ar, respectively (mm^2)]. Densitometric parameters included volumetric bone mineral density of the entire, trabecular, and cortical bone [Tt.BMD, Tb.BMD, and Ct.BMD, respectively ($\text{mg HA}/\text{cm}^3$)]. Microarchitectural parameters included trabecular bone volume fraction [Tb.BV/TV (-)], trabecular number [Tb.N (mm^{-1})], thickness [Tb.Th (mm)], separation [Tb.Sp (mm)], and heterogeneity [Tb.1/N.SD (mm)], and cortical thickness [Ct.Th (mm)], and porosity [Ct.Po (-)]. Additionally, failure load (FL) was estimated of the segmented HO and distal radii and tibiae by means of micro-finite element (μ FE-) modeling. Linear three-dimensional μ FE-models were generated by converting the bone voxels of the HR-pQCT scans to equally sized brick elements, which were assigned a Poisson's ratio of 0.3 and a Young's modulus of 8748 MPa [18]. An axial compression to 1% strain was then simulated

along the longitudinal axis (*i.e.*, compression with constraint of lateral expansion at the bone endings) to estimate FL, for which Pistoia's criterion was used [19]. For this estimation of FL, it was assumed that the HO experiences a tensile load in the direction of the calve muscles and thus in the direction of the compression load on the tibia; simulating either tension or compression gives, apart from the sign, the same results in FE-modeling.

The resulting values of the bone parameters from all analyses were compared to an age- and gender-matched normative reference group. This normative dataset was obtained in a general Canadian male and female population using the same generation HR-pQCT scanner and analyses as in this case study and has recently been published by Whittier *et al.* (2020) [18].

RESULTS

Scan acquisition

The patients' mobility allowed acquisition of HR-pQCT scans of HO in the left Achilles tendon and around both metatarsals of patient 1 and around the right ankle of patient 2. The HO in the Achilles tendon was visible on the standard scan of the left tibia and required no separate scan. HR-pQCT scans could not be acquired of the halluces and left ankle of patient 2 as he was not able to position his foot in plantar flexion due to ankle ankylosis. His right ankle could be scanned without plantar flexion of the foot but with additional foam for comfort during scan acquisition. Due to the inability of both patients to properly position before the scanner, a distal radius scan could only be made of the left side of patient 1. Distal tibia scans could be obtained of the left and right tibia of both patients. All obtained HR-pQCT scans were of good quality (\leq grade 3 for all stacks); therefore, none of the scans had to be repeated.

Evaluation of the distal radius and tibia

A three-dimensional visualization of the scanned left radius and right tibia of patient 1 is shown in **Figure 1**. Geometry, density, microarchitecture, and FL of the dominant side, the left radius of this patient, were within the 25th - 75th percentile (pctl), except for Ct.BMD that was considerably higher (90th - 98th pctl) (**Table 1**). At the tibia, both patients had low Tt.BMD and Tb.BMD compared to the age- and gender-matched reference group ($<$ 2nd pctl) (**Tables 1 and 2**). The trabecular microarchitectural parameters were below or above the interquartile range (IQR): Tb.BV/TV, Tb.N, and Tb.Th were lower ($<$ 2nd pctl, $<$ 25th pctl, and $<$ 2nd pctl, respectively), and Tb.Sp and Tb.1/N.SD were higher ($>$ 75th pctl and $>$ 90th pctl, respectively). The FL of the tibiae

of both patients was also lower than normative values ($< 2^{\text{nd}}$ pctl). In patient 1, Ct.Ar and Ct.Th were lower in both tibiae (both $< 10^{\text{th}}$ pctl), and Ct.BMD was in the lower half of the IQR. In patient 2, Ct.Ar and Ct.Th were $< 25^{\text{th}}$ pctl in the right tibia, and Ct.BMD was in the upper half of the IQR in both tibiae.

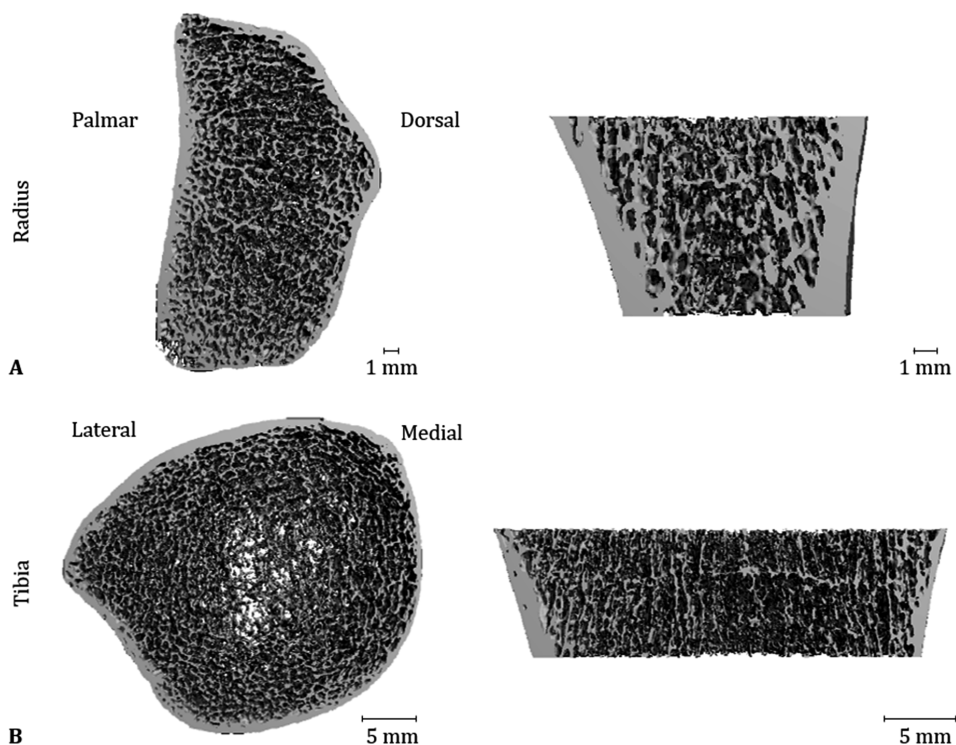


Figure 1. Three-dimensional visualization of the scanned left radius (A) and right tibia (B) of patient 1, obtained with HR-pQCT. A) Quantification revealed a great resemblance of the radius of the fibrodysplasia ossificans progressiva (FOP) patient to that of an age- and gender-matched reference group, except for cortical density that was higher in the FOP patient. B) Quantification revealed major dissimilarities with the age- and gender-matched reference group, especially in total and trabecular density (lower in the patient) and in trabecular and cortical microarchitecture.

Table 1. Bone parameters of the left distal radius and left and right distal tibia of patient 1, a 33-year-old woman, including normative values of the distal radius and tibia of age- and gender-matched controls.

| | Radius | | | | Tibia | | | |
|--|------------|-------------------------|-------------|-------------------------|------------|-------------------------|-------------|-------------------------|
| | Left value | Percentile ^a | Right value | Percentile ^a | Left value | Percentile ^a | Right value | Percentile ^a |
| Geometry (area; mm²) | | | | | | | | |
| Tt.Ar | 247.7 | 25-75 | - | - | 714.6 | 75-90 | 709.1 | 25-75 |
| Tb.Ar | 192.9 | 25-75 | - | - | 627.5 | 75-90 | 622.8 | 75-90 |
| Ct.Ar | 58.2 | 25-75 | - | - | 92.6 | 2-10 | 91.6 | 2-10 |
| Density (BMD; mg HA/cm³) | | | | | | | | |
| Tt.BMD | 336.0 | 25-75 | - | - | 205.3 | <2 | 202.6 | <2 |
| Tb.BMD | 143.1 | 25-75 | - | - | 100.9 | <2 | 95.2 | <2 |
| Ct.BMD | 991.2 | 90-98 | - | - | 934.8 | 25-75 | 955.5 | 25-75 |
| Microarchitecture | | | | | | | | |
| Tb.BV/TV (-) | 0.187 | 25-75 | - | - | 0.143 | <2 | 0.127 | <2 |
| Tb.N (mm ⁻¹) | 1.442 | 25-75 | - | - | 1.149 | 10-25 | 1.162 | 10-25 |
| Tb.Th (mm) | 0.211 | 25-75 | - | - | 0.209 | <2 | 0.202 | <2 |
| Tb.Sp (mm) | 0.649 | 25-75 | - | - | 0.858 | 75-90 | 0.855 | 75-90 |
| Tb.1/N.SD (mm) | 0.225 | 25-75 | - | - | 0.420 | 90-98 | 0.380 | 90-98 |
| Ct.Th (mm) | 1.043 | 25-75 | - | - | 1.078 | 2-10 | 1.013 | <2 |
| Ct.Po (-) | 0.002 | 25-75 | - | - | 0.008 | 25-75 | 0.009 | 25-75 |
| Mechanics (μFE) | | | | | | | | |
| FL (kN) | 2.68 | 25-75 | - | - | 5.28 | <2 | 4.88 | <2 |

Tt: total; Tb: trabecular; Ct: cortical; Ar: area; BMD: volumetric bone mineral density; Tb.BV/TV: trabecular bone volume fraction; Tb.N: trabecular number; Tb.Th: trabecular thickness; Tb.Sp: trabecular separation; Tb.1/N.SD: heterogeneity of the trabecular network; Ct.Th: cortical thickness; Ct.Po: cortical porosity; FL: estimated failure load.

^aPercentile is based on comparison with an age- and gender-matched reference from literature (Whittier *et al.*, 2020).

Evaluation of heterotopic ossification

The HO in the left Achilles tendon of patient 1 was isolated from the neighboring skeletal bone in the scanned region and could therefore be qualitatively as well as quantitatively evaluated (**Figure 2**). The HO constituted a clear cortex and trabecular structure. The cortex appeared thinner than in the neighboring left tibia, but a thickening was present in the axial middle of the scanned region of the HO. The results of the quantitative analysis of the isolated HO and neighboring left tibia are presented in **Table 3**. In the isolated HO, Ct.BMD was below the IQR of the normative dataset (< 2nd pctl), while it was within the IQR in the left distal tibia. Tt.BMD, Tb.BMD, and Ct.Th were below the IQR for both the isolated HO and left tibia. The trabecular microarchitectural parameters were within the IQR for the HO except for Tb.BV/TV (10th - 25th pctl), whereas for the left tibia, Tb.BV/TV, Tb.N, and Tb.Th were lower than the IQR (< 2nd pctl, 10th - 25th pctl, and < 2nd pctl, respectively), and Tb.Sp and Tb.1/N.SD were higher (75th - 90th pctl and 90th - 98th pctl, respectively). FL was

approximately a factor 10 lower in the HO than in the left tibia. It was low compared to normative values (< 2nd pctl). Total bone area was approximately a factor 10 lower in the HO than in the tibia.

Table 2. Bone parameters of the left and right distal tibia of patient 2, a 23-year-old man, including normative values of the distal radius of age- and gender-matched controls.

| Tibia | Left value | Percentile ^a | Right value | Percentile ^a |
|--|------------|-------------------------|-------------|-------------------------|
| Geometry (area; mm²) | | | | |
| Tt.Ar | 849.5 | 25-75 | 831.3 | 25-75 |
| Tb.Ar | 718.9 | 25-75 | 713.7 | 25-75 |
| Ct.Ar | 136.4 | 25-75 | 123.3 | 2-10 |
| Density (BMD; mg HA/cm³) | | | | |
| Tt.BMD | 229.1 | <2 | 232.8 | <2 |
| Tb.BMD | 98.4 | <2 | 113.9 | <2 |
| Ct.BMD | 932.5 | 25-75 | 936.9 | 75-90 |
| Microarchitecture | | | | |
| Tb.BV/TV (-) | 0.1558 | <2 | 0.172 | <2 |
| Tb.N (mm ⁻¹) | 0.855 | <2 | 1.086 | 2-10 |
| Tb.Th (mm) | 0.235 | <2 | 0.233 | <2 |
| Tb.Sp (mm) | 1.170 | >98 | 0.902 | 90-98 |
| Tb.1/N.SD (mm) | 0.827 | >98 | 0.403 | 90-98 |
| Ct.Th (mm) | 1.510 | 25-75 | 1.318 | 10-25 |
| Ct.Po (-) | 0.012 | 25-75 | 0.007 | 10-25 |
| Mechanics (μFE) | | | | |
| FL (kN) | 8.21 | <2 | 7.82 | <2 |

Tt: total; Tb: trabecular; Ct: cortical; Ar: area; BMD: volumetric bone mineral density; Tb.BV/TV: trabecular bone volume fraction; Tb.N: trabecular number; Tb.Th: trabecular thickness; Tb.Sp: trabecular separation; Tb.1/N.SD: heterogeneity of the trabecular network; Ct.Th: cortical thickness; Ct.Po: cortical porosity; FL: estimated failure load.

^aPercentile is based on comparison with an age- and gender-matched reference from literature (Whittier *et al.*, 2020).

The HR-pQCT scans obtained of the other peripheral HO in both patients revealed fusion with the neighboring skeletal bone and could only be qualitatively analyzed. **Figure 3** shows a three-dimensional image of the halluces of patient 1. As can be seen, HO was fused with the phalanx, and at several sites where HO had adjoined the phalanx, the initial cortex was replaced by trabeculae. The trabecular compartments of the HO and phalanx seemed to merge and were surrounded by a cortex of the HO. This neo-cortex appeared thinner than the initial cortex of the phalanx, whereas the trabeculae appeared thicker (data not shown). A similar pattern was found in the right ankle of patient 2 (**Figure 4**): there was fusion of HO with the tibia, fibula, and talus, with partial replacement of the original cortex by trabeculae and a (neo-) cortex surrounding the fused bone structures. Enlargement of the distal tibia was also observed. The HO adjoining the ankle bones seemed to contain relatively more cortical bone than the ankle bones and the other HO lesions inspected. Although all

HO lesions analyzed by HR-pQCT had a density of > 200 HU and thus resembled mature bone, HU was lower in these lesions than in neighboring skeletal bone that had a density of > 350 HU. The only exception was the HO around the ankle, which had a considerable higher HU value than the surrounding talus, tibia, and fibula.

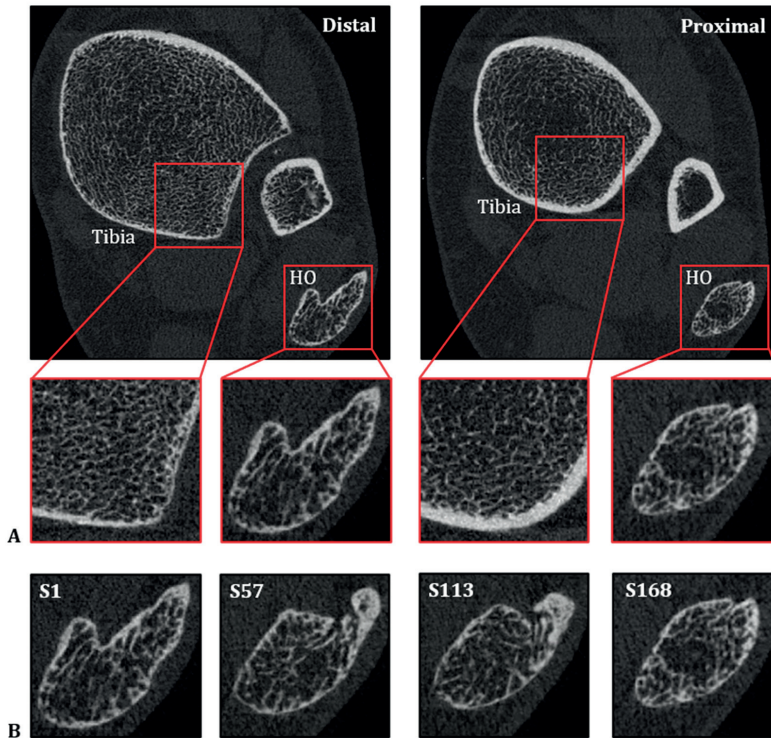


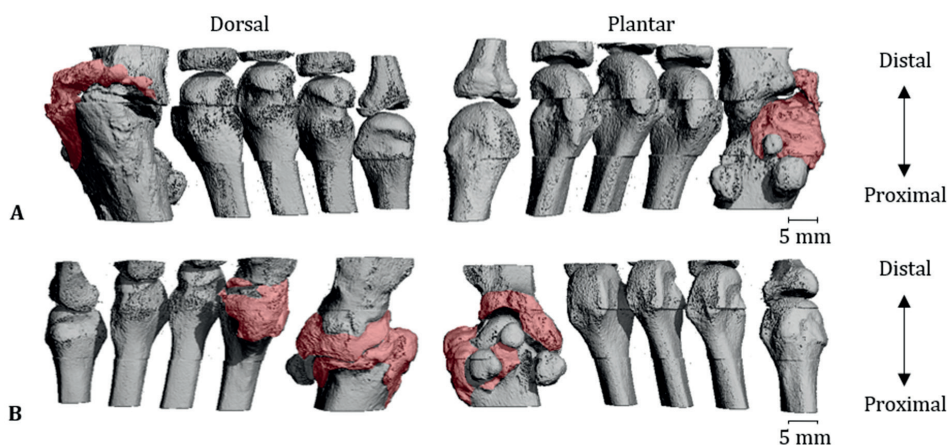
Figure 2. **A)** Distal (left) and proximal (right) slice of the HR-pQCT scan of the left tibia of patient 1, a 33-year-old female fibrodysplasia ossificans progressiva (FOP) patient showing isolated heterotopic ossification (HO) in the Achilles tendon. Quantification showed dissimilarities between the HO and the patient's tibia, especially in trabecular microarchitecture when compared to an age- and gender-matched reference. **B)** Four slices from distal (left) to proximal (right) of the HR-pQCT scan of the left tibia showing HO in the Achilles tendon.

Table 3. Bone parameters of the left distal tibia and isolated heterotopic ossification (HO) in the left Achilles tendon of patient 1, a 33-year old woman, including normative values of the distal tibia with age- and gender-matched controls.

| | HO (left Achilles tendon) | | Left tibia | |
|--|---------------------------|-------------------------|------------|-------------------------|
| | Value | Percentile ^a | Value | Percentile ^a |
| Geometry (area; mm²) | | | | |
| Tt.Ar | 64.9 | <2 | 714.6 | 75-90 |
| Tb.Ar | 49.6 | <2 | 627.5 | 75-90 |
| Ct.Ar | 17.2 | <2 | 92.6 | 2-10 |
| Density (BMD; mg HA/cm³) | | | | |
| Tt.BMD | 271.9 | 10-25 | 205.3 | <2 |
| Tb.BMD | 142.1 | 10-25 | 100.9 | <2 |
| Ct.BMD | 656.7 | <2 | 934.8 | 25-75 |
| Microarchitecture | | | | |
| Tb.BV/TV (-) | 0.195 | 10-25 | 0.143 | <2 |
| Tb.N (mm ⁻¹) | 1.242 | 25-75 | 1.149 | 10-25 |
| Tb.Th (mm) | 0.254 | 25-75 | 0.209 | <2 |
| Tb.Sp (mm) | 0.766 | 25-75 | 0.858 | 75-90 |
| Tb.1/N.SD (mm) | 0.282 | 25-75 | 0.420 | 90-98 |
| Ct.Th (mm) | 0.917 | <2 | 1.078 | 2-10 |
| Ct.Po (-) | 0.013 | 25-75 | 0.008 | 25-75 |
| Mechanics (μFE) | | | | |
| FL (kN) | 0.530 | <2 | 5.28 | <2 |

Tt: total; Tb: trabecular; Ct: cortical; Ar: area; BMD: volumetric bone mineral density; Tb.BV/TV: trabecular bone volume fraction; Tb.N: trabecular number; Tb.Th: trabecular thickness; Tb.Sp: trabecular separation; Tb.1/N.SD: heterogeneity of the trabecular network; Ct.Th: cortical thickness; Ct.Po: cortical porosity; FL: estimated failure load.

^aPercentile is based on comparison with an age- and gender-matched reference from literature (Whittier *et al.*, 2020).


Figure 3. Three-dimensional visualization of the scanned metatarsals of the right (A) and left (B) foot of patient 1. The patient underwent surgery for the correction of a bilateral hallux valgus at the age of 1, resulting in heterotopic ossification (HO) at the operated sites. The pink color visualizes the sites with HO. It should be noted that, due to fusion, the exact border between HO and skeletal bone could not be established.

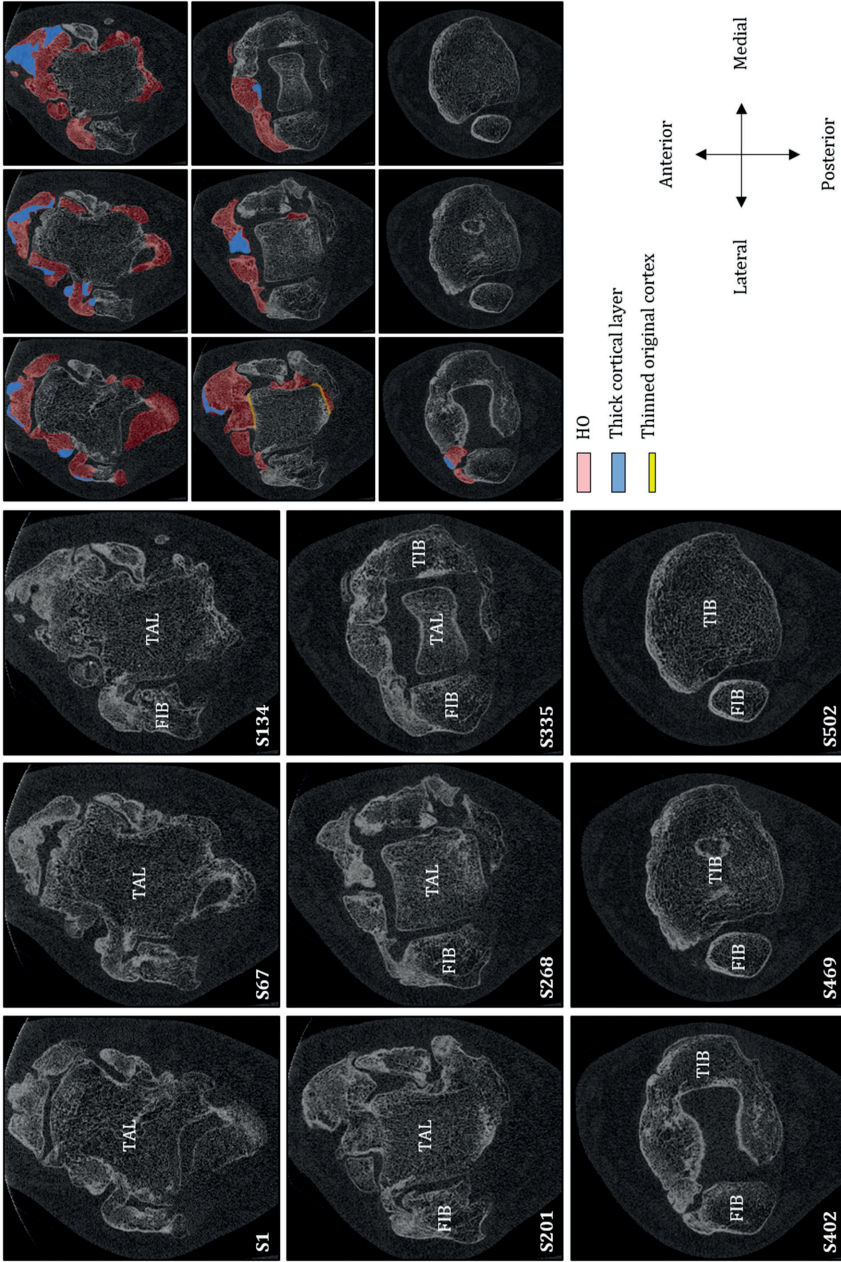


Figure 4. Nine two-dimensional slices of the HR-pQCT scan of a 30.6-mm region of the right ankle of patient 2, a 23-year-old male fibrodysplasia ossificans progressiva (FOP) patient, from distal (S1) to proximal (S502). S1 shows the talus with heterotopic ossification (HO) attached. The original cortical layer of the talus seems disrupted at several sites where HO has fused. (S67–S502) HO has also fused to the fibula. However, a thin cortical layer seems to be present throughout the series. (S201–S502) HO has fused to the tibia; as with the talus, the cortical layer is disrupted at several sites of the fusion. TIB, TAL, and FIB represent tibia, talus, and fibula, respectively. On the right, HO, increased cortical bone, and the thinned cortex are visualized in blue, red, and yellow, respectively. It should be noted that, due to fusion, the exact border between HO and skeletal bone could not be established.

DISCUSSION

The aim of this case study was to assess peripherally located mature HO and skeletal bone of two FOP patients with HR-pQCT and to compare those with each other and with an age- and gender-matched reference group from literature. The HO assessed in both patients was found to merge with neighboring skeletal bone. The cortex of the skeletal bone at sites of fusion appeared to be replaced by trabeculae to form one new entity, constituting trabecular bone surrounded by a (neo-)cortex. Most bone parameters of the isolated HO in the Achilles tendon of one of the patients were found to be within the IQR of age- and gender-matched reference tibia data, whereas most of the neighboring tibia were below or above the IQR. The bone parameters of the distal radius resembled the literature values, except for cortical BMD.

To the best of our knowledge, this is the first study examining HO non-invasively and at a microarchitectural level in living FOP patients. HO around the halluces and ankle of the patients was merged with the neighboring skeletal bone, and it appeared that a neo-cortex was formed, surrounding the HO where it fused with the skeletal bone. However, the thin lining of the original cortical layer of the skeleton was still visible at various regions, suggesting a yet incomplete coalescence. This may indicate that the fusion of HO and skeletal bone and associated remodeling is a slow process, considering the presence of the HO for over 15 years in both patients. The neo-cortex around the halluces appeared thinner than the original skeletal cortex, whereas HO around the ankle consisted of a relatively thick cortical layer, which is perhaps due to the weight-bearing function of the ankle and its associated HO. Both these fused HO and the isolated HO assessed in this case study showed a cortical and trabecular compartment as do skeletal bones, which, in that respect, agrees with previous case reports suggesting that HO of FOP patients has a similar morphology as the skeletal bone [5, 11]. However, these earlier publications have mainly investigated biopsies of early HO lesions that were taken in children for other reasons [5,12,13], while we investigated mature HO lesions as confirmed by CT. Furthermore, the use of HR-pQCT instead of histology enables a quantitative evaluation of HO besides a qualitative assessment, which may provide new insights into HO in FOP.

Today, quantitative assessment of the microarchitecture of HO is scarce. Most mice studies mimicking FOP and HO formation have not quantified the HO microstructure despite the use of high-resolution imaging modalities (*e.g.*, μ CT) [20-23]. In humans, the only study quantifying HO at the microarchitectural level concerned, to our knowledge, an *ex vivo* μ CT study on bone biopsies of non-genetic HO. In that study, surgically removed HO at muscular tissue was analyzed, which revealed variations in microarchitecture between and within lesions and an affected

strength of the HO lesions compared to the skeletal bone [24]. In contrast, we found FL of the isolated HO in the Achilles tendon to be approximately 10% higher than of the neighboring tibia when correcting for the difference in total bone area. This agrees with the assumption in literature that the strength of HO in FOP is preserved, which is based on the observation that (stress) fractures of HO are not often seen in FOP patients [25]. The discrepancy in the findings on strength between the study on non-genetic HO and our case study on genetic HO may, among others, be caused by a different ossification process with distinct histological characteristics between genetic and non-genetic HO [26]. Furthermore, HO in tendons may not be representative for HO in muscles as, for example, trauma-induced muscle HO in FOP appears to be driven through another progenitor lineage than HO formed in ligaments and tendons [27]. This may also contribute to the qualitative differences found at the microarchitectural level between the trauma-induced HO around the ankle of patient 2 and the spontaneously formed HO in the Achilles tendon of patient 1. Notably, the estimated FL in the isolated HO in the Achilles tendon is lower than the peak forces that occur in the Achilles tendon during daily life in healthy individuals (*e.g.*, 1.3-1.5 kN during walking, up to 4 kN during running and jumping [28-30]), which would suggest rupture of the Achilles tendon or fracture of the HO during such activities. However, such peak forces may not be reached in FOP patients due to their reduced ability or inability to fully perform these activities.

The comparison of the quantitative evaluation of the HO in the Achilles tendon with the neighboring tibia showed that the microarchitectural parameters of the HO had better agreement with the age- and gender-matched reference than the left tibia. It is not known what may have caused this difference between HO and neighboring tibia. A different mechanical stimulation may possibly play a role, but a study in larger datasets is needed before any conclusions can be drawn about the possible microarchitectural differences between HO and skeleton. These microarchitectural differences could have contributed to the 10% larger estimated FL of the HO compared to the tibia after accounting for areal differences. The comparison of the HO with the peripheral skeleton raises the question whether the skeletal bone of FOP patients is comparable at the microarchitectural level to an age- and gender-matched reference [31]. Unlike microarchitectural misbalances throughout the entire skeleton in other rare bone diseases [32-35], the microarchitecture of the analyzed radius of patient 1 was found to be comparable to an age- and gender-matched reference population. The tibiae of both FOP patients, in contrast, did show considerable deviations from age- and gender-matched normative data: the total and trabecular BMD were lower, and the trabecular compartment consisted of less and thinner trabeculae in a more heterogeneously formed network. Reduced mobility or a changed mechanical loading in the FOP patients could have contributed to these differences from the normative

data, as could have the frequent glucocorticoid use of both patients [36]. Research in larger datasets is needed to further investigate possible microarchitectural differences between the skeleton of FOP patients and of the general population.

This study has shown that HR-pQCT allows visualization and quantification of BMD, microarchitecture, and the biomechanical properties of mature HO in FOP patients *in vivo*. This imaging modality enables analysis of mature HO in more detail than other imaging modalities while simultaneously exposing patients to a negligible amount of radiation. Furthermore, it is non-invasive, in contrast to bone biopsies for histological analysis; therefore, it does not trigger flare-ups as is the case with biopsies. Consequently, HR-pQCT may be an interesting technique for future research into mature HO in FOP, such as for sequential HR-pQCT imaging to study the development of mineralized HO during a flare-up or the effects of a study drug on mature HO. However, it is likely that the ability of FOP patients to properly position before the gantry of the scanner is restricted as shoulders, elbows, hips, and knees are frequently ankylosed in these patients [4]. This may limit scan acquisition and affect scan quality. The right distal radius of patient 1 and both distal radii and the right ankle of patient 2 could not be scanned for that reason. As a result, it may be challenging to find patients eligible for HR-pQCT scanning, combined with the rarity of FOP and the restriction to peripheral bones, as HO in FOP patients mainly forms more centrally, while peripheral sites are often spared [1,4,37,38].

Several limitations of this case study have to be mentioned. First, we examined HO of two FOP patients, which gives an interesting impression about the skeletal microarchitecture of bone in FOP patients but does limit interpretation. Larger datasets are needed to draw conclusions on the possible differences in BMD, microarchitecture, and strength between HO and skeletal bone and between the skeletal bone of FOP patients and an age- and gender-matched reference population. Second, the estimation of FL using μ FE-analysis and Pistoia's criterion is only validated for the distal radius, and thus its accuracy is not known for HO, further limiting the conclusions on the strength of HO compared to that of the skeletal bone. Third, the two patients in this study were participating in a double-blind placebo-controlled trial at the time of HR-pQCT imaging, and it is unknown whether they were on active treatment that could have influenced the bone parameters. Finally, the quantitative analysis of HO was limited to HO in the Achilles tendon of patient 1 as the other scanned HO was not isolated from the neighboring skeletal bone, which made it impossible to establish the exact border between the HO and the skeletal bone for segmentation of the HO. Nevertheless, qualitative analysis was possible for this HO.

In conclusion, this case study showed that HR-pQCT allows non-invasive assessment of peripherally located HO and the distal radius and tibia in FOP patients, which may provide new insights into skeletal and heterotopic bone in FOP patients at the microarchitectural level. Isolated HO seemed microarchitecturally more comparable to skeletal bone from reference data than the peripheral skeleton of FOP patients. Additionally, HO and skeleton appear to become one entity when contiguous.

ACKNOWLEDGEMENTS

We thank the two fibrodysplasia ossificans progressiva patients for their participation. We also thank Dr. S. K. Boyd for providing the normative dataset.

REFERENCES

- [1] Rogers JC, Geho WB. Fibrodysplasia ossificans progressiva. a survey of forty-two cases. *J Bone Joint Surg Am.* 1979;61:909–914.
- [2] Cohen RB, Hahn GV, Tabas JA, et al. The natural history of heterotopic ossification in patients who have fibrodysplasia ossificans progressiva. a study of forty-four patients. *J Bone Joint Surg Am.* 1993;75:215–219.
- [3] Kaplan FS, Le Merrer M, Glaser DL, et al. Fibrodysplasia ossificans progressiva. *Best Pract Res Clin Rheumatol.* 2008;22:191–205.
- [4] Pignolo RJ, Bedford-Gay C, Liljestrom M, et al. The natural history of flare-ups in fibrodysplasia ossificans progressiva (FOP): a comprehensive global assessment. *J Bone Miner Res.* 2016;31:650–656.
- [5] Kaplan FS, Tabas JA, Gannon FH, Finkel G, Hahn GV, Zasloff MA. The histopathology of fibrodysplasia ossificans progressiva. An endochondral process. *J Bone Joint Surg Am.* 1993;75:220–230.
- [6] Gannon FH, Valentine BA, Shore EM, Zasloff MA, Kaplan FS. Acute lymphocytic infiltration in an extremely early lesion of fibrodysplasia ossificans progressiva. *Clin Orthopaed Related Res.* 1998;346:19–25.
- [7] Gannon FH, Glaser D, Caron R, Thompson LD, Shore EM, Kaplan FS. Mast cell involvement in fibrodysplasia ossificans progressiva. *Hum Pathol.* 2001;32:842–848.
- [8] Pignolo RJ, Shore EM, Kaplan FS. Fibrodysplasia ossificans progressiva: clinical and genetic aspects. *Orphanet J Rare Dis.* 2011;6:80.
- [9] Lutwak L. Myositis ossificans progressiva. mineral, metabolic and radioactive calcium studies of the effects of hormones. *Am J Med.* 1964;37:269–293.
- [10] Kaplan FS, Strear CM, Zasloff MA. Radiographic and scintigraphic features of modeling and remodeling in the heterotopic skeleton of patients who have fibrodysplasia ossificans progressiva. *Clin Orthopaed Related Res.* 1994;304:238–247.
- [11] Mahboubi S, Glaser DL, Shore EM, Kaplan FS. Fibrodysplasia ossificans progressiva. *Pediatric Radiol.* 2001;31:307–314.
- [12] Jayasundara JA, Punchihewa GL, de Alwis DS. An unusual case of adult onset progressive heterotopic ossification suggesting a variant form of fibrodysplasia ossificans progressiva. *Singapore Med J.* 2012;53:e83–e86.
- [13] Kamal AF, Novriansyah R, Rahyussalim, Prabowo Y, Siregar NC. Fibrodysplasia ossificans progressiva: difficulty in diagnosis and management a case report and literature review. *J Orthopaed Case Rep.* 2015;5:26–30.
- [14] Kitterman JA, Kantanie S, Rocke DM, Kaplan FS. Iatrogenic harm caused by diagnostic errors in fibrodysplasia ossificans progressiva. *Pediatrics* 2005;116:e654–e661.
- [15] Boutroy S, Bouxsein ML, Munoz F, Delmas PD. In vivo assessment of trabecular bone microarchitecture by high-resolution peripheral quantitative computed tomography. *J Clin Endocrinol Metab.* 2005;90:6508–6515.
- [16] Botman E, Rajmakers P, Yaqub M, et al. Evolution of heterotopic bone in fibrodysplasia ossificans progressiva: an [(18)F]NaF PET/CT study. *Bone* 2019;124:1–6.
- [17] Pialat JB, Burghardt AJ, Sode M, Link TM, Majumdar S. Visual grading of motion induced image degradation in high resolution peripheral computed tomography: impact of image quality on measures of bone density and micro-architecture. *Bone* 2012;50:111–118.

- [18] Whittier D, Burt L, Hanley D, Boyd S. Sex- and site-specific reference data for bone microarchitecture in adults measured using second-generation HR-pQCT. *J Bone Miner Res.* 2020;35:2151–2158.
- [19] Pistoia W, van Rietbergen B, Lochmuller EM, Lill CA, Eckstein F, Ruegsegger P. Estimation of distal radius failure load with micro-finite element analysis models based on three-dimensional peripheral quantitative computed tomography images. *Bone* 2002;30:842–848.
- [20] Brownley RC, Agarwal S, Loder S, et al. Characterization of heterotopic ossification using radiographic imaging: evidence for a paradigm shift. *PLoS One* 2015;10:e0141432.
- [21] Hatsell SJ, Idone V, Wolken DM, et al. ACVR1R206H receptor mutation causes fibrodysplasia ossificans progressiva by imparting responsiveness to activin A. *Sci Transl Med.* 2015;7:303ra137.
- [22] Chakkalakal SA, Uchibe K, Convente MR, et al. Palovarotene inhibits heterotopic ossification and maintains limb mobility and growth in mice with the human ACVR1(R206H) fibrodysplasia ossificans progressiva (FOP) mutation. *J Bone Miner Res.* 2016;31:1666–1675.
- [23] Upadhyay J, Xie L, Huang L, et al. The expansion of heterotopic bone in fibrodysplasia ossificans progressiva is activin a-dependent. *J Bone Miner Res.* 2017;32:2489–2499.
- [24] Trieb K, Meryk A, Senck S, Naismith E, Grubeck-Loebenstien B. Immunological and morphological analysis of heterotopic ossification differs to healthy controls. *BMC Musculoskelet Disord* 2018;19:327.
- [25] Einhorn TA, Kaplan FS. Traumatic fractures of heterotopic bone in patients who have fibrodysplasia ossificans progressiva. a report of 2 cases. *Clin Orthopaed Related Res.* 1994;173–177.
- [26] Meyers C, Lisiecki J, Miller S, et al. Heterotopic ossification: a comprehensive review. *JBMR Plus* 2019;3:e10172.
- [27] Dey D, Bagarova J, Hatsell SJ, et al. Two tissue-resident progenitor lineages drive distinct phenotypes of heterotopic ossification. *Sci Transl Med.* 2016;8:366ra163.
- [28] Fukashiro S, Komi PV, Jarvinen M, Miyashita M. In vivo achilles tendon loading during jumping in humans. *Eur J Appl Physiol Occup Physiol.* 1995;71:453–458.
- [29] Finni T, Komi PV, Lukkariniemi J. Achilles tendon loading during walking: application of a novel optic fiber technique. *Eur J Appl Physiol Occup Physiol.* 1998;77:289–291.
- [30] Hosseini HS, Dunki A, Fabech J, et al. Fast estimation of Colles' fracture load of the distal section of the radius by homogenized finite element analysis based on HR-pQCT. *Bone* 2017;97:65–75.
- [31] Burt LA, Liang Z, Sajobi TT, Hanley DA, Boyd SK. Sex-and site-specific normative data curves for HR-pQCT. *J Bone Miner Res.* 2016;31:2041–2047.
- [32] Folkestad L, Hald JD, Hansen S, et al. Bone geometry, density, and microarchitecture in the distal radius and tibia in adults with osteogenesis imperfecta type I assessed by high-resolution pQCT. *J Bone Miner Res.* 2012;27:1405–1412.
- [33] Kocijan R, Muschitz C, Haschka J, et al. Bone structure assessed by HR-pQCT, TBS and DXL in adult patients with different types of osteogenesis imperfecta. *Osteoporos Int.* 2015;26:2431–2440.
- [34] Arruda M, Coelho MC, Moraes AB, et al. Bone mineral density and microarchitecture in patients with autosomal dominant osteopetrosis: a report of two cases. *J Bone Miner Res.* 2016;31:657–662.
- [35] Butscheidt S, Rolvien T, Kornak U, et al. Clinical significance of DXA and HR-pQCT in Autosomal Dominant Osteopetrosis (ADO II). *Calcif Tissue Int.* 2018;102:41–52.
- [36] Ilias I, Zoumakis E, Ghayee H. An overview of glucocorticoid induced osteoporosis. In: Feingold KR, Anawalt B, Blackman MR, et al, eds. *Endotext.* South Dartmouth (MA): MDText.com, Inc.; 2000.

- [37] Smith R, Russell RG, Woods CG. Myositis ossificans progressiva. clinical features of eight patients and their response to treatment. *J Bone Joint Surg Br.* 1976;58:48–57.
- [38] Connor JM, Evans DA. Fibrodysplasia ossificans progressiva. the clinical features and natural history of 34 patients. *J Bone Joint Surg Br.* 1982;64:76–83.



4

Chapter 4

Effect of denosumab compared with risedronate on bone strength in patients initiating or continuing glucocorticoid treatment

Piet P.M.M. Geusens, Melissa S.A.M. Bevers, Bert van Rietbergen, Osvaldo D. Messina, Eric Lespessailles, Beatriz Oliveri, Roland Chapurlat, Klaus Engelke, Arkadi Chines, Shuang Huang, Kenneth G. Saag, and Joop P. van den Bergh

J. Bone Miner. Res. 2022, 37(6): 1136-1146.

ABSTRACT

In a randomized clinical trial in patients initiating glucocorticoid therapy (GC-I) or on long-term therapy (GC-C), denosumab every 6 months increased spine and hip bone mineral density at 12 and 24 months significantly more than daily risedronate. The aim of this study was to evaluate the effects of denosumab compared with risedronate on bone strength and microarchitecture measured by high-resolution peripheral quantitative computed tomography (HR-pQCT) in GC-I and GC-C. A subset of 110 patients had high-resolution peripheral quantitative computed tomography (HR-pQCT) scans of the distal radius and tibia at baseline and at 12 and 24 months. Cortical and trabecular microarchitecture were assessed with standard analyses and failure load (FL) with micro-finite element analysis. At the radius at 24 months, FL remained unchanged with denosumab and significantly decreased with risedronate in GC-I (-4.1%, 95% confidence interval [CI] -6.4, -1.8) and, in GC-C, it significantly increased with denosumab (4.3%, 95% CI 2.1, 6.4) and remained unchanged with risedronate. Consequently, FL was significantly higher with denosumab than with risedronate in GC-I (5.6%, 95% CI 2.4, 8.7, $p < 0.001$) and in GC-C (4.1%, 95% CI 1.1, 7.2, $p = 0.011$). We also found significant differences between denosumab and risedronate in percentage changes in cortical and trabecular microarchitectural parameters in GC-I and GC-C. Similar results were found at the tibia. To conclude, this HR-pQCT study shows that denosumab is superior to risedronate in terms of preventing FL loss at the distal radius and tibia in GC-I and in increasing FL at the radius in GC-C, based on significant differences in changes in the cortical and trabecular bone compartments between the treatment groups in GC-I and GC-C. These results suggest that denosumab could be a useful therapeutic option in patients initiating GC therapy or on long-term GC therapy and may contribute to treatment decisions in this patient population.

INTRODUCTION

Patients who use glucocorticoids (GC) are at increased risk of vertebral and non-vertebral fractures, immediately when they initiate (GC-I) or continue treatment (GC-C) [1-3]. In a randomized phase 3 clinical trial, gains in areal bone mineral density (aBMD) by dual-energy X-ray absorptiometry (DXA) were greater with denosumab than with risedronate at the lumbar spine, femoral neck, total hip, and radius at 12 and 24 months of treatment in both GC-I and GC-C [4,5], but that study did not provide insights into changes in cortical and trabecular microarchitecture or bone strength.

High-resolution peripheral quantitative computed tomography (HR-pQCT) allows assessment of bone microarchitecture and strength to evaluate disease and treatment effects [6]. Earlier cross-sectional case-control studies using HR-pQCT reported disturbed cortical and trabecular microarchitecture and decreased bone stiffness at the distal radius and tibia in patients on long-term oral or inhaled GC [7,8], but data on the effects of treatment on bone microarchitecture and strength in GC-induced osteoporosis (GIOP) are lacking. In postmenopausal women, positive effects have been described with denosumab and risedronate on bone microarchitecture using HR-pQCT [9-11] and with denosumab on bone strength using QCT [9,12,13]. However, the pathophysiology of bone loss in GIOP is different from postmenopausal osteoporosis (PMOP) [14-19], and thus the treatment effects of denosumab and risedronate on bone microarchitecture and strength in PMOP cannot be extrapolated to GIOP. Therefore, and in view of the differences in the effects on aBMD between denosumab and risedronate in GC-I and GC-C [4,5], the aim of this study was to evaluate changes in cortical and trabecular microarchitecture and estimated bone strength assessed with HR-pQCT during 24 months with denosumab compared with risedronate in GC-I and GC-C.

METHODS

Study population and design

The study population of this HR-pQCT study included a subgroup of GC-treated patients enrolled in a phase 3, double-blind, double-dummy, and active-controlled clinical trial on the effects of denosumab compared with risedronate on aBMD (NCT01575873). Study population and design of this multicenter study have previously been described in detail [4,5]. The study was conducted in accordance with the Declaration of Helsinki and followed the International Conference for Harmonization Guidelines for Good Clinical Practice. An independent review board

approved the study design for each center. Written informed consent was obtained from each patient before study participation.

HR-pQCT imaging

HR-pQCT scans were taken from patients who consented to participate in this substudy and who were treated in centers with access to an HR-pQCT scanner. This included a total of 110 (56 denosumab, 54 risedronate) of the 590 GC-treated patients participating in the main study. The HR-pQCT scans in all participating centers were acquired using the first-generation XtremeCT scanner (XtremeCT, Scanco Medical AG, Bruttisellen, Switzerland), and none of the centers switched to the second-generation scanner during study duration. All centers applied the same scan protocol using the default clinical settings defined by the manufacturer of the scanner to scan a standardized region of the distal radius and tibia [20]. Additionally, cross-validation was performed using a dedicated phantom (QRM Forearm QC phantom, QRM GmbH, Mohrendorf, Germany) that was scanned at all study sites. This phantom consisted of a European forearm phantom coupled to a QRM calibration phantom, which allowed for correction of potential X-ray field inhomogeneities.

Scan-quality assessment and analyses were performed centrally. Baseline and follow-up scans were registered using standard automatic two-dimensional slice-matching, followed by analysis of the common bone volume of interest according to the standard evaluation protocol [20,21]. Additionally, bone strength was estimated in terms of failure load (FL) and bone stiffness using standard linear-elastic micro-finite element (μ FE-) analysis [20,22]. If the common volume (*ie*, number of slices overlapping at all three visits) was < 60 , the radius or tibia scans of all visits of the corresponding patient were excluded from analysis. Cortical assessments were not performed for movement artifacts of grade 2 or higher on a scale of 1 (no movement) to 4 (severe movement) [23].

Statistical analysis

Repeated-measures mixed-effects models were used to estimate the percentage changes from baseline in each treatment group. Consistent with the main study [4,5], the models were adjusted for treatment (main effect) and baseline value (covariate). Duration of prior GC-use (< 12 months versus ≥ 12 months) was an additional covariate in the models for GC-C. Percentage changes were expressed as least-square means with 95%-confidence intervals (95%-CI). Additionally, the difference between the least-square means of denosumab and risedronate was estimated and expressed as least-square means with 95%-CI and p value (significance level $\alpha = 0.05$; not adjusted for multiple comparisons).

RESULTS

Baseline characteristics were balanced between the two treatment groups within the GC-I and GC-C subpopulations, except for lumbar spine *T*-score in GC-C (**Tables 1 and 2**). Because of insufficient slice overlap among visits (< 60 slices), radius scans from three patients and tibia scans from one patient were excluded from analysis. Common number of slices was > 80 for all patients except for five patients at the radius and two patients at the tibia (60-80 slices). Additionally, the radius scans of one patient with an old radius fracture and one patient with inconsistent laterality of follow-up compared with baseline were excluded from analysis. The data of another patient were excluded for being an outlier due to the near absence of trabecular bone. For five visits, cortical parameters were not assessed in the radius because of movement artifacts.

Table 1. Baseline characteristics.

| | GC-initiating | | GC-continuing | |
|--|---------------------------------|-------------------------------|---------------------------------|-------------------------------|
| | Risedronate (<i>N</i> = 24) | Denosumab (<i>N</i> = 32) | Risedronate (<i>N</i> = 30) | Denosumab (<i>N</i> = 24) |
| Female sex | 15 (62.5) | 19 (59.4) | 28 (93.3) | 19 (79.2) |
| Premenopause | 0 (0.0) | 1 (5.3) | 0 (0.0) | 1 (5.3) |
| Postmenopause | 15 (100.0) | 18 (94.7) | 28 (100.0) | 18 (94.7) |
| Age (years) | 66.0 ± 13.1 | 68.5 ± 9.8 | 64.2 ± 8.8 | 63.6 ± 9.8 |
| Race | | | | |
| White | 24 (100.0) | 32 (100.0) | 30 (100.0) | 23 (95.8) |
| Asian | 0 (0.0) | 0 (0.0) | 0 (0.0) | 0 (0.0) |
| Black or African American | 0 (0.0) | 0 (0.0) | 0 (0.0) | 1 (4.2) |
| Other | 0 (0.0) | 0 (0.0) | 0 (0.0) | 0 (0.0) |
| Baseline daily GC dose (mg) ^a | 18.91 ± 9.91 | 21.41 ± 15.68 | 10.32 ± 6.52 | 11.33 ± 4.95 |
| Duration of prior GC use | | | | |
| < 12 months | 24 (100.0) | 32 (100.0) | 4 (13.3) | 4 (16.7) |
| ≥ 12 months | 0 (0.0) | 0 (0.0) | 26 (86.7) | 20 (83.3) |
| BMD <i>T</i> -score (DXA) | | | | |
| Lumbar spine | -0.77 ± 1.83 ^b | -0.98 ± 1.95 | -2.60 ± 1.08 | -1.64 ± 1.80 |
| Total hip | -0.77 ± 0.79 | -1.15 ± 0.97 ^b | -1.73 ± 0.86 | -1.62 ± 0.85 |

GC = glucocorticoid; BMD = bone mineral density, DXA = dual-energy X-ray absorptiometry.

Data are reported as *n* (%) or mean ± standard deviation.

^aDose in prednisone equivalents.

^bAssessed in *N*-1 individuals.

Table 2. Baseline characteristics of HR-pQCT measurements in patients initiating glucocorticoid therapy (GC-I) or on long-term therapy (GC-C) at the distal radius and tibia.

| | GC-initiating | | GC-continuing | |
|------------------------------------|------------------------------|---------------------------|-----------------------------|---------------------------|
| | Risedronate (N = 24) | Denosumab (N = 32) | Risedronate (N = 30) | Denosumab (N = 24) |
| Distal radius | n = 24 | n = 29 | n = 21 | n = 20 |
| μFE | | | | |
| Stiffness (kN/mm) | 77.8 ± 28.6 ^a | 75.3 ± 33.4 ^b | 49.7 ± 9.81 ^c | 59.6 ± 23.1 ^f |
| FL (kN) | 3.94 ± 1.40 ^a | 3.78 ± 1.64 ^b | 2.51 ± 0.50 ^c | 2.98 ± 1.17 ^f |
| Total bone | | | | |
| Total volume (mm ³) | 2842.5 ± 639.1 ^c | 3060.5 ± 822.7 | 2538.6 ± 447.2 ^g | 2603.6 ± 658.4 |
| Tt.BMD (mg HA/cm ³) | 279.2 ± 75.8 | 267.5 ± 69.5 | 213.5 ± 54.3 | 236.0 ± 70.0 |
| Cortical bone | | | | |
| Cortical volume (mm ³) | 522.5 ± 148.9 ^c | 535.8 ± 162.7 | 416.3 ± 71.4 ^g | 458.5 ± 98.3 |
| Ct.BMD (mg HA/cm ³) | 792.1 ± 69.4 | 790.7 ± 77.3 | 787.4 ± 48.4 | 777.5 ± 104.8 |
| Ct.Th (mm) | 0.68 ± 0.23 | 0.67 ± 0.24 | 0.53 ± 0.13 | 0.58 ± 0.23 |
| Ct.Po (%) | 2.55 ± 1.12 ^c | 2.75 ± 1.24 | 2.67 ± 1.10 ^g | 2.83 ± 1.34 ^h |
| Trabecular bone | | | | |
| Tb.BMD (mg HA/cm ³) | 149.1 ± 49.7 | 140.0 ± 46.8 | 95.2 ± 42.9 | 106.6 ± 50.3 |
| Tb.BV/TV (-) | 0.12 ± 0.04 | 0.12 ± 0.04 | 0.08 ± 0.04 | 0.09 ± 0.04 |
| Tb.N (mm ⁻¹) | 1.78 ± 0.37 | 1.71 ± 0.39 | 1.36 ± 0.44 | 1.44 ± 0.47 |
| Tb.Th (mm) | 0.07 ± 0.01 | 0.07 ± 0.01 | 0.06 ± 0.01 | 0.06 ± 0.01 |
| Tb.Sp (mm) | 0.52 ± 0.15 | 0.56 ± 0.21 | 0.79 ± 0.40 | 0.72 ± 0.30 |
| Distal tibia | n = 24 | n = 29 | n = 24 | n = 21 |
| μFE | | | | |
| Stiffness (kN/mm) | 197.8 ± 56.3 ^d | 194.4 ± 65.5 ^b | 134.4 ± 27.6 ^h | 155.9 ± 37.8 ^c |
| FL (kN) | 9.99 ± 2.76 ^d | 9.85 ± 3.20 ^b | 6.90 ± 1.44 ^h | 7.95 ± 1.83 ^c |
| Total bone | | | | |
| Total volume (mm ³) | 6866.2 ± 1096.0 ^a | 6963.0 ± 1315.9 | 6462.9 ± 1013.9 | 6345.7 ± 911.2 |
| Tt.BMD (mg HA/cm ³) | 259.5 ± 69.7 | 261.7 ± 55.3 | 192.8 ± 41.0 | 232.2 ± 53.4 |
| Cortical bone | | | | |
| Cortical volume (mm ³) | 1048.5 ± 319.8 ^a | 1085.5 ± 347.2 | 803.1 ± 140.5 | 925.5 ± 140.4 |
| Ct.BMD (mg HA/cm ³) | 805.3 ± 61.6 | 795.1 ± 60.9 | 793.5 ± 61.2 | 800.2 ± 88.2 |
| Ct.Th (mm) | 1.03 ± 0.37 | 1.04 ± 0.35 | 0.73 ± 0.14 | 0.89 ± 0.27 |
| Ct.Po (%) | 7.16 ± 1.75 ^a | 7.43 ± 2.12 | 7.40 ± 3.18 | 7.60 ± 2.88 |
| Trabecular bone | | | | |
| Tb.BMD (mg HA/cm ³) | 151.3 ± 42.2 | 155.1 ± 32.3 | 106.3 ± 41.4 | 127.6 ± 45.8 |
| Tb.BV/TV (-) | 0.13 ± 0.04 | 0.13 ± 0.03 | 0.09 ± 0.03 | 0.11 ± 0.04 |
| Tb.N (mm ⁻¹) | 1.72 ± 0.38 | 1.81 ± 0.31 | 1.44 ± 0.40 | 1.63 ± 0.46 |
| Tb.Th (mm) | 0.07 ± 0.01 | 0.07 ± 0.01 | 0.06 ± 0.01 | 0.07 ± 0.01 |
| Tb.Sp (mm) | 0.53 ± 0.13 | 0.50 ± 0.10 | 0.68 ± 0.19 | 0.62 ± 0.32 |

μFE = micro-finite element; FL = failure load; Tt.BMD = total bone mineral density; Ct.BMD = cortical bone mineral density; Ct.Th = cortical thickness; Ct.Po = cortical porosity; Tb.BMD = trabecular bone mineral density; Tb.BV/TV = trabecular bone volume fraction; Tb.N = trabecular number; Tb.Th = trabecular thickness; Tb.Sp = trabecular separation.

Data are reported as mean ± standard deviation.

N = number of randomized patients enrolled in the HR-pQCT substudy; n = number of patients with observed data

^an = 22. ^bn = 25. ^cn = 23. ^dn = 21. ^en = 15. ^fn = 14. ^gn = 20. ^hn = 19

Significant differences between risedronate and denosumab are reported in bold (two-sample independent *t* test; *p* < 0.05).

Evaluation of estimated bone strength

In GC-I, FL significantly increased compared with baseline at 12 months with denosumab (radius: 1.8%, 95%-CI 0.1, 3.6; tibia: 1.7%, 95%-CI 0.1, 3.4) and did not change with risedronate (**Table 3; Figure 1**). This led to significant differences in percentage change between the two drugs (radius: 3.3%, $p = 0.013$; tibia: 2.5%, $p = 0.043$). At 24 months, FL remained unchanged with denosumab, while it significantly decreased compared with baseline with risedronate at the radius (-4.1%, 95%-CI -6.4, -1.8). This resulted in a significant between-treatment difference at the radius (5.6%, $p < 0.001$) and also at the tibia (3.2%, $p = 0.013$), although the changes at the tibia at 24 months did not reach significance. Similar results were found in stiffness.

In GC-C, FL remained unchanged with denosumab and risedronate at 12 months and significantly increased with denosumab (radius: 4.3%, 95%-CI 2.1, 6.4) and remained unchanged with risedronate at 24 months (**Table 3; Figure 1**). Corresponding difference between denosumab and risedronate at 24 months was significant (radius: 4.1%, $p = 0.011$). Changes and differences in stiffness were similar.

Table 3. Percentage change from baseline in μ FE-based parameters describing bone strength at the distal radius and tibia in patients initiating glucocorticoid therapy (GC-I) or on long-term therapy (GC-C).

| | | Distal radius | | Distal tibia | |
|----------------------|-------------|------------------------|--------------------------|------------------------|------------------------|
| | | Month 12 | Month 24 | Month 12 | Month 24 |
| GC-initiating | | $n_D = 25, n_R = 22$ | $n_D = 23, n_R = 20$ | $n_D = 25, n_R = 21$ | $n_D = 23, n_R = 18$ |
| FL | DMAb (N=32) | 1.8 (0.1, 3.6) | 1.4 (-0.7, 3.6) | 1.7 (0.1, 3.4) | 1.6 (-0.1, 3.2) |
| | RIS (N=24) | -1.5 (-3.4, 0.4) | -4.1 (-6.4, -1.8) | -0.8 (-2.6, 1.0) | -1.6 (-3.5, 0.2) |
| | DMAb-RIS | 3.3 (0.7, 5.9)* | 5.6 (2.4, 8.7)† | 2.5 (0.1, 4.9)* | 3.2 (0.7, 5.7)* |
| Stiffness | DMAb | 1.5 (-0.3, 3.4) | 0.9 (-1.3, 3.1) | 2.1 (0.1, 4.1) | 1.8 (-0.2, 3.7) |
| | RIS | -1.9 (-3.9, 0.1) | -4.4 (-6.8, -2.0) | -0.8 (-3.0, 1.5) | -1.6 (-3.8, 0.6) |
| | DMAb-RIS | 3.5 (0.8, 6.1)* | 5.3 (2.0, 8.5)* | 2.9 (-0.1, 5.9) | 3.3 (0.4, 6.3)* |
| GC-continuing | | $n_D = 14, n_R = 14$ | $n_D = 12, n_R = 12$ | $n_D = 14, n_R = 18$ | $n_D = 13, n_R = 16$ |
| FL | DMAb (N=24) | 1.8 (-1.4, 5.1) | 4.3 (2.1, 6.4) | 1.8 (-1.7, 5.3) | 3.1 (-0.3, 6.4) |
| | RIS (N=30) | -0.2 (-3.5, 3.0) | 0.1 (-2.0, 2.3) | 0.1 (-3.0, 3.2) | 0.2 (-2.8, 3.2) |
| | DMAb-RIS | 2.0 (-2.6, 6.7) | 4.1 (1.1, 7.2)* | 1.7 (-3.1, 6.5) | 2.9 (-1.8, 7.5) |
| Stiffness | DMAb | 1.2 (-2.2, 4.6) | 3.6 (1.6, 5.5) | 2.3 (-1.9, 6.4) | 3.7 (-0.3, 7.6) |
| | RIS | -0.4 (-3.9, 3.0) | -0.1 (-2.0, 1.9) | 0.2 (-3.4, 3.9) | 0.1 (-3.4, 3.6) |
| | DMAb-RIS | 1.6 (-3.3, 6.6) | 3.6 (0.9, 6.4)* | 2.0 (-3.6, 7.7) | 3.5 (-1.9, 8.9) |

FL = failure load; DMAb = denosumab; RIS = risedronate.

Data are reported as least-square means (95%-confidence interval).

N = number of randomized patients enrolled in the HR-pQCT substudy; n_D = number of patients with observed data receiving denosumab; n_R = number of patients with observed data receiving risedronate

Percentage changes with and differences between the treatment groups are based on repeated-measures mixed-effects models adjusted for treatment and baseline value (GC-initiating) or treatment, baseline value, and duration of prior GC use (< 12 months versus \geq 12 months) (GC-continuing). Significant changes within and differences between the treatment groups are reported in bold ($p < 0.05$). * $p < 0.05$ and † $p \leq 0.001$ for differences between the treatment groups.

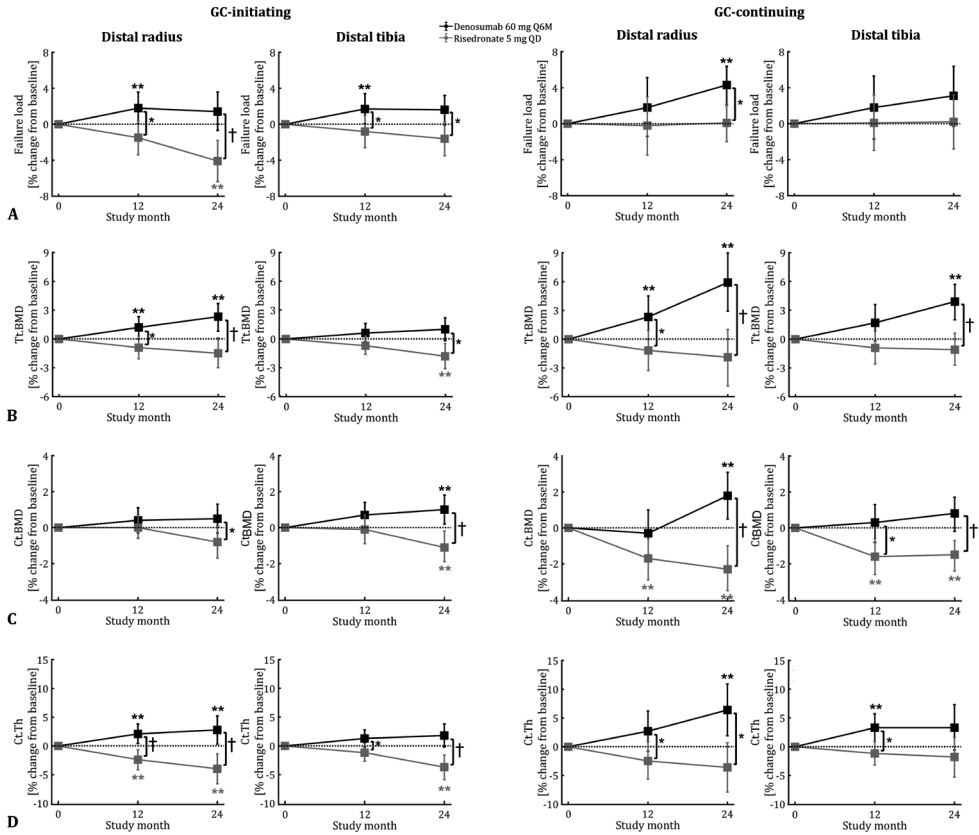


Figure 1. Percentage changes from baseline in bone failure load (A), total bone mineral density (Tr.BMD) (B), cortical BMD (Ct.BMD) (C), and cortical thickness (Ct.Th) (D) at the distal radius and tibia with 60 mg of subcutaneous denosumab every 6 months or 5 mg of oral risedronate daily in patients initiating (<3 months) or continuing glucocorticoid treatment (≥3 months). Significant changes within the treatment groups compared with baseline are denoted with ** ($p < 0.05$); significant changes between the treatment groups are denoted with * ($p < 0.05$) and † ($p \leq 0.001$).

Evaluation of bone volume

In GC-I and GC-C, significant changes with and differences between denosumab and risedronate were not found in total volume, but they were found in cortical volume (Tables 4 and 5). In GC-I at 12 months, cortical volume significantly increased with denosumab (radius: 1.8%, 95%-CI 0.3, 3.3; tibia: 1.0%, 95%-CI 0.0, 2.0) and remained unchanged with risedronate. Consequently, the differences between denosumab and risedronate were significant (radius: 3.0%, $p = 0.008$; tibia: 1.8%, $p = 0.021$). At 24 months, it significantly changed at the radius with denosumab (2.9%, 95%-CI 1.4, 4.5) and risedronate (-2.1%, 95%-CI -3.7, -0.4) with corresponding significant between-treatment difference (5.0%, $p < 0.001$). Although the change at the tibia at 24 months did not reach significance, corresponding between-treatment

difference did (2.5%, $p = 0.028$). In GC-C, cortical volume remained unchanged with denosumab and risedronate at 12 months. At 24 months, it significantly increased with denosumab (radius: 3.1%, 95% CI 0.5, 5.6; tibia: 5.0%, 95%-CI 1.8, 8.1) and decreased with risedronate (tibia: -2.9%, 95%-CI -5.7, -0.1), resulting in significant between-treatment differences (radius: 4.8%, $p = 0.013$; tibia: 7.9%, $p = 0.001$).

Evaluation of BMD and bone microarchitecture

In GC-I, total BMD (Tt.BMD) significantly increased with denosumab at the radius at 12 months (1.2%, 95%-CI 0.0, 2.3) and 24 months (2.3%, 95%-CI 0.8, 3.7), whereas it remained unchanged with risedronate (**Table 4; Figure 1**). Corresponding differences between denosumab and risedronate at the radius were significant (12 months: 2.1%, $p = 0.015$; 24 months: 3.7%, $p < 0.001$). At the tibia, it remained unchanged with denosumab, whereas it significantly decreased with risedronate at 24 months (-1.8%, 95%-CI -3.1, -0.5), leading to a significant between-treatment difference at this time point (2.9%, $p = 0.002$).

Significant changes and differences were also found in the cortical bone compartment (**Table 4; Figure 1**). Cortical BMD (Ct.BMD) remained unchanged at 12 months at the radius and tibia with denosumab and risedronate, whereas at 24 months, it significantly changed at the tibia (denosumab: 1.0%, 95% CI 0.2, 1.8; risedronate: -1.1%, 95%-CI -1.9, -0.2) with corresponding significant between-treatment difference (2.1%, $p < 0.001$). Although it did not change significantly at the radius at 24 months, corresponding between-treatment difference did (1.4%, $p = 0.027$). Cortical thickness (Ct.Th) showed more pronounced changes. At the radius, it significantly increased with denosumab at 12 and 24 months (2.1%, 95%-CI 0.4, 3.8, and 2.8%, 95%-CI 0.3, 5.2, respectively), whereas it significantly decreased with risedronate (12 months: -2.4%, 95%-CI -4.2, -0.7; 24 months: -4.0%, 95%-CI -6.6, -1.4), resulting in significant between-treatment differences (12 months: 4.6%, $p < 0.001$; 24 months: 6.7%, $p < 0.001$). At the tibia, Ct.Th remained unchanged with denosumab, whereas it significantly decreased with risedronate at 24 months (-3.7%, 95%-CI -5.9, -1.6), leading to a significant difference between denosumab and risedronate at 24 months (5.5%, $p < 0.001$) but also at 12 months (2.5%, $p = 0.024$). Cortical porosity (Ct.Po) remained unchanged with denosumab and risedronate at both time points and scan locations except for a significant increase at 24 months with denosumab at the radius and with risedronate at the tibia.

Table 4. Percentage change from baseline in parameters describing bone volume, density, and microarchitecture of the distal radius and tibia in patients initiating glucocorticoid therapy (GC-I).

| | | Distal radius | | Distal tibia | |
|-----------------|-----------------|---|---|---|---|
| | | Month 12 ($n_D = 24$, $n_R = 23$) | Month 24 ($n_D = 24$, $n_R = 21$) | Month 12 ($n_D = 25$, $n_R = 23$) | Month 24 ($n_D = 24$, $n_R = 20$) |
| Total volume | DMAb ($N=32$) | -1.3 (-2.9, 0.2) | -0.9 (-2.4, 0.6) ^b | -0.2 (-0.8, 0.3) | -0.1 (-0.6, 0.5) ^d |
| | RIS ($N=24$) | -0.4 (-2.0, 1.2) ^a | 0.6 (-1.1, 2.2) ^b | -0.2 (-0.8, 0.3) ^c | -0.5 (-1.1, 0.2) ^d |
| | DMAb-RIS | -1.0 (-3.2, 1.2) | -1.5 (-3.7, 0.7) | -0.0 (-0.8, 0.7) | 0.4 (-0.4, 1.2) |
| Tt.BMD | DMAb | 1.2 (0.0, 2.3) | 2.3 (0.8, 3.7) | 0.6 (-0.3, 1.6) | 1.0 (-0.2, 2.2) |
| | RIS | -0.9 (-2.1, 0.3) | -1.5 (-3.0, 0.1) | -0.7 (-1.6, 0.3) | -1.8 (-3.1, -0.5) |
| | DMAb-RIS | 2.1 (0.4, 3.8)* | 3.7 (1.6, 5.8)† | 1.3 (-0.1, 2.6) | 2.9 (1.1, 4.6)* |
| Cortical volume | DMAb | 1.8 (0.3, 3.3) | 2.9 (1.4, 4.5)^b | 1.0 (0.0, 2.0) | 1.0 (-0.5, 2.5) ^d |
| | RIS | -1.2 (-2.8, 0.4) ^a | -2.1 (-3.7, -0.4)^b | -0.8 (-1.9, 0.3) ^c | -1.5 (-3.2, 0.1) ^d |
| | DMAb-RIS | 3.0 (0.8, 5.2)* | 5.0 (2.7, 7.3)† | 1.8 (0.3, 3.3)* | 2.5 (0.3, 4.8)* |
| Ct.BMD | DMAb | 0.4 (-0.3, 1.1) | 0.5 (-0.3, 1.3) | 0.7 (-0.1, 1.4) | 1.0 (0.2, 1.8) |
| | RIS | 0.0 (-0.6, 0.7) | -0.8 (-1.7, 0.1) | -0.1 (-0.9, 0.7) | -1.1 (-1.9, -0.2) |
| | DMAb-RIS | 0.4 (-0.6, 1.3) | 1.4 (0.2, 2.5)* | 0.7 (-0.4, 1.8) | 2.1 (0.9, 3.2)† |
| Ct.Th | DMAb | 2.1 (0.4, 3.8) | 2.8 (0.3, 5.2) | 1.3 (-0.2, 2.8) | 1.8 (-0.2, 3.8) |
| | RIS | -2.4 (-4.2, -0.7) | -4.0 (-6.6, -1.4) | -1.2 (-2.7, 0.4) | -3.7 (-5.9, -1.6) |
| | DMAb-RIS | 4.6 (2.1, 7.0)† | 6.7 (3.2, 10.3)† | 2.5 (0.3, 4.7)* | 5.5 (2.6, 8.5)† |
| Ct.Po | DMAb | 1.9 (-4.6, 8.3) | 12.5 (4.1, 21.0)^b | 2.7 (-2.5, 7.9) | 1.4 (-2.6, 5.5) ^d |
| | RIS | 3.4 (-3.4, 10.2) ^a | 8.1 (-1.0, 17.1) ^b | 1.6 (-4.0, 7.3) ^c | 6.2 (1.6, 10.8)^d |
| | DMAb-RIS | -1.5 (-10.9, 7.9) | 4.5 (-7.9, 16.9) | 1.1 (-6.7, 8.8) | -4.7 (-10.9, 1.5) |
| Tb.BMD | DMAb | 1.3 (-0.2, 2.8) | 3.4 (1.5, 5.3) | 0.5 (-0.3, 1.3) | 0.8 (-0.5, 2.0) |
| | RIS | -0.0 (-1.6, 1.5) | 0.1 (-1.9, 2.1) | 0.1 (-0.7, 1.0) | -0.5 (-1.8, 0.9) |
| | DMAb-RIS | 1.3 (-0.8, 3.5) | 3.3 (0.5, 6.0)* | 0.4 (-0.8, 1.5) | 1.2 (-0.6, 3.1) |
| Tb.BV/TV | DMAb | 1.5 (-0.1, 3.1) | 3.8 (1.8, 5.7) | 0.8 (-0.1, 1.7) | 1.3 (0.0, 2.7) |
| | RIS | 0.4 (-1.3, 2.0) | 1.0 (-1.1, 3.1) | 0.7 (-0.3, 1.6) | 0.4 (-1.0, 1.9) |
| | DMAb-RIS | 1.1 (-1.1, 3.4) | 2.8 (-0.1, 5.7) | 0.1 (-1.2, 1.4) | 0.9 (-1.1, 2.9) |
| Tb.N | DMAb | 2.7 (-0.7, 6.1) | 6.3 (2.3, 10.2) | -0.8 (-4.5, 3.0) | 2.2 (-1.8, 6.3) |
| | RIS | 3.2 (-0.3, 6.6) | 3.8 (-0.4, 8.0) | 0.1 (-3.8, 4.0) | 0.5 (-3.9, 4.9) |
| | DMAb-RIS | -0.5 (-5.3, 4.4) | 2.4 (-3.3, 8.2) | -0.8 (-6.3, 4.6) | 1.7 (-4.3, 7.7) |
| Tb.Th | DMAb | -1.0 (-4.0, 2.0) | -1.5 (-4.3, 1.3) | 2.8 (-1.0, 6.6) | 0.2 (-3.4, 3.7) |
| | RIS | -1.8 (-4.8, 1.3) | -2.5 (-5.5, 0.5) | 0.9 (-3.0, 4.8) | 0.1 (-3.8, 4.0) |
| | DMAb-RIS | 0.8 (-3.5, 5.1) | 1.0 (-3.1, 5.1) | 1.9 (-3.6, 7.4) | 0.0 (-5.2, 5.3) |
| Tb.Sp | DMAb | -2.4 (-5.9, 1.0) | -5.8 (-9.7, -2.0) | 1.6 (-2.1, 5.4) | -1.3 (-5.1, 2.5) |
| | RIS | -2.4 (-5.9, 1.1) | -2.7 (-6.9, 1.4) | 0.5 (-3.4, 4.4) | -0.2 (-4.4, 3.9) |
| | DMAb-RIS | -0.1 (-5.0, 4.9) | -3.1 (-8.7, 2.6) | 1.1 (-4.3, 6.6) | -1.1 (-6.7, 4.6) |

DMAb = denosumab; RIS = risedronate; Tt.BMD = total bone mineral density; Ct.BMD = cortical bone mineral density; Ct.Th = cortical thickness; Ct.Po = cortical porosity; Tb.BMD = trabecular bone mineral density; Tb.BV/TV = trabecular bone volume fraction; Tb.N = trabecular number; Tb.Th = trabecular thickness; Tb.Sp = trabecular separation.

Data are reported as least-square means (95%-confidence interval). N = number of randomized patients enrolled in the HR-pQCT substudy; n_D = number of patients with observed data receiving denosumab; n_R = number of patients with observed data receiving risedronate. ^a $n_R = 22$. ^b $n_R = 20$ and $n_D = 23$. ^c $n_R = 21$. ^d $n_R = 18$ and $n_D = 23$.

Percentage changes with and differences between the treatment groups are based on repeated-measures mixed-effects models adjusted for treatment and baseline value. Significant changes within and differences between the treatment groups are reported in bold ($p < 0.05$). * $p < 0.05$ and † $p \leq 0.001$ for differences between the treatment groups.

Table 5. Percentage change from baseline in parameters describing bone volume, density, and microarchitecture of the distal radius and tibia in patients on long-term glucocorticoid therapy (GC-C).

| | | Distal radius | | Distal tibia | |
|-----------------|----------------------|---|---|---|---|
| | | Month 12 | Month 24 | Month 12 | Month 24 |
| | | (<i>n_D</i> = 14, <i>n_R</i> = 16) | (<i>n_D</i> = 12, <i>n_R</i> = 13) | (<i>n_D</i> = 15, <i>n_R</i> = 19) | (<i>n_D</i> = 13, <i>n_R</i> = 16) |
| Total volume | DMAb (<i>N</i> =24) | 0.9 (-1.3, 3.1) | -0.2 (-2.0, 1.6) | -0.0 (-0.8, 0.8) ^a | -0.3 (-1.4, 0.7) |
| | RIS (<i>N</i> =30) | 0.4 (-1.8, 2.6) ^a | 0.1 (-1.7, 1.9) ^b | 0.5 (-0.3, 1.2) ^c | 0.3 (-0.7, 1.2) |
| | DMAb-RIS | 0.5 (-2.7, 3.6) | -0.3 (-2.9, 2.2) | -0.5 (-1.6, 0.6) | -0.6 (-2.0, 0.8) |
| Tt.BMD | DMAb | 2.3 (0.0, 4.5) | 5.9 (2.9, 9.0) | 1.7 (-0.2, 3.6) | 3.9 (2.0, 5.7) |
| | RIS | -1.2 (-3.3, 0.9) | -1.9 (-4.9, 1.0) | -0.9 (-2.6, 0.8) | -1.1 (-2.7, 0.6) |
| | DMAb-RIS | 3.5 (0.4, 6.6)* | 7.9 (3.5, 12.2)† | 2.6 (-0.1, 5.2) | 4.9 (2.4, 7.5)† |
| Cortical volume | DMAb | 1.8 (-0.1, 3.8) | 3.1 (0.5, 5.6) | 1.2 (-1.1, 3.6) ^a | 5.0 (1.8, 8.1) |
| | RIS | -0.6 (-2.5, 1.4) ^a | -1.8 (-4.3, 0.8) ^b | -1.0 (-3.0, 1.1) ^c | -2.9 (-5.7, -0.1) |
| | DMAb-RIS | 2.4 (-0.4, 5.2) | 4.8 (1.1, 8.6)* | 2.2 (-1.0, 5.4) | 7.9 (3.5, 12.3)† |
| Ct.BMD | DMAb | -0.3 (-1.5, 1.0) | 1.8 (0.5, 3.1) | 0.3 (-0.8, 1.3) | 0.8 (-0.2, 1.7) |
| | RIS | -1.7 (-2.9, -0.6) | -2.3 (-3.5, -1.0) | -1.6 (-2.6, -0.6) | -1.5 (-2.4, -0.7) |
| | DMAb-RIS | 1.5 (-0.2, 3.2) | 4.1 (2.3, 5.9)† | 1.9 (0.4, 3.3)* | 2.3 (1.0, 3.6)† |
| Ct.Th | DMAb | 2.7 (-0.8, 6.2) | 6.4 (1.9, 10.9) | 3.3 (0.9, 5.7) | 3.3 (-0.6, 7.3) |
| | RIS | -2.5 (-5.7, 0.8) | -3.6 (-7.9, 0.7) | -1.2 (-3.2, 0.9) | -1.8 (-5.3, 1.6) |
| | DMAb-RIS | 5.2 (0.3, 10.0)* | 10.0 (3.5, 16.5)* | 4.5 (1.2, 7.8)* | 5.2 (-0.7, 11.0) |
| Ct.Po | DMAb | 5.9 (-2.8, 14.7) ^c | 0.6 (-15.7, 16.8) ^d | -0.5 (-6.8, 5.9) ^a | 6.1 (-1.1, 13.3) |
| | RIS | 0.3 (-8.2, 8.7) ^a | 14.1 (-1.4, 29.7) ^b | 2.3 (-3.2, 7.9) ^c | -3.5 (-10.0, 3.0) |
| | DMAb-RIS | 5.7 (-6.5, 17.8) | -13.6 (-36.3, 9.2) | -2.8 (-11.2, 5.6) | 9.6 (-0.1, 19.3) |
| Tb.BMD | DMAb | 1.4 (-2.4, 5.2) | 4.7 (0.0, 9.4) | 0.4 (-1.9, 2.6) | 3.1 (1.1, 5.1) |
| | RIS | -2.0 (-5.5, 1.6) | -2.1 (-6.6, 2.4) | -0.7 (-2.7, 1.3) | -0.2 (-2.0, 1.6) |
| | DMAb-RIS | 3.4 (-1.8, 8.6) | 6.8 (0.3, 13.3)* | 1.1 (-2.0, 4.1) | 3.3 (0.6, 6.0)* |
| Tb.BV/TV | DMAb | 1.9 (-1.2, 5.1) | 5.3 (1.5, 9.2) | 0.9 (-1.4, 3.1) | 3.7 (1.5, 5.8) |
| | RIS | 0.3 (-2.6, 3.3) | 0.2 (-3.5, 3.9) | 0.8 (-1.2, 2.8) | 1.3 (-0.7, 3.2) |
| | DMAb-RIS | 1.6 (-2.7, 5.9) | 5.1 (-0.3, 10.5) | 0.1 (-2.9, 3.1) | 2.4 (-0.6, 5.3) |
| Tb.N | DMAb | 3.7 (-1.1, 8.4) | 5.9 (1.0, 10.7) | -0.6 (-6.3, 5.0) | 2.7 (-4.8, 10.2) |
| | RIS | -1.4 (-5.9, 3.1) | -1.0 (-5.7, 3.7) | -1.9 (-6.9, 3.1) | 1.8 (-4.9, 8.6) |
| | DMAb-RIS | 5.1 (-1.5, 11.6) | 6.9 (0.1, 13.7)* | 1.2 (-6.4, 8.8) | 0.8 (-9.3, 11.0) |
| Tb.Th | DMAb | -1.0 (-5.3, 3.4) | 1.2 (-3.9, 6.4) | 4.0 (-1.8, 9.9) | 3.8 (-1.8, 9.3) |
| | RIS | 1.5 (-2.6, 5.5) | 0.5 (-4.5, 5.4) | 2.8 (-2.4, 8.0) | -0.7 (-5.7, 4.3) |
| | DMAb-RIS | -2.4 (-8.4, 3.5) | 0.8 (-6.4, 8.0) | 1.2 (-6.7, 9.2) | 4.4 (-3.2, 12.0) |
| Tb.Sp | DMAb | -3.2 (-8.0, 1.5) | -5.0 (-9.6, -0.3) | 1.8 (-4.2, 7.9) | -1.3 (-8.5, 5.8) |
| | RIS | 1.8 (-2.7, 6.3) | 1.3 (-3.2, 5.7) | 2.7 (-2.7, 8.1) | -0.7 (-7.1, 5.7) |
| | DMAb-RIS | -5.0 (-11.6, 1.5) | -6.2 (-12.7, 0.2) | -0.9 (-9.0, 7.3) | -0.6 (-10.3, 9.0) |

DMAb = denosumab; RIS = risedronate; Tt.BMD = total bone mineral density; Ct.BMD = cortical bone mineral density; Ct.Th = cortical thickness; Ct.Po = cortical porosity; Tb.BMD = trabecular bone mineral density; Tb.BV/TV = trabecular bone volume fraction; Tb.N = trabecular number; Tb.Th = trabecular thickness; Tb.Sp = trabecular separation. Data are reported as least-square means (95%-confidence interval).

N = number of randomized patients enrolled in the HR-pQCT substudy; *n_D* = number of patients with observed data receiving denosumab; *n_R* = number of patients with observed data receiving risedronate.

^a*n_R* = 14 and/or *n_D* = 14. ^b*n_R* = 12. ^c*n_D* = 13. ^d*n_D* = 11. ^e*n_R* = 18.

Percentage changes with and differences between the treatment groups are based on repeated-measures mixed-effects models adjusted for treatment, baseline value, and duration of prior GC-use (< 12 months versus ≥ 12 months). Significant changes within and differences between the treatment groups are reported in bold (*p* < 0.05). **p* < 0.05 and †*p* ≤ 0.001 for differences between the treatment groups.

Less prominent changes and differences were found in the trabecular bone compartment (**Table 4**). Trabecular BMD (Tb.BMD) remained unchanged at 12 months with denosumab and risedronate and significantly changed at 24 months with denosumab (radius: 3.4%, 95%-CI 1.5, 5.3) but not with risedronate, resulting in a significant difference between denosumab and risedronate at this time point (radius: 3.3%, $p = 0.020$). Similarly, trabecular bone volume fraction (Tb.BV/TV), number (Tb.N), thickness (Tb.Th), and separation (Tb.Sp) remained unchanged with denosumab and risedronate at 12 and 24 months except with denosumab at 24 months at the radius in Tb.BV/TV, Tb.N, and Tb.Sp and at the tibia in Tb.BV/TV, but these changes did not lead to significant differences between denosumab and risedronate.

In GC-C, Tt.BMD significantly increased with denosumab at 12 months (radius: 2.3%, 95%-CI 0.0, 4.5) and 24 months (radius: 5.9%, 95%-CI 2.9, 9.0; tibia: 3.9%, 95%-CI 2.0, 5.7), whereas it remained unchanged at both time points with risedronate (**Table 5; Figure 1**). Corresponding differences between denosumab and risedronate were significant at 12 months (radius: 3.5%, $p = 0.030$) and 24 months (radius: 7.9%, $p = 0.001$; tibia: 4.9%, $p < 0.001$).

Similar to GC-I, compartmental changes and differences in GC-C were mainly found in the cortical bone (**Table 5; Figure 1**). At 12 months, Ct.BMD remained unchanged with denosumab and significantly decreased with risedronate (radius: -1.7%, 95%-CI -2.9, -0.6; tibia: -1.6%, 95%-CI -2.6, -0.6), resulting in a significant between-treatment difference at the tibia (1.9%, $p = 0.014$) but not at the radius. At 24 months, Ct.BMD significantly increased with denosumab (radius: 1.8%, 95% CI -0.5, 3.1) and significantly decreased with risedronate (radius: -2.3%, 95%-CI -3.5, -1.0; tibia: -1.5%, 95%-CI -2.4, -0.7) with corresponding significant between-treatment differences (radius: 4.1%, $p < 0.001$; tibia: 2.3%, $p = 0.001$). Ct.Th in contrast did not change significantly with risedronate at 12 months at the radius and tibia but significantly increased with denosumab at the tibia (3.3%, 95%-CI 0.9, 5.7), resulting in a significant between-treatment difference (4.5%, $p = 0.010$). Although the changes at the radius did not reach significance at 12 months, the between-treatment difference did (5.2%, $p = 0.038$). At 24 months, Ct.Th remained unchanged with risedronate, whereas it significantly increased with denosumab at the radius (6.4%, 95%-CI 1.9, 10.9) with corresponding significant difference between denosumab and risedronate (10.0%, $p = 0.004$). No significant changes and differences were found in Ct.Po.

Less pronounced changes and differences were found in the trabecular bone compartment (**Table 5**). Tb.BMD remained unchanged at 12 months with denosumab and risedronate and significantly changed at 24 months with denosumab (radius:

4.7%, 95%-CI 0.0, 9.4; tibia: 3.1%, 95%-CI 1.1, 5.1) and not with risedronate, resulting in significant differences between denosumab and risedronate at 24 months (radius: 6.8%, $p = 0.042$; tibia: 3.3%, $p = 0.018$). Similar as in GC-I, no significant changes with and differences between denosumab and risedronate were found in the trabecular microarchitecture parameters except for a significant change at 24 months with denosumab at the radius in Tb.BV/TV, Tb.N, and Tb.Sp and at the tibia in Tb.BV/TV with a corresponding just significant between-treatment difference in Tb.N at the radius.

DISCUSSION

The aim of this HR-pQCT study was to assess changes in cortical and trabecular microarchitecture and estimated bone strength during 24 months with denosumab compared with risedronate in GC-I and GC-C. We found that FL was maintained with denosumab at the radius and tibia in GC-I at 24 months, whereas it decreased with risedronate at the radius, leading to a significant difference in FL at the radius and tibia in favor of denosumab. In GC-C at 24 months, FL significantly increased with denosumab at the radius, whereas it was maintained with risedronate, resulting in a significant difference in FL in favor of denosumab at the radius.

In GC-I, maintenance of FL at the radius at 24 months with denosumab coincided with an increase in Ct.Th, which is compatible with the rapid reduction of bone resorption, filling of existing resorption sites, and appearance of fewer newly excavated sites at the endosteum, similar to a previous report of denosumab in PMOP [9]. Simultaneously, Ct.BMD remained unchanged, which indicates that the expected loss in Ct.BMD [7,8] due to increased intracortical bone remodeling after initiating high-dose GC [24] did not occur with denosumab. Ct.Po increased at 24 months, which, together with the unchanged Ct.BMD, could be the result of the inclusion of highly mineralized trabeculae in the endosteal border of the cortex. With risedronate, in contrast, FL at the radius decreased at 24 months, which coincided with a decrease in Ct.Th and consequent significant difference from denosumab (in favor of denosumab). This effect on Ct.Th indicates that risedronate, as opposed to denosumab, could not halt endosteal bone loss in GC-I, which is the result of increased osteoclast activity by GCs [25], also at the endosteal site of the cortex [26,27]. Different effects were found at the tibia, *eg*, with denosumab, FL was also maintained at the tibia at 24 months but with an increase in Ct.BMD and not in Ct.Th, and with risedronate, Ct.BMD was not maintained at the tibia as was found at the radius but decreased. The latter may be explained by the coinciding increase in Ct.Po at the tibia, which indicates that intracortical bone remodeling remained unchanged with risedronate at the radius

but not at the tibia. The differences between the radius and tibia suggest a role of the loading of bones, which can be affected by the suppressive effect of GCs on osteocytes and osteoblasts [28].

Interestingly, different treatment effects were found in GC-C compared with GC-I. In GC-C, FL increased at the radius at 24 months with denosumab, which coincided with an increase in Ct.Th and Ct.BMD. At the tibia, these parameters were maintained with denosumab. With risedronate, FL was also maintained but coincided with a decrease in Ct.BMD. This implies that risedronate could not prevent the loss of Ct.BMD with long-term GC [7,8], as opposed to denosumab. Ct.Th was maintained with risedronate at both scan sites and both time points, which contrasts with the decrease observed in GC-I.

In both subpopulations, few changes and differences were found with and between denosumab and risedronate in the trabecular bone compartment. At 24 months, Tb.BMD and Tb.N increased with denosumab at the radius in GC-I and at radius and tibia in GC-C, whereas these parameters were maintained with risedronate, leading to a significantly higher percentage change between denosumab and risedronate. These changes indicate that trabecular bone was preserved with risedronate and increased with denosumab, which is in line with changes in aBMD in the spine and trochanter with denosumab and risedronate [5]. Additionally, the increase in Tb.BMD in GC-I and GC-C with denosumab, together with the changes in Ct.BMD, contributed to a significant increase in Tt.BMD in both subpopulations, which was significantly higher than the changes with risedronate.

The larger effect of denosumab compared with risedronate on bone strength among GC-C users in this study, who had low aBMD *T*-score at baseline, agrees with previous findings in postmenopausal women with low BMD. Using QCT, Genant and colleagues showed significant and progressive increases in polar moment of inertia (PMI), a measure for bone strength, at the ultradistal, distal, and proximal radius starting 6 months after treatment with denosumab [12]. Seeman and colleagues found similar increases in PMI at the distal radius with denosumab and reported this effect to be superior over that with alendronate [9]. They found, however, an increase in PMI and a maintained Ct.BMD with alendronate, whereas we found a maintained FL and a decrease in Ct.BMD with risedronate. This difference between risedronate and alendronate agrees with previously reported larger gains in lumbar spine, femoral neck, and total hip aBMD at 24 months with alendronate than with risedronate in postmenopausal women with low BMD without GC-use [29]. Interestingly, the results for Tt.BMD were in general similar to those for FL. Further studies are needed

to analyze which bone parameters influence changes in FL in GC users and to what degree.

Aside from Tt.BMD (GC-C) and Tb.BMD (GC-I and GC-C), the changes in FL and stiffness and multiple other HR-pQCT parameters were less than pooled least significant changes (LSCs) at the individual level [30]; nevertheless, they may be clinically relevant at the group level in clinical trials. Although the LSC of total hip aBMD in postmenopausal women has been found to be approximately 4.5% [31,32], a recent meta-analysis of placebo-controlled clinical trials on anti-osteoporosis drugs showed that an increase in mean total hip aBMD of 2% was associated with a decrease in vertebral and hip fracture risk of 28% and 16%, respectively [33]. Furthermore, a difference in mean change between treatment and placebo in total hip aBMD of more than 1.4%, 3.2%, and 2.1% was associated with risk reductions of vertebral, hip, and non-vertebral fractures, respectively [34]. The authors concluded that these levels of mean aBMD changes over time and differences between groups support aBMD as a surrogate outcome for fracture outcomes at the group level in randomized trials of new osteoporosis therapies [33,34]. By analogy, in Tt.BMD, we found significant changes with denosumab of 1.2% to 5.9% and differences between denosumab and risedronate of 2.1% to 7.9%, which are similar to or exceed these changes in total hip aBMD. Besides that, mean HR-pQCT parameters at the group level have been found to improve fracture prediction beyond femoral neck BMD alone, with FL having the strongest association [35]. Also in FL, we found significant changes with denosumab and differences between denosumab and risedronate that were similar to or larger than these clinically relevant changes in total hip aBMD. In analogy with the studies of Bouxsein and colleagues [33] and Black and colleagues [34] on the use of DXA as a surrogate marker for the effect on fractures, further study is needed to investigate the association between the level of changes and between-treatment differences in HR-pQCT parameters on the one hand and the effect on fracture risk on the other hand to better elucidate the clinical relevance of changes in the HR-pQCT parameters with anti-osteoporosis drugs [36]. Also, the correlation between changes and differences in FL with changes and differences in other HR-pQCT parameters requires further study.

The findings of the current study can contribute to treatment decisions for fracture prevention in GC-I and GC-C. With only limited fracture data from clinical trials on GIOP, fracture reduction with GIOP treatments is mostly based on an extrapolation of fracture risk reductions ascertained in clinical trials on treatments of osteoporosis in general [37]. In clinical trials in postmenopausal women, changes in lumbar spine, femoral neck, and total hip aBMD are considered a useful surrogate endpoint for fracture [33]. However, the relation between aBMD and fracture risk is different in

GIOP than PMOP, with a higher fracture risk in GC users than nonusers with the same aBMD [14-19,37]. HR-pQCT parameters and FL improve fracture prediction beyond femoral neck aBMD [35]. In GC-I, with only moderately low *T*-scores, the aim of fracture prevention is then to preserve FL, whereas in GC-C, with considerably lower *T*-scores reflecting already mechanically compromised bone, the aim is to increase FL. As such, HR-pQCT assessment may give additional insights into bone strength in clinical trials that are not powered to evaluate fracture prevention, especially when limited study populations can be included, such as in GC-I and GC-C.

Both aims were attained by denosumab but not by risedronate in this study, but awareness is needed regarding desired therapeutic option. For example, the effects of drug discontinuation require attention. In contrast to risedronate and other bisphosphonates, denosumab is not incorporated into the bone matrix. Correspondingly, recent data indicate an increased bone turnover after discontinuation of denosumab resulting in rapid BMD loss and an increased risk of multiple vertebral fractures [38]. It is therefore important that treatment with denosumab should not be stopped without considering alternative antiresorptive treatment [39]. Another possible difference between anti-osteoporosis drugs that requires attention is the adherence rate due to differences in drug administration. Nevertheless, in this study, the adherence rate was high for both oral and injectable administration: based on the determination of “important protocol deviations” after medical review by the original study site and team, only 8.2% and 0.9% missed > 20% of an oral product (placebo or risedronate) during the first 12 and 24 months, respectively, and none of the patients missed an injectable (placebo or denosumab) during the entire study duration.

Despite the strengths and its novelty, this study has several limitations. First, data were obtained using the first-generation HR-pQCT scanner, which limits direct measurement of trabecular microarchitecture to Tb.N and the quantification of Ct.Po to pores larger than the scan resolution [20]. Use of the second-generation HR-pQCT scanner with higher resolution would have allowed more detailed assessment of trabecular microarchitecture and Ct.Po and may have an improved reproducibility but was not available in the participating centers. Second, only standard HR-pQCT parameters were quantified. However, BMD is influenced by void volumes, whereas volumetric tissue mineral density purely examines mineralized bone. The latter parameter may therefore provide better understanding of the combined effects of denosumab on Ct.BMD, Ct.Th, and Ct.Po (*eg*, the increase in Ct.BMD in GC-C at 24 months without a coinciding decrease in Ct.Po) but was not calculated. Furthermore, the standard parameters do not provide detailed insights into endosteal changes. For example, the unchanged total bone volume and increased Ct.Th with denosumab at the radius at 24 months in GC-C suggest that the corresponding

increase in FL could be the result of endocortical changes. However, quantification of such changes requires more advanced analysis methods, such as the recent method to separately segment compact-appearing cortical bone and cortical transitional zones to evaluate cortical parameters in greater detail in each segment [40]. Third, we indicated the significance of changes from baseline and for differences between treatment groups without correction for multiplicity, as in other studies reporting the multiple parameters generated with HR-pQCT during treatment versus placebo or between drugs (*eg*, Seeman and colleagues [9] and Tsai and colleagues [10]). When using a false discovery rate (FDR)-based adjustment to correct for multiple testing to reject false positive results, we found that the differences between denosumab and risedronate at 24 months remained significant at the radius for FL, stiffness, Tt.BMD, cortical volume, and Ct.Th in GC-I and for Tt.BMD, Ct.BMD, and Ct.Th in GC-C, and at the tibia for Tt.BMD, Ct.BMD, and Ct.Th in GC-I and for Tt.BMD, cortical volume, and Ct.BMD in GC-C. Trabecular parameters were not significantly different any more between treatment groups after FDR adjustment.

In conclusion, in this HR-pQCT study, we found that denosumab was superior to risedronate in terms of preventing FL and Tt.BMD loss in GC-I at the radius and tibia and in increasing FL and Tt.BMD in GC-C at the radius. We also identified underlying differences in changes in the cortical and trabecular bone compartments between denosumab and risedronate in GC-I and GC-C. These results suggest that denosumab could be a useful therapeutic option in patients initiating GC therapy or on long-term GC therapy and may contribute to treatment decisions in this patient population.

REFERENCES

- [1] Amiche MA, Albaum JM, Tadrous M, et al. Fracture risk in oral glucocorticoid users: a Bayesian meta-regression leveraging control arms of osteoporosis clinical trials. *Osteoporos Int.* 2016;27:1709-1718.
- [2] Van Staa TP, Leufkens HGM, Abenhaim L, Zhang B, Cooper C. Use of oral corticosteroids and risk of fractures. *J Bone Miner Res.* 2000;15: 993-1000.
- [3] Van Staa TP, Leufkens HGM, Cooper C. The epidemiology of corticosteroid-induced osteoporosis: a meta-analysis. *Osteoporos Int.* 2002;13:777-787.
- [4] Saag KG, Wagman RB, Geusens P, et al. Denosumab versus risedronate in glucocorticoid-induced osteoporosis: a multicentre, randomised, double-blind, active-controlled, double-dummy, non-inferiority study. *Lancet Diabetes Endocrinol.* 2018;6:445-454.
- [5] Saag KG, Pannacciulli N, Geusens P, et al. Denosumab versus risedronate in glucocorticoid-induced osteoporosis: final results of a twenty-four-month randomized, double-blind, double-dummy trial. *Arthritis Rheumatol.* 2019;71:1174-1184.
- [6] Lespessailles E, Hambli R, Ferrari S. Osteoporosis drug effects on cortical and trabecular bone microstructure: a review of HR-pQCT analyses [review]. *BoneKey Rep.* 2016;5:836.
- [7] Sutter S, Nishiyama KK, Kepley A, et al. Abnormalities in cortical bone, trabecular plates, and stiffness in postmenopausal women treated with glucocorticoids. *J Clin Endocrinol Metab.* 2014;99:4231-4240.
- [8] Liu Y, Dimango E, Bucovsky M, et al. Abnormal microarchitecture and stiffness in postmenopausal women using chronic inhaled glucocorticoids. *Osteoporos Int.* 2018;29:2121-2127.
- [9] Seeman E, Delmas PD, Hanley DA, et al. Microarchitectural deterioration of cortical and trabecular bone: differing effects of denosumab and alendronate. *J Bone Miner Res.* 2010;25:1886-1894.
- [10] Tsai JN, Uihlein AV, Burnett-Bowie SM, et al. Comparative effects of teriparatide, denosumab, and combination therapy on peripheral compartmental bone density, microarchitecture, and estimated strength: the DATA-HRpQCT study. *J Bone Miner Res.* 2015;30:39-45.
- [11] Bala Y, Chapurlat R, Cheung AM, et al. Risedronate slows or partly reverses cortical and trabecular microarchitectural deterioration in postmenopausal women. *J Bone Miner Res.* 2014;29:380-388.
- [12] Genant HK, Engelke K, Hanley DA, et al. Denosumab improves density and strength parameters as measured by QCT of the radius in postmenopausal women with low bone mineral density. *Bone.* 2010;47:131-139.
- [13] Keaveny TM, McClung MR, Genant HK, et al. Femoral and vertebral strength improvements in postmenopausal women with osteoporosis treated with denosumab. *J Bone Miner Res.* 2014;29:158-165.
- [14] Carbonare LD, Arlot ME, Chavassieux PM, Roux JP, Portero NR, Meunier PJ. Comparison of trabecular bone microarchitecture and remodeling in glucocorticoid-induced and postmenopausal osteoporosis. *J Bone Miner Res.* 2001;16:97-103.
- [15] Lane NE, Yao W. New insights into the biology of glucocorticoid-induced osteoporosis [perspectives]. *IBMS BoneKey.* 2011;8:229-236.
- [16] Van Staa TP, Laan RF, Barton IP, Cohen S, Reid DM, Cooper C. Bone density threshold and other predictors of vertebral fracture in patients receiving oral glucocorticoid therapy. *Arthritis Rheumatol.* 2003;48:3224-3229.
- [17] Weinstein RS, Jia D, Powers CC, et al. The skeletal effects of glucocorticoid excess override those of orchidectomy in mice. *Endocrinology.* 2004;145:1980-1987.
- [18] Seibel MJ, Cooper MS, Zhou H. Glucocorticoid-induced osteoporosis: mechanisms, management, and future perspectives [review]. *Lancet Diabetes Endocrinol.* 2013;1:59-70.

- [19] Adami G, Saag KG. Glucocorticoid-induced osteoporosis: 2019 concise clinical review [review]. *Osteoporos Int.* 2019;30:1145-1156.
- [20] Whittier DE, Boyd SK, Burghardt AJ, et al. Guidelines for the assessment of bone density and microarchitecture in vivo using high-resolution peripheral quantitative computed tomography. *Osteoporos Int.* 2020;31:1607-1627.
- [21] Pialat JB, Burghardt AJ, Sode M, Link TM, Majumdar S. Visual grading of motion induced image degradation in high resolution peripheral computed tomography: impact of image quality on measures of bone density and microarchitecture. *Bone.* 2012;50:111-118.
- [22] Pistoia W, van Rietbergen B, Lochmuller EM, Lill CA, Eckstein F, Rügsegger P. Estimation of distal radius failure load with micro-finite element analysis models based on three-dimensional peripheral quantitative computed tomography images. *Bone.* 2002;30: 842-848.
- [23] Engelke K, Stampa B, Timm W, et al. Short-term in vivo precision of BMD and parameters of trabecular architecture at the distal forearm and tibia. *Osteoporos Int.* 2011;23:2151-2158.
- [24] Vedi S, Elkin SL, Compston JE. A histomorphometric study of cortical bone of the iliac crest in patients treated with glucocorticoids. *Calcif Tissue Int.* 2005;77:79-83.
- [25] Jia D, O'Brien CA, Stewart SA, Manolagas SC, Weinstein RS. Glucocorticoids act directly on osteoclasts to increase their life span and reduce bone density. *Endocrinology.* 2006;147:5592-5599.
- [26] Piemontese M, Onal M, Xiong J, et al. Suppression of autophagy in osteocytes does not modify the adverse effects of glucocorticoids on cortical bone. *Bone.* 2015;75:18-26.
- [27] Aeberli D, Schett G. Cortical remodeling during menopause, rheumatoid arthritis, glucocorticoid and bisphosphonate therapy [review]. *Arthritis Res Ther.* 2013;15:208.
- [28] O'Brien CA, Jia D, Plotkin LI, et al. Glucocorticoids act directly on osteoblasts and osteocytes to induce their apoptosis and reduce bone formation and strength. *Endocrinology.* 2004;145:1835-1841.
- [29] Bonnick S, Saag KG, Kiel DP, et al. Comparison of weekly treatment of postmenopausal osteoporosis with alendronate versus risedronate over two years. *J Clin Endocrinol Metab.* 2006;91:2631-2637.
- [30] Mikolajewicz N, Bishop N, Burghardt AJ, et al. HR-pQCT measures of bone microarchitecture predict fracture: systematic review and meta-analysis. *J Bone Miner Res.* 2020;35:446-459.
- [31] Lodder MC, Lems WF, Ader HJ, et al. Reproducibility of bone mineral density measurement in daily practice. *Ann Rheu Dis.* 2004;63: 285-289.
- [32] El Maghraoui A, Do Santos Zounon AA, Jroundi I, et al. Reproducibility of bone mineral density measurements using dual X-ray absorptiometry in daily clinical practice. *Osteoporosis Int.* 2005;16:1742-1748.
- [33] Bouxsein ML, Eastell R, Lui L, et al. Change in bone density and reduction in fracture risk: a meta-regression of published trials. *J Bone Miner Res.* 2019;34:632-642.
- [34] Black DM, Bauer DC, Vittinghoff E, et al. Treatment-related changes in bone mineral density as a surrogate biomarker for fracture risk reduction: meta-regression analyses of individual patient data from multiple randomised controlled trials. *Lancet Diabetes Endocrinol.* 2020; 8(8):672-682.
- [35] Samelson EJ, Broe KE, Xu H, et al. Cortical and trabecular bone micro-architecture as an independent predictor of incident fracture risk in older women and men in the bone microarchitecture international consortium (BoMIC): a prospective study. *Lancet Diabetes Endocrinol.* 2019;7:34-43.
- [36] Van den Bergh JP, Szulc P, Cheung AM, Bouxsein M, Engelke K, Chapurlat R. The clinical application of high-resolution peripheral computed tomography (HR-pQCT) in adults: state of the art and future directions. *Osteoporosis Int.* 2021;32:1465-1485.

- [37] Buckley L, Guyatt G, Fink HA, et al. 2017 American College of Rheumatology guideline for the prevention and treatment of glucocorticoid-induced osteoporosis [special article]. *Arthritis Rheumatol.* 2017;69:1521-1537.
- [38] Tsourdi E, Langdahl B, Cohen-Solal M, et al. Discontinuation of denosumab therapy for osteoporosis: a systematic review and position statement by ECTS. *Bone.* 2017;105:11-17.
- [39] Tsourdi E, Zillikens MC, Meier C, et al. Fracture risk and management of discontinuation of denosumab therapy: a systematic review and position statement by ECTS. *J Clin Endocrinol Metab.* 2021;106:264-281.
- [40] Zebaze R, Ghasem-Zadeh A, Mbala A, Seeman E. A new method of segmentation of compact-appearing, transitional and trabecular compartments and quantification of cortical porosity from high resolution peripheral quantitative computed tomographic images. *Bone.* 2013;54:8-20.



5

Chapter 5

Bone microarchitecture and strength changes during teriparatide and zoledronic acid treatment in a patient with pregnancy and lactation-associated osteoporosis with multiple vertebral fractures

Melissa S.A.M. Bevers [†], Sanne Treurniet [†], Caroline E. Wyers, Dimitra Micha, Bernd P. Teunissen, Mariet W. Elting, Joop P. van den Bergh [‡], Elisabeth M.W. Eekhoff [‡]

[†] These authors have contributed equally to this work and share first authorship

[‡] These authors have contributed equally to this work and share last authorship

ABSTRACT

Pregnancy- and lactation-associated osteoporosis (PLO) is a rare form of osteoporosis, of which the pathogenesis and best treatment options are unclear. In this report, we describe the case of a 34-year old woman diagnosed with severe osteoporosis and multiple vertebral fractures after her first pregnancy, who was subsequently treated with teriparatide (TPTD) and zoledronic acid (ZA). We describe the clinical features, imaging examination, and genetic analysis. Substantial improvements were observed in areal and volumetric bone mineral density (BMD), microarchitecture, and strength between 7 and 40 months postpartum as assessed by dual-energy X-ray absorptiometry at the total hip and spine and by high-resolution peripheral quantitative CT at the distal radius and tibiae. At the hip, spine, and distal radius, these improvements were mainly enabled by treatment with TPTD and ZA, while at the distal tibiae, physiological recovery and postpartum physiotherapy due to leg pain after stumbling may have played a major role. Additionally, the findings show that, despite the improvements, BMD, microarchitecture, and strength remained severely impaired in comparison with healthy age- and gender-matched controls at 40 months postpartum. Genetic analysis showed no monogenic cause for osteoporosis, and it is suggested that PLO in this woman could have a polygenic origin with possible susceptibility based on familiar occurrence of osteoporosis.

INTRODUCTION

Pregnancy and lactation-associated osteoporosis (PLO) is a rare form of osteoporosis, characterized by back pain and vertebral compression fractures, that affects women during pregnancy and early postpartum [1]. Hormonal-mediated adaptations to fulfill an increased calcium demand can cause physiological bone loss during pregnancy and lactation, while additional factors (*e.g.* genetics) may contribute to the pathological bone loss in PLO [2]. Although bone mineral density (BMD) restores spontaneously post-weaning in most women, some present postpartum with persistent severe back pain and progressive height loss due to severe osteoporosis and vertebral fractures. In severe cases, treatment with anti-osteoporosis drugs can be considered although optimal treatment and pharmacological need are incompletely known [1]. In this case report, we describe a 34-year old woman diagnosed with multiple vertebral fractures after pregnancy and the effects of treatment with teriparatide (TPTD) and zoledronic acid (ZA) on bone microarchitecture and strength assessed with high-resolution peripheral quantitative CT (HR-pQCT).

CASE PRESENTATION

A 34-year old woman presented in a local hospital with severe back pain. Seven months earlier, she gave birth to her first child after an uncomplicated pregnancy and delivery. During the second trimester of pregnancy, she had a period of heavy pain in her right leg after stumbling. Heavy back pain started during the third trimester. At the moment of presentation, she was breastfeeding her child. Her medical history revealed a herniated nucleus pulposus 6 years earlier, no previous fractures, and a regular menstrual cycle before pregnancy. Her father was diagnosed with osteoporosis at the age of 48 and her mother and sister with osteopenia. No other osteoporosis-related risk factors were present. X-ray examination, magnetic resonance imaging (MRI), and dual-energy X-ray absorptiometry (DXA) revealed multiple vertebral compression fractures (Th8 and Th12), height loss of all mid and low thoracic vertebra (quantification not available), lumbar spine end plate indentation, and osteoporosis (*T*-score lumbar spine: -4.2; total hip: -2.7). She had lost 4 cm of her best recalled height; her body mass index was normal (25 kg/m²). Laboratory tests showed normal biochemistries, hematology, and thyroid level, and a 25-hydroxy vitamin D level of 54 nmol/L (ref. > 50 nmol/L). Based on these findings, she was advised cessation of breastfeeding and supplementation of calcium and vitamin D.

One month later, 8 months postpartum, she was referred to Amsterdam UMC outpatient clinic for further analysis. Next generation sequencing was performed with a panel including 19 osteoporosis and osteogenesis imperfecta related genes (**Supplementary Material 1**) [3], followed by whole exome sequencing (trio-analysis with DNA of her parents). Genetic and biochemical analyses revealed no monogenic mutation nor secondary causes of osteoporosis, so she was diagnosed with PLO. We advised her to continue calcium and vitamin D supplementation. Eleven months postpartum, DXA examination showed improvements in lumbar spine and total hip areal BMD (aBMD) (**Figure 1A**) and HR-pQCT examination in volumetric BMD, bone microarchitecture, and strength (in terms of failure load) at the distal radius and distal tibiae (**Figures 1B, 2, and 3; Supplementary Material 2 and 3**). Nevertheless, the woman experienced increased back pain, indicating progressive height loss of the vertebrae, and aBMD remained low (*T*-score lumbar spine: -3.7; total hip: -2.3). This worried her as she desired to have a second child. Therefore, 15 months postpartum, after shared decision-making, TPTD 20 µg/day was prescribed for 1 year followed by one dose of ZA. We advised her to postpone a second pregnancy until 1 year after the ZA-dose.

Three consecutive DXA and HR-pQCT examinations showed further improvements. Lumbar spine and total hip aBMD increased by 25.8% and 13.0%, respectively, between 11 and 40 months postpartum, resulting in *T*-scores in the osteopenic range (-2.2 and -1.6, respectively) (**Figure 1A**). DXA vertebral fracture assessment showed multiple compression fractures, which were not further increased since the start of TPTD treatment (**Figure 1C**). The distal radius showed increases between 7 and 39 months postpartum greatly exceeding least-significant changes (LSCs) from literature in total and trabecular BMD (+9.3% and +23.2%, respectively), trabecular bone volume fraction and thickness (+19.8% and +7.2%, respectively), and failure load (+16.8%) (**Figures 1B and 2A**) [4]. Increases in all other parameters except cortical porosity were within several percentage points above or below LSCs (**Supplementary Material 2**). The distal tibiae also showed increases largely exceeding LSCs in total BMD (left tibia: +14.0%; right tibia: +40.2%), trabecular BMD (left: +15.1%; right: +27.3%), trabecular bone volume fraction (left: +14.7%; right: +29.2%), trabecular thickness (left: +4.4%; right: +9.2%), and failure load (left: +21.1%; right: +49.5%) and additionally in cortical BMD (left: +2.5%; right: +21.1%), area (left: +11.2%; right: +26.1%), thickness (left: +10.6%; right: +17.7%), and porosity (left: +62.4%; right: -45.0%) (**Figures 1B and 3A**). Other changes were within percentage points around LSCs (**Supplementary Material 3**). Most parameters at 39 months postpartum remained nevertheless at the lowest 2-10 percentile of an age- and gender-matched normative dataset [5,6].

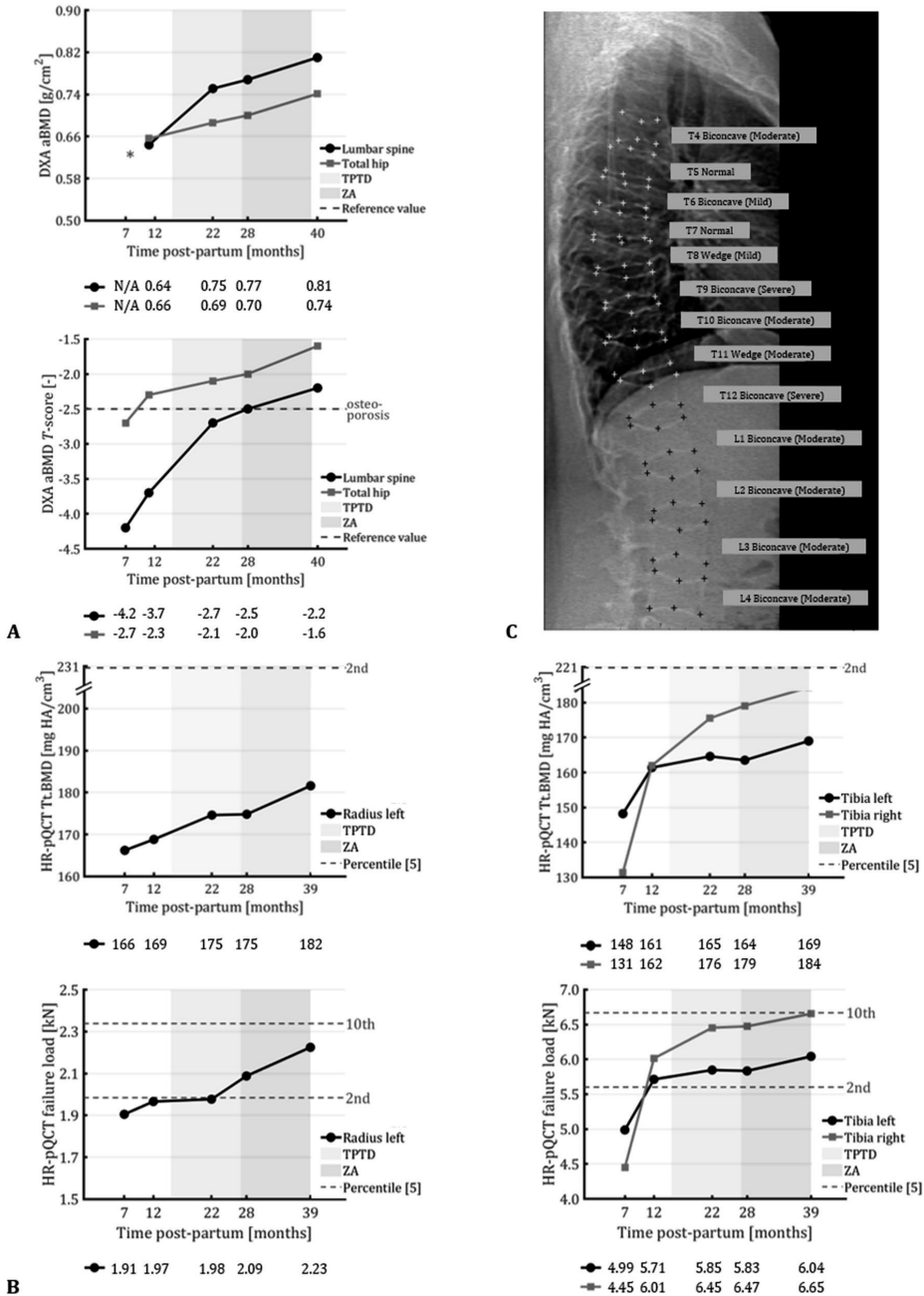


Figure 1. **A**) Changes in areal BMD values (top) and *T*-scores (bottom) of the woman's lumbar spine (black) and total hip (grey) from DXA examinations between 7 and 40 months postpartum. **B**) Changes in total BMD (top) and failure load (bottom) at the woman's left distal radius (left) and both distal tibiae (right) from HR-pQCT examinations between 7 and 39 months postpartum. **C**) Instantaneous vertebral assessment (IVA) of the woman's spine from the DXA examination at 40 months postpartum. TPTD is teriparatide, ZA is zoledronic acid, * indicates not available, and the dotted grey lines indicate the *T*-score that defines osteoporosis (**A**) and the percentile scores from age- and gender-matched normative data (**B**) [5].

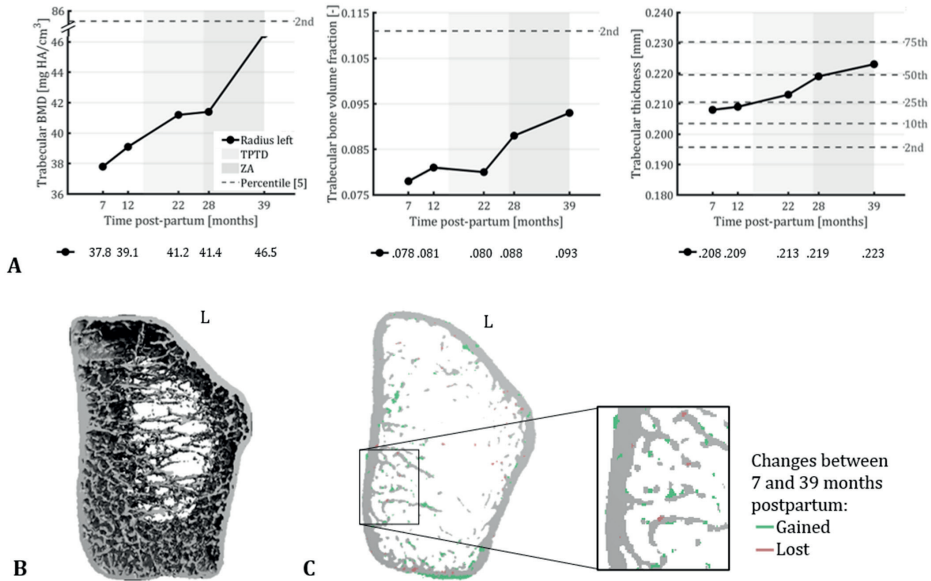


Figure 2. **A)** Changes in parameters at the woman’s left distal radius from HR-pQCT examinations between 7 and 39 months postpartum that greatly exceeded least-significant changes from literature at 39 months. TPTD is teriparatide, ZA is zoledronic acid, and the dotted grey lines indicate percentile scores from age- and gender-matched normative data [5]. **B)** Three-dimensional visualization of the HR-pQCT scan of the left distal radius at 7 months postpartum. **C)** Axial mid-slice of the left distal radius showing bone gain (green) and loss (pink) between 7 and 39 months postpartum from HR-pQCT examinations.

DISCUSSION

Most women experience no or modest decreases in aBMD during pregnancy and larger decreases during lactation with spontaneous recovery postweaning [7]. Additionally, they may experience a decrease in volumetric BMD and changes in bone microarchitecture at the distal tibia and proximal radius [8,9]. In PLO, bone loss is aggravated, and impaired volumetric BMD and bone microarchitecture have been reported compared to healthy controls [10] and healthy lactating women [11]. The woman in this report also had a severely impaired aBMD, volumetric BMD, and bone microarchitecture compared to healthy controls, which even after treatment persisted until 40 months postpartum.

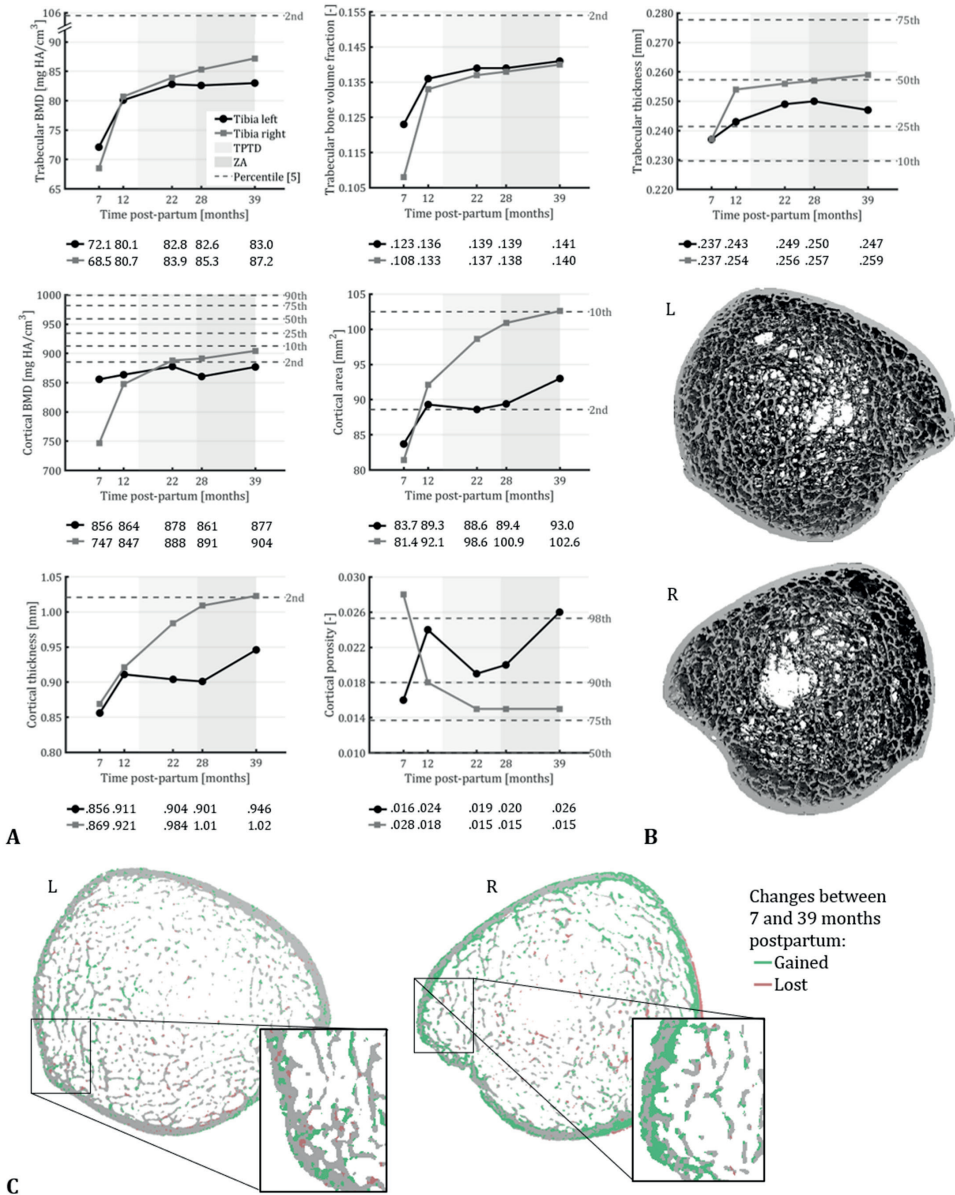


Figure 3. A) Changes in trabecular parameters (top) and cortical parameters (middle, bottom) at the woman's left (black) and right (grey) distal tibia from HR-pQCT examinations between 7 and 39 months postpartum that greatly exceeded least-significant changes from literature at 39 months. TPTD is teriparatide, ZA is zoledronic acid, and the dotted grey lines indicate percentile scores from age- and gender-matched normative data [5]. B) Three-dimensional visualization of the HR-pQCT scan of the distal tibiae at 7 months postpartum. C) Axial mid-slice of the distal tibiae showing bone gain (green) and loss (pink) between 7 and 39 months postpartum from HR-pQCT examinations.

In line with previous studies [7,8,10,11], the trabecular bone was more affected than the cortical bone but recovered earlier. At 7 months postpartum, aBMD *T*-score was worse at the lumbar spine (predominantly trabecular) than at the total hip (cortical and trabecular), and trabecular BMD was relatively lower than cortical BMD at the distal radius and tibia. Until 40 months postpartum, lumbar spine aBMD showed larger increases than total hip aBMD, and trabecular BMD increased more at the radius and tibia than cortical BMD. The increase in trabecular BMD seemed the result of thickening of existing trabeculae and possibly the fusion of neighboring trabeculae. Nevertheless, a large increase was found in cortical BMD at the right tibia, possibly due to the filling of cortical pores and an increase in tissue mineralization. Despite the improvements, BMD and microarchitecture remained severely impaired at 40 months postpartum compared to healthy controls. This could have contributed to compensatory periosteal bone apposition in order to improve bone strength, as reflected by the changes in cortical and trabecular area and previously also suggested by Kovacs [7].

A possible factor in the pathological bone loss in PLO is heredity. Recent studies showed that multiple genetic mutations, in *LRP5* and *WNT1*, can aggravate bone loss in PLO [2,10,12,13]. Although no monogenic cause was found in this woman, osteoporosis and osteopenia occur in her immediate family. Additionally, HR-pQCT scans of her mother's distal radius and tibia showed similar cortical discrepancies (**Supplementary Material 4**). It suggests a polygenic origin in this patient with unknown contribution of both her parents' side.

Currently, there is no clinical guideline for the management of patients with PLO, and treatment strategy remains challenging and controversial due to the lack of intervention-controlled research. Termination of breastfeeding is important but may not be sufficient, especially in case of multiple vertebral fractures [14]. Prolonged bisphosphonate treatment is suggested to be successful [15], but bisphosphonates accumulate in the skeleton and can be released in a subsequent pregnancy, possibly harming the fetus. TPTD does not accumulate in the body and has been found to increase aBMD, relieve pain, and prevent new vertebral fractures in PLO [16-18]. It also results in greater increases in aBMD compared to no TPTD treatment in PLO [19]. Interestingly, Lee *et al.* showed no significant difference in aBMD 3 years after discontinuation of TPTD treatment between PLO-patients with and without successive antiresorptive therapy [20]. It suggests that it may be advantageous not to start antiresorptive treatment after TPTD discontinuation when a PLO-patient desires to have children in the future. As this finding was not available when the woman presented at our hospital, we treated her with one dose of ZA after TPTD.

The largest improvements were generally seen during TPTD treatment and until 1 year after the ZA-dose, albeit site-dependent. At the distal radius, lumbar spine, and hip, the largest changes occurred during treatment. At the distal tibiae in contrast, they occurred before treatment. The latter may be due to spontaneous recovery and possibly also due to the physiotherapy that the woman followed after pregnancy because of right leg pain after stumbling during pregnancy. The stumbling and consequent disuse of the right leg for 5 months may also explain the worse HR-pQCT parameters at 7 months at the right tibia compared to the left tibia.

CONCLUSION

This case report showed the follow-up of a woman with multiple vertebral fractures due to PLO without an identified monogenic cause. Treatment with teriparatide and zoledronic acid resulted in substantial improvements in bone mineral density, microarchitecture, and strength although larger improvements were observed before treatment at the tibiae. Nevertheless, bone quality remained considerably impaired compared to healthy controls at 40 months postpartum.

REFERENCES

- [1] Jia P, Wang R, Yuan J, et al. A case of pregnancy and lactation-associated osteoporosis and a review of the literature. *Arch Osteoporos* 2020;15:94.
- [2] Winter EM, Ireland A, Butterfield NC, et al. Pregnancy and lactation, a challenge for the skeleton. *Endocr Connect* 2020;9:R143-r157.
- [3] Claeys L, Storoni S, Eekhoff M, et al. Collagen transport and related pathways in Osteogenesis Imperfecta. *Hum Genet* 2021;140:1121–1141.
- [4] Kemp TD, de Bakker CMJ, Gabel L, et al. Longitudinal bone microarchitectural changes are best detected using image registration. *Osteoporos Int* 2020;31:1995–2005.
- [5] Whittier DE, Burt LA, Hanley DA, Boyd SK. Sex- and site-specific reference data for bone microarchitecture in adults measured using second-generation HR-pQCT. *J Bone Miner Res* 2020;35:2151–2158.
- [6] Whittier DE, Boyd SK, Burghardt AJ, et al. Guidelines for the assessment of bone density and microarchitecture in vivo using high-resolution peripheral quantitative computed tomography. *Osteoporos Int* 2020;31:1607–1627.
- [7] Kovacs CS. Maternal mineral and bone metabolism during pregnancy, lactation, and post-weaning recovery. *Physiol Rev* 2016;96:449–547.
- [8] Brembeck P, Lorentzon M, Ohlsson C, Winkvist A, Augustin H. Changes in cortical volumetric bone mineral density and thickness, and trabecular thickness in lactating women postpartum. *J Clin Endocrinol Metab* 2015;100:535–543.
- [9] Breasail M, Prentice A, Ward K. Pregnancy-related bone mineral and microarchitecture changes in women aged 30 to 45 years. *J Bone Miner Res* 2020;35:1253–1262.
- [10] Butscheidt S, Tsourdi E, Rolvien T, et al. Relevant genetic variants are com-mon in women with pregnancy and lactation-associated osteoporosis (PLO) and predispose to more severe clinical manifestations. *Bone* 2021;147:115911.
- [11] Scioscia MF, Vidal M, Sarli M, et al. Severe bone microarchitecture impairment in women with pregnancy and lactation-associated osteoporosis. *J Endocr Soc* 2021;5:bvab031.
- [12] Campos-Obando N, Oei L, Hoefsloot LH, et al. Osteoporotic vertebral fractures during pregnancy: be aware of a potential underlying genetic cause. *J Clin Endocrinol Metab* 2014;99:1107–1111.
- [13] Cook FJ, Mumm S, Whyte MP, Wenkert D. Pregnancy-associated osteoporosis with a heterozygous deactivating LDL receptor-related protein 5 (LRP5) mutation and a homozygous methylenetetrahydrofolate reductase (MTHFR) polymorphism. *J Bone Miner Res* 2014;29:922–928.
- [14] Kyvernitakis I, Reuter TC, Hellmeyer L, Hars O, Hadji P. Subsequent fracture risk of women with pregnancy and lactation-associated osteoporosis after a median of 6 years of follow-up. *Osteoporos Int* 2018;29:135–142.
- [15] O’Sullivan SM, Grey AB, Singh R, Reid IR. Bisphosphonates in pregnancy and lactation-associated osteoporosis. *Osteoporos Int* 2006;17:1008–1012.
- [16] Hellmeyer L, Boekhoff J, Hadji P. Treatment with teri-paratide in a patient with pregnancy-associated osteoporosis. *Gynecol Endocrinol* 2010;26:725–728.
- [17] Choe EY, Song JE, Park KH, et al. Effect of teriparatide on pregnancy and lactation-associated osteoporosis with multiple vertebral fractures. *J Bone Miner Metab* 2012;30:596–601.
- [18] Polat SB, Evranos B, Aydin C, Cuhaci N, Ersoy R, Cakir B. Effective treatment of severe pregnancy and lactation-related osteoporosis with teriparatide: case report and review of the literature. *Gynecol Endocrinol* 2015;31:522–525.

- [19] Hong N, Kim JE, Lee SJ, Kim SH, Rhee Y. Changes in bone mineral density and bone turnover markers during treatment with teriparatide in pregnancy- and lactation-associated osteoporosis. *Clin Endocrinol* 2018;88:652–658.
- [20] Lee S, Hong N, Kim KJ, Park CH, Lee J, Rhee Y. Bone density after teriparatide discontinuation with or without antiresorptive therapy in pregnancy- and lactation-associated osteoporosis. *Calcif Tissue Int.* 2021.

SUPPLEMENTARY MATERIAL 1

Panel with osteoporosis and osteogenesis imperfecta related genes used for the next generation sequencing (NGS).

Supplementary Material 1 - Table 1. NGS panel with osteoporosis and osteogenesis imperfecta related genes.

| |
|-----------------|
| <i>ALPL</i> |
| <i>BMP1</i> |
| <i>COL1A1</i> |
| <i>COL1A2</i> |
| <i>CREB3L1</i> |
| <i>CRTAP</i> |
| <i>FKBP10</i> |
| <i>IFITM5</i> |
| <i>LEPRE1</i> |
| <i>LRP5</i> |
| <i>PLOD2</i> |
| <i>PLS3</i> |
| <i>PPIB</i> |
| <i>SERPINF1</i> |
| <i>SERPINH1</i> |
| <i>SP7</i> |
| <i>TAPT1</i> |
| <i>TMEM38B</i> |
| <i>WNT1</i> |

SUPPLEMENTARY MATERIAL 2

Bone geometry, bone mineral density, bone microarchitecture, and strength at the distal radius of the women with PLO assessed with high-resolution peripheral quantitative CT (HR-pQCT).

Supplementary Material 2 - Table 1. Geometry, BMD, and microarchitecture at the left distal radius of the women with PLO assessed with HR-pQCT.

| | Visit 1 (7.3 mo PP) | | Visit 2 (12.1 mo PP) | | Visit 3 (22.0 mo PP) | | Visit 4 (28.2 mo PP) | | Visit 5 (39.9 mo PP) | |
|---------------------------------|------------------------|-----------------------------|-------------------------|-----------------------------|-------------------------|-----------------------------|-------------------------|-----------------------------|-------------------------|-----------------------------|
| | Value | Change w.r.t visit 1 (%) | Value | Change w.r.t visit 1 (%) | Value | Change w.r.t visit 1 (%) | Value | Change w.r.t visit 1 (%) | Value | Change w.r.t visit 1 (%) |
| Geometry | | | | | | | | | | |
| Tb.Ar (mm ²) | 244.3 | 244.1 | -0.1 | 242.7 | -0.6 | 242.9 | -0.6 | 242.2 | -0.8 | 75-90 |
| Ct.Ar (mm ²) | 44.1 | 44.1 | +0.2 | 45.6 | +3.4 | 45.3 | +2.9 | 46.1 | +4.6 | 2-10 |
| Volumetric density | | | | | | | | | | |
| Tt.BMD (mg HA/cm ³) | 166.2 | 168.8 | +1.6 | 174.6 | +5.1 | 174.8 | +5.2 | 181.6 | +9.3 | <2 |
| Tb.BMD (mg HA/cm ³) | 37.8 | 39.1 | +3.5 | 41.2 | +9.1 | 41.4 | +9.6 | 46.5 | +23.2 | <2 |
| Ct.BMD (mg HA/cm ³) | 913.6 | 922.5 | +1.0 | 917.8 | +0.5 | 923.5 | +1.1 | 923.9 | +1.1 | 25-75 |
| Microarchitecture | | | | | | | | | | |
| Tb.BV/TV (-) | 0.078 | 0.081 | +3.9 | 0.080 | +2.7 | 0.088 | +13.4 | 0.093 | +19.8 | <2 |
| Tb.N (mm ⁻¹) | 0.498 | 0.504 | +1.2 | 0.468 | -5.9 | 0.476 | -4.4 | 0.479 | -3.7 | <2 |
| Tb.Th (mm) | 0.208 | 0.209 | +0.6 | 0.213 | +2.8 | 0.219 | +5.5 | 0.223 | +7.2 | 25-75 |
| Tb.Sp (mm) | 2.030 | 2.001 | -1.5 | 2.185 | +7.6 | 2.126 | +4.7 | 2.122 | +4.5 | <2* |
| Tb.1/N.SD (mm) | 1.727 | 1.682 | -2.6 | 1.767 | +2.3 | 1.793 | +3.8 | 1.813 | +4.9 | <2* |
| Ct.Th (mm) | 0.735 | 0.727 | -1.0 | 0.751 | +2.2 | 0.746 | +1.6 | 0.761 | +3.6 | 2-10 |
| Ct.Po (-) | 0.002 | 0.002 | +15.7 | 0.001 | -29.0 | 0.002 | +16.3 | 0.002 | -1.9 | 25-75* |

Tt: total, Tb: trabecular, Ct: cortical, Ar: area, BMD: bone mineral density, BV/TV: bone volume fraction, N: number, Th: thickness, Sp: separation, 1/N.SD: heterogeneity, Po: porosity. Parameter values were obtained from the overlapping portions of the radius on the HR-pQCT scans between the visits after slice-matching (92% of 168 slices). The time between brackets indicates months postpartum at each visit. * indicates parameters for which the percentile scores are reversed (e.g. a score of < 2 represents a value larger, and thus worse, than the 98th percentile). Percentile scores are according to the normative dataset of Whittier DE, *et al.* 2020 J Bone Miner Res 35:2151-2158.

Supplementary Material 2 - Table 2. Strength at the left distal radius of the women with PLO estimated with micro-finite element analysis from HR-pQCT.

| | Visit 1 (7.3 mo PP) | | Visit 2 (12.1 mo PP) | | Visit 3 (22.0 mo PP) | | Visit 4 (28.2 mo PP) | | Visit 5 (39.9 mo PP) | |
|-------------------|--------------------------------|-------------------------------------|---------------------------------|-------------------------------------|---------------------------------|-------------------------------------|---------------------------------|-------------------------------------|---------------------------------|-------------------------------------|
| | Value | Change w.r.t visit 1 (%) | Value | Change w.r.t visit 1 (%) | Value | Change w.r.t visit 1 (%) | Value | Change w.r.t visit 1 (%) | Value | Change w.r.t visit 1 (%) |
| Strength | | | | | | | | | | |
| Failure load (kN) | 1.905 | +3.2 | 1.966 | +3.8 | 1.977 | +3.8 | 2.088 | +9.6 | 2.225 | +16.8 |

Parameter values were obtained from the entire HR-pQCT scans without registration of the HR-pQCT scans between the visits. The time between brackets indicates months postpartum at each visit. Percentile scores are according to the normative dataset of Whittier DE, *et al.* 2020 J Bone Miner Res 35:2151-2158.

SUPPLEMENTARY MATERIAL 3

Bone geometry, bone mineral density, bone microarchitecture, and strength at the distal tibiae of the women with PLO assessed with high-resolution peripheral quantitative CT (HR-pQCT).

Supplementary Material 3 - Table 1. Geometry, BMD, and microarchitecture at the left distal tibia of the women with PLO of the assessed with HR-pQCT.

| | Visit 1 (7.3 mo PP) | | Visit 2 (12.1 mo PP) | | Visit 3 (22.0 mo PP) | | Visit 4 (28.2 mo PP) | | Visit 5 (39.9 mo PP) | |
|---------------------------------|------------------------|-----------------------------|-------------------------|-----------------------------|-------------------------|-----------------------------|-------------------------|-----------------------------|-------------------------|-----------------------------|
| | Value | Change w.r.t visit 1 (%) | Value | Change w.r.t visit 1 (%) | Value | Change w.r.t visit 1 (%) | Value | Change w.r.t visit 1 (%) | Value | Change w.r.t visit 1 (%) |
| Geometry | | | | | | | | | | |
| Tb.Ar (mm ²) | 747.9 | 742.2 | -0.8 | 743.0 | -0.6 | 742.2 | -0.8 | 738.5 | -1.2 | 90-98 |
| Ct.Ar (mm ²) | 83.7 | 89.3 | +6.7 | 88.6 | +5.9 | 89.4 | +6.8 | 93.0 | +11.2 | 2-10 |
| Volumetric density | | | | | | | | | | |
| Tt.BMD (mg HA/cm ³) | 148.2 | 161.4 | +8.9 | 164.6 | +11.1 | 163.5 | +10.3 | 169.0 | +14.0 | <2 |
| Tb.BMD (mg HA/cm ³) | 72.1 | 80.1 | +11.1 | 82.8 | +14.8 | 82.6 | +14.6 | 83.0 | +15.1 | <2 |
| Ct.BMD (mg HA/cm ³) | 855.8 | 863.6 | +0.9 | 877.7 | +2.6 | 860.5 | +0.6 | 876.9 | +2.5 | <2 |
| Microarchitecture | | | | | | | | | | |
| Tb.BV/TV (-) | 0.123 | 0.136 | +10.5 | 0.139 | +13.6 | 0.139 | +13.6 | 0.141 | +14.7 | <2 |
| Tb.N (mm ⁻¹) | 0.882 | 0.887 | +0.6 | 0.879 | -0.4 | 0.882 | +0.0 | 0.882 | +0.0 | <2 |
| Tb.Th (mm) | 0.237 | 0.243 | +2.5 | 0.249 | +5.0 | 0.250 | +5.6 | 0.247 | +4.4 | 25-75 |
| Tb.Sp (mm) | 1.102 | 1.079 | -2.1 | 1.095 | -0.6 | 1.096 | -0.6 | 1.084 | -1.6 | <2* |
| Tb.1/N.SD (mm) | 0.494 | 0.482 | -2.5 | 0.530 | +7.3 | 0.525 | +6.4 | 0.510 | +3.3 | <2* |
| Ct.Th (mm) | 0.856 | 0.911 | +6.4 | 0.904 | +5.6 | 0.901 | +5.3 | 0.946 | +10.6 | <2 |
| Ct.Po (-) | 0.016 | 0.024 | +53.7 | 0.019 | +17.9 | 0.020 | +26.4 | 0.026 | +62.4 | <2* |

Tt: total, Tb: trabecular, Ct: cortical, Ar: area, BMD: bone mineral density, BV/TV: bone volume fraction, N: number, Th: thickness, Sp: separation, 1/N.SD: heterogeneity, Po: porosity. Parameter values were obtained from the overlapping portions of the tibiae on the HR-pQCT scans between the visits after slice-matching (95% of 168 slices). The time between brackets indicates months postpartum at each visit. * indicates parameters for which the percentile scores are reversed (e.g. a score of < 2 represents a value larger, and thus worse, than the 98th percentile). Percentile scores are according to the normative dataset of Whittier DE, *et al.* 2020 J Bone Miner Res 35:2151-2158.

Supplementary Material 3 - Table 2. Geometry, BMD, and microarchitecture at the right distal tibia of the women with PLO assessed with HR-pQCT.

| | Visit 1 (7.3 mo PP) | | Visit 2 (12.1 mo PP) | | Visit 3 (22.0 mo PP) | | Visit 4 (28.2 mo PP) | | Visit 5 (39.9 mo PP) | |
|---------------------------------|------------------------|-----------------------------|-------------------------|-----------------------------|-------------------------|-----------------------------|-------------------------|-----------------------------|-------------------------|-----------------------------|
| | Value | Change w.r.t visit 1 (%) | Value | Change w.r.t visit 1 (%) | Value | Change w.r.t visit 1 (%) | Value | Change w.r.t visit 1 (%) | Value | Change w.r.t visit 1 (%) |
| Geometry | | | | | | | | | | |
| Tb.Ar (mm ²) | 758.1 | 747.7 | -1.4 | 741.3 | -2.2 | 739.3 | -2.5 | 737.4 | -2.7 | 90-98 |
| Ct.Ar (mm ²) | 81.4 | 92.1 | +13.2 | 98.6 | +21.2 | 100.9 | +23.9 | 102.6 | +26.1 | 10-25 |
| Volumetric density | | | | | | | | | | |
| Tt.BMD (mg HA/cm ³) | 131.4 | 162.0 | +23.2 | 175.5 | +33.5 | 179.1 | +36.3 | 184.3 | +40.2 | <2 |
| Tb.BMD (mg HA/cm ³) | 68.5 | 80.7 | +17.8 | 83.9 | +22.6 | 85.3 | +24.5 | 87.2 | +27.3 | <2 |
| Ct.BMD (mg HA/cm ³) | 746.6 | 847.4 | +13.5 | 888.0 | +18.9 | 891.2 | +19.4 | 904.4 | +21.1 | 2-10 |
| Microarchitecture | | | | | | | | | | |
| Tb.BV/TV (-) | 0.108 | 0.133 | +22.5 | 0.137 | +26.1 | 0.138 | +26.9 | 0.140 | +29.2 | <2 |
| Tb.N (mm ⁻¹) | 0.816 | 0.798 | -2.1 | 0.792 | -2.9 | 0.787 | -3.5 | 0.783 | -4.0 | <2 |
| Tb.Th (mm) | 0.237 | 0.254 | +7.4 | 0.256 | +7.9 | 0.257 | +8.4 | 0.259 | +9.2 | 25-75 |
| Tb.Sp (mm) | 1.204 | 1.221 | +1.4 | 1.228 | +2.0 | 1.244 | +3.3 | 1.244 | +3.4 | <2* |
| Tb.1/N.SD (mm) | 0.560 | 0.689 | +23.2 | 0.752 | +34.3 | 0.768 | +37.1 | 0.813 | +45.2 | <2* |
| Ct.Th (mm) | 0.869 | 0.921 | +6.0 | 0.984 | +13.2 | 1.009 | +16.0 | 1.023 | +17.7 | 2-10 |
| Ct.Po (-) | 0.028 | 0.018 | -34.0 | 0.015 | -48.0 | 0.015 | -48.0 | 0.015 | -45.0 | 10-25* |

Tt: total, Tb: trabecular, Ct: cortical, Ar: area, BMD: bone mineral density, BV/TV: bone volume fraction, N: number, Th: thickness, Sp: separation, 1/N.SD: heterogeneity, Po: porosity.

Parameter values were obtained from the overlapping portions of the tibiae on the HR-pQCT scans between the visits after slice-matching (98% of 168 slices). The time between brackets indicates months postpartum at each visit. * indicates parameters for which the percentile scores are reversed (e.g. a score of < 2 represents a value larger, and thus worse, than the 98th percentile). Percentile scores are according to the normative dataset of Whittier DE, *et al.* 2020 | Bone Miner Res 35:2151-2158.

Supplementary Material 3 - Table 3. Strength at the left and right distal tibiae of the women with PLO estimated with micro-finite element analysis from HR-pQCT.

| | Visit 1 (7.3 mo PP) | | Visit 2 (12.1 mo PP) | | Visit 3 (22.0 mo PP) | | Visit 4 (28.2 mo PP) | | Visit 5 (39.9 mo PP) | |
|--------------------------|------------------------|-----------------------------|-------------------------|-----------------------------|-------------------------|-----------------------------|-------------------------|-----------------------------|-------------------------|-----------------------------|
| | Value | Change w.r.t visit 1 (%) | Value | Change w.r.t visit 1 (%) | Value | Change w.r.t visit 1 (%) | Value | Change w.r.t visit 1 (%) | Value | Change w.r.t visit 1 (%) |
| Failure load (kN) | | | | | | | | | | |
| Distal tibia left | 4.988 | +14.5 | 5.713 | +17.2 | 5.847 | +17.0 | 5.834 | +17.0 | 6.042 | +21.1 |
| Distal tibia right | 4.451 | +35.1 | 6.014 | +45.0 | 6.453 | +45.4 | 6.473 | +49.5 | 6.653 | +49.5 |
| | | | | | | | | | | Percentile score |
| | | | | | | | | | | 2-10 |
| | | | | | | | | | | 2-10 |

Parameter values were obtained from the entire HR-pQCT scans without registration of the HR-pQCT scans between the visits. The time between brackets indicates months postpartum at each visit. Percentile scores are according to the normative dataset of Whittier DE, *et al.* 2020 J Bone Miner Res 35:2151-2158.

SUPPLEMENTARY MATERIAL 4

Bone geometry, BMD, and microarchitecture at the left distal radius and tibia of the mother of the women with PLO assessed with high-resolution peripheral quantitative CT (HR-pQCT).

Supplementary Material 4 - Table 1. Geometry, BMD, and microarchitecture at the left distal radius and tibia of the mother of the women with PLO assessed with HR-pQCT.

| | Distal radius | | Distal tibia | |
|---------------------------------|---------------|------------------|--------------|------------------|
| | Value | Percentile score | Value | Percentile score |
| Geometry | | | | |
| Tb.Ar (mm ²) | 308.7 | ≥98 | 899.4 | ≥98 |
| Ct.Ar (mm ²) | 42.3 | 2-10 | 76.0 | <2 |
| Volumetric density | | | | |
| Tt.BMD (mg HA/cm ³) | 191.7 | <2 | 152.1 | <2 |
| Tb.BMD (mg HA/cm ³) | 116.0 | 25-75 | 106.6 | 2-10 |
| Ct.BMD (mg HA/cm ³) | 782.7 | <2 | 719.3 | <2 |
| Microarchitecture | | | | |
| Tb.BV/TV (-) | 0.159 | 25-75 | 0.164 | 10-25 |
| Tb.N (mm ⁻¹) | 1.217 | 25-75 | 1.139 | 25-75 |
| Tb.Th (mm) | 0.223 | 25-75 | 0.238 | 10-25 |
| Tb.Sp (mm) | 0.805 | 25-75* | 0.855 | 25-75* |
| Tb.1/N.SD (mm) | 0.317 | 25-75* | 0.327 | 25-75* |
| Ct.Th (mm) | 0.614 | <2 | 0.750 | <2 |
| Ct.Po (-) | 0.004 | 75-90* | 0.022 | 25-75* |

Tt: total, Tb: trabecular, Ct: cortical, Ar: area, BMD: bone mineral density, BV/TV: bone volume fraction, N: number, Th: thickness, Sp: separation, 1/N.SD: heterogeneity, Po: porosity.

* indicates parameters for which the percentile scores are reversed (*e.g.* a score of < 2 represents a value larger, and thus worse, than the 98th percentile). Percentile scores are according to the normative dataset of Whittier DE, *et al.* 2020 J Bone Miner Res 35:2151-2158.

PART 2

HR-pQCT for distal radius and
scaphoid fractures



6

Chapter 6

The contribution of lower-mineralized tissue to the healing of conservatively-treated distal radius fractures assessed using HR-pQCT

Melissa S.A.M. Bevers[†], Frans L. Heyer[†], Caroline E. Wyers, Bert van Rietbergen, Piet P.M.M. Geusens, Heinrich M.J. Janzing, Okke Lambers Heerspink, Martijn Poeze, Joop P. van den Bergh

[†] These authors have contributed equally to this work and share first authorship

ABSTRACT

High-resolution peripheral quantitative CT (HR-pQCT) enables quantitative assessment of distal radius fracture healing. In previous studies, lower-mineralized tissue formation was observed on HR-pQCT scans, starting early during healing, but the contribution of this tissue to the stiffness of distal radius fractures is unknown. Therefore, the aim of this study was to investigate the contribution of lower-mineralized tissue to the stiffness of fractured distal radii during the first twelve weeks of healing. We did so by combining the results from two series of micro-finite element (μ FE-) models obtained using different density thresholds for bone segmentation. Forty-five postmenopausal women with a conservatively-treated distal radius fracture had HR-pQCT scans of their fractured radius at baseline (BL; 1-2 weeks post-fracture), 3-4 weeks, 6-8 weeks, and 12 weeks post-fracture. Compression stiffness (S) was computed using two series of μ FE-models from the scans: one series (M_{single}) included only higher-mineralized tissue (> 320 mg HA/cm³), and one series (M_{dual}) differentiated between lower-mineralized tissue (200-320 mg HA/cm³) and higher-mineralized tissue. μ FE-elements were assigned a Young's Modulus of 10 GPa (higher-mineralized tissue) or 5 GPa (lower-mineralized tissue), and an axial compression test to 1% strain was simulated. The contribution of the lower-mineralized tissue to S was quantified as the ratio S_{dual}/S_{single} . Changes during healing were quantified using linear mixed effects models and expressed as estimated marginal means (EMMs) with 95%-confidence intervals (95%-CI). Median time to cast removal was 5.0 (IQR: 1.1) weeks. S_{dual} and S_{single} gradually increased during healing to a significantly higher value than BL at 12 weeks post-fracture (both $p < 0.0001$). In contrast, S_{dual}/S_{single} was significantly higher than BL at 3-4 weeks post-fracture ($p = 0.0010$), remained significantly higher at 6-8 weeks post-fracture ($p < 0.0001$), and then decreased to BL-values at the 12-week visit. EMMs ranged between 1.05 (95%-CI: 1.04-1.06) and 1.08 (95%-CI: 1.07-1.10). To conclude, combining stiffness results from two series of μ FE-models obtained using single- and dual-threshold segmentation enables quantification of the contribution of lower-mineralized tissue to the stiffness of distal radius fractures during healing. This contribution is minor but changes significantly around the time of cast removal. Its course and timing during healing may be clinically relevant. Quantification of the contribution of lower-mineralized tissue to stiffness gives a more complete impression of strength recovery post-fracture than the evaluation of stiffness using a single series of μ FE-models.

INTRODUCTION

Distal radius fractures are among the most common fractures in elderly [1,2], but assessment of the healing and union of these fractures is complex. In older individuals, they comprise nearly 20% of all fractures [1]. Their prevalence is increasing, among others due to the aging population and an increased physical activity among elderly [3]. The majority of distal radius fractures in elderly are treated conservatively using cast immobilization [4]. Dutch guidelines prescribe to consider cast treatment for 3-5 weeks depending on fracture displacement and reduction [5]. However, evidence for the optimal immobilization period is limited, especially for reduced fractures [5-8]. The development of evidence-based guidelines is furthermore challenging due to a lack of consensus on and subjectivity of assessing distal radius fracture healing and union [9], which is a problem for fractures in general [10,11]. The assessment of fracture union in clinical practice often includes a physical and radiographic examination [9-11]. Factors, such as biological and biomechanical ones, are not standardly evaluated in clinical practice, but they are essential in fracture healing [12,13]. Such factors could be clinically valuable when they capture changes during the healing process that provide insights into whether a fracture can be clinically considered as healed (*i.e.* when a fracture is able to resist the loading that is associated with daily activities).

High-resolution peripheral quantitative CT (HR-pQCT) enables detailed assessment of changes during fracture healing [14-19]. In conservatively-treated distal radius fractures in postmenopausal women, large visual changes around the fracture region have been observed on HR-pQCT scans early during healing [15]. Specifically, trabeculae became 'blurred' and thereby less well distinguishable from three to four weeks post-fracture and were re-distinguishable again later during healing [15]. These changes were suggested to reflect the formation and concomitant and subsequent remodeling of woven bone, known phases in fracture healing that are important in the stabilization of a fracture and the formation of new bone [20-22]. In the same studies, the stiffness of the fractured radii, computed using micro-finite element (μ FE-) analysis, increased significantly compared to baseline later during healing and continued to increase months after cast removal [15,16]. The early lower-mineralized tissue is not standardly included in μ FE-models from HR-pQCT scans to compute stiffness, and available HR-pQCT data are inconclusive about the differences in the computed stiffness of distal radius fractures during healing between μ FE-models that include lower-mineralized tissue and standard μ FE-models that do not include this tissue [15,18]. Consequently, the contribution of the lower-mineralized tissue to fracture stiffness is unknown. Recently, multiple density thresholds between 200 and 680 mg HA/cm³ were used for trabecular bone in an HR-pQCT study on local bone remodeling during distal radius fracture healing to evaluate trabecular bone around

the fracture region with densities lower and higher than normally evaluated in HR-pQCT analyses ($> 320 \text{ mg HA/cm}^3$) [17]. Application of such method to generate multiple series of μ FE-models that include tissue of different densities may enable study of the contribution of lower-mineralized tissue to fracture stiffness.

The reported differences between the timing of cast removal and the changes in computed stiffness suggest a difference between the clinical and biomechanical perspective of a healed fracture [15,16]. Possibly, the lower-mineralized tissue could contribute to explaining this difference and play a role in the biomechanical recovery of distal radius fractures early during healing which is not quantified when using a single series of μ FE-models. By using multiple density thresholds to develop two series of μ FE-models that include tissue of different densities, the aim of this study was to investigate the contribution of lower-mineralized tissue to the stiffness of fractured distal radii during the first twelve weeks of healing. Additionally, we evaluated bone mineral density as well as the contribution of lower-mineralized tissue to bone volume fraction using a similar dual-threshold approach to get more insights into the formation and mineralization of lower-mineralized tissue during healing.

METHODS

Study design and participants

Data for this study were pooled data obtained from a single-blind randomized controlled trial (RCT) evaluating the effect of calcium and vitamin D supplementation on the healing of distal radius fractures. For that RCT, women aged 50 years and older with a stable distal radius fracture immobilized with a cast were included. Exclusion criteria were: 1) surgical fracture treatment or (bone) surgery of the current fracture side in medical history; 2) active or suspected infection in the past three months; 3) malignancy or pathological fracture in the past twelve months; 4) neuromuscular or neurosensory condition; 5) known systemic or metabolic bone disorder that leads to progressive bone deterioration; 6) active inflammatory disease in the past year; 7) use of oral glucocorticoids in the past twelve months; 8) allergy to any component of the calcium and vitamin D supplements prescribed as part of the RCT; and 9) severe concurrent joint involvement. Women provided written informed consent before study participation. The study protocol was approved by the institutional Medical Ethics Committee (METC registration number NL46035.072.13) and submitted to the Dutch Trial Register.

HR-pQCT imaging

Scan acquisition and grading

HR-pQCT (XtremeCT II, Scanco Medical AG, Switzerland) scans of the fractured distal radius were obtained using default clinical settings [23]. Scans were taken at four visits: the first, baseline (BL) scan at 1-2 weeks after fracture and three follow-up scans at 3-4, 6-8, and 12 weeks post-fracture. The scan protocol was used as in previous HR-pQCT research on distal radius fractures [19]. Using this protocol, a 20.4-mm region (two consecutive stacks) was scanned at each visit, which started 3 mm proximally from the reference line positioned at the proximal edge of the lunate bone. The lunate bone was used for the positioning of the reference line because the standard reference line position at the articular surface of the distal radius may not be possible in case of a distal radius fracture. The acquisition of two stacks was chosen to capture the entire fracture. During scan acquisition, the wrist was immobilized with a fiber-glass cast and additionally placed in a standard motion restraining holder. The cast was retained after cast removal and re-used for the remaining scans. Nevertheless, eleven patients wore a Plaster-of-Paris cast during one or more scan acquisitions due to the planning of their visits at the outpatient clinic, and one of them wore a brace during scan acquisition at another visit. Another patient wore a brace at every visit, and one patient wore no cast at one visit. A scan was repeated once if motion artefacts were observed on the preview slice. Scan time and effective radiation dose were approximately 4 min and 10 μSv per scan, respectively. The scans were reconstructed with an isotropic voxel size of 61 μm . After reconstruction, the quality of each stack of the scans was graded according to the five-point grading system described by Pialat *et al.* [24]. Scans with a grade 4 or 5 in one or both stacks were excluded from analysis; *i.e.*, only scans with grade 1-3 in both stacks were analyzed.

Scan analysis

From the scans with a grade 1-3 in both stacks, the distal radius was contoured and subsequently analyzed. Contouring was performed using an automatic contouring algorithm with manual adjustment in case of visual deviations from the outer bone margins [25]. Thereafter, stiffness in compression (S), bone volume fraction (BV/TV), and bone mineral density (BMD) were determined from the entire contoured bone region on the scans. Scan registration was not performed as three-dimensional registration algorithms did not yield correct alignment results for severe fractures with substantial shape changes during healing [26,27]. BMD was quantified using standard evaluation methods [23]. S and BV/TV were quantified twice, once including only higher-mineralized tissue and once including higher- and lower-mineralized tissue. Higher-mineralized tissue was defined as having a density of $> 320 \text{ mg HA/cm}^3$, equaling the threshold that is standardly used in HR-pQCT analyses for trabecular bone [23]. Lower-mineralized tissue was defined as having a density of 200-320 mg

HA/cm³ based on the range of density thresholds previously used in an HR-pQCT study on local bone remodeling during distal radius fracture healing [17]. The thresholds of 200 mg HA/cm³ and 320 mg HA/cm³ correspond to approximately 17% and 27%, respectively of the assumed maximum density of fully mineralized bone by the manufacturer of the scanner (1200 mg HA/cm³) [23].

To compute the two values of S , two series of linear micro-finite element (μ FE-) models were used (**Figure 1**). Both models were generated by conversion of the bone voxels of the HR-pQCT scans to equally-sized μ FE-elements. For one series of models (M_{single}), the bone voxels were obtained by segmentation of the distal radii from the scans using a threshold of 320 mg HA/cm³. For the second series of models (M_{dual}), a dual-threshold segmentation approach was adopted. Using this approach, the distal radii were segmented from the scans using a threshold of 200 mg HA/cm³, followed by erosion of the resulting binarized image by one voxel to remove partial volume effect voxels. The result was then combined with the single-threshold model M_{single} to obtain the dual-threshold model M_{dual} that differentiates between higher-mineralized (> 320 mg HA/cm³) and lower-mineralized (200-320 mg HA/cm³) tissue. The μ FE-elements of both models were assigned a Poisson's Ratio of 0.3 and a Young's Modulus of 10 GPa for the higher-mineralized tissue, conform standard protocol [23]. For the lower-mineralized tissue, we used three different Young's Moduli in three separate analyses. Based on our defined density range for the lower-mineralized tissue (200-320 mg HA/cm³) and higher-mineralized tissue (320-1200 mg HA/cm³), we estimated a three times lower average density for the lower-mineralized tissue than for the higher-mineralized tissue. By assuming a linear relationship between the density and Young's Modulus for woven bone [28], we estimated also a three-times lower Young's Modulus (*i.e.* 3 GPa). Based on that estimate, we used a Young's Modulus of 1 GPa and 5 GPa for the lower-mineralized tissue. We additionally used a value of 10 GPa for this tissue (*i.e.* equal to the Modulus of the higher-mineralized tissue). An axial compression to 1% strain was then applied to the μ FE-models to calculate S as the reaction force over the applied displacement: S_{single} from M_{single} and S_{dual1} , S_{dual5} , and S_{dual10} from M_{dual} using a Young's Modulus of 1, 5, or 10 GPa, respectively for the lower-mineralized tissue. To compute the two values of BV/TV, the bone was segmented from the scans using a density threshold of either 200 mg HA/cm³ (BV/TV₂₀₀) or 320 mg HA/cm³ (BV/TV₃₂₀). For all parameters, all other settings regarding the segmentation and preprocessing of the scans were kept as default for second-generation HR-pQCT; *i.e.* Gaussian filtering with $\sigma = 0.8$ and support = 1 voxel [23]. The contribution of the lower-mineralized tissue to S and BV/TV was defined as the ratio of two stiffness parameters (S_{dual}/S_{single}) and the ratio of the two BV/TV parameters (simplifying to BV₂₀₀/BV₃₂₀), respectively.

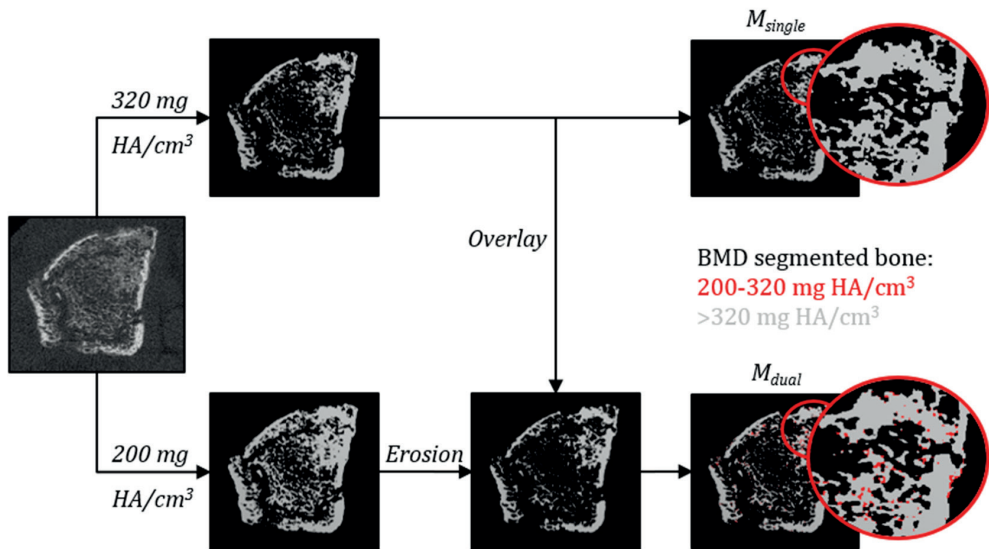


Figure 1. Overview of the two series of micro-finite element (μ FE-) models generated from the HR-pQCT scans of fractured distal radii during healing. One series (top) was based on segmentation of the distal radius using a threshold of 320 mg HA/cm³ and thereby included only higher-mineralized tissue (> 320 mg HA/cm³). The other series (bottom) was based on a dual-threshold segmentation approach, for which the distal radius was segmented using a threshold of 200 mg HA/cm³, followed by erosion by one voxel and then combination with the single-threshold model. This model thereby differentiated between higher-mineralized (> 320 mg HA/cm³) and lower-mineralized (200-320 mg HA/cm³) tissue.

Statistical analysis

Data were analyzed after pooling the data of the study groups. Results per study group are in **Supplementary Material 1**. To quantify the differences in the absolute values and ratio of S and BV/TV over time, linear mixed-effect models (LMMs) were used. In the models, time post-fracture was included as fixed effect, the individual patients as random intercept, and age as covariate. The values from the LMMs at each timepoint were expressed as estimated marginal means (EMMs) with 95%-confidence intervals (95%-CI). The significance of the differences in the EMMs between timepoints was determined on a pairwise-basis. Multiple comparisons were adjusted using Bonferroni, and the significance level was set at $\alpha = 0.05$. The statistical analyses were performed in SPSS (SPSS 26.0, IBM Corp., Armonk, NY, USA) and R (R Foundation for Statistical Computing, Version R-3.6.2 for Windows, Vienna, Austria).

RESULTS

Patient characteristics

In total, 52 women with a conservatively-treated distal radius fracture were included in this study of whom 48 completed the visits until 12 weeks post-fracture (**Figure 2**). One of the 48 women missed the study visit at 6-8 weeks, so a total of 191 HR-pQCT scans was available. Of these scans, 29 were excluded from quantitative analysis: all scans of three women (*i.e.* 12 scans) due to insufficient quality of one or both stacks of three out of the four obtained HR-pQCT scans and 17 scans of 11 other women due to insufficient quality of one or both stacks of those scans. Resultingly, 162 scans of 45 women were quantitatively analyzed: 43, 38, 39, and 42 scans per visit. Characteristics of this cohort are listed in **Table 1**. The duration of cast treatment was 5.0 (interquartile range: 1.1) weeks in the 45 women. It ranged between 3.6 and 6.4 weeks for all but one who had cast treatment for only 1.7 weeks and wore a brace for an additional 2.6 weeks due to heavy swelling and pain while wearing the cast.

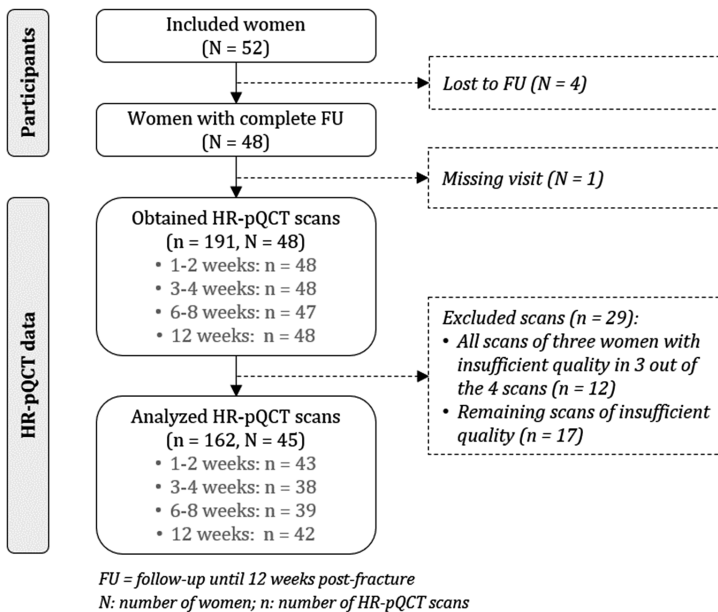


Figure 2. Study participants and HR-pQCT data analyzed for this study.

Table 1. Baseline characteristics of the women with analyzed HR-pQCT data ($N = 45$).

| | |
|--------------------------------------|-------------|
| Age [year] | 64.9 (13.9) |
| Calcium intake [mg/day] ^a | 755 (425) |
| < 1000 | 28 (66.7) |
| < 1200 | 39 (92.9) |
| 25(OH)D level [nmol/L] | 56 (48) |
| < 50 | 17 (37.8) |
| < 75 | 30 (66.7) |
| PTH [pmol/L] | 5.1 (3.5) |
| aBMD T -score [-] ^b | |
| Femoral neck | -2.0 (1.0) |
| Total hip | -1.4 (1.2) |
| Lumbar spine | -2.0 (1.3) |
| Osteoporosis [yes] | 17 (37.8) |

Values are reported as median (interquartile range) or number (%).

25(OH)D, 25-hydroxy-vitamin D. PTH, parathyroid hormone. aBMD, areal bone mineral density from dual-energy X-ray absorptiometry.

^a $n = 42$. ^b $n = 43$.

S, BV/TV, and BMD during fracture healing

The changes during healing in S are visualized in **Figure 3**. S_{single} and S_{dual5} gradually increased over time to become significantly higher than BL at the 12-week visit (both $p < 0.0001$; **Figure 3A**). At the 12-week visit, they were also significantly higher than at the visits at 3-4 weeks (both $p < 0.0001$) and 6-8 weeks (S_{single} : $p < 0.0001$; S_{dual5} : $p = 0.0001$) post-fracture. Similar changes were found when a lower or higher Young's Modulus was used for the lower-mineralized tissue in the dual-threshold μ FE-models (**Figure 3B**). S_{dual1} was significantly higher than BL at 12 weeks post-fracture ($p < 0.0001$). At this timepoint, it was also significantly higher than at 3-4 weeks ($p < 0.0001$) and 6-8 weeks ($p = 0.0001$) post-fracture. S_{dual10} was significantly higher than BL at 6-8 weeks ($p = 0.0384$) and 12 weeks ($p < 0.0001$) post-fracture. At 12 weeks, it was additionally significantly higher than at 3-4 weeks ($p < 0.0001$) and 6-8 weeks ($p = 0.0002$). The interindividual variation was considerable for all parameters of S .

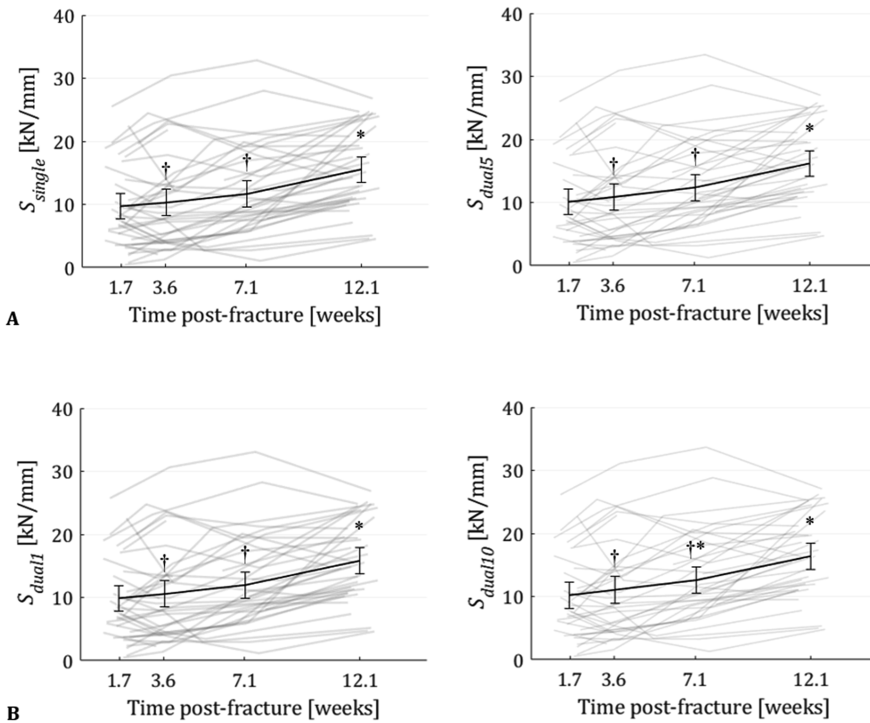


Figure 3. Changes during fracture healing in stiffness **A)** from the single-threshold μ FE-model (left) and the dual-threshold μ FE-model with a Young's Modulus of 5 GPa for the lower-mineralized tissue (right); and **B)** from the dual-threshold μ FE-models with a Young's Modulus of 1 GPa (left) and 10 GPa (right) for the lower-mineralized tissue. The black lines denote estimated marginal means with 95%-confidence intervals. * and † denote a significant difference from the first and last visit, respectively ($p < 0.05$).

The changes during healing in BV/TV and BMD followed different courses (**Figure 4**). BV/TV₃₂₀ and BV/TV₂₀₀ significantly increased compared to BL at 3-4 weeks post-fracture ($p = 0.0403$ and $p = 0.0003$, respectively; **Figure 4A**). They remained significantly higher than BL at 6-8 weeks post-fracture (BV/TV₃₂₀: $p = 0.0043$; BV/TV₂₀₀: $p = 0.0002$) and at 12 weeks post-fracture (BV/TV₃₂₀: $p = 0.0022$; BV/TV₂₀₀: $p = 0.0443$). BMD also significantly increased compared to BL at 3-4 weeks post-fracture ($p = 0.0108$; **Figure 4B**). It returned to BL-values at 6-8 and 12 weeks post-fracture. At 12 weeks post-fracture, BMD was significantly lower than at 3-4 weeks post-fracture ($p = 0.0061$). Similar as for the S parameters, the interindividual variation was considerable for the two BV/TV parameters and BMD.

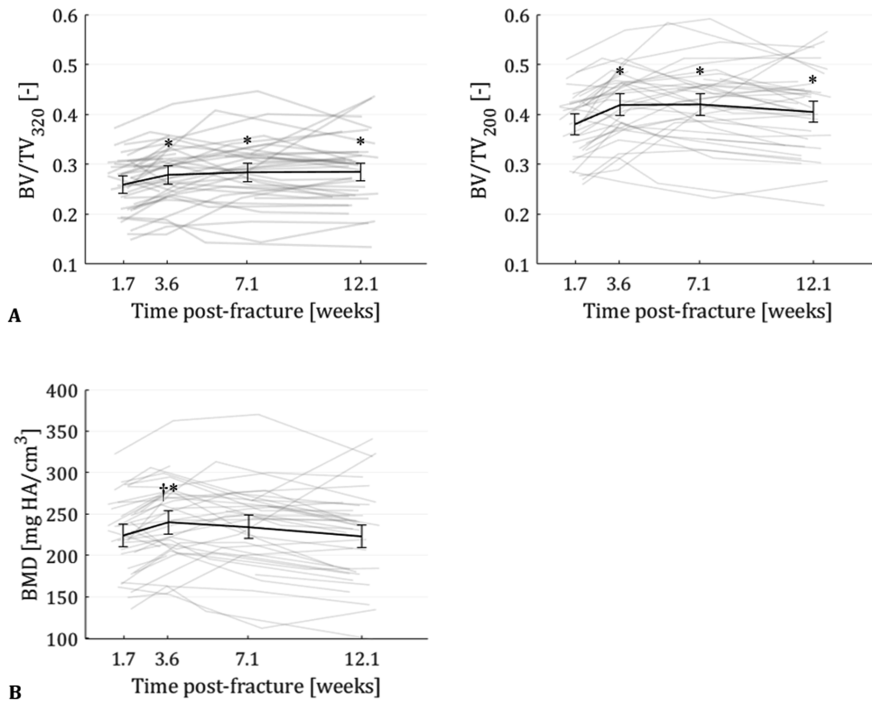


Figure 4. Changes during fracture healing in **A**) bone volume fraction based on a density threshold for segmentation of 320 mg HA/cm³ (left) and of 200 mg HA/cm³ (right); and in **B**) bone mineral density. The black lines denote estimated marginal means with 95%-confidence intervals. * and † denote a significant difference from the first and last visit, respectively ($p < 0.05$).

Contribution of lower-mineralized tissue during healing

The changes in the ratio S_{dual}/S_{single} showed a different course during healing than the changes in S (**Figure 5**). The ratio significantly increased compared to BL at 3-4 weeks post-fracture ($p = 0.0010$), remained significantly higher than BL at 6-8 weeks post-fracture ($p < 0.0001$), and then decreased to BL-values at the 12-week visit (**Figure 5A**). At this timepoint, the ratio was significantly lower than at 3-4 weeks and 6-8 weeks (both $p < 0.0001$) post-fracture. The EMMs ranged between 1.05 (95%-CI: 1.04-1.06) at 1-2 and 12 weeks post-fracture and 1.08 (1.07-1.10) at 6-8 weeks; *i.e.* the contribution of lower-mineralized tissue to S was 5-8% at the group level. At the individual level, the ratio ranged between 1.01 and 1.22 (*i.e.* a contribution of 1-22%). Similar results were found when a lower or higher Young's Modulus was used for the lower-mineralized tissue in the dual-threshold μ FE-model (**Figure 6**). The EMMs for the ratio ranged between 1.02 (1.01-1.03) at 12 weeks and 1.04 (1.03-1.04) at 3-4 and 6-8 weeks when a Young's Modulus of 1 GPa (S_{dual1}/S_{single}) was used and between 1.06 (1.05-1.08) at 12 weeks and 1.11 (1.09-1.12) at 6-8 weeks when a Young's

Modulus of 10 GPa (S_{dual10}/S_{single}) was used. At the individual level, the ratio ranged between 1.00 and 1.12 (S_{dual1}/S_{single}) and between 1.01 and 1.32 (S_{dual10}/S_{single}).

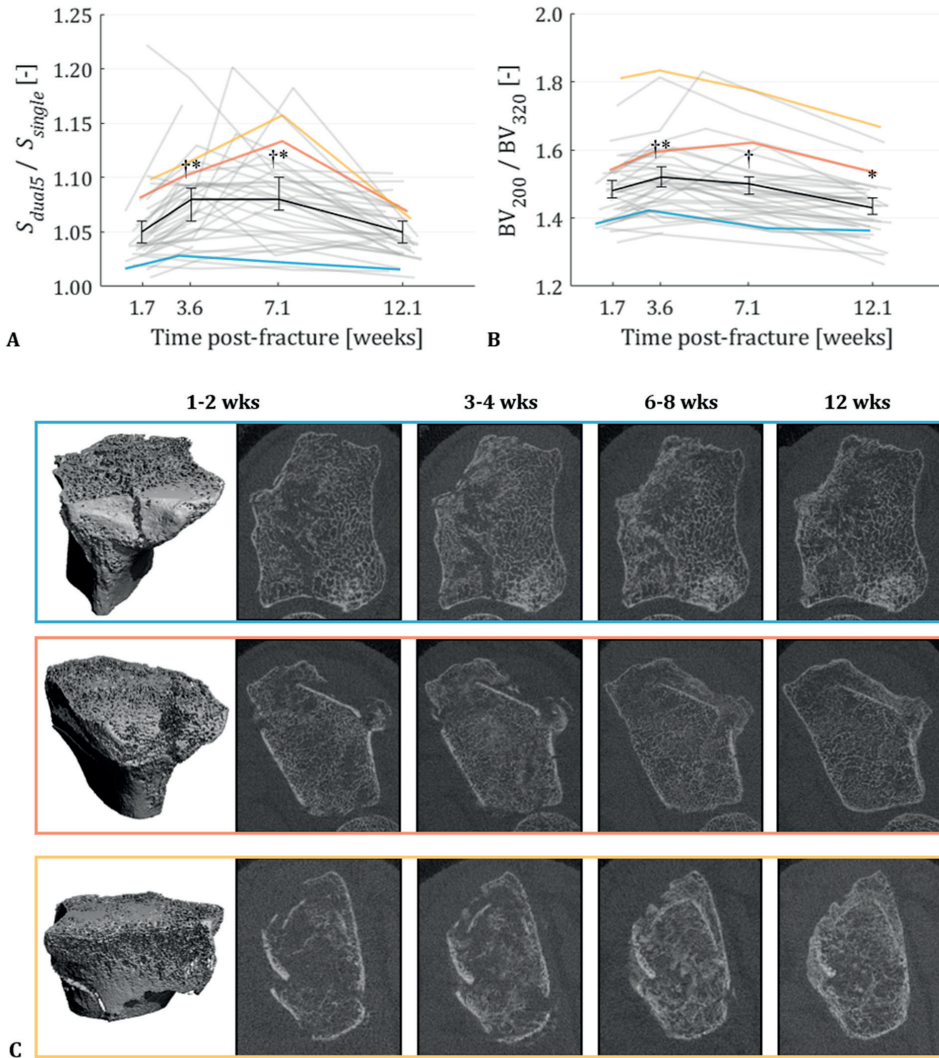


Figure 5. Changes during fracture healing in the contribution of lower-mineralized tissue to **A)** stiffness represented by the ratio of stiffness from the dual-threshold μ FE-model with a Young's Modulus of 5 GPa for the lower-mineralized tissue and the single-threshold μ FE-model; and **B)** bone volume fraction represented by the ratio of bone volume fraction obtained using a segmentation threshold of 200 mg HA/cm³ and of 320 mg HA/cm³. The black lines denote estimated marginal means with 95%-confidence intervals. * and † denote a significant difference from the first and last visit, respectively ($p < 0.05$). **C)** Comparable HR-pQCT slices during healing of three fractures with corresponding contribution of lower-mineralized tissue to stiffness and bone volume fraction. For visualization purposes, the scans were three-dimensionally registered based on their largest common height [27].

A similar course was found for the changes in the ratio BV_{200}/BV_{320} during healing (**Figure 5B**). It significantly increased compared to BL at 3-4 weeks post-fracture ($p = 0.0023$) and subsequently decreased to become significantly lower than BL at 12 weeks post-fracture ($p < 0.0001$). At 12 weeks, the ratio was significantly lower than at 3-4 and 6-8 weeks post-fracture (both $p < 0.0001$). The EMMs ranged between 1.43 (1.41-1.46) and 1.52 (1.49-1.55). **Figure 5C** shows three examples of fractures of visually varying severity and course and corresponding contribution of lower-mineralized tissue to S and BV/TV during healing.

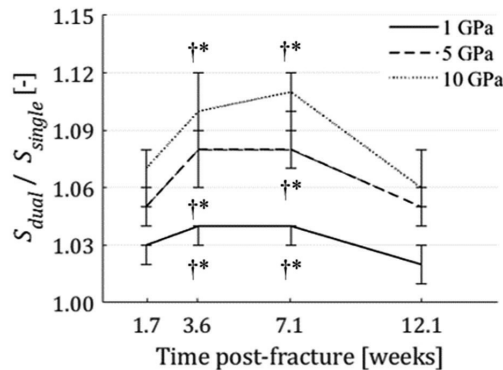


Figure 6. Changes during fracture healing in the contribution of lower-mineralized tissue to stiffness represented by the ratio of stiffness from a dual-threshold μ FE-model with a Young's Modulus of 1, 5, or 10 GPa for the lower-mineralized tissue and the single-threshold μ FE-model. The lines denote estimated marginal means with 95%-confidence intervals. * and † denote a significant difference from the first and last visit, respectively ($p < 0.05$).

DISCUSSION

The aim of this study was to investigate the contribution of lower-mineralized tissue to the stiffness of fractured distal radii derived from HR-pQCT during the first twelve weeks of healing by using multiple density thresholds to develop two series of μ FE-models that include tissue of different mineralization densities. Additionally, we quantified bone mineral density and the contribution of lower-mineralized tissue to bone volume fraction to evaluate the formation and mineralization of lower-mineralized tissue during healing. While the stiffness of the distal radius fractures significantly increased compared to BL at the 12-week visit, the contribution of lower-mineralized tissue to the stiffness increased significantly compared to BL at 3-4 weeks and 6-8 weeks post-fracture. The course and statistical significance of the longitudinal changes were independent of the Young's Modulus used for the lower-mineralized tissue in the dual-threshold μ FE-model (between 1 and 10 GPa). When using a Young's Modulus of 5 GPa for the lower-mineralized tissue, the magnitude of the

contribution of the lower-mineralized tissue to stiffness was 5-8% at the group level and 1-22% at the individual level. The contribution of lower-mineralized tissue to bone volume fraction had a similar course during healing but larger magnitude. Bone mineral density significantly increased compared to BL at 3-4 weeks and returned to BL-values thereafter.

Combining stiffness results that are obtained using different density thresholds for segmentation enables quantification of the contribution of lower-mineralized tissue to the stiffness of fractured distal radii during healing. The contribution of this tissue to stiffness significantly increased compared to BL at 3-4 and 6-8 weeks post-fracture. At 3-4 weeks post-fracture, bone volume fraction and bone mineral density were also significantly higher than at BL, together with a significantly increased contribution of lower-mineralized tissue to bone volume fraction. These changes suggest the formation of lower-mineralized tissue early during healing. The timing of these changes co-occurs with visual changes of trabecular structures around the fracture region reported from 3 to 4 weeks post-fracture [15] and is consistent with the findings in a histological study on human specimens of distal radius fractures, where (woven) bone formation was observed between 2 and 4 weeks post-fracture but not in the first week after fracture [29]. At later timepoints, the contribution of lower-mineralized tissue to bone volume fraction decreased. This suggests remodeling of the lower-mineralized tissue towards higher-mineralized bone. Together, the changes we found during healing support the general knowledge on the early phases of fracture healing; *i.e.* formation and concomitant and subsequent remodeling of woven bone [20-22].

The changes in the contribution of lower-mineralized tissue to stiffness preceded the changes in stiffness, which significantly increased compared to BL at 6-8 or 12 weeks post-fracture depending on the Young's Modulus for the lower-mineralized tissue. Together with the changes in the contribution of lower-mineralized tissue to bone volume fraction during healing, it suggests that predominantly mature bone, formed by remodeling of early lower-mineralized bone, contributes to the recovery of biomechanical strength after fracture. Stiffness from μ FE-analysis may continue to increase until months after cast removal [16,18]. Simultaneously, Dutch guidelines prescribe cast treatment after a distal radius fracture for only 3-5 weeks [5]. At that time, we found limited signs of biomechanical fracture recovery as assessed by the stiffness from μ FE-analysis but a significant increase compared to BL in the contribution of lower-mineralized tissue to this stiffness. Possibly, the lower-mineralized tissue provides sufficient fracture stabilization for cast removal, which is captured by changes in the contribution of lower-mineralized tissue to stiffness but not by changes in stiffness. That is, quantification of the contribution of lower-mineralized tissue to stiffness provides quantitative information about the early phases of fracture healing, which

may be clinically most relevant. It additionally gives a more complete impression of strength recovery post-fracture than the evaluation of stiffness using a single series of μ FE-models.

In contrast to the course and timing of the contribution of lower-mineralized tissue to stiffness during healing, the magnitude of this contribution is likely less physiologically accurate due to the used methodology. For example, the erosion step used to obtain the dual-threshold μ FE-models might have led to an underestimation of the magnitude due to the potential exclusion of lower-mineralized voxels in the μ FE-models that were not the effect of partial volume effects but true voxels of lower-mineralized tissue. Additionally, the material properties of lower-mineralized tissue are not fully known, for which reason we used a range of Young's Moduli (1-10 GPa) in our dual-threshold μ FE-models. The upper value of this range (10 GPa) equals the value often used for mature bone in μ FE-models from HR-pQCT data and can thus be considered as the theoretical maximum. This value likely overestimates the material properties of the lower-mineralized tissue and thereby the contribution of this tissue to stiffness. It is unknown whether the lower value of the chosen range (1 GPa) would be the physiological minimum. The material properties of the lower-mineralized tissue may also not be constant between regions and during the fracture healing process [30]. Besides that, the estimates of stiffness may not be fully accurate. While μ FE-models similar to our single-threshold model accurately estimate failure load at the distal radius [31], μ FE-analysis can considerably overestimate the stiffness of fractured bones depending on the type of fracture [32]. More detailed μ FE-models (*e.g.* gray-value based with density-dependent material properties [33,34]) could possibly provide more accurate estimates, but the sole contribution of lower-mineralized tissue to stiffness cannot be quantified using a single series of FE-models, independent of the amount of detail. We did not experimentally validate our findings on the contribution of lower-mineralized tissue to stiffness. Such validation would also be challenging if not impossible because lower-mineralized tissue would not be easily separable from the rest of the bone tissue, and mechanical loads cannot be applied to solely this tissue. Nevertheless, our results suggest that the magnitude of the contribution of lower-mineralized tissue to stiffness as assessed by HR-pQCT is minor, and that the course and timing of the contribution during healing may be clinically relevant.

There was large inter- and intraindividual variability in the evaluated parameters, which could be associated with fracture type and patient characteristics. Fracture pattern and severity varied highly among the participants and might influence the extent to which lower-mineralized tissue is formed during healing and thereby the extent to which it contributes to the healing process. Furthermore, fracture dislocations during healing may cause differences in the scanned and analyzed bone region over time,

which could have contributed to the large and abrupt longitudinal changes observed at the individual level. Similarly, patient characteristics, such as age and bone quality, might have contributed to the interindividual variation. Age and postmenopausal osteoporosis may influence biological and mechanical factors involved in multiple phases of fracture healing [35-37], although evidence mainly comes from animal studies and is not convincing in clinical studies [36,37]. Additionally, in osteoporotic bone with less and lower-mineralized bone tissue, the contribution of lower-mineralized tissue might be relatively larger than in healthy bone, possibly further influenced by the phenotype of osteoporotic bone microarchitecture [38]. Further research into the role of lower-mineralized tissue in fracture healing may include fracture pattern and severity and patient characteristics to improve our understanding of the fracture healing process in elderly and the effects of fracture type.

Another important aspect regarding the inter- and intraindividual variability is the reproducibility of our methodology. Repositioning errors between visits and motion artefacts might have contributed to the differences between participants and within participants between timepoints. Motion artefacts are partly inherent to the use of HR-pQCT and μ FE-analysis: the relatively long scan time of HR-pQCT increases the risk of patient movement, and the large detail of both techniques increases the potential effects of this movement on the quantified parameters. Scanning multiple stacks furthermore introduces a specific type of motion artefacts, stack shifts. Such shifts may potentially influence HR-pQCT parameters, but this influence is unknown. In a pilot study, we evaluated the effects of correcting stack shifts using an in-house developed stack registration algorithm on the stiffness from μ FE-analysis at the contralateral, non-fractured distal radius of the participants of the current study. Using this algorithm, a two-layer overlap was artificially generated between the two stacks of an HR-pQCT scan, followed by three-dimensional rigid registration to compute an in-plane translation that was then applied to one of two stacks to reduce the stack shift. Preliminary analyses on 76 contralateral HR-pQCT scans showed that the median absolute percentage change in stiffness after stack shift correction was 0.94% (interquartile range 1.8%), and it was $\leq 1\%$ in 40 out of the 76 scans (52.6%; data not shown). Further study is however warranted to evaluate the need and the effects of a stack shift correction. Nevertheless, the fracture-, patient-, and reproducibility-related factors challenge the interpretation of results obtained with our methodology at the individual level as changes in the parameters during healing may not be solely the result of metabolic changes but also of these factors.

In contrast, at the group level in clinical studies, where a combination of objective and subjective outcome measures is recommended to assess fracture healing [39], our methodology could be used to obtain quantitative and objective data on early

changes during fracture healing based on detailed microarchitectural information of a fracture. The contribution of lower-mineralized tissue to stiffness could for example be a valuable measure. It requires however multiple μ FE-analyses, which is computationally expensive. The contribution of lower-mineralized tissue to bone volume fraction is easier to compute and computationally less expensive and had a similar course during fracture healing. The magnitude was however considerably higher, which may result among others from differences in computation (*e.g.* an erosion step was used in the generation of the dual-threshold μ FE-models but not in the computation of bone volume fraction) and relative contribution of the voxels (*e.g.* included voxels may not all have contributed to a measurable extent to stiffness due to for example their location outside the fracture region, while all included voxels add to bone volume fraction). Nevertheless, the contribution of lower-mineralized tissue to bone volume fraction could be an alternative measure for the contribution to stiffness in the quantification of early changes during fracture healing.

Our study has several limitations. First, we used a scan protocol in which scan length and region were fixed for each participant, independent of the size and precise location of the fracture. Consequently, the fracture was not entirely captured in all participants. Furthermore, this protocol has likely resulted in a variable fracture volume relative to the scanned volume among participants, thereby potentially underestimating the contribution of lower-mineralized tissue to the fracture healing in participants with a relatively small fracture. Future studies may therefore consider the use of a scan protocol with variable scan length and region and evaluation of subregions within the scanned bone that contain the fracture. Second, we based the density threshold for the lower-mineralized tissue on the thresholds used in a previous HR-pQCT study on distal radius fracture healing, in which the participants were younger than the participants in our study [17]. However, as the degree of mineralization of lower-mineralized tissue may not depend on age, we used the same threshold as in that study for uniformity. Furthermore, a lower threshold could potentially lead to a more noisy segmentation result and to the inclusion of tissue that likely does not add to the stabilization of a fracture. Third, the scan region may have differed within participants between timepoints due to repositioning errors and the use of the lunate bone to determine the scan region which position with respect to the distal radius is not fixed. We did not align the scans to correct these potential differences in scan region because three-dimensional registration algorithms did not yield accurate results for severe fractures with substantial shape changes during healing [26,27]. A previously explored registration algorithm based on aligning fracture fragments was not evaluated [40]. Fourth, we did not correct for differences in the cast worn during scan acquisition nor for stack shifts. A cast can cause systematic errors in HR-pQCT parameters due to beam hardening, but correction is difficult as cast interference depends on among

others cast type and thickness [41,42]. Stack shifts could potentially influence HR-pQCT parameters, but the effects are unknown. As mentioned previously, preliminary analyses on contralateral HR-pQCT scans of the participants of the current study showed that the median absolute percentage change in stiffness after stack shift correction was $\leq 1\%$ (data not shown), but further evaluation is required to study the need and the effects of a stack shift correction. Fifth, the automatically obtained contours of the fractured distal radii required considerable manual adjustment, which is subjective, especially in largely compressed fractures and due to lower-mineralized tissue formation. However, all adjustments were performed by the same investigator (MB), and μ FE-parameters are little influenced by the periosteal contouring as long as all bone is included in the contoured region. Recently, an automatic contouring algorithm has been developed for fractured distal radii, but this algorithm was not available for use in our center [43]. Finally, as mentioned previously, the computed stiffness and contribution of lower-mineralized tissue to stiffness are likely not fully physiologically accurate [32], and therefore the magnitude of the contribution of the lower-mineralized tissue to stiffness may not be fully accurate. Nevertheless, the course and timing of the contribution agree with general knowledge on fracture healing, and quantification of early changes may have clinical relevance.

To conclude, combining stiffness results from two series of μ FE-models obtained using single- and dual-threshold segmentation enables quantification of the contribution of lower-mineralized tissue to fracture stiffness. The contribution of this tissue to the stiffness of conservatively-treated distal radius fractures is minor but changes significantly early during healing and around the time of cast removal. Together with changes in the contribution of lower-mineralized tissue to bone volume fraction, it may reflect the formation of woven bone and its subsequent and concomitant remodeling to mature bone. While the magnitude of the contribution to stiffness during healing may physiologically not be fully accurate, the course and timing of this contribution could be clinically relevant. Quantification of the contribution of lower-mineralized tissue to stiffness additionally gives a more complete impression of strength recovery post-fracture than the evaluation of stiffness using a single series of μ FE-models alone.

ACKNOWLEDGEMENTS

We thank Sania Moharir, BSc for her help in studying the effects of stack shifts on μ FE-analyses as part of her Master graduation project.

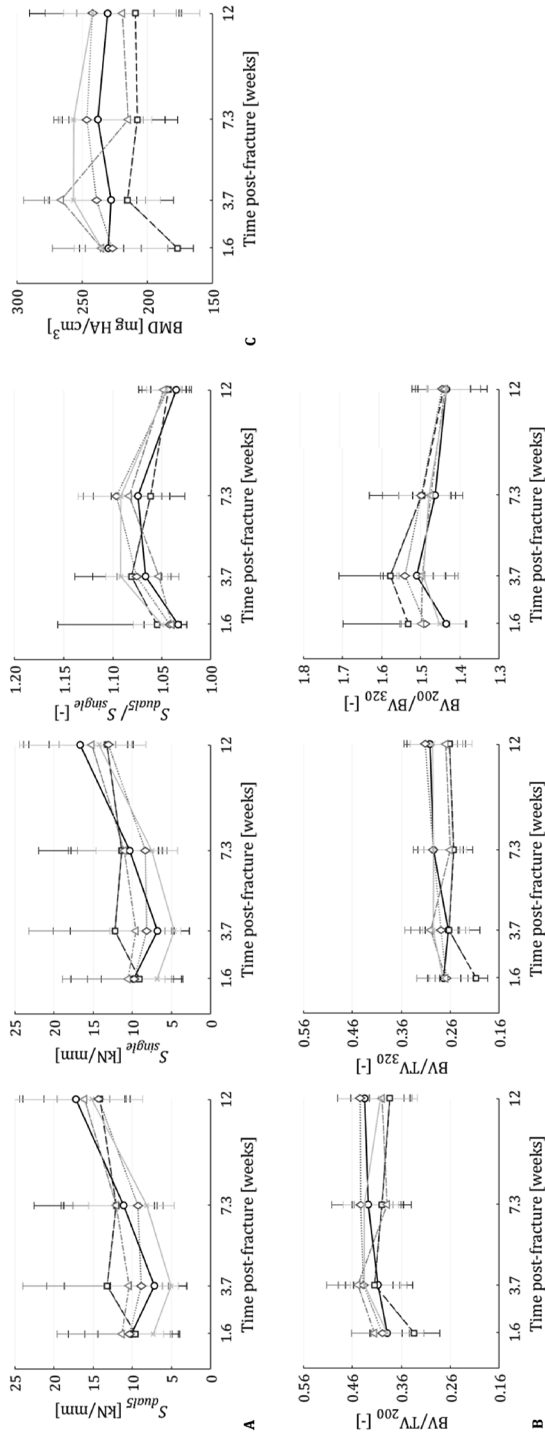
REFERENCES

- [1] Baron JA, Karagas M, Barrett J, et al. Basic epidemiology of fractures of the upper and lower limb among Americans over 65 years of age. *Epidemiology*. 1996;7(6):612–618.
- [2] Karl JW, Olson PR, Rosenwasser MP. The epidemiology of upper extremity fractures in the United States, 2009. *J Orthop Trauma* 2015;29(8):e242–e244.
- [3] Nellans KW, Kowalski E, Chung KC. The epidemiology of distal radius fractures. *Hand Clin*. 2012;28(2):113–125.
- [4] Chung KC, Shauver MJ, Birkmeyer JD. Trends in the United States in the treatment of distal radial fractures in the elderly. *J Bone Joint Surg Am*. 2009;91(8):1868.
- [5] NVVH, “Distale radiusfracturen – Duur immobilisatie bij distale radiusfracturen”. Richtlijndatabase. https://richtlijndatabase.nl/richtlijn/distale_radiusfracturen/duur_immobilisatie_bij_distale_radiusfracturen.html, 2021. Accessed 1 April 2023 [Dutch].
- [6] Bentohami A, van Delft EAK, Vermeulen J, et al. Non-or minimally displaced distal radial fractures in adult patients: three weeks versus five weeks of cast immobilization—a randomized controlled trial. *J Wrist Surg*. 2019;8(1):43–48.
- [7] Christersson A, Larsson S, Östlund B, Sandén B. Radiographic results after plaster cast fixation for 10 days versus 1 month in reduced distal radius fractures: a prospective randomised study. *J Orthop Surg Res*. 2016;11(1):1–8.
- [8] Christersson A, Larsson S, Sandén B. Clinical outcome after plaster cast fixation for 10 days versus 1 month in reduced distal radius fractures: a prospective randomized study. *Scand J Surg*. 2018;107(1):82–90.
- [9] Goldhahn J, Beaton D, Ladd A, Macdermid J, Hoang-Kim A. Recommendation for measuring clinical outcome in distal radius fractures: a core set of domains for standardized reporting in clinical practice and research. *Arch Orthop Trauma Surg*. 2014;134:197–205.
- [10] Corrales LA, Morshed S, Bhandari M, Miclau III T. Variability in the assessment of fracture-healing in orthopaedic trauma studies. *J Bone Joint Surg Am*. 2008;90(9):1862.
- [11] Dijkman BG, Sprague S, Schemitsch EH, Bhandari M. When is a fracture healed? Radiographic and clinical criteria revisited. *J Orthop Trauma* 2010;24:S76–S80.
- [12] Morshed S. Current options for determining fracture union. *Adv Med*. 2014.
- [13] Lopas LA, Shen H, Zhang N, et al. Clinical assessments of fracture healing and basic science correlates: is there room for convergence? *Curr Osteoporosis Rep*. 2022:1–12.
- [14] Mueller TL, Wirth AJ, van Lenthe GH, et al. Mechanical stability in a human radius fracture treated with a novel tissue-engineered bone substitute: a non-invasive, longitudinal assessment using high-resolution pQCT in combination with finite element analysis. *J Tissue Eng Regen Med*. 2011;5(5):415–420.
- [15] de Jong JJ, Willems PC, Arts JJ, et al. Assessment of the healing process in distal radius fractures by high resolution peripheral quantitative computed tomography. *Bone* 2014;64:65–74.
- [16] de Jong JJ, Heyer FL, Arts JJ, et al. Fracture repair in the distal radius in postmenopausal women: a follow-up 2 years Postfracture using HRpQCT. *J Bone Miner Res*. 2016;31(5):1114–1122.
- [17] Atkins PR, Stock K, Ohs N, et al. Formation dominates resorption with increasing mineralized density and time postfracture in cortical but not trabecular bone: a longitudinal HRpQCT imaging study in the distal radius. *JBMR Plus* 2021;5(6):e10493.
- [18] Spanswick P, Whittier D, Kwong C, Korley R, Boyd S, Schneider P. Restoration of stiffness during fracture healing at the distal radius, using HR-pQCT and finite element methods. *J Clin Densitom*. 2021;24(3):422–432.

- [19] Heyer FL, de Jong JJ, Willems PC, et al. The effect of bolus vitamin D3 supplementation on distal radius fracture healing: a randomized controlled trial using HR-pQCT. *J Bone Miner Res.* 2021;36(8):1492–1501.
- [20] Marsell R, Einhorn TA. The biology of fracture healing. *Injury* 2011;42:551–555.
- [21] Sandberg OH, Aspenberg P. Inter-trabecular bone formation: a specific mechanism for healing of cancellous bone: a narrative review. *Acta Orthop.* 2016;87(5):459–465.
- [22] Inoue S, Otsuka H, Takito J, Nakamura M. Decisive differences in the bone repair processes of the metaphysis and diaphysis in young mice. *Bone Rep.* 2018:81–88.
- [23] Whittier DE, Boyd SK, Burghardt AJ, et al. Guidelines for the assessment of bone density and microarchitecture in vivo using high-resolution peripheral quantitative computed tomography. *Osteoporos Int.* 2020;31:1607–1627.
- [24] Pialat JB, Burghardt AJ, Sode M, Link TM, Majumdar S. Visual grading of motion induced image degradation in high resolution peripheral computed tomography: impact of image quality on measures of bone density and micro-architecture. *Bone* 2012;50(1):111–118.
- [25] Buie HR, Campbell GM, Klinck RJ, MacNeil JA, Boyd SK. Automatic segmentation of cortical and trabecular compartments based on a dual threshold technique for in vivo micro-CT bone analysis. *Bone* 2007;41(4):505–515.
- [26] Ellouz R, Chapurlat R, van Rietbergen B, Christen P, Pialat JB, Boutroy S. Challenges in longitudinal measurements with HR-pQCT: evaluation of a 3D registration method to improve bone microarchitecture and strength measurement reproducibility. *Bone* 2014;63:147–157.
- [27] van Rietbergen B, Biver E, Chevalley T, Ito K, Chapurlat R, Ferrari S. A novel HR-pQCT image registration approach reveals sex-specific changes in cortical bone retraction with aging. *J Bone Miner Res.* 2021;36(7):1351–1363.
- [28] Mora-Macías J, García-Florencio P, Pajares A, Miranda P, Domínguez J, Reina-Romo E. Elastic modulus of woven bone: correlation with evolution of porosity and x-ray greyscale. *Ann Biomed Eng.* 2021;49:180–190.
- [29] Aspenberg P, Sandberg O. Distal radial fractures heal by direct woven bone formation. *Acta Orthop.* 2013;84(3):297–300.
- [30] Manjubala I, Liu Y, Epari DR, et al. Spatial and temporal variations of mechanical properties and mineral content of the external callus during bone healing. *Bone* 2009;45(2):185–192.
- [31] Arias-Moreno AJ, Hosseini HS, Bevers MSAM, Ito K, Zysset P, van Rietbergen B. Validation of distal radius failure load predictions by homogenized-and micro-finite element analyses based on second-generation high-resolution peripheral quantitative CT images. *Osteoporos Int.* 2019;30:1433–1443.
- [32] Arias-Moreno AJ, Ito K, van Rietbergen B. Micro-finite element analysis will overestimate the compressive stiffness of fractured cancellous bone. *J Biomech.* 2016;49(13):2613–2618.
- [33] Shefelbine SJ, Simon U, Claes L, et al. Prediction of fracture callus mechanical properties using micro-CT images and voxel-based finite element analysis. *Bone* 2005;36(3):480–488.
- [34] Suzuki T, Matsuura Y, Yamazaki T, et al. Biomechanics of callus in the bone healing process, determined by specimen-specific finite element analysis. *Bone* 2020;132:115212.
- [35] Augat P, Simon U, Liedert A, Claes L. Mechanics and mechano-biology of fracture healing in normal and osteoporotic bone. *Osteoporos Int.* 2005;16:S36–S43.
- [36] Giannoudis P, Tzioupis C, Almalki T, Buckley R. Fracture healing in osteoporotic fractures: is it really different?: a basic science perspective. *Injury* 2007;38(1):S90–S99.
- [37] Gorter EA, Reinders CR, Krijnen P, Appelman-Dijkstra NM, Schipper IB. The effect of osteoporosis and its treatment on fracture healing a systematic review of animal and clinical studies. *Bone Rep.* 2021;15:101117.

- [38] Whittier DE, Samelson EJ, Hannan MT, et al. Bone microarchitecture phenotypes identified in older adults are associated with different levels of osteoporotic fracture risk. *J Bone Miner Res.* 2022;37(3):428–439.
- [39] Goldhahn J, Angst F, Simmen BR. What counts: outcome assessment after distal radius fractures in aged patients. *J Orthop Trauma* 2008;22:S126–S130.
- [40] de Jong JJ, Christen P, Plett RM, et al. Feasibility of rigid 3D image registration of high-resolution peripheral quantitative computed tomography images of healing distal radius fractures. *PLoS One* 2017;12(7):e0179413.
- [41] de Jong JJ, Arts JJ, Meyer U, et al. Effect of a cast on short-term reproducibility and bone parameters obtained from HR-pQCT measurements at the distal end of the radius. *J Bone Joint Surg Am.* 2016;98(5):356–362.
- [42] Whittier DE, Manske SL, Boyd SK, Schneider PS. The correction of systematic error due to plaster and fiberglass casts on HR-pQCT bone parameters measured in vivo at the distal radius. *J Clin Densitom.* 2019;22(3):401–408.
- [43] Ohs N, Collins CJ, Tourolle DC, et al. Automated segmentation of fractured distal radii by 3D geodesic active contouring of in vivo HR-pQCT images. *Bone* 2021;147:115930.

SUPPLEMENTARY MATERIAL 1



Supplementary Material 1 - Figure 1. Changes during fracture healing for each study group separately in **A)** stiffness from the dual-threshold μ FE-model (left) and single-threshold μ FE-model (middle) and the ratio between the two stiffness parameters (right); **B)** bone volume fraction at a density threshold of 200 mg HA/cm³ (left) and 320 mg HA/cm³ (middle) and the ratio between the two bone volume fraction parameters; and **C)** bone mineral density. The lines represent median values and the 25th and 75th percentile. Only the results of women with available data on daily calcium intake and serum vitamin D level are included in the graphs (N = 42). Study groups: Ctrl = control; Ca = calcium supplementation; Ca + low vitD = calcium and low-dose vitamin D supplementation; Ca + high vitD = calcium and high-dose vitamin D supplementation; Already use = use of calcium and/or vitamin D supplements at the time of inclusion.



7

Chapter 7

The feasibility of high-resolution peripheral quantitative computed tomography (HR-pQCT) in patients with suspected scaphoid fractures

Melissa S.A.M. Bevers, Anne M. Daniels, Caroline E. Wyers, Bert van Rietbergen, Piet P.M.M. Geusens, Sjoerd Kaarsemaker, Heinrich M.J. Janzing, Pascal F.W. Hannemann, Martijn Poeze, Joop P. van den Bergh

J. Clin. Densitom. 2020, 23(3): 432-442.

ABSTRACT

Introduction

Diagnosing scaphoid fractures remains challenging. High-resolution peripheral quantitative computed tomography (HR-pQCT) might be a potential imaging technique, but no data are available on its feasibility to scan the scaphoid bone *in vivo*.

Methodology

Patients (≥ 18 years) with a clinically suspected scaphoid fracture received an HR-pQCT scan of the scaphoid bone (three 10.2-mm stacks, 61- μm voxel size) with their wrist immobilized with a cast. Scan quality assessment and bone contouring were performed using methods originally developed for HR-pQCT scans of radius and tibia. The contouring algorithm was applied on coarse hand-drawn pre-contours of the scaphoid bone, and the resulting contours (AUTO) were manually corrected (sAUTO) when visually deviating from bone margins. Standard morphologic analyses were performed on the AUTO- and sAUTO-contoured bones.

Results

Ninety-one patients were scanned. Two out of the first five scans were repeated due to poor scan quality (40%) based on standard quality assessment during scanning, which decreased to three out of the next 86 scans (3.5%) when using an additional thumb cast. Nevertheless, after excluding one scan with an incompletely scanned scaphoid bone, *post hoc* grading revealed a poor quality in 14.9% of the stacks and 32.9% of the scans in the remaining 85 patients. After excluding two scans with contouring problems due to scan quality, bone indices obtained by AUTO- and sAUTO-contouring were compared in 83 scans. All AUTO-contours were manually corrected, resulting in significant but small differences in densitometric and trabecular indices ($< 1.0\%$).

Conclusions

In vivo HR-pQCT scanning of the scaphoid bone is feasible in patients with a clinically suspected scaphoid fracture when using a cast with thumb part. The proportion of poor-quality stacks is similar to radius scans, and AUTO-contouring appears appropriate in good- and poor-quality scans. Thus, HR-pQCT may be promising for diagnosis of and microarchitectural evaluations in suspected scaphoid fractures.

INTRODUCTION

Scaphoid fractures account for approximately 60-75% of all carpal fractures [1-4] and can have long-term complications when they are not immediately treated. The treatment is usually conservative (*i.e.* cast) for stable and nondisplaced fractures and operative (*e.g.* screw fixation) for unstable or displaced fractures [5]. A delay in treatment may cause healing complications and increased healing time and an increased risk for a scaphoid nonunion [6,7]. A scaphoid nonunion, in turn, is challenging to treat successfully and can cause carpal instability and osteoarthritis [8].

Early diagnosis and adequate treatment of scaphoid fractures is thus important, but immediate diagnosis remains challenging. Plain radiography is typically used at initial presentation, but misses up to 25% of scaphoid fractures compared to magnetic resonance imaging, computed tomography (CT), and bone scintigraphy [9]. While these advanced imaging techniques have a better sensitivity and specificity than radiography [10,11], they lack good positive predictive values, and their improved sensitivity is generally associated with a reduced specificity and *vice versa* [12,13]. Consequently, there is no consensus today on a gold standard imaging technique for scaphoid fractures [14,15].

High-resolution peripheral quantitative CT (HR-pQCT) may be a potential alternative imaging technique. It is a noninvasive technique that provides 3-dimensional images of peripheral bones at a low radiation dose and with a spatial resolution higher than of currently used imaging techniques [16]. Its high resolution may enable recognizing more and smaller scaphoid fractures than currently used techniques and enables microarchitectural bone evaluations of (fractured) scaphoid bones, which have already provided new insights into fracture mechanism, nonunion etiology, and optimal screw fixation and design in cadaveric bones [17-21].

Although the use of HR-pQCT in scaphoid fractures may thus be interesting for diagnostic and research purposes, the feasibility of *in vivo* HR-pQCT scanning of the scaphoid bone is not yet fully explored. To our knowledge, Reina *et al.* performed the only *in vivo* HR-pQCT study on the scaphoid bone thus far, investigating the patterns in trabecular bone between normal dominant and nondominant radial carpal bones [22]. In that study, nothing was reported about motion artefacts or image quality of the HR-pQCT scans. However, it is unknown whether subject motion is comparable or worse in scaphoid bone scans compared to radius or tibia scans as 3 stacks rather than 1 stack are needed to capture the entire scaphoid bone [23] and whether image quality is adequate for application in clinical practice. This study, therefore, explored the feasibility of *in vivo* HR-pQCT scanning of the scaphoid bone in patients with

a clinically suspected scaphoid fracture. Scan-quality assessment and scaphoid bone contouring were performed using methods originally developed for HR-pQCT scans of radius and tibia, and differences in bone indices were determined between contours with and without manual correction.

METHODS

Study design and population

All consecutive patients (aged ≥ 18 yrs.) presenting between December 2017 and October 2018 at the emergency department of VieCuri Medical Centre Venlo (The Netherlands) within 1 week after trauma with a clinically suspected scaphoid fracture were eligible for study participation. Patients were excluded in case of pregnancy or a previous ipsilateral scaphoid fracture in medical history. All included patients gave written consent prior to participation. The study protocol (METC registration number NL62476.068.17) was approved by an independent Medical Ethics Committee and complied with the Declaration of Helsinki of 1975, revised in 2000.

The included patients followed the standard diagnostic protocol for suspected scaphoid fractures. They were subjected to standard plain radiography at initial presentation followed by immobilization of the wrist with a synthetic nonfiberglass cast. Within 10 days after initial presentation, a clinical reassessment was performed to determine treatment strategy. In addition to this standard protocol and independent of the outcome of the clinical reassessment, all included patients received an HR-pQCT scan.

HR-pQCT imaging

HR-pQCT (XtremeCT II, Scanco Medical AG, Switzerland) scans of the scaphoid bone were performed on a 30.6-mm region of the wrist (3 consecutive 10.2-mm stacks) with the reference line at the longitudinal sagittal ridge between the scaphoid bone and lunate fossa at the articular surface of the distal radius (**Figure 1**). During scanning, the wrist was immobilized with a synthetic nonfiberglass cast, and standard motion restraining holders for HR-pQCT scanning were used. Synthetic casts have been found to affect scan quality and bone parameters only marginally [24]. Total scan time was 6.0 min, subjecting the patients to an effective radiation dose of approximately 15 μSv . X-ray tube voltage and intensity were 68 kV and 1460 μA , respectively, and integration time was 43 ms. The images were reconstructed using an isotropic voxel size of 61 μm , resulting in 504 consecutive slices [25].

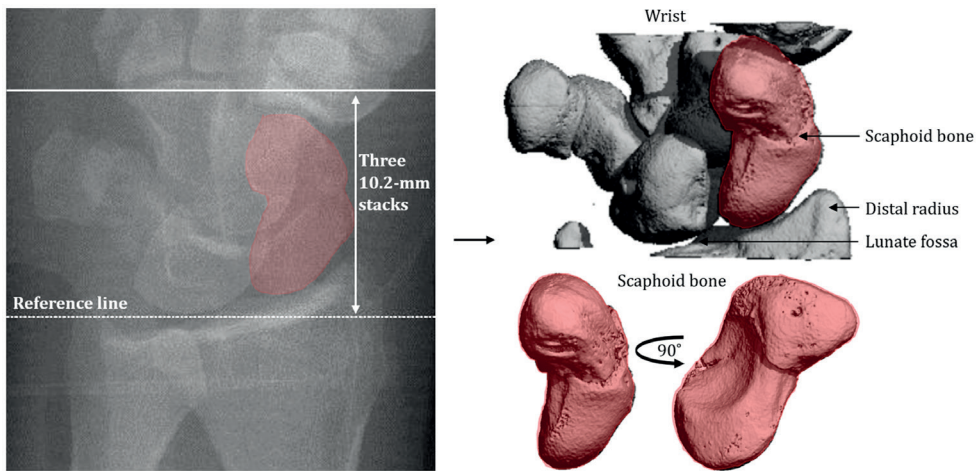


Figure 1. Scout view showing the reference line used to scan the scaphoid bone (left) and a 3-dimensional view of the scanned region of the wrist (right top) and of the scaphoid bone (right bottom).

Scan-quality assessment

Scan quality was graded using the grading system used by Pialat *et al.* to grade HR-pQCT scans of the distal radius and tibia [26]. A single low-resolution slice of each stack of the scans was graded by the operator during scan acquisition (standard grading). Scans were completely repeated once when the quality of at least 1 stack had a grade > 3 . The scan with the best quality in the 3 stacks was included for further analyses. Additionally, scan quality was *post hoc* graded by 1 researcher using the same grading system on multiple full-resolution slices of each stack (*post hoc* grading). More specifically, the first slice in which the scaphoid bone appeared was determined, and from that slice on every tenth slice was graded. Based on these gradings, an overall grade was determined for each stack. The entire scan was assigned a good quality when each of the 3 stacks had a grade 1-3 and a poor quality when at least 1 stack had a grade > 3 .

Scaphoid fracture assessment

All HR-pQCT scans were evaluated by an experienced radiologist to assess fractures.

Scaphoid bone contouring

To investigate the quantitative potential of HR-pQCT in scaphoid bones, the scaphoid bones were contoured in the scans. Initially, the automatic contouring algorithm, originally developed to contour radius and tibia and similar to the algorithm for automatic contouring of the periosteal and endosteal margins of radius and tibia [27],

was used to contour the scaphoid bone. However, its application on the scaphoid bone scans resulted in severe contouring problems, including contouring the wrong bone (**Figure 2A**) and multiple bones (**Figure 2B**). Therefore, its application was changed from the entire scan of the scaphoid bone to coarse hand-drawn precontours of the bone. Moreover, the lower threshold for binarization was changed from the default 120 to 105 per 1000 as the cortex of the scaphoid bone is thinner and less mineralized than that of radius and tibia. The resulting contouring algorithm (AUTO) thus comprised manual drawing of coarse precontours of the scaphoid bone followed by application of the automatic contouring algorithm with adjusted settings on these coarse contours, which solved the problems of applying the contouring algorithm on entire scans (**Figures 2C-D**). As a separate study procedure, the obtained AUTO contours were manually corrected (sAUTO) by 1 researcher when visually deviating from the margins of the scaphoid bone.

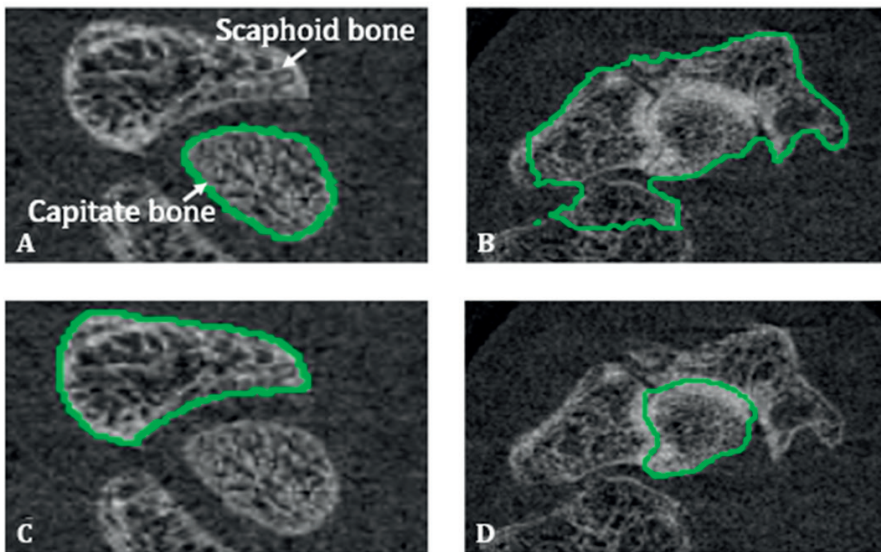


Figure 2. Problems of the automatic contouring algorithm originally developed for radius and tibia in contouring **A**) the correct bone, and **B**) only 1 bone. These problems were solved when applying the algorithm on coarse hand-drawn precontours of the scaphoid bone (**C-D**).

Quantitative analysis

Standard morphologic analyses were performed on the AUTO- and sAUTO-contoured scaphoid bones. Bone and tissue mineral density (BMD and TMD, respectively) were determined, as were the ratio of bone volume to total volume (BV/TV) and trabecular number (Tb.N), thickness (Tb.Th), and separation (Tb.Sp). The trabecular indices were calculated using distance transformation [28]. Cortical indices were not determined because of the lack of a clear cortical layer in the scaphoid bone.

Statistical analysis

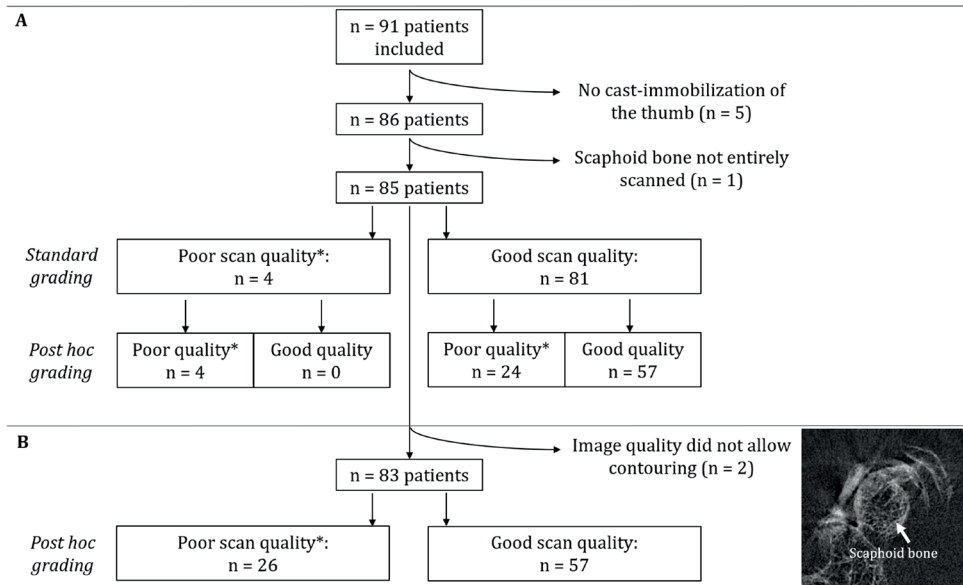
The quantitative measures obtained were statistically analyzed (IBM SPSS Statistics for Windows, Version 25.0. Armonk, NY: IBM Corp). Normality of the distribution of the data was analyzed using Shapiro-Wilk tests. Differences in patient characteristics between poor- and good-quality scans were analyzed using Mann-Whitney U tests and Chi-Square tests and determinants of scan quality using uni- and multivariate binomial logistic regression models with covariates age, gender, and the presence of a scaphoid fracture. Differences in bone indices between the AUTO- and sAUTO-contoured scaphoid bones were analyzed using paired-sample *t* tests or related-samples Wilcoxon signed rank tests and performed on the entire dataset and on subgroups with either good-quality scans (grade 1-3 for all 3 stacks of a scan), poor-quality scans (grade 4-5 for at least 1 of the 3 stacks), scans with a scaphoid fracture, or scans without a scaphoid fracture. Additionally, the differences in bone indices between both contouring methods were compared between the good- and poor-quality scans and between the scans with and without a scaphoid fracture within the subgroups of poor- and good-quality scans using Mann-Whitney U tests. All tests were 2-sided, and the significance level was set at 0.05.

RESULTS

Patient characteristics

Ninety-one patients were included in the study, 45 men (49.5%) and 46 women with a median age of 37 ± 32 and 62 ± 24 yr, respectively. Twenty-four patients (26.4%) were diagnosed with a scaphoid fracture (15 men and 9 women) based on the HR-pQCT scans. Median time between initial presentation at the emergency department and HR-pQCT scanning was 9 days (range: 2-13 days).

The scans of 6 patients were excluded from further analyses (**Figure 3A**). The scans of the first 5 patients were excluded: the scans of 2 out of these first patients (40%) had to be repeated due to a poor quality based on the standard grading. In an attempt to reduce this proportion, the next patients received the original cast (**Figure 4A**) extended with a temporary thumb part (**Figure 4B**). This adaptation lowered the proportion of rescanning due to poor quality to 3.5% (3 out of 86 scans). Only these 86 scans were included in further analyses to keep uniformity in casting procedure among patients. Of these scans, 1 scan was excluded because the scaphoid bone was not entirely scanned due to a wrong positioning of the wrist in the scanner, resulting in a total of 85 included scans (**Figure 3A**).



*A scan with at least one of the three stacks having a grade >3 due to motion artifacts

Figure 3. Flow-chart of the included scans for **A)** the determination of patient characteristics of poor- and good-quality scans based on the standard grading and *post hoc* grading, and **B)** scaphoid bone contouring.



Figure 4. Synthetic nonfiberglass cast used to immobilize the wrist during scanning. **A)** The original cast, and **B)** the original cast (black) extended with a removable thumb cast (blue) seen from a dorsal (top) and volar (bottom) perspective.

Scan-quality assessment

Based on the standard grading, 4 out of the 85 scans (4.7%) were assessed as poor quality, while 28 scans (32.9%) were assessed as poor quality based on the *post hoc* grading (**Figure 3A; Table 1**). Although the standard grading assessed scans as poor quality that were also assessed as poor quality during the *post hoc* grading, it missed 24 poor-quality scans compared to the *post hoc* grading (**Figure 3A**). Patients with poor-quality scans based on the *post hoc* grading were significantly older than those with good-quality scans (**Table 1**), and logistic regression models showed age to be significantly associated with scan quality in a univariate model ($OR_{10\text{yrs}} = 1.47$, 95%-CI = 1.13-1.92) and in multivariate models with gender and/or the presence of a scaphoid fracture as other covariates (**Supplementary Material 1**). More than half of the poor-quality scans had only 1 poor-quality stack (75.0% and 64.3% for standard grading and *post hoc* grading, respectively) (**Table 1**). Stated differently, the *post hoc* grading revealed 18 of 85 scans (21.2%) to have a poor quality in only 1 stack (21.2%) and 38 of 255 stacks (14.9%) to be of poor quality, which was the middle stack in 50% of the scans (**Table 1**). Scans with multiple poor-quality stacks had a poor-quality proximal and distal stack in 50% of the cases (*post hoc* grading; **Table 1**).

Table 1. Patient characteristics according to scan quality.

| Characteristic | Standard grading | | | Post hoc grading | | |
|---------------------------------------|-----------------------------|-----------------------------|----------------|-----------------------------|-----------------------------|----------------|
| | Good quality (grade 1-3) | Poor quality (grade >3)* | <i>p</i> value | Good quality (grade 1-3) | Poor quality (grade >3)* | <i>p</i> value |
| Number (%) | | | | | | |
| All (<i>n</i> = 85) | 81 (95.3) | 4 (4.7) | | 57 (67.1) | 28 (32.9) | |
| Scaphoid fracture (<i>n</i> = 21) | 21 (100.0) | 0 (0.0) | 0.241 | 16 (76.2) | 5 (23.8) | 0.305 |
| No scaphoid fracture (<i>n</i> = 64) | 60 (93.8) | 4 (6.3) | | 41 (64.1) | 23 (35.9) | |
| Gender – Male (%) | 41 (50.6) | 1 (25.0) | 0.317 | 29 (50.9) | 13 (46.4) | 0.700 |
| Median age ± IQR (yr) | 52 ± 38 | 59.5 ± 29 | 0.328 | 47 ± 37 | 64.5 ± 64 | 0.003 |
| Quality distribution over stacks | | | | | | |
| One stack (%) | - | 3 (75.0) | | - | 18 (64.3) | |
| Proximal stack | | 1 (33.3) | | | 3 (16.7) | |
| Middle stack | | 0 (0.0) | | | 9 (50.0) | |
| Distal stack | | 2 (66.7) | | | 6 (33.3) | |
| Two stacks (%) | - | 1 (25.0) | | - | 10 (35.7) | |
| Proximal and middle stack | | 1 (100.0) | | | 3 (30.0) | |
| Proximal and distal stack | | 0 (0.0) | | | 5 (50.0) | |
| Middle and distal stack | | 0 (0.0) | | | 2 (20.0) | |
| Three stacks (%) | - | 0** (0.0) | | - | 0** (0.0) | |

*A scan was assigned a poor quality if at least 1 of the 3 stacks of a scan had a grade >3 due to motion artifacts

**One scan had a scaphoid bone covering only two stacks that were both of poor quality, but is included in the '2 stacks'-group.

p values <0.05 are shown in bold.

Scaphoid bone contouring

The scans of 2 patients out of the 85 included scans were excluded from quantitative analyses because their scan quality did not allow contouring (**Figure 3B**), resulting in 83 scans.

The AUTO-algorithm solved the problems of the automatic algorithm (**Figure 2**), but incorrectly contoured the scaphoid bone in the first and last few slices due to its anatomy, which required manual contour corrections (sAUTO) in all 83 scans (**Figures 5A1 and 2**), as well as scaphoid bones with (displaced) fractures (**Figure 5B**), small joint spaces due to rheumatoid arthritis or osteoarthritis (**Figure 5C**) or thin subchondral bone layers (**Figure 5D**) and scaphoid bones in poor-quality scans (**Figure 5E**). The sAUTO-contours resulted in significant, but small differences in bone indices (**Table 2; Figure 6A**). In the subgroups of good- and poor-quality scans (*post hoc* grading), all indices were significantly different between the AUTO- and sAUTO-contoured scaphoid bones except for Tb.N and BV/TV, respectively (**Table 3**). Nevertheless, all differences were < 0.5% (except Tb.Th < 1.0%) (**Figure 6A**). Percentage differences between both contouring methods were in general larger in the poor-quality scans and reached statistical significance for TMD and the trabecular indices (**Figure 6A**). Within the subgroup of poor-quality scans, differences between the AUTO- and sAUTO-contoured bones were in general larger in scans with multiple poor-quality stacks or a poor-quality middle stack than in those with 1 poor-quality stack or a poor-quality proximal or distal stack (**Supplementary Material 2**). In the subgroups of scans with and without a scaphoid fracture, all indices were significantly different between the AUTO- and sAUTO-contoured bones except for Tb.N in the former and BV/TV in the latter subgroup (**Table 4**). Percentage differences differed significantly between scans with and without a scaphoid fracture for TMD within the subgroup of good-quality scans (*post hoc* grading), and for BV/TV, BMD, and Tb.N within the subgroup of poor-quality scans (**Figure 5B**).

Table 2. Difference in densitometric and trabecular structural bone parameters between automatically contoured scaphoid bone (AUTO) and manually corrected contours (sAUTO).

| Parameter | AUTO (<i>n</i> = 83) | sAUTO (<i>n</i> = 83) | Difference | <i>p</i> value |
|------------------------------|-----------------------|------------------------|---------------------|----------------|
| Densitometric | | | | |
| BV/TV [%] | 53.0 ± 7.85 | 53.0 ± 7.92 | -0.0400 ± 0.130 | 0.004 |
| BMD [mg HA/CC] | 375 ± 59.7 | 375 ± 60.2 | -0.574 ± 0.954 | 0.000 |
| TMD [mg HA/CC] | 769 ± 29.4 | 770 ± 29.4 | -0.834 ± 0.859 | 0.000 |
| Trabecular structural | | | | |
| Tb.N [mm ⁻¹] | 1.75 ± 0.159 | 1.76 ± 0.160 | -0.00120 ± 0.00340 | 0.002 |
| Tb.Th [mm] | 0.450 ± 0.0816 | 0.448 ± 0.0811 | 0.00220 ± 0.00260 | 0.000 |
| Tb.Sp [mm] | 0.521 ± 0.0731 | 0.522 ± 0.0733 | -0.000900 ± 0.00140 | 0.000 |

Values are mean ± SD.

p Values < 0.05 are shown in bold.

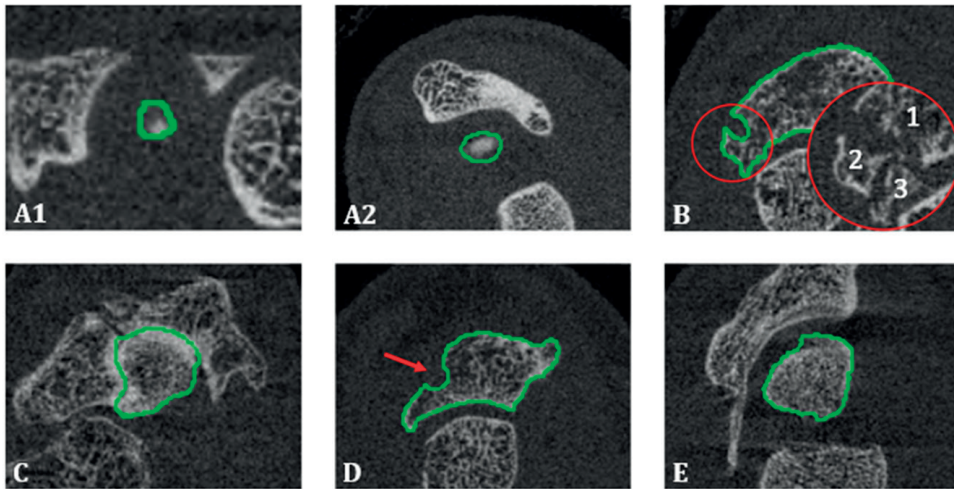


Figure 5. The automatic contouring algorithm applied on coarse hand-drawn precontours (AUTO) incorrectly contoured the scaphoid bone **A**) at the first few (1) and last few (2) slices, and in case of **B**) (displaced) fractures, **C**) small joint spaces, **D**) thin subchondral bone layers, and **E**) poor scan quality.

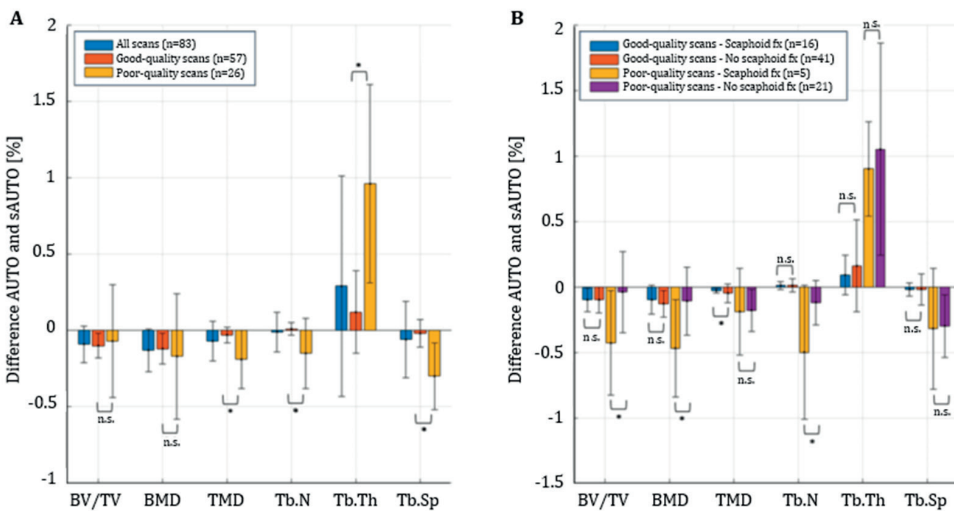


Figure 6. Median (\pm IQR) percentage difference in bone indices between the automatically contoured scaphoid bone without (AUTO) and with (sAUTO) manual corrections for **A**) all scans, good-quality scans, and poor-quality scans, and for **B**) good- and poor-quality scans with and without fractured scaphoid bones. Scan quality is based on *post hoc* grading, and the significance level is set at 0.05.

Table 3. Difference in densitometric and trabecular structural bone parameters between automatically contoured scaphoid bone (AUTO) and manually corrected contours (sAUTO) for the subgroups of good- and poor-quality scans based on *post hoc* grading.

| Parameter | Good quality (grade 1-3; n = 57) | | | Poor quality (grade >3; n = 26)* | | | |
|------------------------------|----------------------------------|----------------|---------------------|----------------------------------|----------------|--------------------|--------------|
| | AUTO | sAUTO | Difference | AUTO | sAUTO | Difference | p value |
| Densitometric | | | | | | | |
| BV/TV [%] | 53.5 ± 7.81 | 53.6 ± 7.84 | -0.0400 ± 0.0700 | 51.7 ± 7.93 | 51.8 ± 8.10 | -0.0400 ± 0.220 | 0.304 |
| BMD [mg HA/CC] | 381 ± 61.4 | 381 ± 61.7 | -0.464 ± 0.517 | 362 ± 54.9 | 363 ± 56.1 | -0.813 ± 1.52 | 0.011 |
| TMD [mg HA/CC] | 774 ± 30.7 | 775 ± 30.8 | -0.447 ± 0.435 | 757 ± 22.5 | 758 ± 22.6 | -1.68 ± 0.949 | 0.000 |
| Trabecular structural | | | | | | | |
| Tb.N [mm ⁻¹] | 1.73 ± 0.148 | 1.73 ± 0.148 | -0.000200 ± 0.00200 | 1.81 ± 0.168 | 1.82 ± 0.172 | -0.00340 ± 0.00470 | 0.001 |
| Tb.Th [mm] | 0.450 ± 0.0886 | 0.449 ± 0.0881 | 0.00110 ± 0.00140 | 0.451 ± 0.0651 | 0.446 ± 0.0648 | 0.00470 ± 0.00270 | 0.000 |
| Tb.Sp [mm] | 0.526 ± 0.0690 | 0.526 ± 0.0692 | -0.000500 ± 0.00120 | 0.511 ± 0.0818 | 0.513 ± 0.0825 | -0.00180 ± 0.00150 | 0.000 |

*A scan was assigned a poor quality if at least 1 of the three stacks of a scan had a grade >3 due to motion artifacts. Values are mean ± SD. p values < 0.05 are shown in bold.

Table 4. Difference in densitometric and structural bone parameters between automatically contoured scaphoid bone (AUTO) and manually corrected contours (sAUTO) for the subgroups of scans with and without a scaphoid fracture based on the HR-pQCT scans.

| Parameter | Scans with scaphoid fracture (n = 21) | | | Scans without scaphoid fracture (n = 62) | | | |
|------------------------------|---------------------------------------|----------------|---------------------|--|----------------|---------------------|--------------|
| | AUTO | sAUTO | Difference | AUTO | sAUTO | Difference | p value |
| Densitometric | | | | | | | |
| BV/TV [%] | 56.0 ± 6.03 | 56.1 ± 6.12 | -0.0900 ± 0.130 | 51.9 ± 8.17 | 52.0 ± 8.23 | -0.0300 ± 0.130 | 0.113 |
| BMD [mg HA/CC] | 395 ± 39.9 | 396 ± 40.5 | -0.825 ± 1.09 | 368 ± 63.9 | 369 ± 64.4 | -0.489 ± 0.899 | 0.000 |
| TMD [mg HA/CC] | 762 ± 31.6 | 763 ± 31.4 | -0.562 ± 0.833 | 771 ± 28.6 | 772 ± 28.5 | -0.926 ± 0.854 | 0.000 |
| Trabecular structural | | | | | | | |
| Tb.N [mm ⁻¹] | 1.80 ± 0.186 | 1.81 ± 0.189 | -0.00190 ± 0.00490 | 1.74 ± 0.146 | 1.74 ± 0.147 | -0.000900 ± 0.00270 | 0.011 |
| Tb.Th [mm] | 0.458 ± 0.0628 | 0.457 ± 0.0619 | 0.00150 ± 0.00200 | 0.447 ± 0.0873 | 0.445 ± 0.0869 | 0.00250 ± 0.00270 | 0.000 |
| Tb.Sp [mm] | 0.495 ± 0.0832 | 0.495 ± 0.0830 | -0.000600 ± 0.00110 | 0.530 ± 0.0677 | 0.531 ± 0.0681 | -0.00100 ± 0.00150 | 0.000 |

Values are mean ± SD. p values < 0.05 are shown in bold.

DISCUSSION

This study showed that *in vivo* HR-pQCT scanning of the scaphoid bone is feasible in patients with a clinically suspected scaphoid fracture. The proportion of repeated scans considerably improved by extending the wrist-immobilizing cast, worn during scanning, with a temporary thumb part. The proportion of *post hoc* graded poor-quality stacks (14.9%) was considerably lower than of poor-quality scans (32.9%). Manual corrections were needed in the AUTO-contours of all scans, but the resulting differences in bone indices were < 1% for all bone indices in good- and poor-quality scans and scans with and without a scaphoid fracture.

A wrist- and thumb-immobilizing cast was necessary to reduce motion artifacts. While 40% of the first 5 scans had to be repeated due to motion artifacts using the original cast based on the standard grading during scan acquisition, extension of this cast with a thumb part lowered this proportion to 3.5%. An additional thumb cast is therefore recommended in future HR-pQCT studies scanning patients with a suspected scaphoid fracture.

Despite this adjusted cast, still 32.9% of the scans were *post hoc* assessed as poor quality, which is considerably higher than the poor-quality rate in 1-stack radius scans (3-19%) [29-32]. This relatively large poor-quality rate may have been caused by movement excursions due to the more distal scan region for scaphoid bone scans [29,31], which seemed to be more common in older patients considering the age dependency in scan quality. Also the necessity to scan 3 stacks to capture the entire scaphoid bone rather than 1 stack may explain the relatively large poor-quality rate as the proportion of poor-quality stacks (14.9%) is in agreement with the poor-quality rates in the radius. This comparable poor-quality stack rate and the recent approved clinical use of HR-pQCT for osteoporosis assessment in adult patients may suggest that the image quality of HR-pQCT is sufficient for diagnosis of scaphoid fractures, but this needs to be further investigated.

Adequate image quality is also required for microarchitectural bone evaluations. Previous studies recommended to repeat or exclude poor-quality radius and tibia scans (*i.e.* 1-stack scans with grade > 3) because of their influence on bone indices [33], but these recommendations might be different for scaphoid bone scans (*i.e.* 3-stack scans). Because bone indices are determined over the entire bone, the relative bone volume affected by subject motion likely influences the effect of subject motion on bone indices. This idea is reinforced by our finding that bone indices were more influenced by manual contour corrections in poor-quality scans with multiple poor-quality stacks or a poor-quality middle stack than in scans with 1 poor-quality stack or a poor-

quality proximal or distal stack. Possibly, an additional distinction within 3-stack poor-quality scans based on relative motion-affected bone volume might reduce the number of scaphoid bone scans that should be repeated or excluded from quantitative analyses, which requires a reproducibility study on the effects of subject motion on bone indices [26].

Microarchitectural evaluations require also proper bone contouring. Applied on coarse hand-drawn precontours, the standard algorithm for automatic radius and tibia contouring appeared to correctly contour the scaphoid bone. Although manual corrections were necessary in all scans, they caused differences in bone indices ($< 0.5\%$, except $Tb.Th < 1.0\%$) smaller than the voxel size of the scans and smaller than longitudinal bone changes in radius and tibia due to ageing, treatment, or repeated scans [26,32,34,35]. It is thus questionable whether manual corrections are needed, especially when taking into account time consumption (5-15 min for good-quality scans and 30-60 min for poor-quality scans) and expected interobserver variability and reduced reproducibility [36]. The ability to automatically contour the scaphoid bone on HR-pQCT scans allows for microarchitectural bone evaluations in suspected scaphoid fractures and possibly also for research into the healing process of these fractures [32].

Although this study was the first to explore the feasibility of *in vivo* HR-pQCT scanning of the scaphoid bone and used a uniform protocol and cast for every patient to allow between-patient comparison [24], it had several limitations. First, only 1 researcher *post hoc* graded scan quality and manually corrected contours, whereas both are known to be subjective in radius and tibia scans [26,36]. The subjectivity in grading may be even larger in scaphoid bone scans considering the discrepancy between standard and *post hoc* grading of 85.7% (*i.e.* the standard grading missed 85.7% of the scans that were *post hoc* assessed as poor quality), which is considerably higher than the 12% reported in literature on 1-stack radius and tibia scans (*i.e.* theoretically 36% in 3-stack scans) [26]. Our large discrepancy may possibly be caused by difficulties in applying the existing quality-grading criteria on scaphoid bone scans as 1 criterium is based on the continuity of the cortical layer, which is extremely thin in the scaphoid bone and which has small interruptions that could reflect transcortical vascular entries rather than cortical discontinuities due to motion artifacts [37]. Further research should therefore investigate inter- and intraobserver variability in grading and manually correcting contours and address the applicability of existing grading systems to scaphoid bone scans. Second, in this study the newest second-generation HR-pQCT scanner was used, whereas many first-generation systems are still in use. The use of the first-generation scanner would have likely resulted in a larger proportion of poor-quality scans because of a longer scanning time (8.4 min

for a 27.1-mm scan using the first-generation 82 μm -resolution scanner and 6.0 min for a 30.6-mm scan using the second-generation 61 μm -resolution scanner [25]). The ability to automatically contour the scaphoid bone, on the other hand, would likely not have been different. Third, stack shifts were observed in the scans of some patients. Although these shifts could have influenced bone indices, they were not accounted for in the analyses because of their expected limited effect on bone indices. Fourth, although the comparable poor-quality stack rate and the recent approved clinical use of HR-pQCT for osteoporosis assessment in adult patients indicates that the image quality of HR-pQCT may be sufficient for diagnosis of scaphoid fractures, its diagnostic performance for scaphoid fractures is currently not known, and it has to be further studied what quality of HR-pQCT scans is needed for adequate diagnosis of these fractures. Fifth, gender was not taken into account in the analyses despite the epidemiological differences between men and women with a fractured scaphoid bone.

In conclusion, *in vivo* HR-pQCT scanning of the scaphoid bone is feasible in patients with a clinically suspected scaphoid fracture when using a cast with thumb part during scanning. The proportion of poor-quality stacks is similar to radius and tibia scans, and automatic contouring starting from coarse hand-drawn precontours is appropriate. HR-pQCT may be promising for diagnosis of scaphoid fractures, for microarchitectural bone evaluations in patients with a suspected scaphoid fracture, and possibly also for research into the healing process of scaphoid fractures.

REFERENCES

- [1] Hove LM. Epidemiology of scaphoid fractures in Bergen, Norway. *Scand J Plast Reconstr Surg Hand Surg.* 1999;33:423–426.
- [2] Dennis HHW, Sze ACK, Murphy D. Prevalence of carpal fracture in Singapore. *J Hand Surg.* 2011;36:278–283.
- [3] Van Onselen EBH, Karim RB, Hage JJ, Ritt MJPF. Prevalence and distribution of hand fractures. *J Hand Surg.* 2003;28:491–495.
- [4] Holloway KL, Moloney DJ, Brennan-Olsen SL, et al. Carpal and scaphoid fracture incidence in south-eastern Australia: an epidemiologic study. *Arch Osteoporos.* 2015;10:10.
- [5] Arsalan-Werner A, Sauerbier M, Mehling IM. Current concepts for the treatment of acute scaphoid fractures. *Eur J Trauma Emerg Surg.* 2016;42:3–10.
- [6] Eddeland A, Eiken O, Hellgren E, Ohlsson N-M. Fractures of the scaphoid. *Scand J Plast Reconstr Surg.* 1975;9:234–239.
- [7] Langhoff O, Andersen JL. Consequences of late immobilization of scaphoid fractures. *J Hand Surg.* 1988;13:77–79.
- [8] Mack GR, Bosse MJ, Gelberman RH, Yu E. The natural history of scaphoid non-union. *J Bone Joint Surg Am.* 1984;66:504–509.
- [9] Brooks S, Wluka AE, Stuckey S, Cicuttini F. The management of scaphoid fractures. *J Sci Med Sport.* 2005;8:181–189.
- [10] Carpenter CR, Pines JM, Schuur JD, et al. Adult scaphoid fracture. *Acad Emerg Med.* 2014;21:101–121.
- [11] Yin Z-G, Zhang J-B, Kan S-L, Wang X-G. Diagnostic accuracy of imaging modalities for suspected scaphoid fractures. *J Bone Joint Surg Br.* 2012;94-B:1077–1085.
- [12] Groves AM, Cheow HK, Balan KK, et al. 16 detector multislice CT versus skeletal scintigraphy in the diagnosis of wrist fractures: value of quantification of ⁹⁹Tcm-MDP uptake. *Br J Radiol.* 2005;78:791–795.
- [13] Mallee W, Doornberg JN, Ring D, et al. Comparison of CT and MRI for diagnosis of suspected scaphoid fractures. *J Bone Joint Surg.* 2011;93:20.
- [14] Groves AM, Kayani I, Syed R, et al. An international survey of hospital practice in the imaging of acute scaphoid trauma. *Am J Roentgenol.* 2006;187:1453–1456.
- [15] Smith JE, House RH, Gallagher J, Phillips A. The management of suspected scaphoid fractures in English hospitals: a national survey. *Eur J Emerg Med.* 2016;23:190.
- [16] Burghardt AJ, Krug R, Majumdar S. Chapter 55: high-resolution imaging techniques for bone quality assessment. In: Feldman D, eds. *Vitamin D*, 2018:1007–1041.
- [17] Su-Bum AL, Hyo-Jin BK, Jae-Myeung CC, et al. Osseous microarchitecture of the scaphoid: cadaveric study of regional variations and clinical implications. *Clin Anat.* 2012;25:203–211.
- [18] Qu G, von Schroeder HP. Trabecular microstructure at the human scaphoid nonunion. *J Hand Surg.* 2008;33:650–655.
- [19] Leventhal EL, Wolfe SW, Walsh EF, Crisco JJ. A computational approach to the “optimal” screw axis location and orientation in the scaphoid bone. *J Hand Surg.* 2009;34:677–684.
- [20] Varga P, Schefzig P, Unger E, et al. Finite element based estimation of contact areas and pressures of the human scaphoid in various functional positions of the hand. *J Biomech.* 2013;46:984–990.
- [21] Varga P, Zysset PK, Schefzig P, et al. A finite element analysis of two novel screw designs for scaphoid waist fractures. *Med Eng Phys.* 2016;38:131–139.
- [22] Reina N, Cavaignac E, Trousdale WH, et al. Laterality and grip strength influence hand bone micro-architecture in modern humans, an HRpQCT study. *J Anat.* 2017;230:796–804.

- [23] Pichler W, Windisch G, Schaffler G, et al. Computer-assisted 3-dimensional anthropometry of the scaphoid. *Orthopedics*. 2010;33.
- [24] de Jong JJA, Arts JJ, Meyer U, et al. Effect of a cast on short-term reproducibility and bone parameters obtained from HR-pQCT measurements at the distal end of the radius. *J Bone Joint Surg Am*. 2016;98:356–362.
- [25] Vilayphiou N, Hämmerle S, Koller B. The 2nd generation of HR-pQCT: progresses in bone microstructure assessment with 61 um voxel size in vivo scans. *J Bone Miner Res*. 2013;28.
- [26] Pialat J, Burghardt AJ, Sode M, et al. Visual grading of motion induced image degradation in high resolution peripheral computed tomography: impact of image quality on measures of bone density and micro-architecture. *Bone*. 2012;50:111–118.
- [27] Burghardt AJ, Buie HR, Laib A, et al. Reproducibility of direct quantitative measures of cortical bone micro-architecture of the distal radius and Tibia by HR-pQCT. *Bone*. 2010;47:519–528.
- [28] Hildebrand T, Rüeggsegger P. A new method for the model-independent assessment of thickness in three-dimensional images. *J Microsc*. 1997;185:67–75.
- [29] Macdonald HM, Nishiyama KK, Kang J, et al. Age-related patterns of trabecular and cortical bone loss differ between sexes and skeletal sites: a population-based HR-pQCT study. *J Bone Miner Res*. 2011;26:50–62.
- [30] Dalzell N, Kaptoge S, Morris N, et al. Bone micro-architecture and determinants of strength in the radius and tibia: age-related changes in a population-based study of normal adults measured with high-resolution pQCT. *Osteoporos Int*. 2009;20:1683–1694.
- [31] Engelke K, Stampa B, Timm W, et al. Short-term in vivo precision of BMD and parameters of trabecular architecture at the distal forearm and tibia. *Osteoporos Int*. 2012;23:2151–2158.
- [32] de Jong JJA, Willems PC, Arts JJ, et al. Assessment of the healing process in distal radius fractures by high resolution peripheral quantitative computed tomography. *Bone*. 2014;64:65–74.
- [33] Pauchard Y, Liphardt A-M, Macdonald HM, et al. Quality control for bone quality parameters affected by subject motion in high-resolution peripheral quantitative computed tomography. *Bone*. 2012;50:1304–1310.
- [34] Gabel L, Macdonald HM, McKay HA. Sex differences and growth-related adaptations in bone microarchitecture, geometry, density, and strength from childhood to early adulthood: a mixed longitudinal HR-pQCT Study. *J Bone Miner Res*. 2017;32:250–263.
- [35] Khosla S, Riggs BL, Atkinson EJ, et al. Effects of sex and age on bone microstructure at the ultradistal radius: a population-based noninvasive in vivo assessment. *J Bone Miner Res*. 2006;21:124–131.
- [36] de Waard EAC, Sarodnik C, Pennings A, et al. Reliability of HR-pQCT derived cortical bone structural parameters when using uncorrected instead of corrected automatically generated endocortical contours in a cross-sectional study: the Maastricht Study. *Calcif Tissue Int*. 2018;103:252–265.
- [37] van Alphen NA, Morsy M, Laungani AT, et al. A three-dimensional micro-computed tomographic study of the intraosseous lunare vasculature: implications for surgical intervention and the development of avascular necrosis. *Plast Reconstr Surg*. 2016;138:869e.

SUPPLEMENTARY MATERIAL 1

Results of univariate and multivariate binomial logistic regression models that predict scan quality.

Supplementary Material 1 - Table 1. Results of univariate and multivariate binomial logistic regression models that predict scan quality.

| Factor | Standard grading | | | Post hoc grading | | | | | | | | | | | | | | | | | | | | | | | | | | |
|-------------------------|------------------|----------------|------------------|------------------|------------------|----------------|------------------|----------------|------------------|----------------|------------------|----------------|------------------|----------------|------------------|----------------|------------------|----------------|------------------|----------------|------------------|----------------|------------------|----------------|------------------|----------------|------------------|--------------|------------------|--------------|
| | Univariate | | | Model 1 | | | | Model 2 | | | | Model 3 | | | | Model 4 | | | | Model 5 | | | | Model 6 | | | | | | |
| | OR (95% CI) | <i>p</i> value | OR (95% CI) | <i>p</i> value | OR (95% CI) | <i>p</i> value | OR (95% CI) | <i>p</i> value | OR (95% CI) | <i>p</i> value | OR (95% CI) | <i>p</i> value | OR (95% CI) | <i>p</i> value | OR (95% CI) | <i>p</i> value | OR (95% CI) | <i>p</i> value | OR (95% CI) | <i>p</i> value | OR (95% CI) | <i>p</i> value | OR (95% CI) | <i>p</i> value | OR (95% CI) | <i>p</i> value | | | | |
| Age (1 yr.) | 1.04 (0.97-1.10) | 0.264 | 1.04 (1.01-1.07) | 0.005 | 1.05 (1.02-1.08) | 0.003 | 1.04 (1.01-1.07) | 0.008 | 1.05 (1.01-1.08) | 0.005 | 1.05 (1.01-1.08) | 0.005 | 1.05 (1.01-1.08) | 0.005 | 1.05 (1.01-1.08) | 0.005 | 1.05 (1.01-1.08) | 0.005 | 1.05 (1.01-1.08) | 0.005 | 1.05 (1.01-1.08) | 0.005 | 1.05 (1.01-1.08) | 0.005 | 1.05 (1.01-1.08) | 0.005 | 1.05 (1.01-1.08) | 0.005 | | |
| Age (10 yrs.) | 1.41 (0.77-2.59) | 0.265 | 1.47 (1.13-1.92) | 0.005 | 1.47 (1.13-1.92) | 0.005 | 1.47 (1.13-1.92) | 0.005 | 1.47 (1.13-1.92) | 0.005 | 1.47 (1.13-1.92) | 0.005 | 1.47 (1.13-1.92) | 0.005 | 1.47 (1.13-1.92) | 0.005 | 1.47 (1.13-1.92) | 0.005 | 1.47 (1.13-1.92) | 0.005 | 1.47 (1.13-1.92) | 0.005 | 1.47 (1.13-1.92) | 0.005 | 1.47 (1.13-1.92) | 0.005 | 1.47 (1.13-1.92) | 0.005 | 1.47 (1.13-1.92) | 0.005 |
| Gender (male) | 0.33 (0.03-3.26) | 0.339 | 0.84 (0.34-2.07) | 0.700 | 1.81 (0.61-5.39) | 0.284 | 0.84 (0.34-2.07) | 0.700 | 1.81 (0.61-5.39) | 0.284 | 0.84 (0.34-2.07) | 0.700 | 1.81 (0.61-5.39) | 0.284 | 0.84 (0.34-2.07) | 0.700 | 1.81 (0.61-5.39) | 0.284 | 0.84 (0.34-2.07) | 0.700 | 1.81 (0.61-5.39) | 0.284 | 0.84 (0.34-2.07) | 0.700 | 1.81 (0.61-5.39) | 0.284 | 0.84 (0.34-2.07) | 0.700 | 1.81 (0.61-5.39) | 0.284 |
| Scaphoid fracture (yes) | 0.00 (0.00--) | 0.998 | 0.56 (0.18-1.72) | 0.309 | 0.98 (0.28-3.43) | 0.978 | 0.56 (0.18-1.72) | 0.309 | 0.98 (0.28-3.43) | 0.978 | 0.56 (0.18-1.72) | 0.309 | 0.98 (0.28-3.43) | 0.978 | 0.56 (0.18-1.72) | 0.309 | 0.98 (0.28-3.43) | 0.978 | 0.56 (0.18-1.72) | 0.309 | 0.98 (0.28-3.43) | 0.978 | 0.56 (0.18-1.72) | 0.309 | 0.98 (0.28-3.43) | 0.978 | 0.56 (0.18-1.72) | 0.309 | 0.98 (0.28-3.43) | 0.978 |

Model 1: age (1 yr.) and gender (male) adjusted, Model 2: age (1 yr.) and fracture (yes) adjusted

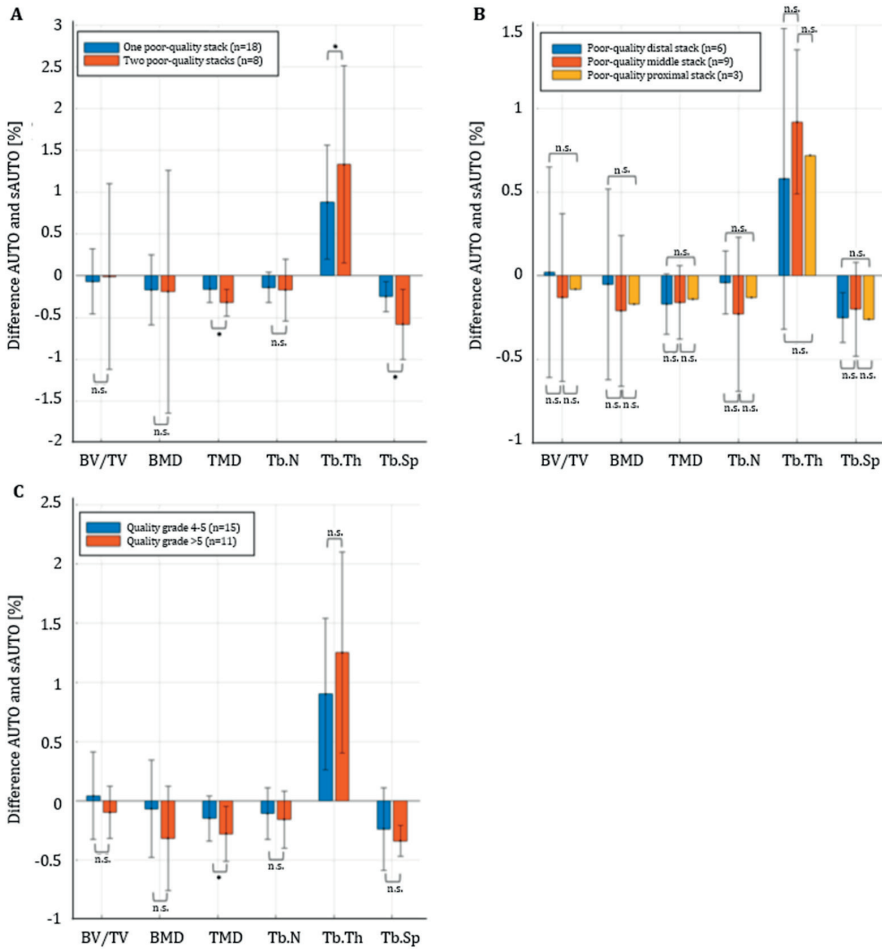
Model 3: age (1 yr.), gender (male), and fracture (yes) adjusted

Model 4: age (10 yr.) and gender (male) adjusted, Model 5: age (10 yr.) and fracture (yes) adjusted

Model 6: age (10 yr.), gender (male), and fracture (yes) adjusted

p values < 0.05 are shown in bold.

SUPPLEMENTARY MATERIAL 2



Supplementary Material 2 - Figure 1. Median (\pm IQR) percentage difference in bone indices between the automatically contoured scaphoid bone without (AUTO) and with (sAUTO) manual corrections for poor-quality scans subdivided into scans with **A**) one or multiple poor stacks, and **B**) one proximal, middle, or distal poor stack. Scan quality is based on *post hoc* grading, and the significance level is 0.05.



8

Chapter 8

Improved detection of scaphoid fractures with high-resolution peripheral quantitative CT compared with conventional CT

Anne M. Daniels, Melissa S.A.M. Bevers, Sander Sassen, Caroline E. Wyers, Bert van Rietbergen, Piet P.M.M. Geusens, Sjoerd Kaarsemaker, Pascal F.W. Hannemann, Martijn Poeze, Joop P. van den Bergh, Heinrich M.J. Janzing

J. Bone Joint Surg. 2020, 102(24): 2138-2145.

ABSTRACT

Background

Computed tomography (CT), magnetic resonance imaging, and bone scintigraphy are second-line imaging techniques that are frequently used for the evaluation of patients with a clinically suspected scaphoid fracture. However, as a result of varying diagnostic performance results, no true reference standard exists for scaphoid fracture diagnosis. We hypothesized that the use of high-resolution peripheral quantitative CT (HR-pQCT) in patients with a clinically suspected scaphoid fracture could improve scaphoid fracture detection compared with conventional CT in the clinical setting.

Methods

The present study included 91 consecutive patients (≥ 18 years of age) who presented to the emergency department with a clinically suspected scaphoid fracture between December 2017 and October 2018. All patients were clinically reassessed within 14 days after first presentation, followed by CT and HR-pQCT. If a scaphoid fracture was present, the fracture type was determined according to the Herbert classification system, and the correlation between CT and HR-pQCT was estimated with use of the Kendall W statistic or coefficient of concordance (W) (the closer to 1, the higher the correlation).

Results

The cohort included 45 men and 46 women with a median age of 52 years (interquartile range, 29-67 years). HR-pQCT revealed a scaphoid fracture in 24 patients (26%), whereas CT revealed a scaphoid fracture in 15 patients (16%). Patients with a scaphoid fracture were younger and more often male. The correlation between CT and HR-pQCT was high for scaphoid fracture type according to the Herbert classification system ($W = 0.793$; 95%-confidence interval, 0.57-0.91; $p < 0.001$) and very high for scaphoid fracture location ($W = 0.955$; 95%,-CI 0.90-0.98; $p < 0.001$).

Conclusions

In the present study, the number of patients diagnosed with a scaphoid fracture was 60% higher when using HR-pQCT as compared with CT. These findings imply that a substantial proportion of fractures - in this study, more than one-third - will be missed by the current application of CT scanning in patients with a clinically suspected scaphoid fracture.

INTRODUCTION

The scaphoid bone is the most commonly fractured carpal bone. Scaphoid fractures represent 2-6% of all fractures and occur mainly in young and active patients 15-40 years of age. In the Netherlands, scaphoid fractures account for 90% of all carpal fractures [1-4]. The scaphoid bone articulates with 5 surrounding bones and therefore serves a key role in the function of the wrist [5]. Inadequate treatment of a scaphoid fracture can lead to malunion, nonunion, and early osteoarthritis [1,6,7]. These complications are associated with pain, decreased range of motion, reduced grip strength, and worse functional outcome. Consequently, early and accurate diagnosis is important. As up to 25% of scaphoid fractures remain radiographically occult with conventional imaging [1,8-10], patients with a suspected scaphoid fracture are generally managed with cast immobilization, and reassessment takes place after approximately 10 days, resulting in a diagnostic delay of up to 2 weeks. According to the existing literature, only 10-20% of clinically suspected fractures are true fractures [4,8,11-14]. This implies that most patients are overtreated, with unnecessary socioeconomic effects, as result of cast immobilization.

Radiographic diagnosis of scaphoid fractures is difficult because of the unique shape, size, and orientation of this carpal bone. Various imaging techniques have been suggested for the improvement of the diagnosis and the reduction of overtreatment. Computed tomography (CT), magnetic resonance imaging (MRI), and bone scintigraphy (BS) are most frequently used today, but all have limitations [11-13,15-24]. None of the investigated diagnostic modalities is both sensitive and specific, and therefore no true reference standard exists. Despite advanced knowledge and imaging methods, diagnosing scaphoid fractures remains challenging, and the preferred imaging technique differs according to hospital. The technique used at the hospital involved in the present study is CT.

The development of high-resolution peripheral quantitative CT (HR-pQCT), a novel high-resolution and low-radiation-dose technique, allows for the assessment of cortical and trabecular bone microarchitecture at the distal parts of the radius and tibia [25,26]. Recent research has shown that studying the fracture healing process of stable distal radial fractures [27,28] and scanning the scaphoid bone in patients with a clinically suspected scaphoid fracture are feasible with HR-pQCT [29]. We hypothesized that the use of HR-pQCT for patients with a clinically suspected scaphoid fracture would improve scaphoid fracture detection when compared with conventional CT in the clinical setting.

METHODS

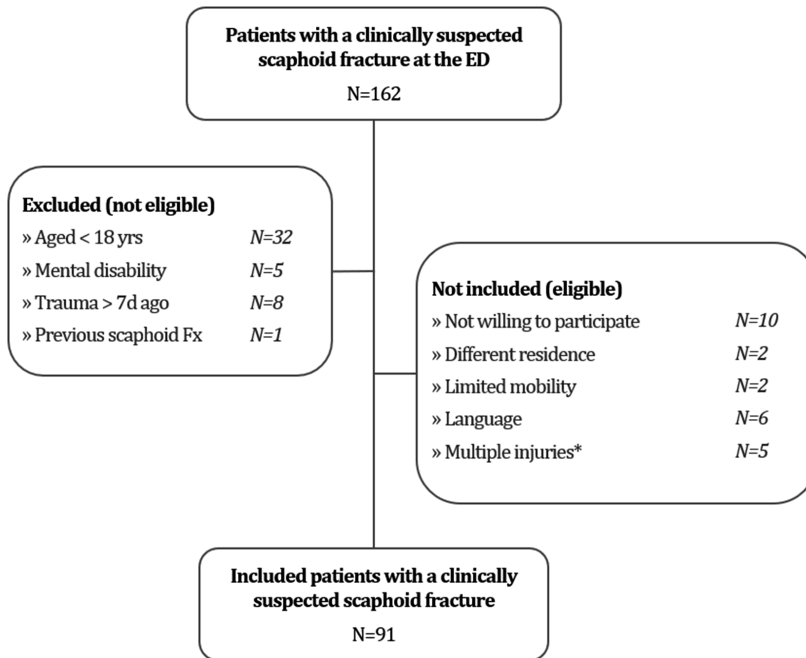
The present study was approved by the medical ethics committee (NL 62476.068.17) and was conducted according to the principles of the Declaration of Helsinki and in accordance with the Medical Research Involving Human Subjects Act (WMO).

Study population

For the present study, all patients with a clinically suspected scaphoid fracture presenting to the emergency department within 1 week after trauma were screened for eligibility. Pregnant women and patients with a previous ipsilateral scaphoid fracture were excluded. Between December 2017 and October 2018, a total of 91 patients ≥ 18 years of age were enrolled in our study (**Figure 1**). In the emergency department, conventional radiographs were made in 4 views: posteroanterior, true lateral, semipronated oblique, and posteroanterior with the wrist in ulnar deviation. Independent of the diagnosis on these initial radiographs, cast immobilization was applied until the definite diagnosis was obtained. All patients, regardless of the findings on the initial radiographs, received written information on the study from their treating physician in the emergency department and were, after granting permission, contacted by telephone within the next 4 days by the investigator to answer any remaining questions that they had regarding the study. CT and HR-pQCT were scheduled immediately following reassessment in the outpatient clinic. According to current clinical practice, this reassessment was performed within 7-14 days after trauma. Informed consent was obtained during this visit and was followed by physical examination, questionnaires, CT, and HR-pQCT. Medical history, smoking status, alcohol use, medication use, hand dominance, and trauma mechanism were registered.

CT scanning

CT of the affected forearm was performed with use of the SOMATOM Definition AS (Siemens). This scanner contains an 80-kW generator and Ultra-Fast Ceramics detector with a rotation time of 1 second (tube voltage, 120 kV; tube current range, 35 μ A; pitch, 0.6; 128 slices; slice thickness, 1.0 mm; slice increment, 0.5 mm). The effective radiation dose of 1 CT scan of the hand and wrist is 46 μ Sv. All scans were conducted with the wrist in a fiberglass cast. According to the local protocol, all scans were reconstructed in the transverse, coronal, and sagittal planes of the wrist. In cases in which no fracture was detected on the 3 conventional reconstructed planes, reconstruction in the plane of the scaphoid was obtained. CT images were uploaded into IMPAX Client software (AGFA).



Fx Fracture
* Concurrent Fx of the ipsilateral lower/upper arm

Figure 1. Flowchart illustrating inclusion and exclusion of patients with a clinically suspected scaphoid fracture at the emergency department (ED).

HR-pQCT scanning

Second-generation HR-pQCT (XtremeCT II; Scanco Medical AG, Switzerland) was used to scan the affected forearm. All scans were conducted with the wrist in a fiberglass cast with a detachable fiberglass cast around the thumb, which was only applied during the HR-pQCT procedure for added stability of the thumb. The forearm was placed into an anatomically shaped holder to obtain a standardized position. On the basis of a scout view, the region of interest was determined, and a reference line was placed on the rim at the joint surface of the distal part of the radius. The standard scan protocol of the distal part of the radius, with an isotropic voxel size of 0.061 mm, was adapted to 3 consecutive stacks of 10.2 mm, resulting in a scanned region of 30.6 mm to cover the entire scaphoid bone. The effective radiation dose of HR-pQCT scanning of the scaphoid is 15 μSv . The maximum dose to which patients were exposed was 30 μSv when repetition of the scan was necessary because of motion artifacts (grade 4-5) [30-33], which were graded according to the manufacturer's protocol and the method of Pialat *et al.* [32]. In the present study, all

scans were considered to be of acceptable quality for fracture assessment, including 3 scans that had grade 4 quality in only 1 of the 3 stacks. Scans were exported in Digital Imaging and Communications in Medicine (DICOM) format. Source images were reconstructed into transverse, coronal, and sagittal planes. All HR-pQCT images and reconstructions were anonymized and uploaded to the local workstation.

Scan evaluation

All CT scans were evaluated by a radiologist (within 48 hours) and a dedicated hand and wrist orthopaedic trauma surgeon (within 1 week); both were blinded to the other's assessment of the patients as well as to their clinical data. They were asked to state the type of fracture (*i.e.*, scaphoid, distal radial, carpal) on the basis of their expert opinion and to classify the scaphoid fracture, if present, according to the Herbert classification system (**Figure 2**) [34]. Additional assessment by a third investigator was used for scans with a discrepant judgment by the 2 observers ($n = 4$). The subsequent decision regarding diagnosis was based on majority assessment.

All HR-pQCT scans were evaluated by a musculoskeletal radiologist. In a previous study, the interobserver agreement for 4 observers (2 musculoskeletal radiologists and 2 orthopaedic trauma surgeons) was shown to be almost perfect regarding scaphoid fracture diagnosis with HR-pQCT in patients with a clinically suspected scaphoid fracture [35]. The observers evaluated each HR-pQCT scan independently and were asked to determine the presence of a scaphoid fracture or other fracture (*i.e.*, distal radial, carpal, metacarpal) on the basis of their expert opinion and to classify the scaphoid fracture, if present, according to the Herbert classification system (**Figure 2**) [34]. The observers were aware of the fact that all patients were clinically suspected of having a scaphoid fracture on the basis of physical examination in the emergency department. All observers were blinded to the diagnosis on conventional radiographs and CT and were not aware of the others' assessments. The observers did not have access to any clinical data on the patients.

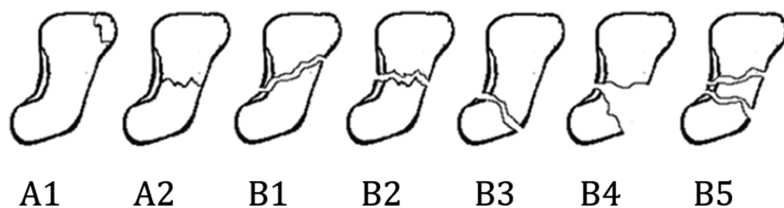


Figure 2. Illustrations depicting the Herbert scaphoid fracture classification system (1984) [34].

Statistical analysis

Statistical analysis was performed with use of SPSS Statistics (version 24; IBM). The distribution of the data was tested with Q-Q (quantile-quantile) plots and Kolmogorov-Smirnov analysis. Normally distributed data are presented as the mean and the standard deviation (SD). Age was non-normally distributed and therefore is presented as the median with the interquartile range (IQR). Chi-square and independent-sample *t* tests were used to analyze differences between patients with a fracture (scaphoid or other) and without a fracture. Crosstab calculation with McNemar testing was conducted to compare the proportions of scaphoid fractures diagnosed on CT and HR-pQCT. The correlation between scaphoid fracture classification and location with CT and HR-pQCT was estimated with use of the Kendall *W* statistic or coefficient of concordance (*W*); the closer to 1, the higher the correlation. Diagnostics performance characteristics were calculated with use of the MedCalc diagnostic test evaluation calculator and are presented as percentages with 95%-confidence intervals (95%-CIs). The level of significance was set at 0.05.

RESULTS

Patient characteristics

All patients were reassessed at the outpatient clinic within 14 days after presentation at the emergency department (median, 10 days; IQR, 6-14 days). The cohort consisted of 45 men and 46 women with a median age of 52 years (IQR, 29-67 years). Men were significantly younger compared with women (37 *versus* 62 years; $p < 0.001$). On CT, 15 patients with a median age of 41 years (IQR, 22-53 years) were diagnosed with a scaphoid fracture. On HR-pQCT, 24 patients with a median age of 44 years (IQR, 35-65 years) were diagnosed with a scaphoid fracture. The number and proportion of scaphoid fractures on CT and HR-pQCT according to sex and age are shown in **Table 1**.

Table 1. Distribution of scaphoid fracture incidence by sex and age group for CT and HR-pQCT diagnosis.

| | Scaphoid fracture (no. [%] of patients) | | | | Total |
|-------------------------|---|-------------|-------------|-----------|------------|
| | 18-29 years | 30-49 years | 50-69 years | 70+ years | |
| CT (n = 15) | | | | | |
| Men | 5 (33.3%) | 3 (20.0%) | 1 (6.7%) | 1 (6.7%) | 10 (66.7%) |
| Women | 1 (6.7%) | 2 (13.3%) | 1 (6.7%) | 1 (6.7%) | 5 (33.3%) |
| HR-pQCT (n = 24) | | | | | |
| Men | 7 (29.2%) | 5 (20.8%) | 2 (8.3%) | 1 (4.2%) | 15 (62.5%) |
| Women | 3 (12.5%) | 3 (12.5%) | 2 (8.3%) | 1 (4.2%) | 9 (37.5%) |

Data are presented as number (%).

Fracture diagnosis

In the entire cohort, 1 nondisplaced triquetral fracture was diagnosed on HR-pQCT but not on CT and 6 distal radial fractures were not diagnosed on HR-pQCT because of the restricted scanned region; those fractures were not registered as missed diagnoses.

Nine scaphoid fractures (37.5%) that were diagnosed with HR-pQCT were not diagnosed with CT, resulting in a significant difference in the proportion of patients with a scaphoid fracture on CT and HR-pQCT ($p = 0.004$) (**Figure 3**). **Figures 4 and 5** demonstrate the CT and HR-pQCT images for 2 patients with a scaphoid fracture that was detected on HR-pQCT but not on CT.

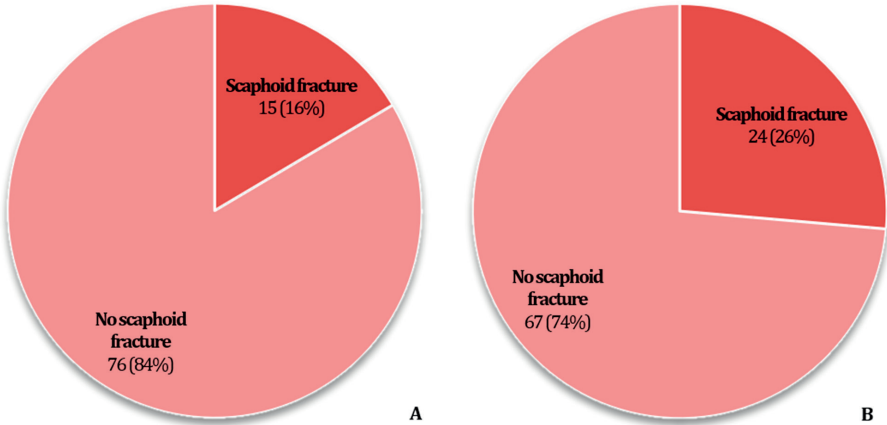


Figure 3. Pie charts showing the rates of scaphoid fracture on CT(A) and HR-pQCT (B) ($p = 0.004$).

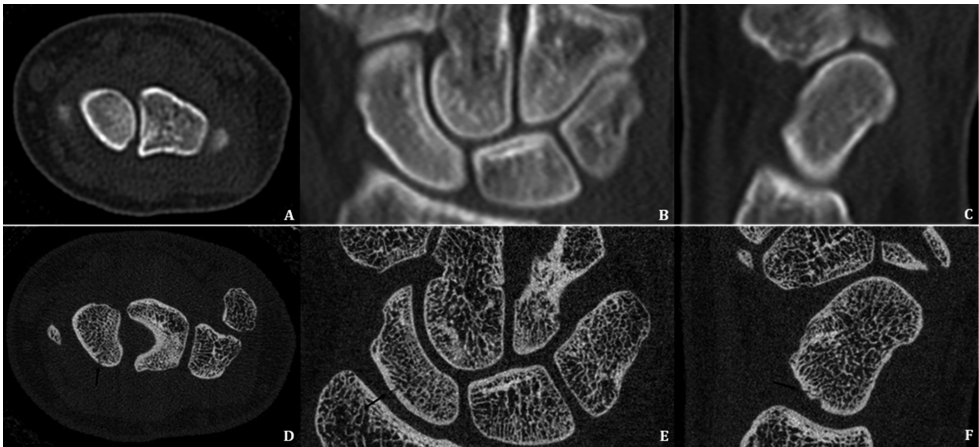


Figure 4. A 25-year-old woman with a type-B3 scaphoid fracture that was diagnosed on HR-pQCT scans. **A-C**) Transverse (**A**), coronal (**B**), and sagittal (**C**) CT slices that were negative for scaphoid fracture. **D-F**) Transverse (**D**), coronal (**E**), and sagittal (**F**) HR-pQCT scans that were positive for scaphoid fracture (arrows).

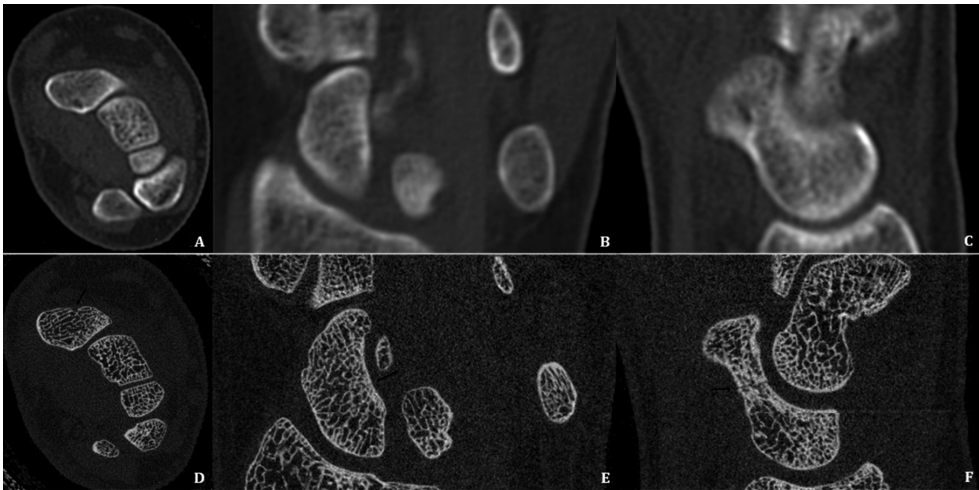


Figure 5. A 38-year-old woman with a type-A2 scaphoid fracture that was diagnosed on HR-pQCT scans. **A-C**) Transverse (**A**), coronal (**B**), and sagittal (**C**) CT slices that were negative for scaphoid fracture. **D-F**) Transverse (**D**), coronal (**E**), and sagittal (**F**) HR-pQCT scans that were positive for scaphoid fracture (arrows).

Two of the 9 patients in whom a scaphoid fracture was diagnosed on HR-pQCT only did not want to receive treatment as they experienced no discomfort as a result of the fracture and refused follow-up. The other 7 patients were managed with cast immobilization for at least 6 weeks, as were the patients in whom a scaphoid fracture was diagnosed on both CT and HR-pQCT. One of those 7 patients had a concurrent fracture of the hamate that was diagnosed on both CT and HR-pQCT.

There was no significant difference between men and women in terms of median age or between patients with and without a scaphoid fracture (on either CT or HR-pQCT) in terms of trauma mechanism (low-energy, high-energy, or sports/bicycle accidents).

Scaphoid fracture classification

The highest proportions of fracture types according to the Herbert classification system were type A1 on CT (40%) and type A2 on HR-pQCT (29%) (**Figures 6A and 6B**). The most common location was distal on CT (53%) and the scaphoid waist on HR-pQCT (46%) (**Figures 7A and 7B**). The correlation between CT and HR-pQCT was high for scaphoid fracture type ($W = 0.793$; 95%-CI, 0.57-0.91; $p < 0.001$) and very high for scaphoid fracture location ($W = 0.955$; 95%-CI, 0.90-0.98; $p < 0.001$). There was no significant difference between type-A and B fractures (as diagnosed on both CT and HR-pQCT) in terms of sex, age, or trauma mechanism (low-energy, high-energy, and sports/bicycle accidents).

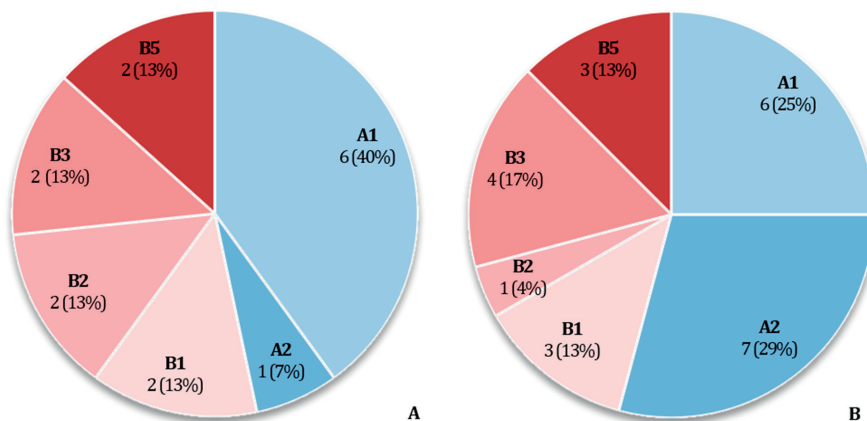


Figure 6. Pie chart showing the Herbert scaphoid fracture classification on CT (A) and HR-pQCT (B) ($W = 0.793$).

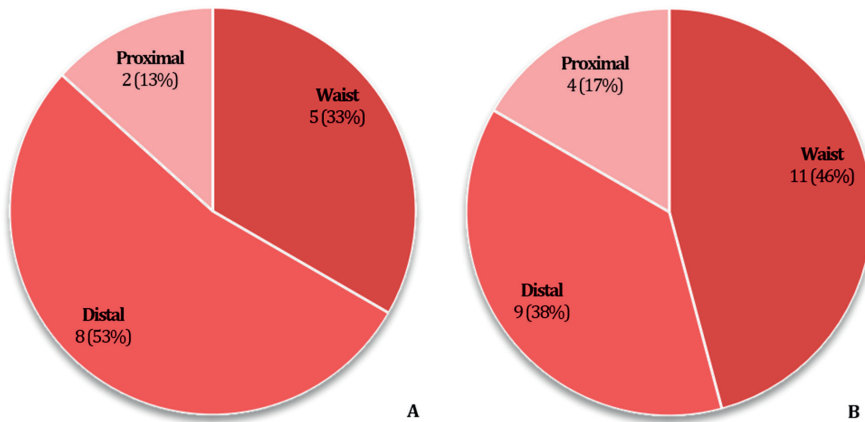


Figure 7. Pie chart showing the scaphoid fracture location assessment on CT (A) and HR-pQCT (B) ($W = 0.955$).

DISCUSSION

To our knowledge, the present study is the first clinical study comparing CT and HR-pQCT for the diagnosis of scaphoid fractures. Many studies examining the use of CT, MRI, and BS for the diagnosis of such fractures have demonstrated a wide variation in diagnostic performance [11,18,21,22,36]. This variation might be a result of the low incidence of scaphoid fractures and the use of different scanning protocols. MRI is an appropriate imaging technique to exclude a scaphoid fracture (specificity, 94-100%) [17,20,22,37,38]. However, MRI is time-consuming, has restricted availability in many hospitals, and is relatively expensive [16]. In contrast, CT is readily available and less expensive. A limitation of CT in diagnosing scaphoid fractures is its relatively low sensitivity compared with MRI and BS and the exposure of patients to radiation [11,18,21,36]. BS has high sensitivity but low specificity [17,21,22,37,38] and is invasive, is time-consuming, and leads to a delay in diagnosis of 3 to 5 days. Most studies have used an unreliable method - namely, repeated radiographs after 6 weeks [22,39-42] - as the reference standard [11,16-18]. The lack of a universal reference standard makes it difficult to compare the results of previous studies and contributes to the described variation.

Current clinical imaging techniques, as described above, lack the ability to assess bone microarchitecture and thereby separately assess cortical and trabecular bone. A noninvasive method that recently became available for the assessment of bone microarchitecture at the distal parts of the radius and tibia is HR-pQCT [43]. Validation and reproducibility studies of HR-pQCT have been performed extensively

for the distal part of the radius [44-47], and, in the last decade, widespread experience has been gathered in the use of this technique for clinical research [48,49]. It is conceivable that distinctions between vascular structures, motion artifacts, and fractures are more apparent with this method because of its higher resolution, which may help to improve scaphoid fracture diagnosis. In the present study, the HR-pQCT scan had to be repeated because of poor quality for only 5 patients, resulting in a mean radiation dose of 16 μ Sv per patient. This lower dose of HR-pQCT as compared with the dose of a CT-scan of the hand/wrist (16 compared with 46 μ Sv) can be explained by the fact that the length of the scanned region with HR-pQCT covers only 30.6 mm at the level of the scaphoid bone, whereas CT covers the scaphoid bone, the distal part of the radius, and all carpal bones. Accordingly, the effective radiation dose of HR-pQCT is very low compared with CT but can be interpreted as equal if the length of the scanned region is taken into account.

In previous studies, we found that HR-pQCT is a feasible and reliable technique for scaphoid fracture diagnosis [29], with “almost perfect” interobserver agreement (Fleiss kappa, 0.91) according to the guidelines by Landis and Koch [35]. In the present study, the number of patients diagnosed with a scaphoid fracture was 60% higher when using HR-pQCT as compared with CT.

In agreement with previous studies [8,50,51], our data showed male predominance and relatively young age in patients with scaphoid fractures. We found no difference in mechanism of injury between patients with a scaphoid fracture, with another type of fracture, and without a fracture in the present study. Regarding scaphoid fracture location, previous studies of adults have demonstrated that scaphoid waist fractures are the most common, inconsistently followed by proximal [4,33,52] and distal [53-55] fractures. In the present study, the most common fractures were type-A1 (tubercle) fractures based on CT and type-A2 fractures based on HR-pQCT (**Figures 6A and 6B**). This finding implies that HR-pQCT detects more clinically relevant fractures. As a result of the relatively small numbers, no hard conclusions can be drawn on this topic yet.

The present study is limited by the lack of a true reference standard; one of the important challenges in diagnosing scaphoid fractures is the development of such a standard. In the present study, we compared a novel technique (HR-pQCT) with an existing technique (CT) for scaphoid fracture detection and found that HR-pQCT detects scaphoid fractures that CT does not. These findings are promising but need to be replicated in other studies, and further research should address the clinical consequences of scaphoid fractures that are missed on CT and investigate the cost-effectiveness of HR-pQCT. Although the implementation of HR-pQCT is

achievable in daily practice as the scanning time for the scaphoid is only 6 minutes, HR-pQCT is currently used for research purposes and substantial processing time is required. In our facility, the costs of an HR-pQCT scan are roughly 3 times higher than the costs of a regular CT-scan. On the basis of current developments related to high-resolution scanners, standard protocols for scanning the scaphoid bone will be developed and image processing and analysis time will most likely be reduced in the near future. The availability of HR-pQCT scanners worldwide remains a limitation. Another limitation of our study is the lack of assessment of intraobserver variability as the observers only assessed the scans once. The present study is strengthened by the relatively large cohort of patients with a clinically suspected scaphoid fracture. Moreover, all included patients underwent both CT and HR-pQCT on the same day.

In conclusion, scaphoid fracture detection is superior with HR-pQCT in comparison with CT. The number of patients with a diagnosed scaphoid fracture was 60% higher when using HR-pQCT as compared with CT. HR-pQCT could be a promising new application for the detection of scaphoid fractures.

REFERENCES

- [1] Tiel-van Buul MM, van Beek EJ, Broekhuizen AH, Bakker AJ, Bos KE, van Royen EA. Radiography and scintigraphy of suspected scaphoid fracture. A long-term study in 160 patients. *J Bone Joint Surg Br.* 1993;75(1):61-65.
- [2] Beeres FJ, Rhemrev SJ, Hogervorst M, den Hollander P, Jukema GN. [Scaphoid fractures: diagnosis and therapy]. *Ned Tijdschr Geneeskd.* 2007;31;151(13):742-747. Dutch.
- [3] van der Molen AB, Groothoff JW, Visser GJ, Robinson PH, Eisma WH. Time off work due to scaphoid fractures and other carpal injuries in the Netherlands in the period 1990 to 1993. *J Hand Surg Br.* 1999;24(2):193-198.
- [4] Kozin SH. Incidence, mechanism, and natural history of scaphoid fractures. *Hand Clin.* 2001;17(4):515-524.
- [5] Taljanovic MS, Karantanas A, Griffith JF, DeSilva GL, Rieke JD, Sheppard JE. Imaging and treatment of scaphoid fractures and their complications. *Semin Musculoskelet Radiol.* 2012;16(2):159-73. Epub 2012 May 30.
- [6] Divelbiss BJ, Adams BD. Electrical and ultrasound stimulation for scaphoid fractures. *Hand Clin.* 2001;17(4):697-701, x-xi.
- [7] Dias JJ, Singh HP. Displaced fracture of the waist of the scaphoid. *J Bone Joint Surg Br.* 2011;93(11):1433-1439.
- [8] Jenkins PJ, Slade K, Huntley JS, Robinson CM. A comparative analysis of the accuracy, diagnostic uncertainty and cost of imaging modalities in suspected scaphoid fractures. *Injury.* 2008;39(7):768-774. Epub 2008 Jun 9.
- [9] Cheung GC, Lever CJ, Morris AD. X-ray diagnosis of acute scaphoid fractures. *J Hand Surg Br.* 2006;31(1):104-109. Epub 2005 Oct 28.
- [10] Lozano-Caldero'n S, Blazar P, Zurakowski D, Lee SG, Ring D. Diagnosis of scaphoid fracture displacement with radiography and computed tomography. *J Bone Joint Surg Am.* 2006;88(12):2695-2703.
- [11] Mallee WH, Wang J, Poolman RW, Kloen P, Maas M, de Vet HC, Doornberg JN. Computed tomography versus magnetic resonance imaging versus bone scintigraphy for clinically suspected scaphoid fractures in patients with negative plain radiographs. *Cochrane Database Syst Rev.* 2015 Jun 5;6:CD010023.
- [12] Adey L, Souer JS, Lozano-Calderon S, Palmer W, Lee SG, Ring D. Computed tomography of suspected scaphoid fractures. *J Hand Surg Am.* 2007;32(1): 61-66.
- [13] Ring D, Lozano-Calderón S. Imaging for suspected scaphoid fracture. *J Hand Surg Am.* 2008;33(6):954-957.
- [14] Rhemrev SJ, Beeres FJ, van Leerdam RH, Hogervorst M, Ring D. Clinical prediction rule for suspected scaphoid fractures: a prospective cohort study. *Injury.* 2010;41(10):1026-1030.
- [15] Karl JW, Swart E, Strauch RJ. Diagnosis of occult scaphoid fractures: a cost-effectiveness analysis. *J Bone Joint Surg Am.* 2015 18;97(22):1860-1868.
- [16] Memarsadeghi M, Breitenseher MJ, Schaefer-Prokop C, Weber M, Aldrian S, Gäbler C, Prokop M. Occult scaphoid fractures: comparison of multidetector CT and MR imaging—initial experience. *Radiology.* 2006;240(1):169-176.
- [17] de Zwart AD, Beeres FJ, Rhemrev SJ, Bartlema K, Schipper IB. Comparison of MRI, CT and bone scintigraphy for suspected scaphoid fractures. *Eur J Trauma Emerg Surg.* 2016;42(6):725-731. Epub 2015 Nov 10.

- [18] Buijze GA, Jørgsholm P, Thomsen NO, Bjorkman A, Besjakov J, Ring D. Diagnostic performance of radiographs and computed tomography for displacement and instability of acute scaphoid waist fractures. *J Bone Joint Surg Am.* 2012 Nov 7; 94(21):1967-1974.
- [19] Rhemrev SJ, Ootes D, Beeres FJ, Meylaerts SA, Schipper IB. Current methods of diagnosis and treatment of scaphoid fractures. *Int J Emerg Med.* 2011 Feb 4;4:4.
- [20] De Zwart AD, Beeres FJ, Ring D, Kingma LM, Coerkamp EG, Meylaerts SA, Rhemrev SJ. MRI as a reference standard for suspected scaphoid fractures. *Br J Radiol.* 2012;85(1016):1098-1101.
- [21] Rhemrev SJ, de Zwart AD, Kingma LM, Meylaerts SA, Arndt JW, Schipper IB, Beeres FJ. Early computed tomography compared with bone scintigraphy in suspected scaphoid fractures. *Clin Nucl Med.* 2010;35(12):931-934.
- [22] Yin ZG, Zhang JB, Kan SL, Wang XG. Diagnosing suspected scaphoid fractures: a systematic review and meta-analysis. *Clin Orthop Relat Res.* 2010;468(3):723-734. Epub 2009 Sep 15.
- [23] Gemme S, Tubbs R. What physical examination findings and diagnostic imaging modalities are most useful in the diagnosis of scaphoid fractures? *Ann Emerg Med.* 2015;65(3):308-309. Epub 2014 Dec 2.
- [24] Carpenter CR, Pines JM, Schuur JD, Muir M, Calfee RP, Raja AS. Adult scaphoid fracture. *Acad Emerg Med.* 2014;21(2):101-121.
- [25] Link TM. Osteoporosis imaging: state of the art and advanced imaging. *Radiology.* 2012;263(1):3-17.
- [26] Burghardt AJ, Krug R, Majumdar S. High-resolution imaging techniques for bone quality assessment. In: Feldman D, Pike JW, Bouillon R, Giovannucci E, Goltzman D, Hewison M, eds, Vitamin D. 4th ed. Academic Press; 2018:1007-1041.
- [27] de Jong JJA, Arts JJC, Willems PC, Bours SPG, Bons JPA, Menheere PPCA, van Rietbergen B, Geusens PP, van den Bergh JPW. Contra-lateral bone loss at the distal radius in postmenopausal women after a distal radius fracture: a two-year follow-up HRpQCT study. *Bone.* 2017;101:245-251. Epub 2017 May 11.
- [28] de Jong JJA, Heyer FL, Arts JJC, Poeze M, Keszei AP, Willems PC, van Rietbergen B, Geusens PP, van den Bergh JPW. Fracture repair in the distal radius in postmenopausal women: a follow-up 2 years postfracture using HRpQCT. *J Bone Miner Res.* 2016;31(5):1114-1122. Epub 2016 Jan 5.
- [29] Bevers MSAM, Daniels AM, Wyers CE, van Rietbergen B, Geusens PPMM, Kaarsemaker S, Janzing HMJ, Hannemann PFW, Poeze M, van den Bergh JPW. The feasibility of high-resolution peripheral quantitative computed tomography (HR-pQCT) in patients with suspected scaphoid fractures. *J Clin Densitom.* 2019;23(3):432-442.
- [30] Pichler W, Windisch G, Schaffler G, Heidari N, Dorr K, Grechenig W. Computer-assisted 3-dimensional anthropometry of the scaphoid. *Orthopedics.* 2010;33(2):85-88.
- [31] Manske SL, Zhu Y, Sandino C, Boyd SK. Human trabecular bone micro-architecture can be assessed independently of density with second generation HR-pQCT. *Bone.* 2015;79:213-221. Epub 2015 Jun 14.
- [32] Pialat JB, Burghardt AJ, Sode M, Link TM, Majumdar S. Visual grading of motion induced image degradation in high resolution peripheral computed tomography: impact of image quality on measures of bone density and micro-architecture. *Bone.* 2012;50(1):111-118. Epub 2011 Oct 13.
- [33] Luria S, Schwarcz Y, Wollstein R, Emelife P, Zinger G, Peleg E. 3-dimensional analysis of scaphoid fracture angle morphology. *J Hand Surg Am.* 2015;40(3):508-514. Epub 2015 Jan 9.
- [34] Herbert TJ, Fisher WE. Management of the fractured scaphoid using a new bone screw. *J Bone Joint Surg Br.* 1984;66(1):114-123.
- [35] Daniels AM, Wyers CE, Janzing HMJ, Sassen S, Loeffen D, Kaarsemaker S, van Rietbergen B, Hannemann PFW, Poeze M, van den Bergh JP. The interobserver reliability of the diagnosis and

- classification of scaphoid fractures using high-resolution peripheral quantitative CT. *Bone Joint J.* 2020;102-B(4):478-484.
- [36] Ilica AT, Ozyurek S, Kose O, Durusu M. Diagnostic accuracy of multidetector computed tomography for patients with suspected scaphoid fractures and negative radiographic examinations. *Jpn J Radiol.* 2011;29(2):98-103. Epub 2011 Feb 27.
- [37] Beeres FJ, Rhemrev SJ, den Hollander P, Kingma LM, Meylaerts SA, le Cessie S, Bartlema KA, Hamming JF, Hogervorst M. Early magnetic resonance imaging compared with bone scintigraphy in suspected scaphoid fractures. *J Bone Joint Surg Br.* 2008;90(9):1205-1209.
- [38] Buijze GA, Mallee WH, Beeres FJ, Hanson TE, Johnson WO, Ring D. Diagnostic performance tests for suspected scaphoid fractures differ with conventional and latent class analysis. *Clin Orthop Relat Res.* 2011;469(12):3400-3407. Epub 2011 Sep 30.
- [39] Low G, Raby N. Can follow-up radiography for acute scaphoid fracture still be considered a valid investigation? *Clin Radiol.* 2005;60(10):1106-1110.
- [40] Munk B, Frøkjaer J, Larsen CF, Johannsen HG, Rasmussen LL, Edal A, Rasmussen LD. Diagnosis of scaphoid fractures. A prospective multicenter study of 1,052 patients with 160 fractures. *Acta Orthop Scand.* 1995;66(4):359-360.
- [41] Tiel-van Buul MM, van Beek EJ, Broekhuizen AH, Nooitgedacht EA, Davids PH, Bakker AJ. Diagnosing scaphoid fractures: radiographs cannot be used as a gold standard! *Injury.* 1992;23(2):77-79.
- [42] Jacobsen S, Hassani G, Hansen D, Christensen O. Suspected scaphoid fractures. Can we avoid overkill? *Acta Orthop Belg.* 1995;61(2):74-78.
- [43] Müller R, Hahn M, Vogel M, Dellling G, Ruegsegger P. Morphometric analysis of noninvasively assessed bone biopsies: comparison of high-resolution computed tomography and histologic sections. *Bone.* 1996;18(3):215-220.
- [44] Pistoia W, van Rietbergen B, Lochmuller EM, Lill CA, Eckstein F, Ruegsegger P. Image-based micro-finite-element modeling for improved distal radius strength diagnosis: moving from bench to bedside. *J Clin Densitom.* 2004;7(2):153-160.
- [45] Macneil JA, Boyd SK. Bone strength at the distal radius can be estimated from high-resolution peripheral quantitative computed tomography and the finite element method. *Bone.* 2008;42(6):1203-1213. Epub 2008 Feb 13.
- [46] Varga P, Pahr DH, Baumbach S, Zysset PK. HR-pQCT based FE analysis of the most distal radius section provides an improved prediction of Colles' fracture load in vitro. *Bone.* 2010;47(5):982-988. Epub 2010 Aug 6.
- [47] Mueller TL, Christen D, Sandercott S, Boyd SK, van Rietbergen B, Eckstein F, Lochmuller EM, Muller R, van Lenthe GH. Computational finite element bone mechanics accurately predicts mechanical competence in the human radius of an elderly population. *Bone.* 2011 Jun 1;48(6):1232-1238. Epub 2011 Mar 2.
- [48] van Rietbergen B, Ito K. A survey of micro-finite element analysis for clinical assessment of bone strength: the first decade. *J Biomech.* 2015 Mar 18;48(5):832-841. Epub 2014 Dec 18.
- [49] de Jong JJ, Willems PC, Arts JJ, Bours SG, Brink PR, van Geel TA, Poeze M, Geusens PP, van Rietbergen B, van den Bergh JP. Assessment of the healing process in distal radius fractures by high resolution peripheral quantitative computed tomography. *Bone.* 2014;64:65-74. Epub 2014 Apr 2.
- [50] Van Tassel DC, Owens BD, Wolf JM. Incidence estimates and demographics of scaphoid fracture in the U.S. population. *J Hand Surg Am.* 2010;35(8):1242-1245.
- [51] Böhler L, Trojan E, Jahna H. The results of treatment of 734 fresh, simple fractures of the scaphoid. *J Hand Surg Br.* 2003;28(4):319-331.

- [52] Schaefer M, Siebert HR. [Fracture of the semilunar bone]. *Unfallchirurg*. 2002;105(6):540-552; quiz 52-3. German.
- [53] Brøndum V, Larsen CF, Skov O. Fracture of the carpal scaphoid: frequency and distribution in a well-defined population. *Eur J Radiol*. 1992;15(2):118-122.
- [54] Dias J, Kantharuban S. Treatment of scaphoid fractures: European approaches. *Hand Clin*. 2017;33(3):501-509.
- [55] Dias JJ, Wildin CJ, Bhowal B, Thompson JR. Should acute scaphoid fractures be fixed? A randomized controlled trial. *J Bone Joint Surg Am*. 2005; 87(10):2160-2168.



9

Chapter 9

Association between bone shape and the presence of a fracture in patients with a clinically suspected scaphoid fracture

Melissa S.A.M. Bevers, Caroline E. Wyers, Anne M. Daniels, Emmanuel A. Audenaert, Sander M.J. van Kuijk, Bert van Rietbergen, Piet P.M.M. Geusens, Sjoerd Kaarsemaker, Heinrich M.J. Janzing, Pascal F.W. Hannemann, Martijn Poeze, Joop P. van den Bergh

ABSTRACT

Scaphoid fractures are difficult to diagnose with current imaging modalities. It is unknown whether the shape of the scaphoid bone, assessed by statistical shape modeling, can be used to differentiate between fractured and non-fractured bones. Therefore, the aim of this study was to investigate whether the presence of a scaphoid fracture is associated with shape modes of a statistical shape model (SSM). Forty-one high-resolution peripheral quantitative computed tomography (HR-pQCT) scans were available from patients with a clinically suspected scaphoid fracture of whom 15 patients had a scaphoid fracture. The scans showed no motion artefacts affecting bone shape. The scaphoid bones were semi-automatically contoured, and the contours were converted to triangular meshes. The meshes were registered, followed by principal component analysis to determine mean shape and shape modes describing shape variance. The first five out of the forty shape modes cumulatively explained 87.8% of the shape variance. Logistic regression analysis was used to study the association between shape modes and fracture presence. The regression models were used to classify the 41 scaphoid bones as fractured or non-fractured using a cut-off value that maximized the sum of sensitivity and specificity. The classification of the models was compared with fracture diagnosis on HR-pQCT. A regression model with four shape modes had an area under the ROC-curve of 72.3% and correctly classified 75.6% of the scaphoid bones (fractured: 60.0%, non-fractured: 84.6%). To conclude, fracture presence in patients with a clinically suspected scaphoid fracture appears to be associated with the shape of the scaphoid bone.

INTRODUCTION

Scaphoid fractures are the most common carpal bone fractures, and they are difficult to diagnose. These fractures account for 60-75% of all carpal bone fractures and predominantly occur in a young and active male population [1-4]. Unnecessary treatment is frequent due to, amongst other reasons, a high false-positive rate with currently used imaging modalities [5]. Simultaneously, 10-30% of scaphoid fractures remains occult with initial radiography, and the lack of a gold standard modality does not exclude that scaphoid fractures remain occult at follow-up [6-12]. There is thus a clear need for an improved diagnosis of scaphoid fractures, and, possibly, identifying factors associated with scaphoid fracture presence may help.

The shape of the scaphoid bone could possibly be such factor. Scaphoid fractures are typically caused by a fall on the outstretched hand with the wrist hyperextended and radially loaded [1,4,13]. In maximum extension, external forces become concentrated at the proximal and distal pole of the scaphoid bone (**Figure 1A**) [13,14]. The forces at the proximal pole stabilize the proximal part of the scaphoid bone together with wrist ligaments between the distal radius and capitate bone, whereas the forces at the distal pole cause a bending moment due to an offset in the force line of action and the curved shape of the scaphoid bone (**Figure 1B**) [13,14]. An excessive bending moment can successively cause a scaphoid fracture, especially at the proximal pole or waist. The shape of the scaphoid bone may play a role in fracture susceptibility after such fall and subsequent loading condition due to its possible influence on bone strength (*e.g.* a thinner and more curved shaped bone may withstand lower bending moments) and on wrist kinematics and loading distributions (*e.g.* by its complex interaction with the surrounding carpal bones and distal radius). Consequently, an association between scaphoid bone shape and the presence of a fracture is possible, also given the variation in anatomy [15], but has not been studied yet.

A reason for this gap may be the complexity to quantify the shape of the scaphoid bone. Attempts to characterize the shape are limited to simplified measures (*e.g.* length, width, presence of specific landmarks) that do not adequately describe the complex three-dimensional shape of the bone [16,17]. Statistical shape models (SSMs) allow description of a mean shape and shape variation in three dimensions and independent of anatomical landmarks. Previously, scaphoid SSMs have been constructed from radiographs or computed tomography (CT) images and aimed to describe interindividual shape variation, segment individual carpal bones, and investigate skeletal maturity and wrist motion patterns [15,18-21]. No scaphoid SSMs have been constructed to study the shape of both fractured and non-fractured scaphoid bones. Therefore, the aim of this study was to investigate whether SSM-based shape

parameters are associated with fracture presence in patients with a clinically suspected scaphoid fracture. A SSM was constructed from a small set of scans obtained with high-resolution peripheral quantitative CT (HR-pQCT), which we have previously found to allow acquisition of scans of good image quality in patients with a suspected scaphoid fracture and to allow diagnosis of scaphoid fractures with good interobserver agreement and with reveal of fractures that were missed with conventional CT [22-24].

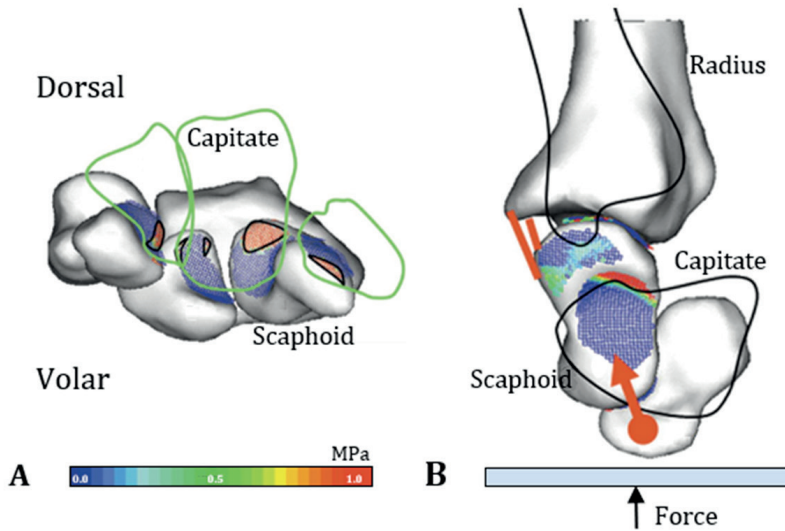


Figure 1. Wrist mechanics in maximum extension showing **A)** the concentration of forces on the proximal and distal pole of the scaphoid bone, and **B)** the consequent stabilization of the proximal pole of the scaphoid bone between the distal radius and capitate bone and the force at the distal pole (red arrow) that can cause a bending moment on the scaphoid bone. Adapted from Majima et al., 2008, with permission from Elsevier.

METHODS

Dataset

HR-pQCT imaging was performed of the scaphoid bone in 91 adult male and female patients who consecutively presented at the emergency department of VieCuri Medical Center (Venlo, The Netherlands) with a suspected scaphoid fracture. Study design and population have previously been described in detail [22-24]. Briefly, according to the hospital's clinical practice, the patients received conventional plain radiographs at initial presentation, followed by immobilization of the wrist in a polyester cast until follow-up due to suspicion of a scaphoid fracture. At follow-up within 7-10 days after initial presentation, physical re-examination was performed. After written informed

consent, the patients underwent HR-pQCT imaging of the scaphoid bone. The HR-pQCT scan (XtremeCT II, Scanco Medical AG, Brüttisellen, Switzerland) constituted a 30.6-mm region (three consecutive stacks) of the wrist covering the entire scaphoid bone. During image acquisition, the wrist was immobilized in the polyester cast with additional removable thumb part for thumb stability and was placed in a standard motion restraining holder. The scans were reconstructed with an isotropic voxel size of 61 μm . Scan quality was evaluated *post hoc* by applying the clinically used grading system for HR-pQCT scans to multiple full-resolution slices of the scans to grade the quality of each stack of a scan [22].

Only scans with three good-quality stacks were used to construct the SSM (Figure 2) as motion artefacts in poor-quality scans could affect bone shape. Sixty-one of the 91 scans were of good quality of which 19 scans were of fractured scaphoid bones and 42 of non-fractured scaphoid bones based on diagnosis on HR-pQCT by an experienced radiologist. Four of the 19 scans with a scaphoid fracture were excluded because of fracture-related discontinuities visible in the bone surface (*e.g.* fracture displacements). Nine of the 42 scans without scaphoid fracture were excluded because of stack shifts affecting the shape of the bone surface and seven others because of bone spurs and cysts. In total, 41 scans were used for SSM construction, 15 of which were of fractured scaphoid bones and 26 of non-fractured scaphoid bones.

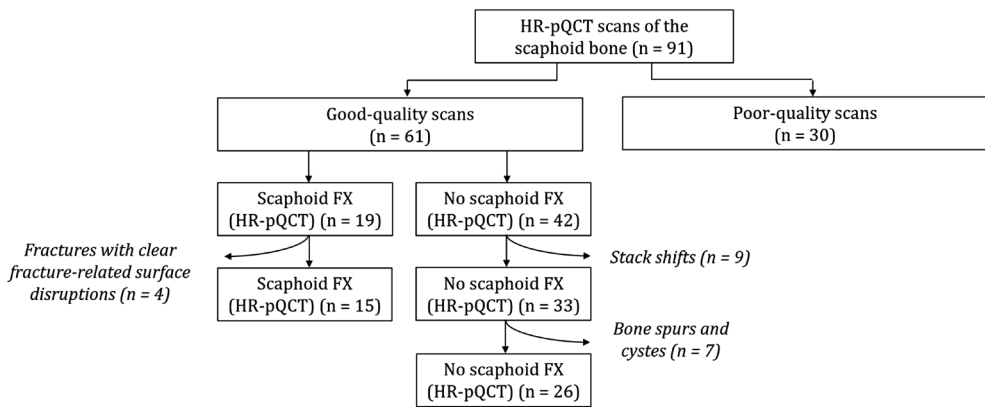


Figure 2. Flowchart of the high-resolution peripheral quantitative computed tomography (HR-pQCT) scans of scaphoid bones diagnosed as fractured or non-fractured on HR-pQCT used to construct a statistical shape model. FX represents fracture.

SSM construction

Contouring and meshing

The scaphoid bones on the HR-pQCT scans were contoured and subsequently meshed prior to SSM construction. The contouring has been described earlier [22]. Briefly, coarse pre-contours were drawn by hand, which were used as starting point for an automatic contouring algorithm that has originally been designed for the radius and tibia and is provided by the manufacturer of the scanner. If necessary, the contours were manually corrected when visually deviating from the outer bone margins to remove any spurs or other erroneous irregularities in the contours. The final contours were converted to three-dimensional masks (Mimics Research 18.0, Materialise NV, Heverlee, Belgium), which in turn were converted to triangular surface meshes with a maximum triangular edge length of 0.5 mm (3-Matic Research 10.0, Materialise NV, Heverlee, Belgium). The meshes were smoothed in MATLAB (Version R2019b, The MathWorks Inc. USA) using Taubin's non-shrinking surface smoothing [25]. To determine the interobserver variability of the contouring process, a subset of eight scans was also contoured by a second investigator following the same procedure. The median of the mean and maximum distance between the contours of this subset were 0.004 mm and 0.245 mm, respectively.

Mesh registration

The smoothed meshes were registered using a publicly available MATLAB-algorithm [26] that has been described in mathematical detail earlier [27]. Briefly, one mesh was randomly selected as template mesh (*source*) to which the other meshes (*targets*) were rigidly and subsequently non-rigidly registered. Rigid registration consisted of a pre-alignment of *target* and *source* according to their principal axes of inertia, which was successively optimized using an adapted rigid iterative closest point (ICP-) approach that minimized the distance between bidirectional point correspondences of *target* and *source* [27,28]. The ~5% largest distances were excluded to overcome unnatural registrations. The original algorithm was expanded with a visual inspection of the pre-alignment and subsequent correction if needed due to the possible lack of clear principal axes in the scaphoid bones. The remaining distances were further minimized by a non-rigid transformation function that was iteratively optimized. The optimized transformation function was refined by an iteratively optimized weighted locally rigid deformation that was applied to the entire mesh to finalize the registration.

SSM construction

The registered meshes were used to construct and optimize the SSM using a publicly available MATLAB-code [29]. Generalized Procrustes alignment was used to align all meshes, followed by principal component analysis (PCA) to describe the statistical mean shape and shape variance among the aligned meshes by forty (*i.e.* the number

of meshes minus one) independent shape modes. The SSM was optimized by using the initial SSM as *a priori* information for the construction of a new SSM. For this purpose, the initial SSM plus its first shape mode were fitted to all original meshes (*i.e.* both *targets* and *source*) to predict the shape of these meshes. Only the first mode was used for this prediction as it explains the largest shape variance among the scaphoid bones. The predicted meshes were then used as individual template meshes to which corresponding original meshes were registered and subsequently used to construct a new SSM, both using the above described algorithms. By replacing the initially used *source* mesh with the individual template meshes, possible bias due to using one randomly selected mesh as *source* was removed, and the proportion of variance explained by each shape mode was increased.

Model accuracy

Accuracy of the optimized SSM was quantified. Each registered mesh was aligned with the SSM excluding ~5% of the mesh points with the largest distances, and root-mean-squared errors (RMSEs) were calculated of the remaining distances between the mesh points of the aligned mesh and the SSM. The RMSEs of each mesh were averaged to determine a mean RMSE per mesh, which were averaged to determine an overall RMSE. The number of shape modes included in the SSM for alignment was varied from one to all forty, and an overall RMSE was computed for each number of modes included.

Statistical analysis

All statistical analyses were performed in R (R Foundation for Statistical Computing, Version R-3.6.2 for Windows, Vienna, Austria). Mann-Whitney U tests and Chi-Square tests were used to determine the significance of age- and gender-differences between patients with and without a fracture. Logistic regression models were constructed with shape modes as predictor variable and fracture presence as dependent variable to investigate the association between fracture presence and shape modes. The shape modes are orthogonal and statistically independent due to the mathematical nature of PCA, so multiple shape modes could be combined in one regression model. Forward stepwise selection using the Wald-test was used to select the modes to include, selecting from only those modes that cumulatively explained $\geq 95\%$ of the shape variance. Bootstrapping was performed with one-thousand repetitions to internally validate the regression model and to prevent overestimation of the model performance. The shrinkage factor resulting from the bootstrapping was used to shrink the regression coefficients of the original regression model to account for potential overfitting. The final regression model consisted of the shrunk coefficients and a re-estimated intercept and satisfied a perfect calibration-in-the-large (*i.e.* agreement between actual fracture proportion in the dataset and mean fracture probabilities predicted by the regression model). Similarly, regression

models were constructed with the same selected shape modes and age or gender. Finally, regression models with only age or gender were constructed.

The models were used to classify the 41 scaphoid bones as fractured or non-fractured. Youden's Index J ($J = \text{sensitivity} + \text{specificity} - 1$) was determined for various cut-off values for the fracture probability, and the optimal cut-off value was defined as the value with the highest J (**Supplementary Material 1**). The optimal cut-off value, rounded to the nearest 0.05, was used for the classification, which was compared to the diagnosis on HR-pQCT. Sensitivity, specificity, and accuracy were computed including 95% Clopper-Pearson intervals [30]. Positive and negative predictive values (PPV and NPV, respectively) were computed including standard logit 95%-confidence intervals [31], and also area under the receiver operator characteristic (ROC-) curve (AUC) was calculated. To compute accuracy, PPV, and NPV, the true fracture rate was set to that of the entire dataset (*i.e.* 24 of 91; 26%). Akaike information criterion (AIC) was determined for the regression models to compare the quality of each regression model.

RESULTS

The patient characteristics are outlined in **Table 1**. Age was not significantly different between the patients with and without a scaphoid fracture, and also gender was evenly distributed among the two groups. The proportion of patients with a high-impact fall was not significantly different between those with and those without a scaphoid fracture. According to Herbert's classification system, the included fracture types constituted types A1 (5x), A2 (4x), B1 (2x), B2 (1x), and B3 (3x) based on the diagnosis on HR-pQCT by an experienced radiologist [32].

Table 1. Demographics of the patients with and without a scaphoid fracture.

| Demographic | Scaphoid fracture ($n = 15$) | No scaphoid fracture ($n = 26$) | p -value |
|------------------|--------------------------------|-----------------------------------|------------|
| Male gender | 7 (46.7) | 13 (50.0) | 0.837 |
| Age [years] | 38 (28.0) | 47 (38.3) | 0.129 |
| High-impact fall | 11 (73.3) | 15 (57.7) | 0.317 |

Data are presented as number (%) or median (IQR).

SSM description

The first shape mode predominantly described the variance in bone size and explained 72.1% of the total shape variance (**Figure 3A**). The second and third mode explained an additional 6.3% and 4.2%, respectively of the shape variance with respect to their

previous modes, and the first five modes cumulatively explained 87.8% of the shape variance. The shape variance described by these first five modes is visualized in **Figure 4A**. The first 13 modes explained 95.3% of the shape variance, and the additional shape variance explained by the next modes was $< 0.5\%$ with respect to their previous modes.

The accuracy of the SSM increased with the number of modes included (**Figure 3B**). The RMSE was 0.48 ± 0.17 mm when only the first mode was included and decreased to 0.19 ± 0.036 mm when the first 13 modes were included. It approached zero when all forty modes were included (0.0035 ± 0.00027 mm). The distance between the original included scaphoid bones and their estimated shape from the SSM was largest at the dorsal boundary of the facet articulating with the capitate bone (**Figure 3B**).

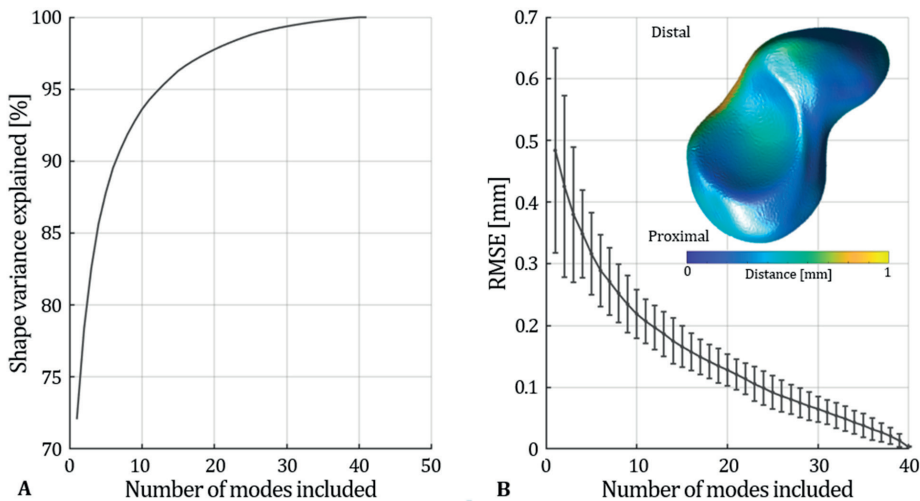


Figure 3. A) Compactness, and B) accuracy of the statistical shape model of the scaphoid bone based on 41 high-resolution peripheral quantitative computed tomography scans of fractured and non-fractured scaphoid bones. The inserted image in (B) shows a colormap of the average distance between the included scaphoid bones and their estimated shape from the statistical shape model. RMSE is root-mean-squared error.

Classification performance

The first 13 shape modes were pre-selected for the construction of logistic regression models because they together explained $\geq 95\%$ (95.3%) of the shape variance, and the forward selection procedure selected four of these modes (modes #13, #8, #7, #3). The first of these modes (mode #13) was significantly different between the fractured and non-fractured scaphoid bones (**Figure 4B**), but it explained $< 1\%$ of the shape variance among the included bones. A regression model with the four selected shape modes had a significant OR of 8.25 and an AUC of 72.3%, which were both considerably

higher compared to regression models with age or gender as predictor variable (**Table 2; Figure 5**). Also the proportion of correctly classified bones (75.6%) was considerably higher for this model compared to the regression models with age or gender. With an optimal cut-off of 0.45, specificity and NPV were $> 80\%$ (**Table 3**). Accounting for age or gender considerably increased the OR of the regression model with the four modes. Accounting for age also increased the AUC due to a higher sensitivity and specificity for sensitivities $> 75\%$. The proportion of correctly classified bones increased slightly (**Table 2; Figure 5**). Accounting for gender did not change the AUC but slightly increased the proportion of correctly classified bones due to an increased proportion of correctly classified non-fractured scaphoid bones (**Table 2; Figure 5**).

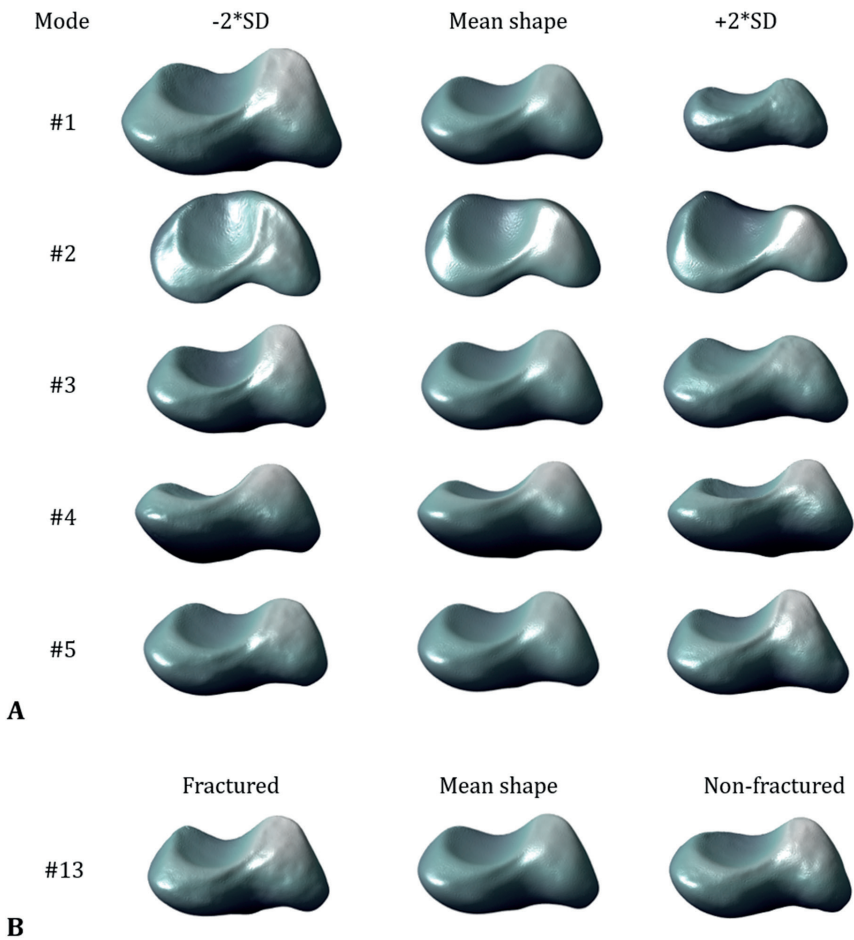


Figure 4. **A)** The first five shape modes of the statistical shape model that cumulatively explained 87.8% of the shape variation among the 41 scaphoid bones used to construct the model. Mean shape and ± 2 times the standard deviation (SD) of the modes are visualized. **B)** Shape variance explained by the thirteenth shape mode of the statistical shape model that was significantly different between the fractured and non-fractured scaphoid bones.

Table 2. Characteristics of five logistic regression models with scaphoid fracture presence as dependent variable.

| Regression model predictor(s) | AIC [-] | AUC [%] | Optimal cut-off [-] | OR (95%-CI) [-] | Correct classification [- (%)] | |
|-------------------------------------|------------|------------|------------------------|--------------------|-----------------------------------|-------------------------|
| | | | | | Fracture (n = 15) | No fracture (n = 26) |
| Age (1 yr.) | 53.3 | 66.4 | 0.25 | 5.57 (1.04-29.8)* | 13 (86.7) | 12 (46.2) |
| Gender (men) | 55.8 | 50.0 | 0.35 | 1.71 (0.03-90.6) | 0 (0.0) | 26 (100.0) |
| Shape mode (four; Wald) | 42.9 | 72.3 | 0.45 | 8.25 (1.87-36.4)* | 9 (60.0) | 22 (84.6) |
| Shape mode (four; Wald) + Age | 39.1 | 81.3 | 0.30 | 31.5 (3.51-282)* | 14 (93.3) | 18 (69.2) |
| Shape mode (four; Wald) + Gender | 43.6 | 71.4 | 0.55 | 21.9 (2.33-206)* | 7 (46.7) | 25 (96.2) |

AIC is Akaike information criterion; AUC is area under the receiver operating characteristic (ROC) curve; and OR is odds ratio. * denotes $p < 0.05$.

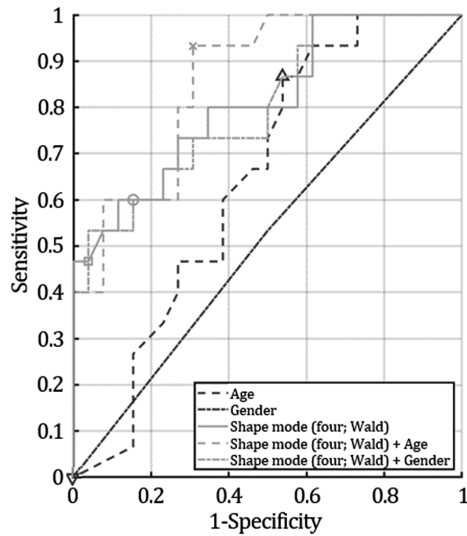


Figure 5. Receiver operating characteristic curves of logistic regression models with scaphoid fracture presence as dependent variable and age, gender, the four shape modes selected with Forward stepwise selection using the Wald-test or the four shape modes + age/gender as predictor variable(s). The symbols in the curves represent the optimal cut-off value for the fracture probabilities estimated by the logistic regression models, rounded to the nearest 0.05 and used to quantify the classification performance of the models.

Table 3. Classification performance of the logistic regression model with four shape modes as predictor variable selected with Forward stepwise selection using the Wald-test and a cut-off value of 0.45. Diagnosis based on HR-pQCT scans was used as true reference.

| | True scaphoid fracture | No scaphoid fracture | Total |
|---------------|------------------------|----------------------|-------|
| Shape modes + | 9 | 4 | 13 |
| Shape modes - | 6 | 22 | 28 |
| Total | 15 | 26 | 41 |
| <hr/> | | | |
| Sensitivity | 60.0 (32.3-83.7) | | |
| Specificity | 84.6 (65.1-95.6) | | |
| PPV | 57.8 (33.7-78.7) | | |
| NPV | 85.8 (76.0-92.0) | | |
| Accuracy | 78.2 (62.6-89.6) | | |
| AUC | 72.3 | | |

PPV and NPV are positive and negative predictive value, respectively.

For computation of accuracy, PPV, and NPV, a true fracture rate of 26% was used.

Values are expressed as percentages with 95%-confidence intervals.

DISCUSSION

The aim of this study was to investigate whether shape parameters from a SSM of the scaphoid bone are associated with the presence of a scaphoid fracture in patients with a clinically suspected fracture. The first five out of forty shape modes cumulatively explained 87.8% of the shape variance among the scaphoid bones, and the first 13 modes explained > 95% of the variance. A logistic regression model with four out of the first 13 modes as predictor variable resulted in a significant OR of 8.25 and an AUC of 72.3%. It correctly classified 75.6% of the scaphoid bones (fractured: 60.0%, non-fractured: 84.6%) when using a cut-off value of 0.45 for fracture probability.

These results suggest that there may be an association between scaphoid bone shape and fracture presence in patients with a suspected fracture. This could be explained by several factors. One factor may be the possible influence of the shape of the bone on its strength. During a fall on the outstretched hand, the scaphoid bone experiences a combination of compression and bending, which causes a bending moment on the scaphoid bone [13,14]. An excessive bending moment can cause a fracture, and a thinner and more curved bone shape could possibly lower the ability to withstand such moment, subsequently increasing fracture susceptibility after a fall. Additionally, the shape of the scaphoid bone may contribute to the amount of force that the bone has to withstand during a fall due to the complex interaction of the scaphoid bone with the surrounding bones and its bridging function of the proximal and distal carpal row, which both could influence wrist kinematics and subsequently loading distributions.

Due to the mathematical nature of shape modes and the explorative nature of this study, it was difficult and beyond the scope of the study to anatomically explain shape differences between fractured and non-fractured scaphoid bones in relation to fracture mechanics, but it is encouraged to investigate this in future studies.

Our SSM was based on HR-pQCT scans, which have a higher resolution than scans made with imaging modalities currently used for scaphoid fracture diagnosis, such as radiography, CT, or magnetic resonance imaging (MRI). The first five shape modes of our SSM explained a larger proportion of shape variance among the included fractured and non-fractured scaphoid bones than a SSM from CT-scans of non-fractured scaphoid bones [15], indicating that our SSM requires less shape modes to explain a certain shape variance than the CT-based SSM in literature. It is however unlikely that the higher resolution of the HR-pQCT scans contributed to this difference as the meshes used for our SSM had an maximum edge length of 0.5 mm, which is a resolution that can also be obtained by clinical whole-body CT-scanners. Furthermore, for the CT-based SSM, the scaphoid bones were scaled as part of the registration, thereby removing variation in bone size and consequently not having a shape mode explaining this variation, whereas we did not scale the bones, leading to our first shape mode that explained > 70% of shape variance mainly arisen from bone size differences. It was beyond the scope of the current study to investigate whether shape differences between fractured and non-fractured scaphoid bones may also be captured with CT, radiography, or MRI, and whether SSMs based on lower-resolution scans allow discrimination between fractured and non-fractured scaphoid bones.

Although not clinically usable given the current prediction rate (75.6%), SSM-based shape could possibly be when incorporated in clinical decision rules together with other patient data when further studied in larger datasets. The use of clinical prediction rules has been suggested as a strategy to improve the challenging diagnosis of scaphoid fractures [5]. Various prediction rules have been investigated earlier for scaphoid fracture diagnosis and combined pre-imaging characteristics, such as physical examination findings, demographic factors, and wrist range of motion and grip strength parameters [33-36]. Imaging-based bone shape could possibly further contribute to discriminating between patients with and without a scaphoid fracture, strengthened by having included only fractures without clearly visible fracture-related surface irregularities, which are more likely to be missed than fractures with more clear surface discontinuities. Furthermore, the lack of significant differences in age and in the proportion of men and high-impact falls between those with and without a scaphoid fracture suggests the possible discriminative ability of bone shape to be independent of age, gender, and trauma magnitude. Body weight was not measured but could possibly influence trauma magnitude. Nevertheless, the current algorithm

needs to be validated in larger series to investigate the robustness of the association between bone shape and fracture presence on HR-pQCT or conventional imaging modalities. Also, the possibility to use the bone shape in clinical prediction rules requires further study.

Bone mineral density (BMD) is another image-based characteristic that can be integrated in a statistical model. Statistical shape and density models have for example been developed of the proximal femur to investigate whether shape and density modes of these models can discriminate between patients without a hip fracture or with an incident or contralateral hip fracture [37-39]. The rationale of including BMD in such studies is related to findings that BMD, usually assessed with dual-energy X-ray absorptiometry (DXA), is associated with osteoporotic fracture risk. Scaphoid fractures represent however a different patient population with generally younger and more active individuals and a different fracture mechanism. The role of BMD on fracture risk or fracture presence is therefore less likely in the scaphoid fracture population compared to the population sustaining an osteoporotic fracture. Bone shape plays in contrast a more likely role in scaphoid fractures due to the complex shape of the scaphoid bone and its anatomical location in the wrist. We therefore did not include BMD but only bone shape in our statistical model.

This study has several limitations. First, the small dataset did not allow differentiation between scaphoid fracture types in constructing the SSM or the logistic regression models, while some of the included fracture types can be more devastating to miss than others (*e.g.* proximal pole fractures, Herbert's type B3) and may be considered clinically more relevant. Moreover, the small dataset increased the risk for overestimating classification performance due to overfitting. A general rule of thumb is to limit the number of predictor variables in a logistic regression model to one per ten events (*i.e.* fractures), which implies overfitting in the regression model with four shape modes. A regression model with one of the four selected modes individually does satisfy this rule of thumb and allowed moderate to fair classification for modes #13 and #8 (**Supplementary Material 2**). Mode #13 explained however < 1% of the total shape variance among the included scaphoid bones, which may suggest the possibility of being a finding related to the small sample size. Mode #8 explained 1.1% of total shape variance. Particular (and small) shape variations could theoretically and anatomically allow discrimination between fractured and non-fractured scaphoid bones, while larger shape variations do not have to (*e.g.* bone size, mode #1, given the even distribution of gender), but study in larger datasets is needed to further investigate the association between bone shape and scaphoid fracture presence. Second, we used both left and right scaphoid bones of both men and women for the construction of our SSM. Using left and right bones may be justified as the shape of the scaphoid

bone appears bilaterally symmetric [40]. In contrast, gender-related shape variances (*e.g.* size) have been found in the scaphoid bone [16,41-43]. However, in our study, gender was evenly distributed among the fractured and non-fractured scaphoid bones and accounted for in the logistic regression models, which justifies the inclusion of both male and female scaphoid bones. Third, due to the novelty of applying HR-pQCT imaging to the scaphoid bone, data on the intra- and interobserver variability of manually correcting the contours are lacking and warrant further study. Finally, as mentioned earlier, we used HR-pQCT scans for SSM construction, which have a higher resolution than imaging modalities currently used for scaphoid fracture diagnosis. Although the used mesh edge lengths are obtainable with whole-body CT, it has to be investigated whether bone shape from lower-resolution scans is associated with fracture presence.

To conclude, this exploratory study showed that the shape of the scaphoid bone quantified with a SSM from HR-pQCT scans seems to be associated with the presence of a scaphoid fracture in patients with a clinically suspected fracture. Further studies are needed to investigate this association, its relationship with fracture mechanics, and possible clinical implications of such association for scaphoid fracture diagnosis.

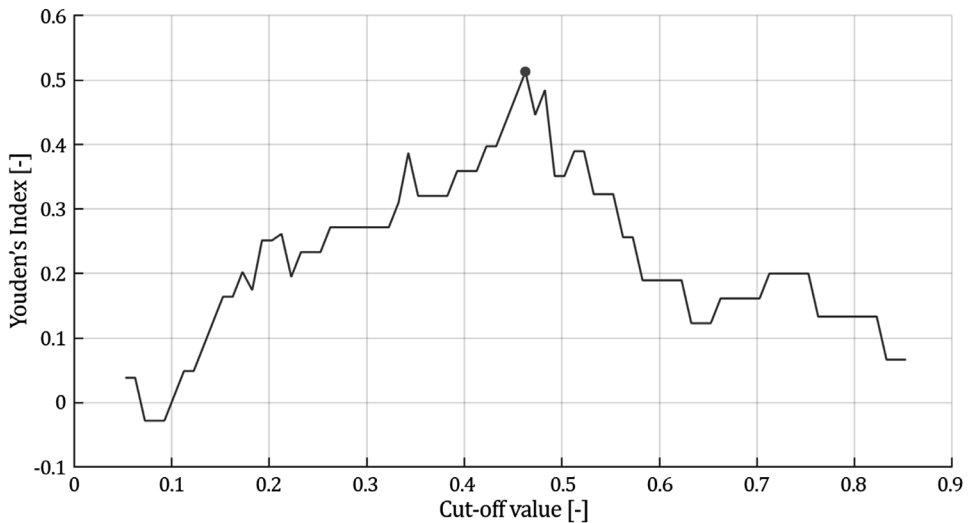
REFERENCES

- [1] Duckworth AD, Jenkins PJ, Aitken SA, Clement ND, Court-Brown CM, McQueen MM. Scaphoid fracture epidemiology. *J Trauma Acute Care Surg.* 2012;72:E41–E45.
- [2] Hove LM. Epidemiology of Scaphoid Fractures in Bergen, Norway. *Scand. J Plast Reconstr Surg Hand Surg.* 1999;33(4):423–426.
- [3] Van Onselen EBH, Karim RB, Hage JJ, Ritt MJPF. Prevalence and distribution of hand fractures. *J Hand Surg Br.* 2003;28(5):491–495.
- [4] Van Tassel DC, Owens BD, Wolf JM. Incidence estimates and demographics of scaphoid fracture in the U.S. population. *J Hand Surg Am.* 2010;35(8):1242–1245.
- [5] Duckworth AD, Ring D, McQueen MM. Assessment of the suspected fracture of the scaphoid. *J Bone Joint Surg Br.* 2011;93-B(6):713–719.
- [6] Brydie A, Raby N. Early MRI in the management of clinical scaphoid fracture. *Br J Radiol.* 2003;76(905):296–300.
- [7] Geijer M, Börjesson AM, Göthlin JH. Clinical utility of tomosynthesis in suspected scaphoid fracture. Pilot Study. *Skeletal Radiol.* 2011;40(7):863–867.
- [8] Hauger O, Bonnefoy O, Moinard M, Bersani D, Diard F. Occult fractures of the waist of the scaphoid: early diagnosis by high-spatial-resolution sonography. *Am J Roentgenol.* 2002;178(5):1239–1245.
- [9] Jenkins PJ, Slade K, Huntley JS, Robinson CM. A comparative analysis of the accuracy, diagnostic uncertainty and cost of imaging modalities in suspected scaphoid fractures. *Injury.* 2008;39(7):768–774.
- [10] Groves AM, Kayani I, Syed R, et al. An international survey of hospital practice in the imaging of acute scaphoid trauma. *Am J Roentgenol.* 2006;187(6):1453–1456.
- [11] Memarsadeghi M, Breitenseher MJ, Schaefer-Prokop C, et al. Occult scaphoid fractures: comparison of multidetector CT and MR imaging—initial experience. *Radiology.* 2006;240(1):169–176.
- [12] Tiel-van Buul MM, van Beek EJ, Broekhuizen AH, Bakker AJ, Bos KE, van Royen EA. Radiography and scintigraphy of suspected scaphoid fracture. A long-term study in 160 patients. *J Bone Joint Surg Br.* 1993;75-B(1):61–65.
- [13] Weber ER, Chao EY. An experimental approach to the mechanism of scaphoid waist fractures. *J Hand Surg Am.* 1978;3(2):142–148.
- [14] Majima M, Horii E, Matsuki H, Hirata H, Genda E. Load transmission through the wrist in the extended position. *J Hand Surg Am.* 2008;33(2):182–188.
- [15] van de Giessen M, Foumani M, Streekstra GJ, et al. Statistical descriptions of scaphoid and lunate bone shapes. *J Biomech.* 2010;43(8):1463–1469.
- [16] Ceri N, Korman E, Gunal I, Tetik S. The morphological and morphometric features of the scaphoid. *J Hand Surg Br.* 2004;29(4):393–398.
- [17] Compson JB, Waterman JK, Heatley FW. The radiological anatomy of the scaphoid. Part 1: Osteology. *J Hand Surg Br.* 1994;19(2):183–187.
- [18] Adeshina SA, Cootes TF, Adams J. Automatic determination of skeletal maturity using statistical models of appearance. *Int J Comput Tech.* 2017;4:1–11.
- [19] Anas EMA, Rasoulian A, Seitel A, et al. Automatic Segmentation of Wrist Bones in CT Using a Statistical Wrist Shape + Pose Model. *IEEE Trans Med Imaging.* 2016;35:1789–1801.
- [20] Foster BH, Shaw CB, Boutin RD, et al. A principal component analysis-based framework for statistical modeling of bone displacement during wrist maneuvers. *J Biomech.* 2019;85:173–181.
- [21] van de Giessen M, Foumani M, Vos FM, et al. A 4D statistical model of wrist bone motion patterns. *IEEE Trans Med Imaging.* 2012;31(3):613–625.

- [22] Bevers MSAM, Daniels AM, Wyers CE, et al. The Feasibility of High-Resolution Peripheral Quantitative Computed Tomography (HR-pQCT) in Patients with Suspected Scaphoid Fractures. *J Clin Densitometry*. 2020;23(3):432–442.
- [23] Daniels AM, Bevers MSAM, Sassen S, et al. Improved detection of scaphoid fractures with High Resolution peripheral Quantitative Computed Tomography compared to conventional CT. *J Bone Joint Surg Am*. 2020;102:2138–2145.
- [24] Daniels AM, Wyers CE, Janzing HMJ, et al. The interobserver reliability of the diagnosis and classification of scaphoid fractures using high-resolution peripheral quantitative CT. *Bone Joint J*. 2020;102-B(4):478–484.
- [25] Taubin G. A signal processing approach to fair surface design. In: Proceedings of the 22nd annual conference on Computer graphics and interactive techniques. Los Angeles, United States. 1995.
- [26] Manu, 2019a. nonrigidICP (<https://www.mathworks.com/matlabcentral/fileexchange/41396>), MATLAB Central File Exchange. Retrieved April 29, 2019.
- [27] Audenaert EA, Van Houcke J, Almeida DF, et al. Cascaded statistical shape model based segmentation of the full lower limb in CT. *Comput Methods Biomech Biomed Eng*. 2019;22(6):644–657.
- [28] Marzola A, Robilotta C, Volpe Y, Governi L, Furferi R. Statistical Shape Model: comparison between ICP and CPD algorithms on medical applications. *Int J Interact Des Manuf*. 2020;15(1):85–89.
- [29] Manu, 2019b. Shape Model Builder (<https://www.mathworks.com/matlabcentral/fileexchange/49940>), MATLAB Central File Exchange. Retrieved April 29, 2019.
- [30] Clopper CJ, Pearson ES. The Use of Confidence or Fiducial Limits Illustrated in the Case of the Binomial. *Biometrika*. 1934;26(4):404–413.
- [31] Mercaldo ND, Lau KF, Zhou XH. Confidence intervals for predictive values with an emphasis to case-control studies. *Stat Med*. 2007;26(10):2170–2183.
- [32] Herbert TJ, Fisher WE. Management of the fractured scaphoid using a new bone screw. *J Bone Joint Surg Br*. 1984;66-B(1):114–123.
- [33] Duckworth AD, Buijze GA, Moran M, et al. Predictors of fracture following suspected injury to the scaphoid. *J Bone Joint Surg Br*. 2012;94-B(7):961–968.
- [34] Mallee WH, Walenkamp MMJ, Mulders MAM, Goslings JC, Schep NWL. Detecting scaphoid fractures in wrist injury: a clinical decision rule. *Arch Orthop Trauma Surg*. 2020;140(4):575–581.
- [35] Parvizi J, Wayman J, Kelly P, Moran CG. Combining the clinical signs improves diagnosis of scaphoid fractures: a prospective study with follow-up. *J Hand Surg Br*. 1998;23(3):324–327.
- [36] Rhemrev SJ, Beeres FJP, van Leerdam RH, Hogervorst M, Ring D. Clinical prediction rule for suspected scaphoid fractures: A Prospective Cohort Study. *Injury*. 2010;41(10):1026–1030.
- [37] Bredbenner TL, Mason RL, Havill LM, Orwoll ES, Nicoletta DP. Fracture risk predictions based on statistical shape and density modeling of the proximal femur. *J Bone Miner Res*. 2014;29(9):2090–2100.
- [38] Goodyear SR, Barr RJ, McCloskey E, et al. Can we improve the prediction of hip fracture by assessing bone structure using shape and appearance modelling? *Bone*. 2013;53(1):188–193.
- [39] Whitmarsh T, Fritscher KD, Humbert L, Del Rio Barquero LM, et al. A statistical model of shape and bone mineral density distribution of the proximal femur for fracture risk assessment. In: Proceedings of the 14th International Conference on Medical Image Computing and Computer-Assisted Intervention – MICCAI 2011. Toronto, Canada.
- [40] ten Berg PWL, Dobbe JGG, Strackee SD, Streekstra GJ. Three-dimensional assessment of bilateral symmetry of the scaphoid: an anatomic study. *Biomed Res Int*. 2015:1–6.

- [41] Heinzlmann AD, Archer G, Bindra RR. Anthropometry of the human scaphoid. *J Hand Surg.* 2007;32(7):1005–1008.
- [42] Letta C, Schweizer A, Fürnstahl P. Quantification of contralateral differences of the scaphoid: a comparison of bone geometry in three dimensions. *Anat Res Int.* 2014:1–5.
- [43] Patterson RM, Elder KW, Viegas SF, Buford WL. Carpal bone anatomy measured by computer analysis of three-dimensional reconstructions of computed tomography images. *J Hand Surg Am.* 1995;20(6):923–929.

SUPPLEMENTARY MATERIAL 1



Supplementary Material 1 - Figure 1. Exemplary graph of the determination of the optimal cut-off value for fracture probability estimated by the logistic regression model with one shape mode as predictor variable and the presence of a scaphoid fracture as dependent variable. Youden's Index (sensitivity + specificity - 1) was determined for various cut-off values, and the optimal cut-off value was defined as the cut-off value with the highest Youden's Index rounded to the nearest 0.05 (*i.e.* 0.45, indicated with the grey dot).

SUPPLEMENTARY MATERIAL 2

Supplementary Material 1 - Table 1. Characteristics of four logistic regression models with scaphoid fracture presence as dependent variable and each of the shape modes selected with Forward stepwise selection individually as predictor variable.

| Regression model predictor | AIC [-] | AUC [%] | Optimal cut-off [-] | OR (95%-CI) [-] | Correct classification [- (%)] | |
|----------------------------|---------|---------|---------------------|-------------------|--------------------------------|----------------------|
| | | | | | Fracture (n = 15) | No fracture (n = 26) |
| Shape mode #13 | 49.7 | 73.7 | 0.45 | 8.40 (1.97-35.8)* | 10 (66.7) | 21 (80.8) |
| Shape mode #8 | 66.4 | 67.4 | 0.35 | 4.40 (1.10-17.7)* | 11 (73.3) | 16 (61.5) |
| Shape mode #7 | 54.3 | 61.7 | 0.35 | 2.75 (0.69-10.9) | 11 (73.3) | 13 (50.0) |
| Shape mode #3 | 55.2 | 51.0 | 0.35 | 1.18 (0.19-7.37) | 13 (86.7) | 4 (15.4) |

AIC is Akaike information criterion; AUC is area under the receiver operating characteristic (ROC) curve; and OR is odds ratio. * denotes $p < 0.05$.



10

Chapter 10

Assessment of the healing of conservatively-treated scaphoid fractures using HR-pQCT

Melissa S.A.M. Bevers, Anne M. Daniels, Bert van Rietbergen, Piet P.M.M. Geusens, Sander M.J. van Kuijk, Sander Sassen, Sjoerd Kaarsemaker, Pascal F.W. Hannemann, Martijn Poeze, Heinrich M.J. Janzing, Joop P. van den Bergh, Caroline E. Wyers

Bone 2021, 153: 116161.

ABSTRACT

Improving the clinical outcome of scaphoid fractures may benefit from adequate monitoring of their healing in order to for example identify complications such as scaphoid nonunion at an early stage and to adjust the treatment strategy accordingly. However, quantitative assessment of the healing process is limited with current imaging modalities. In this study, high-resolution peripheral quantitative computed tomography (HR-pQCT) was used for the first time to assess the changes in bone density, microarchitecture, and strength during the healing of conservatively-treated scaphoid fractures. Thirteen patients with a scaphoid fracture (all confirmed on HR-pQCT and eleven on CT) received an HR-pQCT scan at baseline and three, six, twelve, and 26 weeks after first presentation at the emergency department. Bone mineral density (BMD) and trabecular microarchitecture of the scaphoid bone were quantified, and failure load (FL) was estimated using micro-finite element analysis. Longitudinal changes were evaluated with linear mixed-effects models. Data of two patients were excluded due to surgical intervention after the twelve-week follow-up visit. In the eleven fully evaluable patients, the fracture line became more apparent at 3 weeks. At 6 weeks, individual trabeculae at the fracture region became more difficult to identify and distinguish from neighboring trabeculae, and this phenomenon concerned a larger region around the fracture line at 12 weeks. Quantitative assessment showed that BMD and FL were significantly lower than baseline at all follow-up visits with the largest change from baseline at 6 weeks (-13.6% and -23.7%, respectively). BMD remained unchanged thereafter, while FL increased. Trabecular thickness decreased significantly from baseline at three (-3.9%), six (-6.7%), and twelve (-4.4%) weeks and trabecular number at six (-4.5%), twelve (-7.3%), and 26 (-7.9%) weeks. Trabecular separation was significantly higher than baseline at six (+13.3%), twelve (+19.7%), and 26 (+16.3%) weeks. To conclude, this explorative HR-pQCT study showed a substantial decrease in scaphoid BMD, Tb.Th, and FL during the first 6 weeks of healing of conservatively-treated scaphoid fractures, followed by stabilization or increase in these parameters. At 26 weeks, BMD, trabecular microarchitecture, and FL were not returned to baseline values.

INTRODUCTION

Scaphoid fractures constitute approximately 60-75% of all carpal fractures and have a relatively high incidence in the young and physically active male population [1-4]. They can have a poor clinical outcome when not adequately diagnosed and treated. Delayed and inaccurate diagnosis and inappropriate treatment are among the factors contributing to scaphoid nonunion [5]. Up to 15% of scaphoid fractures develop into scaphoid nonunion [6,7], which can successively cause scaphoid collapse, carpal malalignment and instability, and wrist osteoarthritis, leading to pain and limited functionality [8,9]. Currently, there is no consensus on optimal treatment for scaphoid nonunion, with strategies including internal fixation with screws, K-wires, or mini plates combined with vascularized or non-vascularized bone grafts from mainly the distal radius, medial femoral condyle, or iliac crest [10]. Minimizing the occurrence of a scaphoid nonunion is thus desired considering the consequent additional treatment, prolonged healing times, and possible long-term complications of poor healing. Adequate monitoring of the healing of a scaphoid fracture may help, *e.g.* by enabling early detection of developing complications such as scaphoid nonunion and adjusting treatment strategy accordingly.

However, the possibility to monitor scaphoid fracture healing and to capture changes during healing is limited with current imaging modalities, as is the knowledge regarding the healing process. Today, the monitoring of the healing progress of a scaphoid fracture involves assessment of bone union using for example serial radiography or conventional computed tomography (CT). Radiography is however characterized by a highly subjective evaluation of bone union [11,12]. While conventional CT has been found a reliable and accurate modality to assess scaphoid union and nonunion, assessing partial union is associated with lower interobserver agreement [13], making bone union assessment also on CT partly subjective. Further, radiography and CT cannot provide detailed quantitative information on a microarchitectural level given that their spatial resolution is insufficient to resolve trabecular structures (*e.g.* recently, we used CT with 0.5-mm slice increment for scaphoid fracture diagnosis [14]). Besides that, current knowledge about fracture healing is predominantly based on the healing of diaphyseal fractures that involves mainly cortical bone, while scaphoid fractures concern mainly trabecular bone for which a different healing has been suggested [15-18]. For example, studies on metaphyseal fracture healing in small animals have found that the healing of fractures in trabecular bone is faster and spatially more restricted than fracture healing in cortical bone, and that it resembles direct, intra-membranous ossification on surfaces of pre-existing trabeculae and in bone marrow, with little or no cartilage and callus formation [15,16]. A study on knee arthrodeses and more recently on cancellous bone biopsies of fractured distal radii reported similar observations in

humans [17,18]. Despite these new insights, detailed and quantitative information about fracture healing of trabecular bone in general and of the scaphoid bone in particular remains limited.

High-resolution peripheral quantitative CT (HR-pQCT) may help to bridge this gap in the monitoring of and knowledge about scaphoid fracture healing as it enables quantitative *in vivo* evaluation of bone on a microarchitectural level. De Jong *et al.* have earlier demonstrated the feasibility of using this imaging modality to quantify the healing process of conservatively-treated distal radius fractures [19,20]. Based on qualitative and quantitative evaluation of HR-pQCT scans of these fractures, they suggested that distal radius fracture healing involves the formation of woven bone that subsequently remodels into a trabecular microarchitecture [19]. Thus far, HR-pQCT has mainly been used for the distal radius or tibia, but recently, we have shown that this imaging modality can also acquire good-quality scans of the scaphoid bone in patients with a suspected scaphoid fracture [21]. Additionally, we have found that HR-pQCT had good interobserver agreement in scaphoid fracture diagnosis and classification [22], and that it revealed 60% more individuals with a scaphoid fracture among 91 patients with a suspected fracture than conventional CT [14]. Besides this benefit to scaphoid fracture diagnosis, HR-pQCT imaging may potentially also be beneficial for the healing of scaphoid fractures by allowing a more detailed and objective healing assessment that could improve the knowledge about scaphoid fracture healing and possibly help to optimize scaphoid fracture treatment. However, the potential to monitor scaphoid fracture healing with HR-pQCT has not yet been investigated. Therefore, the aim of this explorative study was to assess the healing of conservatively-treated scaphoid fractures with HR-pQCT.

METHODS

Study design and population

Thirteen patients (8 men, 5 women) aged 18 years and older were included in this prospective cohort study, which was a follow-up of our previously published study in 91 patients (45 men, 46 women) who presented at the emergency department (ED) of VieCuri Medical Center, Venlo (The Netherlands) with a clinically suspected scaphoid fracture. The protocol of this study was approved by an independent Medical Ethics Committee (METC registration number NL62476.068.17). Details about study design, protocol, and population have been earlier described [14,21,22]. Briefly, according to current clinical practice of the hospital, the 91 patients of the main study underwent a standard scaphoid series at first presentation at the ED, followed by wrist immobilization with a polyester cast independent of the diagnosis on the

scaphoid series. First presentation at the ED was at the day of trauma in 49 of 91 patients (53.8%) and 1 day after the day of trauma in 29 patients (31.9%). The other 13 patients presented 2-6 days after the day of trauma at the ED. Within 10 days after first presentation, standard physical examination was performed by a trained surgical resident. Additionally, after providing written informed consent, all 91 patients received a baseline CT and HR-pQCT scan at this timepoint. Fracture diagnosis and treatment strategy were based on the evaluation of these two scans. Inclusion criteria to participate in the current follow-up study included a confirmed scaphoid fracture on the baseline HR-pQCT scan and conservative treatment of this fracture with a standard polyester cast. Thirteen patients, who met these criteria, consented to participate in this follow-up study. In eleven of them, the fracture, confirmed on the baseline HR-pQCT scan, was also confirmed on the baseline CT scan, while in the other two patients, the fracture, confirmed on the baseline HR-pQCT scan, could not be confirmed on the baseline CT scan.

HR-pQCT imaging

HR-pQCT scans were performed of the fractured scaphoid bone at three, six, twelve, and 26 weeks after first presentation at the ED. The scans (XtremeCT II, Scanco Medical AG, Brüttisellen, Switzerland) were acquired using the default clinical *in vivo* settings defined by the manufacturer of the scanner (X-ray tube voltage of 68 kV, intensity of 1460 μ A, and integration time of 43 ms). Scan region included a 30.6-mm region of the wrist (three consecutive stacks of 10.2 mm) to cover the entire scaphoid bone (**Figure 1A**) [14,21,22]. During acquisition of the scans, the wrist was placed in a standard motion restraining holder, while it was immobilized with the polyester cast used for treatment plus an additional single-layer polyester thumb cast (**Figure 1B**). The additional thumb cast was used to improve thumb stability [21], and it was only worn during scan acquisition and retained for each scan. After removal of the treatment cast, this cast was also retained for reuse for the remaining scans. Total scan time was six minutes, and the patients were subjected to an effective dose of approximately 15 μ Sv per scan. The scans were reconstructed with an isotropic voxel size of 61 μ m.

The quality of the scans was graded by the operator during scan acquisition based on the grading system originally developed for radius and tibia HR-pQCT scans and constituted inspection of a low-resolution preview of the mid-slice of each stack [23]. Scans were completely repeated when the quality of at least one of the three stacks of a scan was graded with a grade > 3 [23]. Only one repetition was allowed, and the scan with the best quality was used for further analyses. In our previously published feasibility study, we reported a considerable discrepancy between the standard grading and a *post hoc* grading [21]. Therefore, the quality of each stack of the scans was *post*

hoc graded by one experienced researcher by applying the standard grading system for radius and tibia scans to every tenth full-resolution slice of each stack [21]. Although the scaphoid bone has only a thin outer bone layer compared to the cortex of the distal radius and tibia, motion artefacts in the cortical bone compartment as described in the grading system (*i.e.* horizontal streaking and disruption of the cortical contiguity) could be observed in the outer layer of the scaphoid bone, enabling the use of the standard grading system. The entire scan was assigned a good quality when the three stacks had a *post hoc* grade 1-3 and a poor quality when at least one of the three stacks had a *post hoc* grade > 3 .

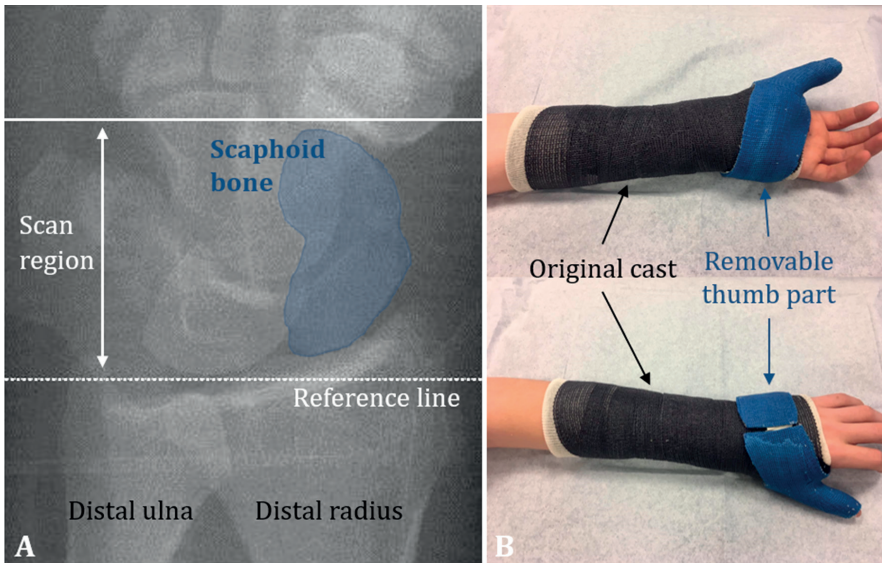


Figure 1. Example of **A**) a scout view to define scan region, and **B**) the polyester cast (black; used for treatment) and removable thumb part (blue; only used during scanning) worn during acquisition of the HR-pQCT scans.

Previously, we found that a relatively large proportion of scaphoid bone scans (32.9%) had at least one poor-quality stack [21], which could cause a substantial proportion of scans of this study to be excluded. Therefore, justified by the fact that bone parameters are determined over an entire bone volume, it was decided not to exclude all poor-quality scans based on *post hoc* grading to ensure the largest possible dataset for the statistical analyses. To decide which poor-quality scans to exclude, a new grade was assigned to the entire scan by multiplying the *post hoc* grade of each stack with the fraction of the bone volume within that stack (*e.g.* if only 20% of the bone was within the stack, its quality was weighted by 20%). In case the newly determined grade was > 3.5 for the entire scan, the scan was excluded; otherwise, the scan was included. The bone volume of a stack was determined by quantifying the bone volume fraction

(BV/TV) of the entire scaphoid bone (*i.e.* including trabecular compartment and outer bone layer) within the stack and subsequently dividing the TV-component of the stack by the TV-component of the entire scan. BV/TV was calculated after standard preprocessing of the scans; that is, after Gaussian filtering with $\sigma = 0.8$ and support = 1 voxel and subsequent bone tissue segmentation with a threshold of 320 mg HA/cm³.

Fracture classification

An experienced musculoskeletal radiologist evaluated the HR-pQCT scans at baseline to classify the fractures according to Herbert's scaphoid fracture classification system [24]. Using this system, a scaphoid fracture was classified as stable (type A) or unstable (type B). Stable fractures were further specified as tubercle (A1) or incomplete waist (A2) fractures, and unstable fractures as distal oblique (B1), complete waist (B2) or proximal pole (B3) fractures, transscaphoid perilunate fracture dislocations (B4) or comminuted fractures (B5). The same radiologist also inspected the scans made at 26 weeks to evaluate fracture consolidation by assessing fracture gap bridging and bone remodeling around the fracture region. Consolidation was defined as bridging of the fracture gap with incomplete or complete remodeling of the trabecular bone and outer bone layer.

Evaluation of bone mineral density and microarchitecture

To allow quantitative evaluation, the scaphoid bones were contoured by application of an automatic contouring algorithm to coarse hand-drawn pre-contours of the scaphoid bone (**Figure 2A**) [21]. The coarse pre-contours were drawn to isolate the scaphoid bone from the other bones on the scans [21]. The automatic algorithm, provided by the manufacturer of the scanner, has originally been developed for radius and tibia contouring on HR-pQCT scans and is similar to the automatic contouring algorithm for the peri- and endosteal margins of the radius and tibia on HR-pQCT scans [25]. For application on the pre-contours, the lower threshold to binarize the scans was changed from the default 120 permille (398.2 mg HA/cm³) to 105 permille (297.7 mg HA/cm³) to account for the thinner and less mineralized outer layer of the scaphoid bone compared to the cortex of the distal radius and tibia. The resulting contours were manually corrected when visually deviating from the outer bone margins.

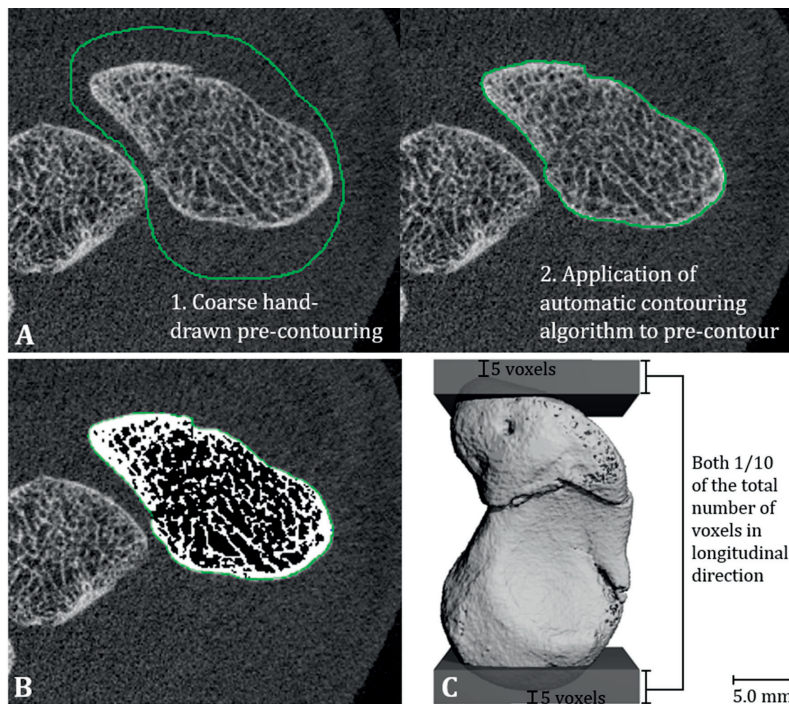


Figure 2. Example of **A)** the contouring approach consisting of coarse pre-contouring of the scaphoid bone by hand to isolate it from the other bones (1) and subsequent application of an automatic algorithm to the pre-contour (2), **B)** the result after pre-processing the scans by Gaussian filtering ($\sigma = 0.8$, support = 1 voxel) and bone tissue segmentation (threshold = 320 mg HA/cm^3), and **C)** the μ FE-approach consisting of alignment of the scaphoid bone along its longest axis and subsequent addition of two stiffer plates at the top and bottom of the scaphoid bone. A compression to 1% strain was applied to the upper plate.

Density and microarchitecture of the contoured scaphoid bones were then quantified using methods based on the standard analysis methods provided by the manufacturer. Conform standard methodology, bone mineral density was calculated directly from the grayscale scans. It was only computed for the entire scaphoid bone (Tt.BMD) and not for the cortical and trabecular compartment. This was done because the thickness of the thin outer bone layer (which is subchondral bone rather than cortical bone) has been found to approximate 1-1.5 times the thickness of an individual trabecula [26], based on which it was chosen to include the outer bone layer in the computation of the trabecular parameters. Consequently, total and trabecular BMD occupied the same bone region, and cortical BMD and cortical microarchitecture were not computed. Besides that, the endocortical contour, standardly determined to separate the cortical and trabecular compartment, was not needed to evaluate trabecular microarchitecture. Instead, the protocol was adjusted so that the obtained outer contour defined the region of interest (*i.e.* the entire scaphoid bone including outer bone layer) from which trabecular microarchitectural parameters were determined. Following

the manufacturer's methodology, the scans were first Gaussian filtered ($\sigma = 0.8$, support = 1 voxel) and the bone tissue segmented (threshold = 320 mg HA/cm³), after which trabecular number (Tb.N), thickness (Tb.Th), and separation (Tb.Sp) were directly measured using the distance transformation method [27]. As all parameters were evaluated for the entire scaphoid bone, no registration was performed between the baseline and follow-up scans. The analyses were performed using the Image Processing Language software provided with the scanner (IPLFE v2.02, Scanco Medical AG, Brüttisellen, Switzerland).

Evaluation of biomechanical parameters

Micro-finite element (μ FE-) modeling was used to estimate the biomechanical properties of the scaphoid bones. As a preprocessing step, the segmented scaphoid bone (obtained from the scan after the filtering and thresholding as explained above) was aligned along its longest axis and placed between two plates (**Figure 2C**). For the alignment, the principal axes of the scaphoid bone were determined by calculation of the principal moments of inertia and aligned to the coordinate system of the scan. This step was performed to ensure 1) a consistent loading direction in all patients; and 2) a role for the fracture in all patients independent of fracture type by loading the major part of the bone. A top and bottom plate were successively added to the scaphoid bone in order to prevent unrealistic stress concentrations due to the complex and irregular shape of the bone. These plates were built from isotropic voxels of 61 μ m, extended the top and bottom endings of the scaphoid bone with a minimum of five voxels, and both had a thickness of one tenth of the number of voxels in longitudinal direction. The plate voxels attaching to the scaphoid bone were fully bonded to the surface nodes of the bone voxels. The resulting models were converted to μ FE-models by conversion of each bone and plate voxel to brick elements of the same size. The elements constituting the scaphoid bone were assigned a Young's Modulus of 10 GPa and a Poisson's Ratio of 0.3 [28], while those constituting the plates were assigned a ten times higher Young's Modulus (*i.e.* 100 GPa) to mimic material stiffer than bone. An axial compression to 1% strain was then applied in longitudinal direction; that is, the nodes at the top plate were suppressed in the three orthogonal directions, and those at the bottom plate were prescribed a strain of 1 in the longitudinal direction and suppressed in the other two directions. The completed simulations were used to calculate bone stiffness as the reaction force over the applied displacement and to estimate failure load (FL) using Pistoia's criterion [29]. The preprocessing, μ FE-model generation, and μ FE-analysis were performed using the provided software (IPLFE v2.02).

Statistical analysis

Statistical analyses were performed in R (R Foundation for Statistical Computing, Version R-3.6.2 for Windows, Vienna, Austria). Linear mixed-effect models (LMMs) were used to model the longitudinal changes in the bone parameters while accounting for clustering of data within patients. Time after first presentation was included as fixed effect and patient identifier as random intercept. Parameter estimation criterion for the LMMs was left as default (*i.e.* restricted maximum likelihood), and no covariates were added to avoid overfitting. The bone parameters at each visit were expressed as estimated marginal means (EMMs) with 95%-confidence intervals, and the significance of the difference of these EMMs between baseline and each follow-up was determined. Also the difference in EMMs between the second follow-up visit and the visits thereafter was determined. The significance level was set at $\alpha = 0.05$ for all tests, and it was not corrected for multiple comparisons due to the small sample size of the study.

RESULTS

Dataset

Eleven of the thirteen included patients completed all five visits (**Figure 3**). Two patients did not show up at twelve ($n = 1$) and 26 ($n = 2$) weeks, but the available data of these patients were included in the LMMs. All data of two patients who did complete the follow-up were excluded from the analyses because of surgery after the visit at 12 weeks due to scaphoid nonunion based on follow-up radiographs, CT, and HR-pQCT. One patient with complete follow-up did not wear the additional thumb cast during acquisition of the baseline scan, but the data of this patient could be included in this study based on sufficient image quality. In total, the data of eleven patients were used for the statistical analyses. Baseline characteristics of these patients are presented in **Table 1**.

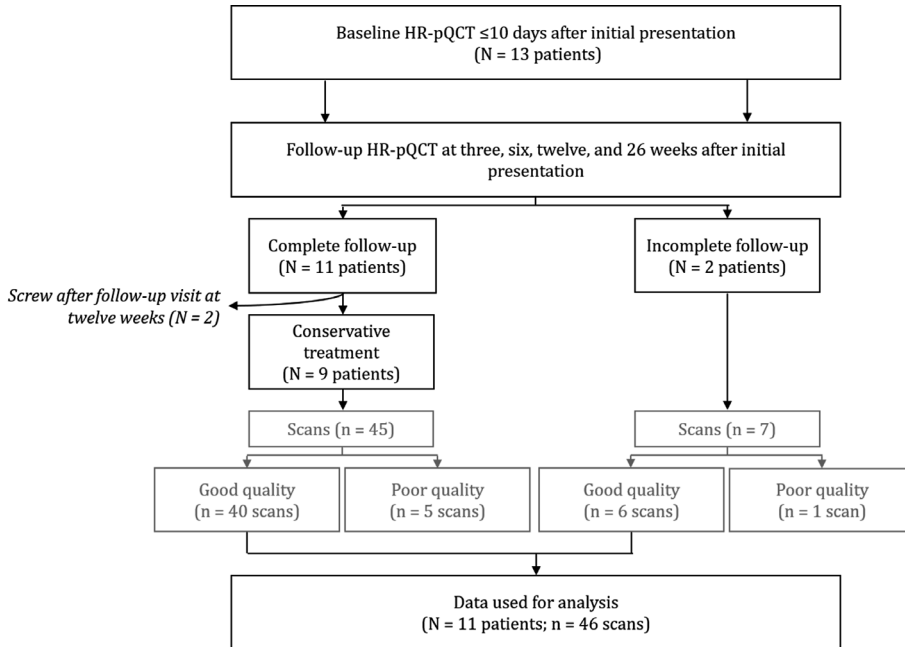


Figure 3. Flowchart showing the obtained HR-pQCT scans and their quality. Only the scans with a good image quality were used to determine bone mineral density, trabecular microarchitecture, and biomechanical properties of the scaphoid bones.

Table 1. Baseline characteristics of the eleven patients with a scaphoid fracture confirmed on HR-pQCT and treated conservatively whose scans were included in the statistical analyses.

| Characteristic | Evaluated patients (n = 11) |
|---|-----------------------------|
| Male gender | 6 (54.5) |
| Age [years] | 47 (19-71, 30) |
| Initial presentation at the emergency department | |
| 0 days after the day of trauma (= at day of trauma) | 5 (45.5) |
| 1 day after the day of trauma | 3 (27.3) |
| 2 days after the day of trauma | 3 (27.3) |
| Herbert fracture type (based on HR-pQCT) | |
| A1 | 4 (36.4) |
| A2 | 0 (0.0) |
| B1 | 2 (18.2) |
| B2 | 0 (0.0) |
| B3 | 3 (27.3) |
| B4 | 0 (0.0) |
| B5 | 2 (18.2) |
| Scaphoid fracture also confirmed on CT | 9 (81.8) |
| Time to cast-removal [weeks] | 6.6 (4.7-12.1, 4.3) |

Values are expressed as median (minimum-maximum, interquartile range) or frequency (percentage).

Fifty-two HR-pQCT scans were acquired in the eleven patients (**Figure 3**). *Post hoc* quality grading revealed fourteen scans (26.9%) with a poor quality in at least one stack due to motion artefacts. Accounting for the relative bone volume affected by the motion artefacts, six HR-pQCT scans (11.5%) remained evaluated as poor quality (**Figure 3**) and were excluded from the statistical analyses. The remaining 46 HR-pQCT scans constituted 11 baseline scans, and 9, 10, 7, and 9 scans taken at three, six, twelve, and 26 weeks after first presentation, respectively. The baseline HR-pQCT scan was taken on average 1.3 ± 0.4 weeks after first presentation at the ED and those at the four follow-up visits 3.2 ± 0.5 weeks, 6.1 ± 0.5 weeks, 12.0 ± 1.1 weeks, and 26.0 ± 0.8 weeks after first presentation.

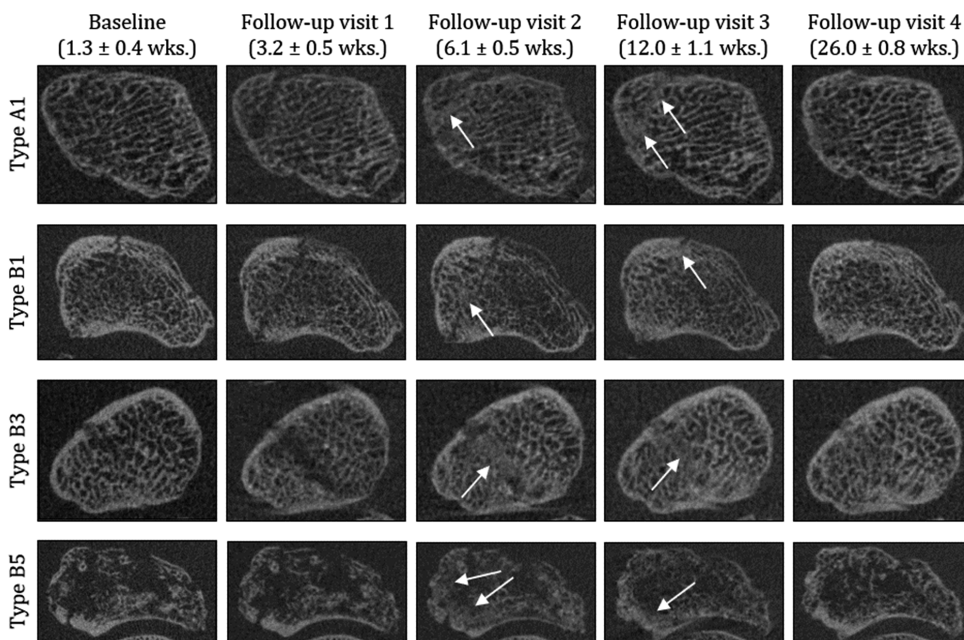


Figure 4. Examples of HR-pQCT slices of four different types of scaphoid fractures at baseline (left column) and each of the four follow-up visits. The slices were obtained after three-dimensional registration of the follow-up scans with the baseline scan. The white arrows show ‘blurring’ of trabecular structures with individual trabeculae becoming less well identifiable and distinguishable from neighboring trabeculae.

Visual assessment

Figures 4 and 5 show examples of the healing of different types of scaphoid fractures. For visualization purposes, the follow-up scans of these examples were three-dimensionally registered with the baseline scan [30]. In general, the fracture line appeared more pronounced at 3 weeks after first presentation compared to baseline with a disrupted outer bone layer and disrupted trabeculae along the fracture line.

Small fracture displacements were observed by visual judgement of one investigator, which might have contributed to a more clearly visible fracture line. At 6 weeks, individual trabeculae at the fracture region became difficult to identify and distinguish from neighboring trabeculae. This ‘blurring’ of trabecular structures was not visible along the entire fracture line at 6 weeks but became more pronounced and occupied a larger region around the fracture line at 12 weeks (**Figure 5**). Finally, at 26 weeks, seven out of the nine fractures with complete follow-up were assessed as consolidated by the radiologist. Two of these seven fractures were assessed as completely bridged but with minor disruptions in the outer bone layer that did not cross the width of the outer layer (*e.g.* **Figure 4, bottom panel**). Further, in another consolidated fracture, a small fracture fragment was not fused but got separated. The two other fractures (types B1 and B3) were assessed as nonconsolidated and had small surface and trabecular disruptions (*e.g.* **Figure 4, third panel**).

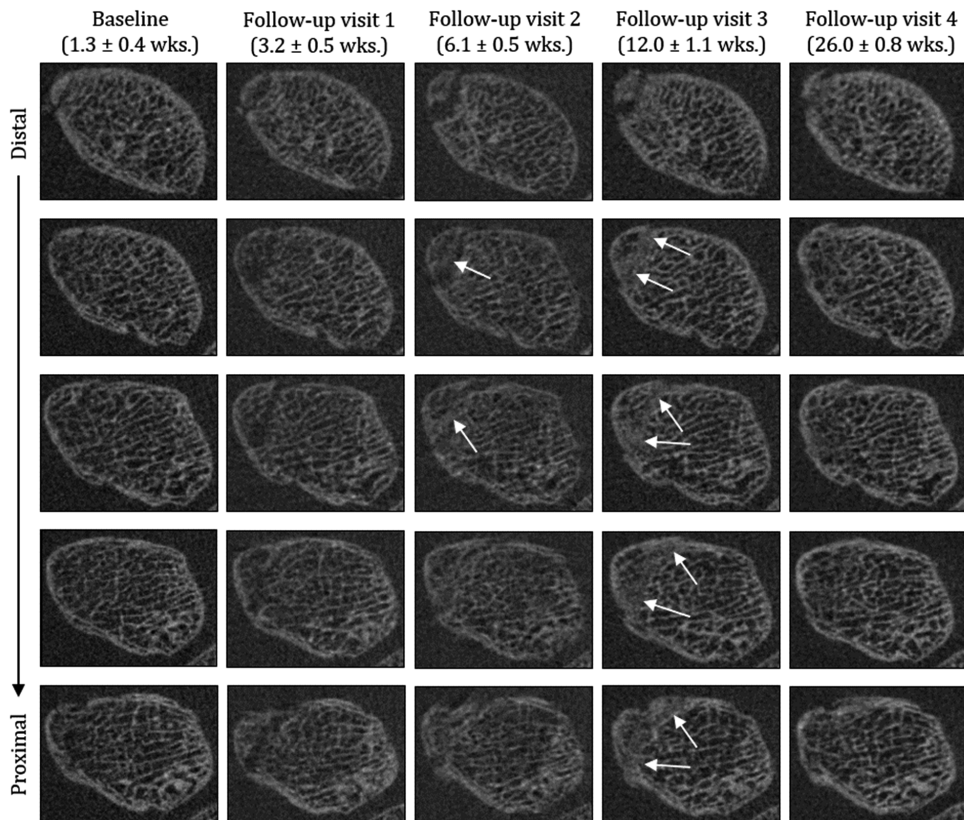


Figure 5. Multiple HR-pQCT slices of a type A1 scaphoid fracture (shown in **Figure 3**, top row) at baseline (left column) and each of the four follow-up visits. The slices were obtained after three-dimensional registration of the follow-up scans with the baseline scan. The white arrows show ‘blurring’ of trabecular structures with individual trabeculae becoming less well identifiable and distinguishable from neighboring trabeculae.

Quantitative assessment

All parameters except Tb.N had the largest change from baseline at six or 12 weeks, and all but Tb.Th remained significantly different from baseline at 26 weeks (**Figure 6; Table 2**). Mean Tt.BMD was significantly lower than baseline throughout the entire follow-up and decreased to the lowest value at six and 12 weeks (-13.6% compared to baseline, both $p < 0.0001$) without significant difference between these timepoints. Tb.Th was significantly different from baseline at three (-3.9%, $p = 0.04$), six (-6.7%, $p = 0.0006$), and twelve (-4.4%, $p = 0.04$) weeks and was significantly higher at 26 weeks compared to 6 weeks ($p = 0.009$). The other microarchitectural parameters were not significantly different from baseline at 3 weeks but became significantly different thereafter. Tb.N was significantly different from baseline at 6 weeks (-4.5%, $p = 0.01$) and gradually decreased to show the largest difference from baseline at 26 weeks (-7.9%, $p = 0.0001$). Tb.Sp was significantly higher than baseline at six (+13.3%, $p = 0.002$), twelve (+19.7%, $p = 0.0001$), and 26 (+16.3%, $p = 0.0004$) weeks. The largest percentage changes from baseline were found for the biomechanical parameters with the largest decrease from baseline at 6 weeks (stiffness: -26.5%; FL: -23.7%, both $p < 0.0001$). Thereafter, they increased to a significant difference at 26 weeks compared to 6 weeks (stiffness: $p = 0.0005$; FL: $p = 0.0004$) but remained significantly lower than baseline (stiffness: -10.9%, $p = 0.009$; FL: -9.5%, $p = 0.01$).

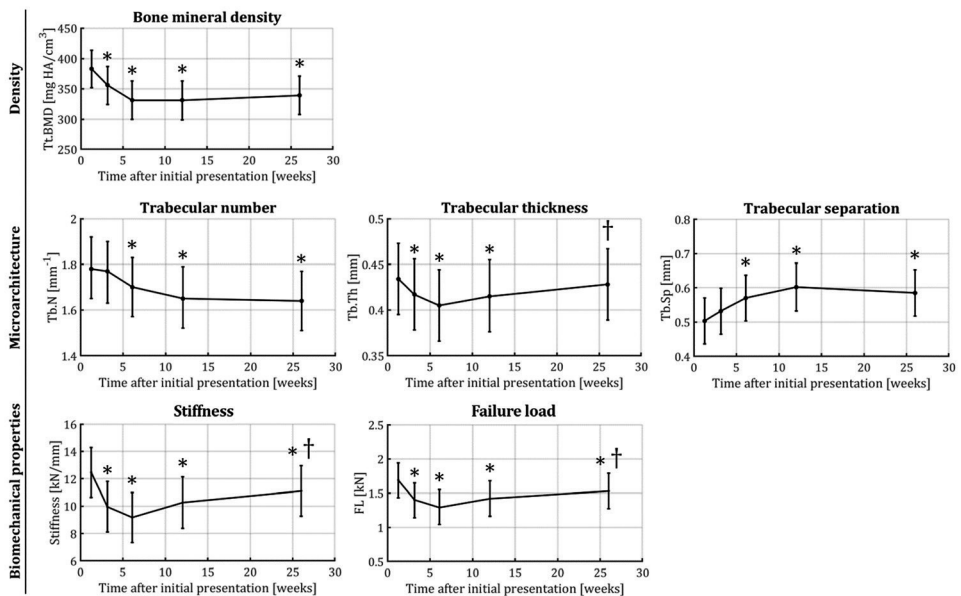


Figure 6. Time course of the estimated marginal means of bone mineral density (top row), trabecular microarchitecture (middle row), and biomechanical properties (bottom row) of the scaphoid bone obtained from linear mixed effect models with time after first presentation at the emergency department as fixed effect. The error bars show 95%-confidence intervals; * denotes statistically significant differences from baseline and † denotes statistically significant differences at twelve and 26 weeks from 6 weeks (both $p < 0.05$; not adjusted for multiple comparisons).

Table 2. Estimated marginal means (EMMs) of the measured bone parameters at baseline and each follow-up visit with 95%-confidence intervals (95% CI) and percentage change from baseline (n = 11 patients).

| Parameter | Baseline (1.3 ± 0.4 weeks after first presentation) | | Follow-up visit 1 (3.2 ± 0.5 weeks after first presentation) | | Follow-up visit 2 (6.1 ± 0.5 weeks after first presentation) | | Follow-up visit 3 (12.0 ± 1.1 weeks after first presentation) | | Follow-up visit 4 (26.0 ± 0.8 weeks after first presentation) | |
|---------------------------------|---|--------------------|--|--------------------|--|--------------------|---|--------------------|---|--------------------|
| | EMM (95% CI) | Change from BL (%) | EMM (95% CI) | Change from BL (%) | EMM (95% CI) | Change from BL (%) | EMM (95% CI) | Change from BL (%) | EMM (95% CI) | Change from BL (%) |
| Densitometric | | | | | | | | | | |
| Tt.BMD [mg HA/cm ³] | 383 (352-414) | -7.05 | 356 (324-387)* | -13.58 | 331 (300-363)* | -13.58 | 331 (299-363)* | -13.58 | 339 (308-371)* | -11.49 |
| Microarchitectural | | | | | | | | | | |
| Tb.N [mm ⁻¹] | 1.78 (1.65-1.92) | -0.56 | 1.77 (1.63-1.90) | -4.49 | 1.70 (1.57-1.83)* | -4.49 | 1.65 (1.52-1.79)* | -7.30 | 1.64 (1.51-1.77)* | -7.87 |
| Tb.Th [mm] | 0.434 (0.395-0.473) | -3.92 | 0.417 (0.378-0.456)* | -6.68 | 0.405 (0.366-0.444)* | -6.68 | 0.415 (0.376-0.455)* | -4.38 | 0.428 (0.389-0.467)† | -1.38 |
| Tb.Sp [mm] | 0.503 (0.437-0.570) | +5.77 | 0.532 (0.464-0.599) | +13.32 | 0.570 (0.503-0.637)* | +13.32 | 0.602 (0.532-0.672)* | +19.68 | 0.585 (0.517-0.653)* | +16.30 |
| Mechanical | | | | | | | | | | |
| Stiffness [kN/mm] | 12.47 (10.64-14.29) | -20.13 | 9.96 (8.11-11.80)* | -26.46 | 9.17 (7.34-11.00)* | -26.46 | 10.26 (8.38-12.15)* | -17.72 | 11.11 (9.26-12.96)*† | -10.91 |
| FL [kN] | 1.69 (1.43-1.94) | -17.20 | 1.40 (1.14-1.65)* | -23.67 | 1.29 (1.04-1.55)* | -23.67 | 1.42 (1.16-1.68)* | -15.98 | 1.53 (1.27-1.79)*† | -9.47 |

Tt.BMD = total volumetric bone mineral density; Tb.N = trabecular number; Tb.Th = trabecular thickness; Tb.Sp = trabecular separation; FL = failure load.

Results are obtained from linear mixed effects models with time after first presentation at the emergency department as fixed effect.

Significant differences ($p < 0.05$; not adjusted for multiple comparisons) from baseline are denoted with * and from follow-up visit 2 (for follow-up visits 3 and 4) are denoted with †.

DISCUSSION

This study used for the first time HR-pQCT to explore the healing of conservatively-treated scaphoid fractures. Visual assessment of the HR-pQCT scans revealed an increased fracture visibility at 3 weeks after first presentation at the ED, followed by ‘blurring’ of trabecular structures around the fracture line at 6 weeks with individual trabeculae becoming hardly indistinguishable from neighboring trabeculae. This ‘blurring’ became more pronounced at 12 weeks. At 26 weeks, seven out of the nine fractures with complete follow-up were consolidated. Quantitative assessment of the scans showed significant changes in BMD, trabecular microarchitecture, and biomechanical properties of the scaphoid bone during fracture healing with the largest change from baseline at six or 12 weeks for all parameters except Tb.N. At 26 weeks, all parameters except Tb.Th remained significantly different from baseline.

The results may suggest that the healing of the scaphoid fractures assessed in this study consists of two phases. The healing process seemed to be initiated by a significant decrease compared to baseline in BMD, Tb.Th, and stiffness and FL until 6 weeks after first presentation (first phase), co-occurring with an increased visibility of the fracture line at 3 weeks after first presentation. Decreases in areal BMD, assessed with dual-energy X-ray absorptiometry (DXA), have previously been reported five to 10 weeks after first presentation compared to baseline in the proximal and distal part of the scaphoid bone in sixteen individuals with a conservatively-treated scaphoid waist fracture [31]. In that study, decreases in areal BMD were also found in the ipsilateral uninjured distal radius, and the authors hypothesized that part of the bone loss in the scaphoid bone during fracture healing could be the result of wrist immobilization [31]. Bone resorption has also been reported in a case series on nondisplaced scaphoid fractures using CT five to 7 weeks post-fracture [32]. The assessed fractures healed without surgical intervention, and the authors suggested that bone resorption may be part of the normal scaphoid fracture healing process [32]. Changes in the scaphoid bone during scaphoid fracture healing may thus be the result of a complex multifactorial process. Consequently, the observed initial decrease in total scaphoid BMD could be a result of the actual fracture healing process and of wrist immobilization but possibly also of trauma-induced bone atrophy and reduced blood supply due to a (partially) disrupted vascular network. Also small fracture displacements could have contributed to the decrease in BMD.

During the subsequent phase at twelve and 26 weeks after first presentation, BMD, Tb.Th, stiffness, and FL did not further decrease but stabilized or increased. Nevertheless, all parameters except Tb.Th remained significantly different from baseline at 26 weeks after first presentation. The reduced BMD compared to baseline

at 12 weeks agrees with the above-mentioned case series that reported continued resorption in two out of the five patients nine to 16 weeks post-fracture [32]. Combined with the considerable changes between twelve and 26 weeks, our findings suggest that the healing of scaphoid fractures is a slow process that takes months after cast removal and is not completed at 26 weeks. Physical and radiographical assessment of bone union, on which cast removal is based, seem thus not to coincide with densitometric, microarchitectural, and biomechanical recovery. So, activities of daily life may not require full biomechanical recovery, supporting the clinical advice to increase wrist loading gradually as pain allows after cast removal, as previously also noted in an HR-pQCT study on distal radius fracture healing [20]. Studies have reported significant associations between (changes in) μ FE-parameters and (changes in) patient reported pain and function outcome measures during healing in patients with a distal radius fracture [33,34]. Further research is encouraged to investigate the association between biomechanical recovery and functional outcome of scaphoid fractures and to identify whether time to cast removal could influence biomechanical recovery, which in turn may help to optimize guidelines for conservative treatment strategies for (nondisplaced) scaphoid fractures [35].

Our findings show differences from results of HR-pQCT studies on the healing of conservatively-treated distal radius fractures [19,20]. For example, we observed hardly identifiable and indistinguishable trabeculae around the fracture line at six and 12 weeks, while similar 'blurring' of trabecular structures was seen at already three to four weeks in the healing of distal radius fractures. Combined with a coinciding increase in trabecular BMD, this observation in the distal radius fractures was earlier suggested to reflect woven bone formation [19]. We did not find a coinciding increase in BMD, but that may among others be due to the subtlety of the scaphoid fractures and consequently of the 'blurred' trabecular region, especially when compared to more compressed distal radius fractures. Additionally, we found opposite changes in BMD, Tb. Th, and Tb.Sp, and FL during the first 12 weeks of healing compared to the HR-pQCT studies on distal radius fracture healing. Although our sample size does not allow generalization of the findings, this could imply possible differences in the healing process and timing of scaphoid fractures compared to distal radius fractures. Possible differences could for example be related to the blood supply in the scaphoid bone, which is more tenuous and can be disrupted after fracture [36-38], possibly delaying hematoma formation and inflammation. However, the consequent effects on fracture healing remain to be elucidated as inflammation may play a different role in metaphyseal fracture healing than known from diaphyseal fracture healing [15]. Also, (external) callus formation, found in mechanically unstable distal radius fractures probably from periosteum of the neighboring shaft [15], is less likely in scaphoid fractures due to the predominance of articular cartilage and thus lack of periosteum

as well as a limited surrounding space in the wrist [39]. Consequently, excessive inter-fragmentary micromotion due to fracture instability, fracture fragmentation, and finger movements [24,40] may disrupt or delay the formation of osseous bridges between fracture fragments that seems to be important in metaphyseal fracture healing [15]. Future studies on scaphoid fracture healing should investigate the role of vascularity and micromotion on scaphoid fracture healing. Further, they should include a separate analysis of the fractured and intact region of the scaphoid bone including study of bone formation and resorption for varying threshold values in both subregions to investigate changes at the fracture region more detailed as recently done by Atkins *et al.* in distal radius fractures [41]. Additionally, future research should evaluate the other carpal bones longitudinally, which may provide insights into the possible effects of bone atrophy and wrist immobilization that could impact both the scaphoid bone and surrounding carpal bones.

The ability to assess the healing of scaphoid fractures on the microarchitectural level *in vivo* may improve knowledge about the healing process in general and for example the development of scaphoid nonunion in particular. For example, study of the healing of different scaphoid fracture types may provide new insights into the healing process and the timing of healing of the various fracture types and also into possible differences between the types (*e.g.* proximal pole fractures that can be more challenging fractures than other scaphoid fracture types). Such insights could possibly help to optimize treatment strategy for each fracture type. Further, the use of HR-pQCT could improve knowledge about developing scaphoid nonunion and possibly reveal changes in microarchitecture between patients with and without developing nonunion. In an *ex vivo* study using micro-CT, it was earlier reported that bone density and trabecular microarchitecture of the proximal and distal portions of excised scaphoid nonunion specimens were significantly different from the same regions of nonfractured scaphoid bones [42]. In our cohort, two patients had a surgical intervention due to a suspected scaphoid nonunion on radiography, CT, and HR-pQCT at 12 weeks, and good-quality scan data of these two patients showed a considerably larger decrease from baseline in Tb.Th at three, six, and 12 weeks compared to the other patients. However, the exploratory design of our study did not allow evaluation of whether early longitudinal changes differed significantly between patients with and without a suspected scaphoid nonunion and of whether such early changes could possibly help to predict a nonunion, which in turn requires further study.

Despite the novelty of this study, it has several limitations. First, the small dataset did not allow generalization of our findings as well as inclusion of covariates, such as age, gender, and fracture type, in the linear mixed-effects models to explore their influence on fracture healing. Further, we did not adjust for multiple comparisons as that would

be at the expense of the power of the study, which was already limited by our sample size. This may increase the risk of type-II errors, but that is acceptable due to the explorative and fundamental nature of this study. Second, the additional thumb cast, only worn during scan acquisition to reduce motion artefacts [21], was not yet used at baseline in one patient, but all data of this patient were included as the thumb cast was single-layered and may thus have had limited effect on radiation absorption and consequently bone parameters. Third, the ‘blurring’ of trabecular structures around the fracture line at six and 12 weeks could affect the bone parameters as earlier also reported in an HR-pQCT study on distal radius fractures [19] although the amount of ‘blurring’ and callus was relatively small compared to that observed in the distal radius fractures. To take into account these lower mineralized ‘blurred’ structures and study the fracture healing in more detail, additional analyses were performed for varying threshold values as suggested by Atkins *et al.* [41] in the entire scaphoid bone. However, these analyses did not reveal new insights compared to using the default threshold value as the relative changes over time were very similar for all chosen thresholds (data not shown). Similarly, fracture size relative to the entire scaphoid bone volume may influence longitudinal changes in BMD and microarchitecture, which are averaged over the entire bone volume, and may have also contributed to the considerable interindividual variation found. We evaluated the bone parameters in the entire scaphoid bone to assess the changes in the entire bone during healing, but as mentioned earlier, further research into scaphoid fracture healing should include separate analysis of the fractured and intact bone region including analysis for multiple threshold values in both subregions [41]. Fourth, the irregular and complex shape of the scaphoid bone challenged μ FE-analysis. *In vivo*, scaphoid bones may experience a combination of force and moment components [40]. While the applied force in our simulation may cause a moment component considering the curved shape of the scaphoid bone, *in vivo* loading conditions are more complex. However, although other approaches (*e.g.* other boundary conditions, material properties, or loading directions) may have been possible, and the used Pistoia criterion is not validated for scaphoid bones, the consequent use of one approach and one criterion allowed study of longitudinal changes aimed for. Fifth, due to the novelty of the application, data on the reproducibility of HR-pQCT scanning and contouring of the scaphoid bone are scarce. Recently, we have investigated the interobserver variability of the contouring process. Our results showed that the median of the mean and maximum distance between the contours was 0.004 mm and 0.245 mm, respectively [43]. Further, we reported small but significant differences (< 1%) in density and trabecular microarchitecture between automatic contours without and with manual corrections [21], which might suggest a relatively small effect of correcting the contours. Nevertheless, the influence of motion artefacts and manual contour corrections on bone parameters is unknown and requires future research. Finally, no scans of the

contralateral scaphoid bone were available to explore the extent to which the fractured scaphoid bone restored to pre-fracture values, provided that there is bilateral symmetry on the microarchitectural level. Instead, we could only compare with baseline data, which may not well represent pre-fracture values as for example small fractures can already substantially affect biomechanical parameters. It should be considered to include contralateral scans in future HR-pQCT studies on scaphoid fracture healing.

To conclude, HR-pQCT imaging can provide new insights into the healing of scaphoid fractures. In this explorative study, we found that the healing of the conservatively-treated scaphoid fractures was initiated by significant decreases in bone mineral density, trabecular thickness, and failure load until 6 weeks after first presentation at the emergency department, followed by stabilization or increase of these parameters. Density, bone microarchitecture, and failure load did not return to their baseline values at 26 weeks after first presentation.

REFERENCES

- [1] Hove ML. Epidemiology of scaphoid fractures in Bergen, Norway. *Scand J Plast Reconstr Surg Hand Surg.* 1999;33(4):423–426.
- [2] Van Onselen EBH, Karim RB, Hage JJ, Ritt MJPF. Prevalence and distribution of hand fractures. *J Hand Surg.* 2003;28:491–495.
- [3] Leslie I, Dickson R. The fractured carpal scaphoid. Natural history and factors influencing outcome. *J Bone Joint Surg Br.* 1981;63-B(2):225–230.
- [4] Duckworth AD, Jenkins PJ, Aitken SA, Clement ND, Court-Brown CM, McQueen MM. Scaphoid fracture epidemiology. *J Trauma Acute Care Surg.* 2012;72(2):E41.
- [5] Wong K, Von Schroeder HP. Delays and poor management of scaphoid fractures: factors contributing to nonunion. *J Hand Surg.* 2011;36(9):1471–1474.
- [6] Filan SL, Herbert TJ. Herbert screw fixation of scaphoid fractures. *J Bone Joint Surg.* 1996;78-B:519–529.
- [7] Langhoff O, Andersen JL. Consequences of late immobilization of scaphoid fractures. *J Hand Surg.* 1988;13(1):77–79.
- [8] Mack GR, Bosse MJ, Gelberman RH, Yu E. The natural history of scaphoid non-union. *J Bone Joint Surg Am.* 1984;66(4):504–509.
- [9] Ruby LK, Leslie BM. Wrist arthritis associated with scaphoid nonunion. *Hand Clin.* 1987;3(4):529–539.
- [10] Pinder RM, Brkljac M, Rix L, Muir L, Brewster M. Treatment of scaphoid nonunion: a systematic review of the existing evidence. *J Hand Surg.* 2015;40(9):1797–1805.
- [11] Dias JJ, Taylor M, Thompson J, Brenkel IJ, Gregg PJ. Radiographic signs of union of scaphoid fractures. An analysis of inter-observer agreement and reproducibility. *J Bone Joint Surg Br.* 1988;70(2):299–301.
- [12] Hackney LA, Dodds SD. Assessment of scaphoid fracture healing. *Curr Rev Musculoskelet Med.* 2011;4(1):16–22.
- [13] Hannemann PFW, Brouwers L, van der Zee D, et al. Multiplanar reconstruction computed tomography for diagnosis of scaphoid waist fracture union: a prospective cohort analysis of accuracy and precision. *Skelet Radiol.* 2013;42:1377–1382.
- [14] Daniels AM, Bevers MSAM, Wyers CE, et al. Improved detection of scaphoid fractures with high resolution peripheral quantitative computed tomography compared to conventional CT. *J Bone Joint Surg.* 2020;102(24):2138–2145.
- [15] Sandberg OH, Aspenberg P. Inter-trabecular bone formation: a specific mechanism for healing of cancellous bone: a narrative review. *Acta Orthop.* 2016;87(5):459–465.
- [16] Inoue S, Otsuka H, Takito J, Nakamura M. Decisive differences in the bone repair processes of the metaphysis and diaphysis in young mice. *Bone Reports.* 2018;81–88.
- [17] Charnley J, Baker SL. Compression arthrodesis of the knee: a clinical and histological study. *J Bone Joint Surg Br.* 1952;34(2):187–199.
- [18] Aspenberg P, Sandberg OH. Distal radial fractures heal by direct woven bone formation. *Acta Orthop.* 2013;84(3):297–300.
- [19] de Jong JJ, Willems PC, Arts JJ, et al. Assessment of the healing process in distal radius fractures by high resolution peripheral quantitative computed tomography. *Bone.* 2014;64:65–74.
- [20] de Jong JJ, Heyer FL, Arts JJ, et al. Fracture repair in the distal radius in postmenopausal women: a follow-up 2 years postfracture using HRpQCT. *J Bone Miner Res.* 2016;31(5):1114–1122.

- [21] Bevers MSAM, Daniels AM, Wyers CE, et al. The feasibility of high-resolution peripheral quantitative computed tomography (HR-pQCT) in patients with suspected scaphoid fractures. *J Clin Densitom.* 2019;23(3):432–442.
- [22] Daniels AM, Wyers CE, Janzing HM, et al. The interobserver reliability of the diagnosis and classification of scaphoid fractures using high-resolution peripheral quantitative CT. *Bone Joint J.* 2020;102(4):478–484.
- [23] Pialat JB, Burghardt AJ, Sode M, Link TM, Majumdar S. Visual grading of motion induced image degradation in high resolution peripheral computed tomography: impact of image quality on measures of bone density and micro-architecture. *Bone.* 2012;50(1):111–118.
- [24] Herbert TJ, Fisher WE. Management of the fractured scaphoid using a new bone screw. *J Bone Joint Surg Br.* 1984;66(1):114–123.
- [25] Burghardt AJ, Buie HR, Laib A, Majumdar S, Boyd SK. Reproducibility of direct quantitative measures of cortical bone micro-architecture of the distal radius and tibia by HR-pQCT. *Bone.* 2010;47(3):519–528.
- [26] Su-Bum AL, Hyo-Jin BK, Jae-Myeung CC, et al. Osseous microarchitecture of the scaphoid: cadaveric study of regional variations and clinical implications. *Clin Anat.* 2012;25(2):203–211.
- [27] Hildebrand T, Rüegsegger P. A new method for the model-independent assessment of thickness in three-dimensional images. *J Microsc.* 1997;185(1):67–75.
- [28] van Rietbergen B, Weinans H, Huiskes R, Odgaard A. A new method to determine trabecular bone elastic properties and loading using micromechanical finite-element models. *J Biomech.* 1995;28(1):69–81.
- [29] Pistoia W, van Rietbergen B, Lochmüller E-M, Lill CA, Eckstein F, Rüegsegger P. Estimation of distal radius failure load with micro-finite element analysis models based on three-dimensional peripheral quantitative computed tomography images. *Bone.* 2012;30(6):842–848.
- [30] Ellouz R, Chapurlat R, van Rietbergen B, Christen P, Pialat J, Boutroy S. Challenges in longitudinal measurements with HR-pQCT: evaluation of a 3D registration method to improve bone microarchitecture and strength measurement reproducibility. *Bone.* 2014;63:147–157.
- [31] Madeley NJ, Stephen AB, Downing ND, Davis TRC. Changes in scaphoid bone density after acute fracture. *J Hand Surg.* 2006;31(4):368–370.
- [32] Fan S, Suh N, Grewal R. Observation of bony resorption during scaphoid fracture healing: a case series. *J Hand Surg Eur.* 2020;45(8):874–876.
- [33] Heyer FL, de Jong JJA, Willems PC, et al. Long-term functional outcome of distal radius fractures is associated with early post-fracture bone stiffness of the fracture region: an HR-pQCT exploratory study. *Bone.* 2019;127:510–516.
- [34] Spanswick PJC, Whittier DE, Kwong C, Korley R, Boyd SK, Schneider PS. Improvements in radiographic and clinical assessment of distal radius fracture healing by FE-estimated bone stiffness. *Bone Rep.* 2021;14:100748.
- [35] Paulus MC, Braunstein J, Merenstein D, et al. Variability in orthopedic surgeon treatment preferences for nondisplaced scaphoid fractures: a cross-sectional survey. *J Orthop.* 2016;13(4):337–342.
- [36] Gelberman RH, Menon J. The vascularity of the scaphoid bone. *J Hand Surg.* 1980;5(5):508–513.
- [37] Panagis JS, Gelberman RH, Taleisnik J, Baumgaertner M. The arterial anatomy of the human carpus. Part II: the intraosseous vascularity. *J Hand Surg.* 1983;8(4):375–382.
- [38] Morsy M, Sabbagh MD, van Alphen NA, Laungani AT, Kadar A, Moran SL. The vascular anatomy of the scaphoid: new discoveries using micro-computed tomography imaging. *J Hand Surg Am.* 2019;44(11):928–938.

- [39] Slade III JF, Dodds SD. Minimally invasive management of scaphoid nonunions. *Clin Orthop Relat Res.* 2006;445:108–119.
- [40] Erhart J, Unger E, Schefzig P, et al. In vitro experimental investigation of the forces and torque acting on the scaphoid during light grasp. *J Orthop Res.* 2016;34:1734–1742.
- [41] Atkins PR, Stock K, Ohs N, et al. Formation dominates resorption with increasing mineralized density and time postfracture in cortical but not trabecular bone: a longitudinal HRpQCT imaging study in the distal radius. *JBMR Plus.* 2021;5(6):e10493.
- [42] Qu G, Von Schroeder HP. Trabecular microstructure at the human scaphoid nonunion. *J Hand Surg.* 2008;33(5):650–655.
- [43] Bevers MSAM, Wyers CE, Daniels AM, et al. Association between bone shape and the presence of a fracture in patients with a clinically suspected scaphoid fracture. *J Biomech.* 2021.



11

Chapter 11

General discussion

The objective of this thesis was to study the use of high-resolution peripheral quantitative computed tomography (HR-pQCT) to assess bone microarchitecture and strength in (rare) bone-affecting conditions, the response to treatment with anti-osteoporosis medication (AOM), and distal radius and scaphoid fractures. **Chapters 2-5** of this thesis described the assessment of bone microarchitecture and strength using HR-pQCT in osteogenesis imperfecta (OI) and fibrodysplasia ossificans progressiva (FOP) and in response to AOM-treatment in glucocorticoid-induced osteoporosis (GIOP) and pregnancy- and lactation-associated osteoporosis (PLO). **Chapters 6-10** described the use of HR-pQCT for the assessment of distal radius fracture healing and for the diagnosis and healing assessment of scaphoid fractures. In this chapter, the main findings, clinical implications, and limitations of the studies presented in this thesis are discussed, followed by a conclusion and future perspectives.

BONE MICROARCHITECTURE AND STRENGTH IN DISEASE

Osteogenesis imperfecta

OI is a rare and clinically heterogeneous disorder associated with structural and material bone defects and a consequent increased fracture risk [1-3]. In **Chapter 2**, we investigated bone microarchitecture and strength in a large cohort of 118 adults with OI and addressed the use of HR-pQCT in this disorder, related to the occurrence of short stature and bone deformities in OI [1]. Our study demonstrated that HR-pQCT can be used for bone microarchitecture and strength assessments in adults with OI, but that several aspects require attention. For example, we could obtain HR-pQCT scans without difficulties in most study participants, but the standard patient positioning had to be adjusted in some to enable scan acquisition. Furthermore, the scan region can be influenced by short extremities, bone deformities such as bending or changed anatomic alignments after fracture, and positioning difficulties (*e.g.* inability to fully extend the knee for the tibia scan). To minimize the influence of short extremities, we used an extremity-length dependent scan protocol instead of the standard, non-extremity-length dependent protocol [4]. Use of the standard protocol could lead to relatively proximal scan regions in short extremities as the scan region in that protocol is located at a fixed distance from the distal endplate of the radius and tibia. It might influence HR-pQCT parameters and thereby reduce the accuracy of comparisons between study groups and with normative data. This protocol has nevertheless been used in previous comparative HR-pQCT studies in OI [5-7]. However, given the subjectivity of measuring extremity length, further research is needed to determine whether an extremity-length dependent protocol leads to different HR-pQCT parameters than the standard scan protocol. To objectively detect potential other deviations in the scan region in our cohort, we developed an algorithm to quantify the

axial angle of the HR-pQCT scans. Using the axial angle of available HR-pQCT scans of a small group of young women as reference, we considered 11% of the radius scans and 13% of the tibia scans in our cohort as having a deviated axial angle. Z -scores < -4 or > 4 occurred more frequently for total and trabecular parameters in these scans than in the scans without deviated axial angle. Firm conclusions could not be drawn from these findings due to the limitations of our approach to detect deviated scan regions: we defined the deviation of a scan region by the axial scan angle, which may not detect all possible deviated scan regions due to bone deformities, and based the definition of a deviated axial angle on HR-pQCT data of a small group of young women. Our findings nevertheless demonstrate that deviations of the scan region may be important to consider when using HR-pQCT in OI.

Another aspect is the reliability of standard HR-pQCT analyses in OI due to microarchitectural inhomogeneities. We observed large trabecular void volumes, which corresponded with non-meaningful values for trabecular number and separation. Local sclerotic regions in the trabecular compartment did not result in similarly extreme values for trabecular thickness but may nevertheless influence the interpretation of this parameter. Other inhomogeneities were not included in the analyses (*e.g.* locally increased periosteal porosity with mineralization densities below the density threshold for segmentation) or are not evaluated using standard analyses (*e.g.* coarse periosteal surfaces). To get a more complete impression of the microarchitectural inhomogeneities in OI, advanced HR-pQCT analyses would be valuable. For example, evaluation of the variation of HR-pQCT parameters of cortical and trabecular microarchitecture gives more objective insights into the microarchitectural heterogeneity in the cortical and trabecular compartment, and the use of multiple segmentation thresholds would enable quantification of the amount of lower-mineralized bone tissue observed mainly near the periosteal surface. Besides that, an algorithm may be developed to quantify local sclerotic regions in the trabecular bone. An algorithm to quantify trabecular void volumes has recently been developed [8], which showed that exclusion of void volumes from the HR-pQCT analyses improved trabecular parameters in adults from normative datasets [8]. It would be of interest to apply the same algorithm to HR-pQCT scans of the OI-population to explore the prevalence and size of trabecular void volumes in OI as compared to in non-OI populations and to evaluate trabecular microarchitecture in OI after exclusion of such void volumes from the HR-pQCT analyses.

Besides these methodological aspects, our study revealed that BMD, bone microarchitecture, and strength were reduced in OI as compared to age- and gender-matched controls from normative data. While the microarchitectural parameters may need correction due to the microarchitectural heterogeneities, parameters from

micro-finite element (μ FE-) analysis take into account the heterogeneities and thus do not have to be corrected for the heterogeneities. Up to 5% of the participants had a Z -score < -4 for stiffness and failure load (FL) from μ FE-analysis. It is yet unknown to what extent the bone strength estimates from HR-pQCT reflect the actual bone strength and fracture risk in OI as these estimates are based on solely structural properties of bone, while the material properties can also be affected in OI [9]. Our results may thus overestimate the actual bone strength in OI and thus demonstrate the impairment of the bone strength already due to the structural defects of bone. The detailed insights from HR-pQCT cannot be obtained using dual-energy X-ray absorptiometry (DXA), which is clinically used to evaluate bone quality by assessing areal bone mineral density (aBMD). aBMD may, as a single two-dimensional parameter, not fully describe the complexity and heterogeneity of OI. The insights from HR-pQCT may help to improve treatments in OI for the reduced structural bone quality. Specifically, our findings suggest that it could be of potential added value to perform clinical trials on the effects of anabolic AOMs in OI, which by their mechanism of action could improve bone microarchitecture [10]. This is important as the optimal treatment strategy for the reduced bone quality in OI is unknown, and clinical data on the effects of AOMs in OI are scarce [11].

Fibrodysplasia ossificans progressiva

FOP is a rare disorder characterized by the progressive formation of heterotopic ossifications (HOs) in ligaments, tendons, and muscles [12]. Microscopic study of HO is limited in FOP because invasive medical interventions (*e.g.* bone biopsies) are contraindicated in this disorder as they can trigger HO formation [13,14]. In **Chapter 3**, we explored the use of HR-pQCT in FOP. In two patients, we could obtain HR-pQCT scans of isolated HO in the left Achilles tendon and non-isolated HO around both metatarsals of one patient and of non-isolated HO around the right ankle of the other patient. The isolated and non-isolated HO had a cortical and trabecular compartment. Qualitative assessment of the non-isolated HO revealed fusion with the neighboring skeletal bone with development of a new cortex and remodeling of the original skeletal cortex at the sites of fusion into trabeculae. A thin lining of the original cortex suggested a yet incomplete coalescence, which indicated that the fusion and remodeling progress slowly considering the long presence of the HO in the patients. The isolated HO in the Achilles tendon could also be quantitatively evaluated, which revealed a low BMD as compared to normative tibia data and similar trabecular microarchitecture. These findings confirmed previous suggestions of normal modeling and remodeling and cortical and trabecular organization in HO based on macroscopic data [15].

Although HR-pQCT could contribute to an improved understanding of HO, its application to FOP may be impracticable considering the challenges we experienced. For example, the patients had to be positioned very carefully to prevent any inordinate movements that could potentially trigger HO formation. Furthermore, the patients' mobility was largely restricted due to HO and consequent ankylosis [12,14]. Correspondingly, we could not obtain HR-pQCT scans of the right distal radius of one patient, of both distal radii of the other patient, and of HO around the left ankle and around both metatarsals of one of the patients. Additionally, the evaluation of HO using HR-pQCT is limited to peripherally-located HO, while HO formation in FOP generally starts in the axial skeleton and from proximal to distal regions [12,14]. Besides that, quantitative evaluation of non-isolated HO is challenging because of the difficulty to separate non-isolated HO from neighboring skeletal bone. Future use of HR-pQCT in this disorder may thus be limited.

BONE MICROARCHITECTURE AND STRENGTH WITH TREATMENT

Denosumab and risedronate in glucocorticoid-induced osteoporosis

GIOP is among the most common forms of secondary osteoporosis and induced by glucocorticoids (GCs). In a recent randomized clinical trial on GC-users, it was found that denosumab resulted in larger gains in aBMD than risedronate, which is a current option for AOM-treatment in GC-users [16,17]. The effects of both AOMs on bone microarchitecture and strength in GC-users were not evaluated. In **Chapter 4**, we evaluated these effects in a subgroup of 110 participants of the clinical trial and showed that denosumab could preserve bone strength in GC-initiators (GC-treatment for < 3 months) and improve bone strength in GC-continuers (GC-treatment for \geq 3 months), while risedronate could not. The mean changes in bone strength with denosumab and risedronate were small and smaller than least-significant changes (LSCs) [18], but that does not necessarily mean that they are clinically irrelevant as changes below LSCs at the group level do not exclude changes beyond LSCs in individuals within the group. For example, treatment-related changes in aBMD that were associated with fracture reductions in a meta-analysis of data from mainly postmenopausal women [19] are smaller than corresponding LSCs [20,21]. It is unknown which, and to what extent, changes in HR-pQCT parameters might be associated with fracture reductions in GIOP. Nevertheless, our findings suggest, together with the findings of the main study [16,17], that denosumab could be a useful additional treatment option in GC-users. The availability of multiple treatment options is valuable in this patient population due to the diversity in diseases for which GC-treatment is prescribed [22] and the consequent possible variability in treatment effects. There was also variability

in the diseases for which GC-treatment was described in our study, but the sample size did not allow evaluation of potential differences in the effects of denosumab and risedronate among subgroups.

By using HR-pQCT, we also provided insights into the effects of both AOMs on bone microarchitecture. The changes after 24 months in cortical volume, BMD, and microarchitecture at the distal radius in GC-initiators suggested that denosumab could lead to the filling of existing resorption pits and the appearance of fewer new ones in the cortex and at the endosteal zone between the cortical and trabecular compartment. This suggestion is in line with previous findings after 24 months in postmenopausal women [23]. The same cortical changes were not found with risedronate, which could be explained by the differences in the mechanism of action of denosumab and bisphosphonates, such as risedronate [24]. The changes with and differences between the two AOMs were smaller at the distal tibia, which suggests an influence of the mechanical loading of the bones. Our hypothesis on the endosteal changes with denosumab and risedronate could not be confirmed by the standard HR-pQCT parameters. However, algorithms have been developed to quantify cortical porosity at the endosteal zone and microarchitectural changes in this zone using HR-pQCT [25,26], which may be used for further evaluation of the effects of denosumab and risedronate in GC-users.

The value of HR-pQCT to monitor treatment effects in GIOP could potentially be in the scarcity of fracture data in this disease. Previous clinical trials on AOM-treatment in GIOP were often not powered to evaluate fracture reduction, and changes in aBMD from DXA were used as primary outcome [22]. aBMD has been suggested as a surrogate marker for fracture outcome in clinical trials based on the association with fracture reduction found in a meta-analysis of data from mainly postmenopausal women [19]. This association is yet not necessarily extrapolatable to GIOP due to differences in pathophysiology between GIOP and postmenopausal osteoporosis and a higher fracture risk at similar aBMD values in GC-users than non-users within postmenopausal women [22,27]. Also the diversity in diseases for which GC-treatment is prescribed may not allow for an extrapolation of the association found in postmenopausal women. HR-pQCT then provides more detailed insights into treatment effects than DXA. HR-pQCT parameters have been found to be associated with fracture risk [18,28], but associations between treatment-related changes and fracture reductions are unknown. More research is therefore needed to determine the value of HR-pQCT in monitoring treatment effects in clinical trials, in GIOP as well as in other diseases.

Teriparatide and zoledronic acid in pregnancy- and lactation-associated osteoporosis

PLO is a rare form of secondary osteoporosis. Its pathophysiology is only partly known, and various factors could play a role in the development of PLO [29,30]. Correspondingly, optimal treatment is unknown and requires an individualized approach [29]. In **Chapter 5**, we evaluated the effects of AOM-treatment using HR-pQCT in a severe presentation of PLO in a woman with multiple vertebral fractures and back pain after her first pregnancy. BMD, microarchitecture, and strength from HR-pQCT were highly reduced in the woman at seven months postpartum as compared to normative data. Treatment of one year of teriparatide followed by one zoledronic acid infusion resulted in substantial improvements of BMD, microarchitecture, and strength at the distal radius. In contrast, the largest improvements at the distal tibiae occurred before treatment was initiated, which suggested spontaneous recovery and effects of the physiotherapy followed postpartum. The improvements of several parameters at the distal radius and of most parameters at the distal tibia greatly exceeded LSCs [31]. Despite the improvements, BMD, microarchitecture, and strength remained severely impaired at forty months postpartum as compared to normative data. Since no data were available before pregnancy, it cannot be excluded that the woman may have had an impaired bone quality before pregnancy that deteriorated during pregnancy and lactation. A monogenic cause could not be found in this woman, but the occurrence of osteoporosis and osteopenia in the woman's mother, father, and sister as well as similar cortical discrepancies in the mother's HR-pQCT scans suggested a polygenic origin with unknown contribution of both parents' side.

The value of HR-pQCT to monitor the effects of AOM-treatment at an individual level requires further exploration. DXA is clinically used to evaluate bone quality and fracture risk and to diagnose postmenopausal osteoporosis [32]. Although fracture rates are higher in patients with osteoporosis than in those without and increase with decreasing femoral neck aBMD [33,34], a large proportion of fractures occur in men and women without osteoporosis [34]. DXA thus does not always fully explain a patient's bone quality in relation to the clinical presentation. In such cases, HR-pQCT may provide valuable additional insights. Indeed, HR-pQCT parameters have been found to be significantly associated with fracture risk after adjusting for femoral neck aBMD, albeit with small hazard ratios [28]. Similarly, a set of HR-pQCT parameters and age modestly outperformed a combination of femoral neck aBMD and clinical characteristics in fracture prediction [35]. In our case with PLO, HR-pQCT showed the remaining impairment of BMD, bone microarchitecture, and strength after treatment at forty weeks postpartum. It raised the question whether further treatment was needed in this woman, but treatment strategies based on (solely) HR-pQCT are not advised as HR-pQCT is not incorporated in current guidelines for AOM-

treatment. Therefore, the benefits of HR-pQCT to guide decisions at the individual level in clinical practice requires further elucidation, also including cost-effectiveness.

ASSESSMENT OF DISTAL RADIUS AND SCAPHOID FRACTURES

Distal radius fracture healing

Continuing previous studies of our research group into distal radius fracture healing [36,37], we investigated in **Chapter 6** the contribution of lower-mineralized tissue to stiffness by adopting an approach that combines stiffness results from two series of μ FE-models generated from HR-pQCT scans using either single- or dual-threshold bone segmentation. Our results showed that the contribution of lower-mineralized tissue to stiffness increased during the early phases of fracture healing and decreased thereafter. A similar course was found for the contribution of lower-mineralized tissue to bone volume fraction. It suggested formation of lower-mineralized tissue early during healing and subsequent remodeling, which is consistent with visual changes observed around the fracture region and with the general understanding of fracture healing [36,38,39]. While the course of the contribution of lower-mineralized tissue during healing may be physiologically accurate, the magnitude of the contribution was likely less accurate due to the used methodology, including the steps taken to generate the dual-threshold μ FE-models and the material properties of the lower-mineralized tissue used in these models. Regarding the latter, we used different values for the Young's Modulus of the lower-mineralized tissue in separate analyses; however, it is unknown whether the chosen values are physiologically accurate, and the material properties may furthermore not be constant for all woven bone around the fracture region nor during the fracture healing process [40].

Our study additionally showed that the changes in the contribution of lower-mineralized tissue to stiffness preceded the improvement in stiffness. It suggests, together with the changes in the contribution of lower-mineralized tissue to bone volume fraction during healing, that mature bone predominantly contributes to the recovery of biomechanical strength after fracture and that lower-mineralized tissue has a minor role. The stiffness might increase until months after cast removal [37], which implies that the biomechanical and clinical perspective of a healed fracture differ from each other. The contribution of lower-mineralized tissue to the stiffness early during healing could contribute to explaining this difference; the lower-mineralized tissue possibly provides sufficient initial fracture stabilization for cast removal. Quantification of the contribution of this tissue to stiffness may thus be clinically relevant. It furthermore gives a more complete impression of strength recovery post-fracture

than the evaluation of stiffness using a single series of μ FE-models. A disadvantage of this approach is that performing μ FE-analyses is time-consuming, even more when a μ FE-model is based on multi-stack HR-pQCT data (as in distal radius fractures). The contribution of lower-mineralized tissue to bone volume fraction could be an alternative measure, which is easier and faster to compute. All in all, quantification of lower-mineralized tissue in fractures may be an objective and clinically valuable indication for the extent of fracture healing and the biomechanical recovery over time.

Nevertheless, there are several methodological limitations of this approach. For example, the periosteal contours obtained with the standard contouring algorithm for HR-pQCT visually deviated largely from the outer bone margins of the fractured distal radii, requiring manual adjustment in most scans in our study. Manual adjustment can be highly subjective, particularly in largely compressed fractures and due to lower-mineralized tissue formation. To limit interobserver variability, all periosteal contours were adjusted by one investigator in our study. The endosteal contours were not inspected but are also prone to errors. μ FE-parameters are then preferred as they are not influenced by the periosteal and endosteal contouring as long as all bone is included and the same material properties are assigned to the cortical and trabecular bone. Another limitation is the difficulty to align the scanned bone regions between timepoints. Three-dimensional registration yielded incorrect alignment results in severe distal radius fractures due to dislocations during healing [41,42]. Therefore, the baseline and follow-up scans were not registered in our study, which may have caused differences in scan region between timepoints (*e.g.* due to repositioning errors and the reference line positioning at the lunate bone, which position with respect to the distal radius is not fixed). An alignment approach based on registering fracture fragments may possibly yield better results than the evaluated approaches based on registering entire bone regions [43]. A third limitation is the cast worn during scan acquisition. Casts can cause beam hardening, particularly Plaster-of-Paris casts [44,45]. We aimed to prevent possible effects of the cast by using a fiberglass cast at each visit and retaining it for re-use after cast removal, but this could not be achieved in all patients related to the visits at the outpatient clinic. Consequently, several patients wore Plaster-of-Paris casts at several visits, no casts, or braces. We did not adjust our analyses for the differences in casts due to the limited availability of correction factors. A final issue are motion artefacts, including stack shifts, which are further discussed below. These methodological limitations may reduce the reproducibility and influence (changes in) HR-pQCT parameters during healing. It challenges interpretation, more at an individual level than at the group level where results are averaged over an entire group. Fracture-related factors (*e.g.* compression, fragmentation, and secondary dislocation) further challenge interpretation. As a result, HR-pQCT and our approach may at this

point be especially useful at the group level in clinical studies, where a combination of objective and subjective measures is recommended [46].

Scaphoid fracture diagnosis and healing

Fractures of the scaphoid bone, a carpal bone with unique vascularization and anatomy, are the most common carpal bone fractures. Early and accurate diagnosis and adequate healing monitoring of these fractures are important to reduce the risk of scaphoid nonunion and the consequent degenerative changes and development of osteoarthritis [47,48]. However, diagnosis and healing monitoring are challenging: various imaging modalities are used clinically, and it cannot be excluded that scaphoid fractures are missed with these modalities [49]. Given its high resolution, we studied the potential of using HR-pQCT for these purposes. As the application of HR-pQCT to scaphoid fractures was never published before, we first evaluated this application in **Chapter 7**. Our study demonstrated that HR-pQCT can be used in patients with a clinically suspected scaphoid fracture when a cast with thumb part is used during scan acquisition to reduce motion artefacts. Furthermore, we showed that quantitative analysis of the scaphoid bone is possible using HR-pQCT with minor adjustments of standard protocols (*e.g.* the standard contouring algorithm with a lower density threshold and applied to coarse hand-drawn pre-contours for a correct contouring of the scaphoid bone). These findings encouraged us to evaluate the use of HR-pQCT for scaphoid fracture diagnosis and healing assessment.

In **Chapter 8**, we evaluated the diagnostic performance of HR-pQCT as compared to conventional CT when used at 1-2 weeks after initial presentation in the hospital. While CT revealed a scaphoid fracture in 15 out of the 91 included patients, HR-pQCT revealed a fracture in nine more patients (*i.e.* 24 patients; 60% more than CT). In another study, we additionally showed that the inter-observer reliability of the diagnosis of scaphoid fractures on HR-pQCT was high [50]. We did not evaluate the intra-observer variability nor the cost-effectiveness, which should be evaluated in future research. Also the clinical consequences of scaphoid fractures that are missed on conventional CT and seen on HR-pQCT are yet unknown. Other findings in our research group showed that the diagnostic value of clinical re-examination is limited and that initial radiography and clinical re-examination together also have limited diagnostic performance for scaphoid fractures compared to HR-pQCT [51]. All in all, our studies show that current diagnostic approaches (specifically clinical re-examination, initial radiography, and CT at 1-2 weeks after initial presentation) miss scaphoid fractures that are seen on HR-pQCT scans at 1-2 weeks after initial presentation. These findings have clinical implications (*i.e.* scaphoid fracture diagnosis) as well as implications for research (*i.e.* diagnostic tool used as reference). It is unknown whether HR-pQCT would have the same diagnostic performance when used at

initial presentation. Furthermore, it is unknown how the diagnostic performance of HR-pQCT compares with that of magnetic resonance imaging (MRI), which may have a higher sensitivity, specificity, and accuracy than CT although the lack of a reference standard makes comparison of the performance of imaging modalities for scaphoid fracture diagnosis difficult [52,53]. Nevertheless, our findings show that high-resolution imaging may be advised for scaphoid fracture diagnosis; yet, HR-pQCT and other high-resolution imaging modalities are currently limited available in clinical practice.

Alternatively, clinical prediction rules combining various patient characteristics have been explored to estimate the probability of a true scaphoid fracture at presentation in the hospital [54-58]. Given the anatomic location of the scaphoid bone in the wrist and the curved shape of the bone [59,60], the shape of the scaphoid bone could also be a factor in scaphoid fracture susceptibility after a fall on the outstretched hand. In **Chapter 9**, we explored whether the presence of a scaphoid fracture is associated with the shape of the scaphoid bone as described by a statistical shape model (SSM) from HR-pQCT scans of 26 non-fractured and 15 fractured scaphoid bones. We found that four shape modes of this SSM together correctly classified 76% of the scaphoid bones as fractured or non-fractured, using the diagnosis on HR-pQCT as reference. These findings suggested that there may be an association between scaphoid bone shape and fracture presence. The existence of such association was strengthened by the lack of significant differences in age, gender, and the proportion of high-impact falls between the fractured and non-fractured scaphoid bones in the SSM, which were predictors of a true scaphoid fracture in previously investigated clinical decision rules [55-58]. Furthermore, we included only fractures without clearly visible fracture-related surface irregularities to prevent fracture-related shape effects. Nevertheless, contralateral or prospective data should be used in future studies. Another important limitation of our study was the small sample size and the consequent risk of overestimating the classification performance due to overfitting. Although regression models with one shape mode also enabled moderate to fair classification, the single modes explained only a small proportion of the total shape variance. It indicates the possibility of being a finding related to the small sample size although small particular shape variations could theoretically influence fracture susceptibility after a fall. Furthermore, we could not anatomically explain the shape differences between the fractured and non-fractured scaphoid bones in relation to the fracture mechanics, among others due to the mathematical nature of shape modes. Study in larger datasets is therefore highly needed before firm conclusions can be drawn on the association between scaphoid bone shape and fracture presence. If an association would exist, the use of image-based shape data in clinical decision rules may be evaluated to help to improve the diagnosis of scaphoid fractures when high-resolution modalities cannot be used.

In **Chapter 10**, we used HR-pQCT to explore scaphoid fracture healing in eleven patients with a scaphoid fracture confirmed on HR-pQCT. BMD, trabecular thickness, and bone strength decreased during the first six weeks of healing together with an increased visibility of the fracture line at three weeks. It was followed by a stabilization or increase in these parameters later during healing when trabecular structures became less well distinguishable. The trabecular ‘blurring’ may reflect the formation and subsequent remodeling of lower-mineralized tissue. The changes we found during healing differed from those previously found in distal radius fracture healing (*e.g.* initial increase in BMD, lower-mineralized tissue formation earlier during healing [36]). Although our findings cannot be generalized due to the small sample, they suggest differences in the healing process between scaphoid fractures and distal radius fractures. Such differences could be related to differences in fracture severity, vascularization, anatomy, and anatomic location. We could not statistically evaluate differences in the healing between fracture types (*e.g.* between proximal pole fractures and distal and waist fractures) nor between the participants who got a surgical intervention at follow-up due to a suspected scaphoid nonunion and the other participants without surgical intervention. Such evaluation, as well as early detection of a scaphoid nonunion, would however be highly valuable as nonunion is a problem in scaphoid fracture healing due to the unique vasculature and anatomy of the scaphoid bone, yet without superior treatment [61].

Several aspects should be considered when using HR-pQCT to evaluate scaphoid fracture healing. For example, we adjusted standard evaluation protocols to only compute trabecular parameters and include the cortex in this computation as the outer bone layer (being subchondral rather than cortical bone) had previously been found to approximate 1-1.5 times the trabecular thickness of scaphoid bones [62]. Furthermore, standard compression tests could not be directly applied to μ FE-models of the scaphoid bone due to the complex three-dimensional shape of the bone. We therefore aligned the scaphoid bone along its longest axis and placed it between two artificial plates. Other approaches are however possible for the evaluation of BMD, microarchitecture, and strength of the scaphoid bone, which could influence absolute values. Besides that, similar to our study on distal radius fracture healing, differences in casts between visits can influence intraindividual changes. However, we achieved to use the same cast at each visit and retain it for re-use after cast removal in all but one patient in our study on scaphoid fracture healing. In contrast to distal radius fracture healing studies, scan registration is not relevant when assessing scaphoid fracture healing as the entire scaphoid bone is scanned. Motion artefacts, including stack shifts, may play a larger role in scaphoid fractures than in distal radius fractures, which are discussed in more detail below.

Motion artefacts in multi-stack HR-pQCT

An important aspect in HR-pQCT are motion artefacts, even more in multi-stack HR-pQCT (as for distal radius and scaphoid fractures). Motion artefacts are inherent to the use of HR-pQCT due to the high resolution combined with the relatively long scan time (2 min for a standard single-stack scan). Scanning multi-stack HR-pQCT scans increases the risk of motion artefacts due to longer scan times (*e.g.* 4 min for a two-stack scan of a distal radius fracture and 6 min for a three-stack scan of the scaphoid bone). Also the scan location can increase the risk of motion artefacts (*e.g.* close to the thumb for scaphoid bone scans). While grading scales and evaluation guidelines have been developed for motion artefacts in single-stack HR-pQCT scans [63], the effects of motion artefacts on HR-pQCT parameters have not been studied in multi-stack scans. The effects may furthermore vary with the bone and number of stacks that is scanned. In our study on distal radius fracture healing (two-stack scans), we graded each stack using the quality grading scale for one-stack scans and excluded scans with insufficient quality in one or both stacks. In our study on scaphoid fracture healing (three-stack scans), this approach would have led to the exclusion of a large proportion of scans. It is unknown whether insufficient quality in one stack influences the value of multi-stack HR-pQCT parameters to a relevant extent: HR-pQCT parameters are averaged over the entire bone volume, which is unevenly distributed over the stacks. In our scaphoid fracture healing study, we therefore took into account the bone volume per stack when grading scan quality. The quality of each stack was again graded using the grading scale for one-stack HR-pQCT scans, but use of this scale in scaphoid scans could be subjective: the criterium on the continuity of the cortex is challenging to apply to the scaphoid bone as the outer layer of the scaphoid bone is thin and has small interruptions that reflect transcortical vascular entries.

Multi-stack HR-pQCT imaging furthermore introduces a new type of motion artefacts, stack shifts. The effects of stack shifts on HR-pQCT parameters are unknown, and grading scales for these shifts are lacking. We did not exclude scans with stack shifts from HR-pQCT analyses in our studies, which may have influenced intraindividual changes during fracture healing. In a previous HR-pQCT study on finger joints, stacks were scanned with partial overlap to enable alignment of the stacks by registration of the overlapping region [64]. Alternatively, in a pilot study, we artificially created a two-layer overlap between the stacks of two-stack scans of non-fractured distal radii, followed by three-dimensional rigid registration of the overlapping region to correct a stack shift. Using this algorithm, we found that the median absolute percentage change in stiffness after stack shift correction was < 1%. However, further study on the need and the effects of a stack shift correction is required. The effects of stack shifts may vary per application and would be particularly important in longitudinal studies, more than in cross-sectional studies.

HIGH-RESOLUTION BONE IMAGING IN CLINICAL PRACTICE?

The use of HR-pQCT is largely restricted to research settings, and several challenges limit its implementation in clinical practice [65]. Most importantly, a limited number of HR-pQCT systems are available worldwide. In the Netherlands, presently only two HR-pQCT systems are installed, one in VieCuri Medical Center and one in the research facility of the Maastricht Study, under supervision of the same research group. The clinical implementation is further challenged by several technical issues. For example, the reconstruction time of HR-pQCT scans is long, which further increases when more scans are obtained successively or when multi-stack scans are taken. It slows down the workflow of radiologists who would need the scans for diagnostic purposes and of clinicians who would need the results of bone microarchitecture and strength assessments from the scans to evaluate bone quality. The latter is further delayed by the computational time of especially the μ FE-analysis to estimate bone strength. Additionally, evaluation outputs do not include a comparison with normative data such as in DXA reports, while such comparison is needed for clinical interpretation. Normative data are also scarce, particularly for second-generation HR-pQCT, and based on various input settings for analyses due to a lack of standardization [66]. Results from second-generation systems can also not be compared directly with results from first-generation systems due to differences in spatial resolution and analysis methods [66], but conversion factors have been developed [67,68]. Besides that, HR-pQCT systems have been developed as standalone systems for use in research settings and are therefore not standardly connected to hospital systems (*e.g.* electronic patient record systems, the medical image archiving and communication system PACS), while such connection is required for clinical use. Evaluation outputs with normative comparisons and connections with hospital systems may nevertheless be enabled by combined efforts of the manufacturer and hospital. A final issue is the reproducibility of HR-pQCT assessments, being relevant mainly in longitudinal assessments and reduced by among others motion artefacts and reference line positioning. These and other issues have recently also been described in a position paper on HR-pQCT [65].

Simultaneously, recent developments in clinical imaging increase the possibilities for detailed bone structure assessment. For example, developments in clinical CT imaging (*e.g.* flat-panel CT, cone-beam CT, photon-counting CT) may potentially provide sufficient spatial resolution to evaluate bone microarchitecture [69-72]. Similarly, developments in image sequences and magnetic field strengths in MRI may lead to spatial resolutions in the order of magnitude of trabecular structures [73]. The developments in clinical CT and MR imaging have thus far lower spatial resolutions than HR-pQCT. Clinical CT has furthermore a higher radiation dose than HR-

pQCT. Advantages of these CT and MR developments are however that they concern clinical systems, which eases clinical implementation, and that they have larger field of views. The latter is beneficial in case of mobility restrictions, such as in FOP or severe OI, and enables assessment of axial bones, which have other microarchitectural properties than peripheral bones [74].

CONCLUSION

This thesis showed that HR-pQCT can be used to assess bone microarchitecture and strength in OI and FOP, the effects of AOM-treatment in GIOP and PLO, and the healing of distal radius and scaphoid fractures, and that it improves the diagnosis of scaphoid fractures as compared to conventional CT. HR-pQCT can be used in patients with OI although short stature, bone deformities, and microarchitectural heterogeneity in this disorder require attention. The use of HR-pQCT in patients with FOP is limited due to mobility restrictions. Bone microarchitecture and strength can be assessed in response to AOM-treatment using HR-pQCT at the group and individual level, but the added value of HR-pQCT to DXA for treatment decisions should be further evaluated. Also the association between treatment-related changes in HR-pQCT parameters and fracture risk requires further study. The assessment of fracture healing using HR-pQCT is currently better suited for research at the group level than at an individual level due to difficulties in interpretation related to the reproducibility and fracture characteristics. Standard protocols for scan acquisition and analysis have to be adjusted and new protocols be developed to enable application to specific conditions, and practical and technical challenges need to be overcome for clinical implementation of HR-pQCT.

FUTURE PERSPECTIVES

Osteogenesis imperfecta and fibrodysplasia ossificans progressiva

The use of HR-pQCT in OI warrants further study. Specifically, it should be evaluated whether an extremity-length dependent protocol leads to different HR-pQCT parameters than the standard scan protocol. Furthermore, the occurrence of deviated scan regions and their effects on HR-pQCT parameters should be further investigated and our algorithm to detect such deviations be validated. Additionally, the microarchitectural inhomogeneities in OI require further study, including quantification of the effects of these inhomogeneities (specifically trabecular void volumes [8]) on HR-pQCT parameters. Finally, it should be experimentally evaluated whether μ FE-analysis can accurately estimate bone strength in OI. In future research,

it may be considered to use HR-pQCT together with techniques for bone material assessment, such as nanoindentation and quantitative backscattered electron imaging, to get a more complete impression of the bone quality in OI. Future bone research may direct towards the clinical heterogeneity of OI to get a better understanding of this heterogeneity, *e.g.* by evaluating associations between bone characteristics (from HR-pQCT), patient characteristics, and genotype and by studying whether subgroups exist based on HR-pQCT data [75]. Finally, clinical trials should be performed to evaluate the effects of AOM-treatment on the bone, both in children and adults with OI.

The use of HR-pQCT in FOP is limited due to mobility restrictions. Alternatively, further research should evaluate the use of higher-resolution clinical CT and MRI with larger scanner gantries in FOP, which will likely become clinically available in the (near) future. Such modalities may be combined with other advanced modalities (*e.g.* [18]NaF PET-CT [76]) to study developing and mature HO and the effects of study drugs on HO.

Distal radius and scaphoid fracture healing

The reproducibility of HR-pQCT should be improved to facilitate fracture healing assessment at the individual level. Specifically, HR-pQCT hardware and software should be optimized to reduce motion artefacts, and algorithms for the contouring and registration for scans of distal radius fractures should be further studied and validated [43,77]. Additionally, guidelines should be developed for the quality grading of multi-stack scans, the exclusion of multi-stack scans from quantitative analyses based on their quality, and the correction of stack shifts. Besides that, the ability of HR-pQCT to early detect abnormal fracture healing or healing complications should be further explored [78]. Future fracture healing studies may consider using HR-pQCT (or other higher-resolution modalities). Particularly in distal radius fracture healing studies, strength parameters are recommended as they are not influenced by the periosteal and endosteal contouring as long as all bone is contoured and the cortical and trabecular bone are assigned the same material properties. The use of multiple segmentation thresholds should be considered to enable study of the contribution of lower-mineralization tissue to the fracture healing process. Future research may direct towards the influence of patient and fracture characteristics on fracture healing and the effects of therapies in order to optimize treatment strategies.

Scaphoid fracture diagnosis

The performance of HR-pQCT for scaphoid fracture diagnosis needs to be replicated and extended in future research and the cost-effectiveness be evaluated. Additionally, the clinical consequences of scaphoid fractures that are missed on currently used modalities such as CT or MRI but detected on HR-pQCT should be further

explored. Besides that, clinicians should be aware of the limited diagnostic accuracy of current procedures to diagnose scaphoid fractures. When using HR-pQCT, it is recommended to use a cast with thumb part during scan acquisition. HR-pQCT and other higher-resolution modalities should ideally also be used as reference standard in future research into scaphoid fracture diagnosis. The use of artificial intelligence (AI) has recently been explored to detect scaphoid fractures on medical image data and to identify predictors of a true scaphoid fracture for clinical decision rules [58,79-82] and should be further explored for these purposes. For the identification of predictors of a scaphoid fracture and development of clinical decision rules, both patient characteristics and (low-resolution) imaging characteristics may be evaluated.

HR-pQCT in clinical practice

The clinical value of HR-pQCT beyond DXA requires further elucidation. Specifically, it should be determined, including cost-effectiveness, which patients would benefit from an HR-pQCT assessment. Furthermore, it should be evaluated whether bone microarchitecture and strength assessments from HR-pQCT could guide treatment decisions, especially when aBMD from DXA is moderately low but bone microarchitecture severely deteriorated, and whether treatment-related changes in HR-pQCT parameters are associated with fracture reductions in clinical trials. Besides that, to facilitate clinical implementation of HR-pQCT, costs should be reduced and hardware and software be optimized to improve reproducibility. Optimizations should shorten scan acquisition times to reduce the risk of motion artefacts and fasten scan reconstruction and analysis times to enhance clinical workflow. Additionally, the motion restraining holder for the arm may be re-evaluated and optimized. Furthermore, algorithms to objectively assess motion artefacts should be further studied [83,84] and the possibility to correct motion artefacts be explored. Besides that, a normative comparison should be incorporated in the analysis software, and other programming languages may be implemented to enlarge analysis possibilities and facilitate the use of for example AI without the need of data export. For the incorporation of a normative comparison in the analysis software, normative datasets should be extended, in particular for second-generation HR-pQCT, in men and women of various ethnicities and age ranges and according to standardized protocols for standard and length-dependent scans.

REFERENCES

- [1] Van Dijk FS, Sillence DO. Osteogenesis imperfecta: clinical diagnosis, nomenclature and severity assessment. *Am J Med Genet A*. 2014;164(6):1470-1481.
- [2] Nijhuis WH, Eastwood DM, Allgrove J, et al. Current concepts in osteogenesis imperfecta: bone structure, biomechanics and medical management. *J Child Orthop*. 2019;13(1):1-11.
- [3] Folkestad L, Hald JD, Ersbøll AK, et al. Fracture rates and fracture sites in patients with osteogenesis imperfecta: a nationwide register-based cohort study. *J Bone Miner Res*. 2017;32(1):125-134.
- [4] Bonaretti S, Majumdar S, Lang TF, Khosla S, Burghardt AJ. The comparability of HR-pQCT bone measurements is improved by scanning anatomically standardized regions. *Osteoporos Int*. 2017;28:2115-2128.
- [5] Folkestad L, Hald JD, Hansen S, et al. Bone geometry, density, and microarchitecture in the distal radius and tibia in adults with osteogenesis imperfecta type I assessed by high-resolution pQCT. *J Bone Miner Res*. 2012;27(6):1405-1412.
- [6] Kocijan R, Muschitz C, Haschka J, et al. Bone structure assessed by HR-pQCT, TBS and DXL in adult patients with different types of osteogenesis imperfecta. *Osteoporos Int*. 2015;26:2431-2440.
- [7] Rolvien T, Stürznickel J, Schmidt FN, et al. Comparison of bone microarchitecture between adult osteogenesis imperfecta and early-onset osteoporosis. *Calcif Tissue Int*. 2018;103:512-521.
- [8] Whittier DE, Burt LA, Boyd SK. A new approach for quantifying localized bone loss by measuring void spaces. *Bone*. 2021;143:115785.
- [9] Bishop N. Bone material properties in osteogenesis imperfecta. *J Bone Miner Res*. 2016;31(4):699-708.
- [10] Seeman E, Martin TJ. Antiresorptive and anabolic agents in the prevention and reversal of bone fragility. *Nat Rev Rheumatol*. 2019;15(4):225-236.
- [11] Ralston SH, Gaston MS. Management of osteogenesis imperfecta. *Front Endocrinol*. 2020;10:924.
- [12] Kaplan FS, Glaser DL, Shore EM, et al. The phenotype of fibrodysplasia ossificans progressiva. *Clin Rev Bone Miner Metab*. 2005;3:183-188.
- [13] Kitterman JA, Kantanie S, Rocke DM, Kaplan FS. Iatrogenic harm caused by diagnostic errors in fibrodysplasia ossificans progressiva. *Pediatrics*. 2005;116(5):e654-e661.
- [14] Pignolo RJ, Bedford-Gay C, Liljestrom M, et al. The Natural History of Flare-Ups in Fibrodysplasia Ossificans Progressiva (FOP): A Comprehensive Global Assessment. *J Bone Miner Res*. 2016;31(3):650-6.
- [15] Kaplan FS, Strear CM, Zasloff MA. Radiographic and scintigraphic features of modeling and remodeling in the heterotopic skeleton of patients who have fibrodysplasia ossificans progressiva. *Clin Orthop Rel Res*. 1994;304:238-247.
- [16] Saag KG, Wagman RB, Geusens P, et al. Denosumab versus risedronate in glucocorticoid-induced osteoporosis: a multicentre, randomised, double-blind, active-controlled, double-dummy, non-inferiority study. *Lancet Diabetes Endocrinol*. 2018;6(6):445-454.
- [17] Saag KG, Pannacciulli N, Geusens P, et al. Denosumab versus risedronate in glucocorticoid-induced osteoporosis: final results of a twenty-four-month randomized, double-blind, double-dummy trial. *Arthritis Rheumatol*. 2019;71(7):1174-1184.
- [18] Mikolajewicz N, Bishop N, Burghardt AJ, et al. HR-pQCT measures of bone microarchitecture predict fracture: systematic review and meta-analysis. *J Bone Miner Res* 2020;35:446-59.
- [19] Black DM, Bauer DC, Vittinghoff E, et al. Treatment-related changes in bone mineral density as a surrogate biomarker for fracture risk reduction: meta-regression analyses of individual patient data from multiple randomised controlled trials. *Lancet Diabetes Endocrinol*. 2020;8(8):672-682.

- [20] Lodder MC, Lems WF, Ader HJ, et al. Reproducibility of bone mineral density measurement in daily practice. *Ann Rheu Dis* 2004;63:285-9.
- [21] El Maghraoui A, Do Santos Zounon AA, Jroundi I, et al. Reproducibility of bone mineral density measurements using dual X-ray absorptiometry in daily clinical practice. *Osteoporos Int* 2005;16:1742-8.
- [22] Adami G, Saag KG. Glucocorticoid-induced osteoporosis: 2019 concise clinical review. *Osteoporos Int*. 2019;30:1145-1156.
- [23] Seeman E, Delmas PD, Hanley DA, et al. Microarchitectural deterioration of cortical and trabecular bone: differing effects of denosumab and alendronate. *J Bone Miner Res*. 2010;25(8):1886-1894.
- [24] Baron R, Ferrari S, Russell RGG. Denosumab and bisphosphonates: different mechanisms of action and effects. *Bone*. 2011;48(4):677-692.
- [25] Zebaze R, Ghasem-Zadeh A, Mbala A, Seeman E. A new method of segmentation of compact-appearing, transitional and trabecular compartments and quantification of cortical porosity from high resolution peripheral quantitative computed tomographic images. *Bone*. 2013;54(1):8-20.
- [26] van Rietbergen B, Biver E, Chevalley T, Ito K, Chapurlat R, Ferrari S. A novel HR-pQCT image registration approach reveals sex-specific changes in cortical bone retraction with aging. *J Bone Miner Res*. 2011;36(7):1351-1363.
- [27] Van Staa TP, Laan RF, Barton IP, Cohen S, Reid DM, Cooper C. Bone density threshold and other predictors of vertebral fracture in patients receiving oral glucocorticoid therapy. *Arthritis Rheum*. 2003;48(11):3224-3229.
- [28] Samelson EJ, Broe KE, Xu H, et al. Cortical and trabecular bone microarchitecture as an independent predictor of incident fracture risk in older women and men in the Bone Microarchitecture International Consortium (BoMIC): a prospective study. *Lancet Diabetes Endocrinol*. 2019;7(1):34-43.
- [29] Hardcastle SA. Pregnancy and lactation associated osteoporosis. *CalcifTissue Int*. 2022;110(5):531-545.
- [30] Winter EM, Ireland A, Butterfield NC, et al. Pregnancy and lactation, a challenge for the skeleton. *Endocr Connect*. 2020;9(6):R143.
- [31] Kemp TD, de Bakker CMJ, Gabel L, et al. Longitudinal bone microarchitectural changes are best detected using image registration. *Osteoporos Int*. 2020;31:1995-2005.
- [32] World Health Organization. Assessment of fracture risk and its application to screening for postmenopausal osteoporosis: report of a WHO study group. World Health Organization. 1994.
- [33] Siris ES, Miller PD, Barrett-Connor E, et al. Identification and fracture outcomes of undiagnosed low bone mineral density in postmenopausal women: results from the National Osteoporosis Risk Assessment. *JAMA*. 2001;286(22):2815-2822.
- [34] Schuit SCE, Van der Klift M, Weel AEAM, et al. Fracture incidence and association with bone mineral density in elderly men and women: the Rotterdam Study. *Bone*. 2004;34(1):195-202.
- [35] Whittier DE, Samelson EJ, Hannan MT, et al. A Fracture Risk Assessment Tool for High Resolution Peripheral Quantitative Computed Tomography. *J Bone Miner Res*. 2023.
- [36] de Jong JJ, Willems PC, Arts JJ, et al.. Assessment of the healing process in distal radius fractures by high resolution peripheral quantitative computed tomography. *Bone*. 2014;64:65-74.
- [37] de Jong JJ, Heyer FL, Arts JJ, et al. Fracture repair in the distal radius in postmenopausal women: a follow-up 2 years Postfracture using HRpQCT. *J Bone Miner Res*. 2016;31(5):1114-1122.
- [38] Einhorn TA, Gerstenfeld LC. Fracture healing: mechanisms and interventions. *Nat Rev Rheumatol*. 2015;11(1):45-54.
- [39] Sandberg OH, Aspenberg P. Inter-trabecular bone formation: a specific mechanism for healing of cancellous bone: A narrative review. *Acta Orthop*. 2016;87(5):459-465.

- [40] Manjubala I, Liu Y, Epari DR, et al. Spatial and temporal variations of mechanical properties and mineral content of the external callus during bone healing. *Bone*. 2009;45(2):185-192.
- [41] Ellouz R, Chapurlat R, van Rietbergen B, Christen P, Pialat J.B, Boutroy S. Challenges in longitudinal measurements with HR-pQCT: evaluation of a 3D registration method to improve bone microarchitecture and strength measurement reproducibility. *Bone*. 2014;63:147-157.
- [42] van Rietbergen B, Biver E, Chevalley T, Ito K, Chapurlat R, Ferrari S. A novel HR-pQCT image registration approach reveals sex-specific changes in cortical bone retraction with aging. *J Bone Miner Res*. 2021;36(7):1351-1363.
- [43] de Jong JJ, Christen P, Plett RM, et al. Feasibility of rigid 3D image registration of high-resolution peripheral quantitative computed tomography images of healing distal radius fractures. *PloS One*. 2017;12(7):e0179413.
- [44] de Jong JJ, Arts JJ, Meyer U, et al. Effect of a cast on short-term reproducibility and bone parameters obtained from HR-pQCT measurements at the distal end of the radius. *J Bone Joint Surg*. 2016;98(5):356-362.
- [45] Whittier DE, Manske SL, Boyd SK, Schneider PS. The correction of systematic error due to plaster and fiberglass casts on HR-pQCT bone parameters measured in vivo at the distal radius. *J Clin Densitom*. 2019;22(3):401-408.
- [46] Goldhahn J, Angst F, Simmen BR. What counts: outcome assessment after distal radius fractures in aged patients. *J Orthop Trauma*. 2008;22:S126-S130.
- [47] Hackney LA, Dodds SD. Assessment of scaphoid fracture healing. *Curr Rev Musculoskelet Med*. 2011;4:16-22.
- [48] Mack GR, Bosse MJ, Gelberman RH, Yu E. The natural history of scaphoid non-union. *J Bone Joint Surg*. 1984;66(4):504-509.
- [49] Duckworth AD, Ring D, McQueen MM. Assessment of the suspected fracture of the scaphoid. *J Bone Joint Surg*. 2011;93(6):713-719.
- [50] Daniels AM, Wyers CE, Janzing HM, et al. The interobserver reliability of the diagnosis and classification of scaphoid fractures using high-resolution peripheral quantitative CT. *Bone Joint J*. 2020;102(4):478-484.
- [51] Daniels AM, Kranendonk J, Wyers CE, et al. What Is the Diagnostic Performance of Conventional Radiographs and Clinical Reassessment Compared With HR-pQCT Scaphoid Fracture Diagnosis? *Clin Orthop Relat Res*. 2023;481(1):97-104.
- [52] Yin ZG, Zhang JB, Kan SL, Wang XG. Diagnostic accuracy of imaging modalities for suspected scaphoid fractures: meta-analysis combined with latent class analysis. *J Bone Joint Surg Br*. 2012;94(8):1077-1085.
- [53] Bäcker HC, Wu CH, Strauch RJ. Systematic review of diagnosis of clinically suspected scaphoid fractures. *J Wrist Surg*. 2020;9(1):081-089.
- [54] Parvizi J, Wayman J, Kelly P, Moran CG. Combining the clinical signs improves diagnosis of scaphoid fractures: a prospective study with follow-up. *J Hand Surg Eur Vol*. 1998;23B:324-327.
- [55] Rhemrev SJ, Beeres FJP, Van Leerdam RH, Hogervorst M, Ring D. Clinical prediction rule for suspected scaphoid fractures: A Prospective Cohort Study. *Injury*. 2010;41:1026-1030.
- [56] Duckworth AD, Buijze GA, Moran M, et al. Predictors of fracture following suspected injury to the scaphoid. *J Bone Joint Surg Br*. 2012;94B:961-968.
- [57] Mallee WH, Walenkamp MMJ, Mulders MAM, Goslings JC, Schep NWL. Detecting scaphoid fractures in wrist injury: a clinical decision rule. *Arch Orthop Trauma Surg*. 2020;140:575-581.
- [58] Bulstra AEJ, Buijze GA, Cohen A, et al. A machine learning algorithm to estimate the probability of a true scaphoid fracture after wrist trauma. *J Hand Surg*. 2022;47(8):709-718.

- [59] Weber ER, Chao EY. An experimental approach to the mechanism of scaphoid waist fractures. *J Hand Surg Am.* 1978;3:142-148.
- [60] Majima M, Horii E, Matsuki H, Hirata H, Genda E. Load transmission through the wrist in the extended position. *J Hand Surg Am.* 2008;33:182-188.
- [61] Pinder RM, Brkljac M, Rix L, Muir L, Brewster M. Treatment of scaphoid nonunion: a systematic review of the existing evidence. *J Hand Surg.* 2015;40(9):1797-1805.
- [62] Su-Bum AL, Hyo-Jin BK, Jae-Myeung CC, et al. Osseous microarchitecture of the scaphoid: cadaveric study of regional variations and clinical implications. *Clin Anat.* 2012;25(2):203-211.
- [63] Pialat JB, Burghardt AJ, Sode M, Link TM, Majumdar S. Visual grading of motion induced image degradation in high resolution peripheral computed tomography: impact of image quality on measures of bone density and micro-architecture. *Bone.* 2012;50(1):111-118.
- [64] Brunet SC, Kuczynski MT, Bhatla JL, et al. The utility of multi-stack alignment and 3D longitudinal image registration to assess bone remodeling in rheumatoid arthritis patients from second generation HR-pQCT scans. *BMC Medical Imaging.* 2020;20:1-10.
- [65] Van den Bergh JP, Szulc P, Cheung AM, Bouxsein M, Engelke K, Chapurlat R. The clinical application of high-resolution peripheral computed tomography (HR-pQCT) in adults: state of the art and future directions. *Osteoporos Int.* 2021;32(8):1465-1485.
- [66] Whittier DE, Boyd SK, Burghardt AJ, et al. Guidelines for the assessment of bone density and microarchitecture in vivo using high-resolution peripheral quantitative computed tomography. *Osteoporos Int.* 2020;31:1607-1627.
- [67] Agarwal S, Rosete F, Zhang C, et al. In vivo assessment of bone structure and estimated bone strength by first-and second-generation HR-pQCT. *Osteoporos Int.* 2016;27:2955-2966.
- [68] Manske SL, Davison EM, Burt LA, Raymond DA, Boyd SK. The estimation of second-generation HR-pQCT from first-generation HR-pQCT using in vivo cross-calibration. *J Bone Miner Res.* 2017;32(7):1514-1524.
- [69] Mulder L, van Rietbergen B, Noordhoek NJ, Ito K. Determination of vertebral and femoral trabecular morphology and stiffness using a flat-panel C-arm-based CT approach. *Bone.* 2012;50(1):200-208.
- [70] Reichardt B, Sarwar A, Bartling SH, et al. Musculoskeletal applications of flat-panel volume CT. *Skeletal Radiol.* 2008;37:1069-1076.
- [71] Mys K, Varga P, Gueorguiev B, Hemmatian H, Stockmans F, van Lenthe GH. Correlation between cone-beam computed tomography and high-resolution peripheral computed tomography for assessment of wrist bone microstructure. *J Bone Miner Res.* 2019;34(5):867-874.
- [72] Willeminck MJ, Persson M, Pourmorteza A, Pelc NJ, Fleischmann D. Photon-counting CT: technical principles and clinical prospects. *Radiology.* 2018;289(2):293-312.
- [73] Chang G, Boone S, Martel D, et al. MRI assessment of bone structure and microarchitecture. *J Magn Reson Imaging.* 2017;46(2):323-337.
- [74] Eckstein F, Matsuura M, Kuhn V, et al. Sex differences of human trabecular bone microstructure in aging are site-dependent. *J Bone Miner Res.* 2007;22(6):817-824.
- [75] Whittier DE, Samelson EJ, Hannan MT, et al. Bone microarchitecture phenotypes identified in older adults are associated with different levels of osteoporotic fracture risk. *J Bone Miner Res.* 2022;37(3):428-439.
- [76] Eekhoff EMW, Botman E, Netelenbos JC, et al. [18F] NaF PET/CT scan as an early marker of heterotopic ossification in fibrodysplasia ossificans progressiva. *Bone.* 2018;109:143-146.
- [77] Ohs N, Collins CJ, Tourolle DC, et al. Automated segmentation of fractured distal radii by 3D geodesic active contouring of in vivo HR-pQCT images. *Bone.* 2021;147:115930.

- [78] Heyer FL, de Jong JJ, Smeets RJ, et al. A case report of abnormal fracture healing as detected with high-resolution peripheral quantitative computed tomography. *J Clin Densitom.* 2017;20(4):486-489.
- [79] Ozkaya E, Topal FE, Bulut T, Gursoy M, Ozuysal M, Karakaya Z. Evaluation of an artificial intelligence system for diagnosing scaphoid fracture on direct radiography. *Eur J Trauma Emerg Surg.* 2020:1-8.
- [80] Langerhuizen DW, Bulstra AEJ, Janssen SJ, et al. Is deep learning on par with human observers for detection of radiographically visible and occult fractures of the scaphoid? *Clin Orthop Relat Res.* 2020;478(11):2653.
- [81] Hendrix N, Scholten E, Vernhout B, et al. Development and validation of a convolutional neural network for automated detection of scaphoid fractures on conventional radiographs. *Radiol Artif Intell.* 2021;3(4):e200260.
- [82] Yoon AP, Lee YL, Kane RL, Kuo CF, Lin C, Chung KC. Development and validation of a deep learning model using convolutional neural networks to identify scaphoid fractures in radiographs. *JAMA Netw Open.* 2021;4(5):e216096-e216096.
- [83] Sode M, Burghardt AJ, Pialat JB, Link TM, Majumdar S. Quantitative characterization of subject motion in HR-pQCT images of the distal radius and tibia. *Bone.* 2011;48(6):1291-1297.
- [84] Walle M, Eggemann D, Atkins PR, et al. Motion grading of high-resolution quantitative computed tomography supported by deep convolutional neural networks. *Bone.* 2023;166:116607.



12

Chapter 12

Summary

Samenvatting

SUMMARY

In this thesis, we studied the use of high-resolution peripheral quantitative computed tomography (HR-pQCT) for the assessment of bone microarchitecture and strength in the rare conditions osteogenesis imperfecta (OI) and fibrodysplasia ossificans progressiva (FOP) and in response to treatment with anti-osteoporosis medication (AOM) in glucocorticoid-induced osteoporosis (GIOP) and pregnancy- and lactation-associated osteoporosis (PLO) and for the assessment of the healing of distal radius fractures and the diagnosis and healing of scaphoid fractures.

Chapter 1 sets out the background and outline of this thesis. It describes the structural properties of bones that form the skeleton and clinically available techniques to assess these properties, and it introduces HR-pQCT to assess bone structure at the micrometer level.

In **Chapter 2**, we assessed bone microarchitecture and strength using HR-pQCT in 118 adults with OI. OI is a rare, genetic disorder that is primarily characterized by an increased bone fragility and fracture risk due to defects in bone structure and material. We used an extremity-length dependent HR-pQCT scan protocol to take into account the short stature in OI. Bone mineral density (BMD) and microarchitecture were reduced as compared to age- and gender-matched normative data, particularly of the trabecular compartment. Also bone strength was reduced. 11% of the radius scans and 13% of the tibia scans had a deviated axial angle as compared to scans of 13 young women used as reference. In the scans with a deviated axial angle, the proportion of Z -scores < -4 or > 4 for total and trabecular parameters was significantly higher than in the scans without a deviated axial angle. Besides that, we observed local microarchitectural inhomogeneities. Most pronounced were trabecular void volumes, which appeared to correspond with a severely reduced trabecular number and increased trabecular separation. We concluded that mainly the trabecular bone and bone strength are reduced in OI and that HR-pQCT can be used in the majority of adults with OI without difficulties. Nevertheless, HR-pQCT scans can have a deviated axial angle due to bone deformities in OI, and standard HR-pQCT analyses may not always be reliable due to microarchitectural inhomogeneities.

In **Chapter 3**, we explored the use of HR-pQCT in two patients with FOP. FOP is a rare, genetic condition that is characterized by the progressive formation of heterotopic ossifications (HOs) in ligaments, tendons, and muscles. In the two patients, we could obtain HR-pQCT scans of HO in an Achilles tendon and around the metatarsals and ankle, but not all peripherally-located HO could be scanned due to the patients' mobility restrictions. The scanned HO had a cortical and trabecular compartment. The

non-isolated HO was fusing with the neighboring skeletal bone with development of a neo-cortex and partial replacement of the original skeletal cortex with trabeculae. The isolated HO in the Achilles tendon could be quantitatively evaluated, which revealed a low BMD and normal trabecular microarchitecture as compared to normative data of the distal tibia. BMD, microarchitecture, and strength were normal at the distal radius but reduced at the distal tibiae as compared to normative data. Our study provided insights into HO in FOP. However, the use of HR-pQCT is challenging in patients with FOP due to mobility restrictions, and it is limited to peripherally-located HO. Future research should therefore explore the use of high-resolution imaging modalities with larger gantries than HR-pQCT in FOP.

GIOP is one of the most common forms of secondary osteoporosis and induced by glucocorticoid (GC-) treatment. In a recent randomized clinical trial in GC-users, it was shown that treatment with denosumab improved areal BMD (aBMD) significantly more than treatment with risedronate. In **Chapter 4**, we evaluated the effects of both AOMs on bone microarchitecture and strength using HR-pQCT in a subset of 110 participants of the clinical trial. We found that in GC-initiators (GC-treatment for < 3 months), failure load (FL) at the distal radius remained unchanged at 24 months of treatment with denosumab and significantly decreased with risedronate (-4.1%, [95%-confidence interval: -6.4, -1.8]). In GC-continuers at 24 months of treatment, FL significantly increased with denosumab (+4.3%, [2.1, 6.4]) and remained unchanged with risedronate. Correspondingly, FL was significantly higher with denosumab than with risedronate (GC-initiators: $p < 0.001$; GC-continuers: $p = 0.011$). We also found significant differences in the effects of both AOMs on cortical and trabecular microarchitecture. Similar results were found at the tibia. We concluded that denosumab could preserve bone strength in GC-initiators and improve bone strength in GC-continuers, while risedronate could not. It suggests that denosumab may be a useful therapeutic option in patients initiating GC-therapy or on long-term GC-therapy.

In **Chapter 5**, we studied the use of HR-pQCT in a patient with PLO, a rare form of secondary osteoporosis that is characterized by back pain and vertebral fractures during pregnancy and early postpartum. The patient, a 34-year old woman, had PLO and multiple vertebral fractures after her first pregnancy. At seven months postpartum, she had a severely reduced BMD, microarchitecture, and strength as compared to normative data. One-year treatment with teriparatide and one successive zoledronic acid infusion resulted in substantial improvements in BMD, microarchitecture, and strength at the distal radius, while larger improvements were found before treatment at the distal tibiae. The latter suggested spontaneous recovery and a role of mechanical loading and physiotherapy followed postpartum. Despite the improvements, BMD,

microarchitecture, and strength remained highly reduced after treatment at forty weeks postpartum. A monogenic cause could not be found. However, osteoporosis and osteopenia occurred in the woman's mother, father, and sister, and her mother had similar cortical discrepancies on HR-pQCT. It suggested that PLO in this woman could have a polygenic origin with possible susceptibility based on the familiar occurrence of osteoporosis.

In **Chapter 6**, we investigated the contribution of lower-mineralized tissue to the stiffness of fractured distal radii during the first 12 weeks of healing. Forty-five postmenopausal women with a conservatively-treated distal radius fracture had HR-pQCT scans of their fractured radius at baseline (1-2 weeks post-fracture), 3-4 weeks, 6-8 weeks, and 12 weeks post-fracture. We quantified the stiffness of the distal radius fractures using a series of micro-finite element (μ FE-) models from HR-pQCT data that included only higher-mineralized tissue (>320 mg HA/cm³) and a series of μ FE-models that differentiated between lower-mineralized tissue (200-320 mg HA/cm³) and higher-mineralized tissue. The ratio of the two stiffness values - reflecting the contribution of lower-mineralized tissue to stiffness - was significantly higher than baseline at 3-4 weeks ($p = 0.0010$) and 6-8 weeks ($p < 0.0001$) and returned to baseline-values at 12 weeks. Estimated marginal means were between 1.05 and 1.08. We concluded that the contribution of lower-mineralized tissue to the fracture healing can be quantified by combining the results obtained using different density thresholds for bone segmentation. The contribution to stiffness reflects the formation and remodeling of lower-mineralized tissue during fracture healing. This contribution was minor but changed early during healing and around cast removal and may therefore be clinically relevant.

In **Chapters 7-10**, we studied the novel application of HR-pQCT to scaphoid fractures. In **Chapter 7**, we explored the feasibility of HR-pQCT imaging of the scaphoid bone in 91 adult patients with a clinically suspected scaphoid fracture, while their wrist was immobilized in a cast. We found that the cast had to be extended with a thumb part during scan acquisition to reduce motion artefacts on the HR-pQCT scans. Application of the standard contouring algorithm yielded visually erroneous contours of the scaphoid bone, which was solved by applying the algorithm to coarse hand-drawn pre-contours and by using a lower density threshold for bone segmentation. Manual adjustment of the resulting contours resulted in significant but small differences in BMD and microarchitecture ($< 1.0\%$). Based on these findings, we concluded that HR-pQCT imaging is feasible in patients with a clinically suspected scaphoid fracture when a cast with thumb extension is used during scan acquisition and that BMD and microarchitecture of the scaphoid bone can be evaluated.

In **Chapter 8**, we subsequently evaluated the performance of HR-pQCT for scaphoid fracture diagnosis as compared to conventional CT. All 91 included patients with a clinically suspected scaphoid fracture had a clinical re-examination within two weeks after first presentation at the emergency department. For the study, they additionally had an HR-pQCT and CT scan at the same day. While CT revealed a scaphoid fracture in 15 out of the 91 patients, HR-pQCT revealed a fracture in 24 patients (*i.e.* 60% more). The correlation between CT and HR-pQCT was high for scaphoid fracture type according to the Herbert classification and for scaphoid fracture location. These findings showed that HR-pQCT is superior to CT in diagnosing scaphoid fractures at 1-2 weeks after initial presentation at the emergency department and that a substantial proportion of scaphoid fractures may be missed by the current use of CT.

In **Chapter 9**, we explored whether the presence of a scaphoid fracture is associated with the shape of the scaphoid bone as described by a statistical shape model (SSM). We generated a SSM from HR-pQCT scans of 26 non-fractured scaphoid bones and of 15 scaphoid bones with a fracture without clearly visible fracture-related surface irregularities. The first five out of the forty shape modes of the SSM cumulatively explained 87.8% of the shape variance among the 41 scaphoid bones. A logistic regression model with four shape modes correctly classified 75.6% of the scaphoid bones as fractured or non-fractured, for which the diagnosis on HR-pQCT was used as reference. Based on these findings, we concluded that the presence of a scaphoid fracture in patients with a clinically suspected fracture may be associated with the shape of the scaphoid bone. Research in larger datasets is needed to further investigate this association.

In **Chapter 10**, we explored the use of HR-pQCT to monitor scaphoid fracture healing in eleven patients with a scaphoid fracture confirmed on HR-pQCT. We observed that the fracture line of the scaphoid fracture became more apparent at 3 weeks after initial presentation at the emergency department. At 6 weeks and more pronounced at 12 weeks, trabeculae around the fracture region became more difficult to identify and distinguish from neighboring trabeculae. BMD, stiffness, and FL were significantly lower than baseline (1-2 weeks after initial presentation) at all follow-up visits (3, 6, 12, and 26 weeks after initial presentation) with the largest change from baseline at 6 weeks (-13.6%, -26.5%, and -23.7%, respectively). Trabecular number was significantly lower than baseline from 6 weeks onwards and trabecular thickness at 3, 6, and 12 weeks. All in all, BMD, trabecular thickness, and strength of scaphoid fractures significantly decreased during the first six weeks of fracture healing, followed by a stabilization or increase. They were not returned to baseline-values at 26 weeks after initial presentation.

In **Chapter 11**, we discussed the main findings, clinical implications, and limitations of the studies in this thesis, followed by a conclusion and future perspectives.

SAMENVATTING

In dit proefschrift bestudeerden we het gebruik van hoge-resolutie perifere kwantitatieve computer tomografie (HR-pQCT) in twee gebieden: 1) het beoordelen van bot-microarchitectuur en botsterkte bij bot-gerelateerde ziekten en behandelingen, specifiek de ziekten osteogenesis imperfecta (OI) en fibrodysplasia ossificans progressiva (FOP) en de behandeling met anti-osteoporose medicatie in glucocorticoïd-geïnduceerde osteoporose (GIOP) en zwangerschaps- en borstvoedingsgeassocieerde osteoporose (PLO); en 2) het diagnosticeren van scaphoïd breuken en het volgen van het genezingsproces van distale radiusbreuken en scaphoïd breuken.

In **Hoofdstuk 1** werd de achtergrond en opzet van dit proefschrift toegelicht. Hierbij werden de structurele eigenschappen van de botten die het skelet vormen beschreven, samen met de klinisch beschikbare technieken om deze eigenschappen te beoordelen. Tevens werd de HR-pQCT techniek, gebruikt voor de beoordeling van de botstructuur op micrometerniveau, nader toegelicht.

In **Hoofdstukken 2-5** (Deel 1) werd het gebruik van HR-pQCT onderzocht bij bot-gerelateerde ziekten en behandelingen. In **Hoofdstuk 2** beoordeelden we de bot-microarchitectuur en botsterkte met HR-pQCT in 118 volwassenen met OI. OI is een zeldzame, genetische aandoening die voornamelijk gekenmerkt wordt door een verhoogde botfragiliteit en een verhoogde kans op botbreuken als gevolg van defecten in de botstructuur en het botmateriaal. We gebruikten een lengte-afhankelijk scanprotocol, zodat rekening gehouden werd met de vaak kleinere lichaamslengte van mensen met OI. Botmineraaldichtheid (BMD) en bot-microarchitectuur waren verminderd in vergelijking met leeftijd- en geslacht-gematchte referentiedata, vooral van het trabeculaire botcompartiment. Ook de botsterkte was verminderd. Daarnaast had 11% van de radius scans en 13% van de tibia scans een afwijkende axiale scanhoek vergeleken met scans van 13 jonge vrouwen. In de scans met een afwijkende axiale scanhoek was het percentage Z-scores < -4 of > 4 significant hoger voor totale en trabeculaire botparameters dan in de scans zonder afwijkende axiale scanhoek. Verder zagen we diverse lokale onregelmatigheden in de bot-microarchitectuur, waarvan lege trabeculaire volumes het meest opvallend waren. Deze onregelmatigheid leek overeen te komen met een zeer sterk verlaagd aantal botbalkjes en een zeer sterk verhoogde afstand tussen de botbalkjes. We concludeerden dat vooral het trabeculaire bot en de botsterkte zijn verminderd in OI en dat HR-pQCT zonder problemen gebruikt kan worden bij de meerderheid van volwassenen met OI. Wel kunnen HR-pQCT scans een afwijkende axiale scanhoek hebben als gevolg van afwijkingen in de ledematen van patiënten met OI en zijn de standaard HR-pQCT analyses niet altijd betrouwbaar als gevolg van lokale onregelmatigheden.

In **Hoofdstuk 3** bestudeerden we het gebruik van HR-pQCT bij twee patiënten met FOP. FOP is een zeldzame, genetische aandoening die wordt gekenmerkt door de progressieve vorming van heterotopie ossificatie (HO) in ligamenten, pezen en spieren. Bij de twee patiënten konden we HR-pQCT scans maken van een geïsoleerde HO in de achillespees en van niet-geïsoleerde HO's rond de middenvoetsbeentjes en enkel. De geïsoleerde HO had een duidelijk corticaal en trabeculair botcompartiment en kon kwantitatief beoordeeld worden, wat een lage BMD en een normale trabeculaire bot-microarchitectuur liet zien in vergelijking met referentiedata van de distale tibia. De niet-geïsoleerde HO's fuseerden met het omliggende skeletale bot, waarbij sprake was van de vorming van een nieuwe cortex en de gedeeltelijke vervanging van de oorspronkelijke skelet-cortex door botbalkjes. Verder waren de BMD, bot-microarchitectuur en botsterkte normaal in de distale radius maar verminderd in de distale tibia in vergelijking met referentiedata. Onze studie heeft inzicht gegeven in HO en skeletaal bot in FOP. Het gebruik van HR-pQCT bij patiënten met FOP is echter uitdagend door bewegingsbeperkingen van de patiënten en beperkt tot perifeer-gelegen HO. Toekomstig onderzoek naar FOP zou daarom gericht moeten zijn op toepassing van hoge-resolutie beeldvormende modaliteiten met een grotere opening dan HR-pQCT.

GIOP is één van de meest voorkomende vormen van secundaire osteoporose. In een recente gerandomiseerde klinische studie in glucocorticoid (GC-) gebruikers werd aangetoond dat een behandeling met denosumab de 2D-BMD significant meer verbeterde dan een behandeling met risedroninezuur. In **Hoofdstuk 4** onderzochten we de effecten van beide medicijnen op de bot-microarchitectuur en botsterkte in een subgroep van 110 deelnemers aan de klinische studie. In GC-starters (GC-behandeling < 3 maanden) vonden we dat failure load (FL; maximale kracht op het bot tot permanente vervorming) in de distale radius onveranderd bleef na 24 maanden van behandeling met denosumab en significant afnam na 24 maanden van behandeling met risedroninezuur (-4,1%; [95%-CI: -6,4; -1,8]). In GC-voortzetteren nam FL in de distale radius na 24 maanden behandeling met denosumab significant toe (+4,3%; [2,1; 6,4]) en bleef deze onveranderd bij behandeling met risedroninezuur. Daarmee was FL in de distale radius significant hoger met denosumab dan met risedroninezuur (GC-starters: $p < 0.001$; GC-voortzetteren: $p = 0.011$). We vonden ook significante verschillen in de effecten van beide medicijnen op de corticale en trabeculaire bot-microarchitectuur in de distale radius. Vergelijkbare resultaten werden gevonden in de distale tibia. We concludeerden dat tijdens behandeling met denosumab FL stabiel bleef bij GC-starters en toenam bij GC-voortzetteren, terwijl dit respectievelijk afnam en stabiel bleef tijdens behandeling met risedroninezuur. Dit suggereert dat denosumab een therapeutische optie is voor volwassenen die starten met een GC-behandeling of reeds langdurig met een GC behandeld worden.

In **Hoofdstuk 5** bestudeerden we het gebruik van HR-pQCT in een patiënte met PLO, een zeldzame vorm van secundaire osteoporose. De patiënte, een 34-jarige vrouw, had PLO met meerdere wervelbreuken na haar eerste zwangerschap. Zeven maanden na de bevalling had ze een zeer sterk verminderde BMD, bot-microarchitectuur en botsterkte vergeleken met referentiedata. Na één jaar behandeling met teriparatide gevolgd door één intraveneuze toediening van zoledroninezuur werd een substantiële verbetering gezien van de BMD, bot-microarchitectuur en botsterkte in de distale radius, terwijl grotere verbeteringen werden gevonden vóór behandeling in de distale tibia. Dit laatste suggereerde een spontaan herstel en een positieve invloed van mechanische belasting en fysiotherapie na de bevalling. Ondanks de verbeteringen bleven na de behandeling op veertig weken postpartum de BMD, bot-microarchitectuur en botsterkte sterk verminderd in vergelijking met referentiedata. Een mono-genetische oorzaak kon niet worden gevonden. Osteoporose en osteopenie kwamen echter voor bij de moeder, vader en zus van de vrouw en daarnaast had haar moeder vergelijkbare corticale afwijkingen op HR-pQCT. Dit suggereert dat PLO bij deze vrouw een poly-genetische oorsprong kan hebben gebaseerd op het familiale voorkomen van osteoporose.

In **Hoofdstukken 6-10** (Deel 2) werd het gebruik van HR-pQCT onderzocht bij distale radiusbreuken en scaphoïd breuken. In **Hoofdstuk 6** onderzochten we de bijdrage van lager-gemineraleerd bot aan de stijfheid van gebroken distale radii tijdens de eerste 12 weken van het genezingsproces. Vijfenveertig postmenopauzale vrouwen met een conservatief behandelde breuk kregen HR-pQCT scans van hun gebroken radius op baseline (1-2 weken na de breuk), 3-4 weken, 6-8 weken en 12 weken na de breuk. We berekenden de stijfheid van de distale radiusbreuken met een serie van micro-eindige elementen (μ FE-) modellen van HR-pQCT data bestaande uit alleen hoger-gemineraleerd bot ($> 320 \text{ mg HA/cm}^3$) en een serie van μ FE-modellen die onderscheid maakte tussen lager-gemineraleerd bot ($200\text{-}320 \text{ mg HA/cm}^3$) en hoger-gemineraleerd bot. De verhouding van de twee stijfheidswaarden – welke de bijdrage van lager-gemineraleerd weefsel aan stijfheid weerspiegelt – was in vergelijking met baseline significant hoger na 3-4 weken ($p = 0,0010$) en 6-8 weken ($p < 0,0001$) en weer vergelijkbaar met baselinewaarden na 12 weken. Het geschatte gemiddelde van de bijdrage van het lager-gemineraleerd weefsel aan stijfheid was 5-8%. We concludeerden dat de bijdrage van lager-gemineraleerd weefsel aan de genezing van distale radiusbreuken gemeten kan worden door het combineren van resultaten verkregen met verschillende afkapwaarden voor dichtheid voor de botsegmentatie. De bijdrage aan de stijfheid weerspiegelt de vorming en remodelering van lager-gemineraleerd weefsel tijdens het genezingsproces. Deze bijdrage was klein maar veranderde tijdens de vroege fase van genezing en rond de periode van gipsverwijdering en kan daarom klinisch relevant zijn.

In **Hoofdstukken 7-10** bestudeerden we de nieuwe toepassing van HR-pQCT op scaphoïd breuken. In **Hoofdstuk 7** onderzochten we allereerst de toepasbaarheid van HR-pQCT op het scaphoïd bot bij 91 volwassenen met een klinische verdenking op een scaphoïd breuk, terwijl hun pols geïmmobiliseerd was met gips. We stelden vast dat tijdens het maken van de HR-pQCT scan een duimspalk aangebracht moest worden om bewegingsartefacten op de scans te verminderen. Daarnaast vonden we dat het gebruik van het standaard contour algoritme resulteerde in visueel verkeerde contouren van het scaphoïd bot. Dit werd opgelost door de toepassing van het standaard algoritme op grove, handgetekende pre-contouren en door het gebruik van een lagere afkapwaarde voor dichtheid voor de botsegmentatie. Handmatige aanpassing van deze contouren resulteerde in significante maar kleine verschillen in de BMD en bot-microarchitectuur ($< 1,0\%$). We concludeerden dat HR-pQCT toepasbaar is bij patiënten met een klinische verdenking op een scaphoïd breuk als een gips met duimspalk wordt gebruikt tijdens het maken van de scan en dat de BMD en bot-microarchitectuur van het scaphoïd bot met HR-pQCT kunnen worden beoordeeld.

In **Hoofdstuk 8** onderzochten we vervolgens de diagnostische waarde van HR-pQCT voor scaphoïd breuken in vergelijking met conventionele CT. Conform de standaardprocedure in VieCuri Medisch Centrum hadden alle 91 geïnccludeerde patiënten met een klinisch verdachte scaphoïd breuk een poliklinische herbeoordeling van de breuk binnen twee weken na het eerste bezoek op de spoedeisende hulp (SEH). Aanvullend werd voor het onderzoek op dezelfde dag een HR-pQCT en CT scan gemaakt. Terwijl met CT een scaphoïd breuk werd gevonden in 15 van de 91 patiënten was dat met HR-pQCT in 24 patiënten (ofwel 60% meer). De correlatie tussen CT en HR-pQCT was hoog voor type scaphoïd breuk (volgens de Herbert classificatie) en scaphoïd breuk locatie. Deze bevindingen lieten zien dat HR-pQCT superieur is ten opzichte van CT in het diagnosticeren van scaphoïd breuken bij gebruik op 1-2 weken na de eerste presentatie op de SEH en dat een substantieel deel van de scaphoïd breuken wordt gemist bij het huidige gebruik van CT.

In **Hoofdstuk 9** onderzochten we of de aanwezigheid van een scaphoïd breuk geassocieerd was met de vorm van het scaphoïd bot, met behulp van een statistisch vormmodel (SSM). We ontwikkelden een SSM van HR-pQCT scans van het scaphoïd bot van 26 volwassen met een niet-gebroken bot en van 15 volwassenen met een gebroken scaphoïd bot zonder duidelijk zichtbare breuk-gerelateerde onregelmatigheden in het botoppervlak. De eerste vijf van de veertig shape modes (wiskundige variabelen die vormvariatie beschrijven) van het SSM verklaarden samen 87,8% van de vormvariantie van de 41 scaphoïd botten. Een logistisch regressiemodel met vier shape modes classificeerde 75,6% van de scaphoïd botten correct als gebroken

of niet-gebroken, waarbij de diagnose op HR-pQCT als referentie werd gebruikt. Gebaseerd op deze bevindingen concludeerden we dat de aanwezigheid van een scaphoïd breuk bij patiënten met een klinische verdenking op een breuk geassocieerd kan zijn met de vorm van het scaphoïd bot. Studies met grotere datasets zijn nodig om deze associatie verder te onderzoeken.

In **Hoofdstuk 10** bestudeerden we het gebruik van HR-pQCT voor het volgen van de genezing van scaphoïd breuken bij elf patiënten. We zagen dat de breuklijn meer zichtbaar werd bij de scan gemaakt bij 3 weken na het eerste bezoek op de SEH. Na 6 weken en nog meer na 12 weken werden de botbalkjes rondom het breukgebied moeilijker te identificeren en te onderscheiden van omliggende botbalkjes. BMD, stijfheid en FL waren significant lager dan baseline (1-2 weken na het eerste bezoek op de SEH) bij elke follow-up visite (3, 6, 12 en 26 weken na het eerste bezoek) met de grootste verandering van baseline bij 6 weken (respectievelijk -13,6%; -26,5% en -23,7%). Het aantal botbalkjes was significant lager in vergelijking met baseline vanaf 6 weken en de dikte van de botbalkjes na 3, 6 en 12 weken. Concluderend namen de BMD, dikte van de botbalkjes en botsterkte van de scaphoïd breuken significant af gedurende de eerste zes weken van de genezing, gevolgd door een stabilisatie of toename. Ze waren niet terug op het niveau van de baselinewaarden 26 weken na het eerste bezoek op de SEH.

In **Hoofdstuk 11** bediscussieerden we de belangrijkste bevindingen, klinische implicaties en beperkingen van de studies in dit proefschrift, gevolgd door een conclusie en beschrijving van de toekomstperspectieven.



A

Addendum

Impact paragraph

Dankwoord

Curriculum vitae

List of publications

IMPACT PARAGRAPH

The bones that form our skeleton have a complex structure. They consist of a dense shell of bone on the outside, called cortical bone, and a complex honeycomb-like network of thin bars and plates of bone on the inside, called trabecular bone. To measure the structure of the cortical and trabecular bone ('bone microarchitecture'), detailed scans are needed that can determine this microarchitecture. DXA (dual-energy X-ray absorptiometry) is routinely used in hospitals to assess bone density, but DXA-scans are not detailed enough to measure bone microarchitecture. Also the scans of the currently used CT- and MRI-scanners in hospitals do not have enough detail for the measurement of bone microarchitecture. Bone microarchitecture can be assessed by performing a bone biopsy for inspection with a microscope, but bone biopsies are highly invasive as they require removal of a small piece of bone from the body. High-resolution peripheral quantitative CT (HR-pQCT) is a special CT-scanner that can generate highly detailed scans, which makes it possible to non-invasively measure the microarchitecture of bones in the region of the lower arm and hand and of the lower leg and foot ('peripheral bones'). In combination with mathematical computer models, it is also possible to estimate bone strength from HR-pQCT scans. Besides that, HR-pQCT can be used to evaluate fractures in peripheral bones in high detail.

In this thesis, we studied the use of HR-pQCT to analyze bone microarchitecture and strength in two rare and genetic disorders, the first being OI (osteogenesis imperfecta). Patients with OI or the 'brittle bone disease' have brittle bones due to defects in bone structure and bone material. As a result, they often have many fractures during life. DXA does not fully explain this high fracture risk in OI. From our study, we learned that HR-pQCT can be used to measure bone microarchitecture and bone strength in most patients with OI, which provides insights into the unique structure of the bone in these patients. These insights may help to improve our knowledge on how patients with OI can be treated. This is important because there is no cure for OI, and the optimal treatment for the poor bone structure in OI is not yet known. Our study also showed technical issues when using HR-pQCT in OI patients. First, it is important to take the short limbs and bone deformities (for example bending) of patients with severe OI into account because they may influence the scan location and thereby the HR-pQCT results. Second, we observed large empty spaces in the trabecular bone of patients with OI, which can influence the interpretation of the HR-pQCT results. This knowledge is important when using HR-pQCT in OI in future studies and in clinical practice.

The second rare and genetic disorder that we studied was FOP (fibrodysplasia ossificans progressiva). Patients with FOP or the ‘stone man disease’ become increasingly stiff during their life because their muscles, tendons, and ligaments slowly turn into bone. It means that bone is forming over time in these patients where it normally does not exist (‘heterotopic ossification’ or ‘HO’). As a result, the mobility and independence of patients with FOP worsen over time, and patients do not get old because there is no cure for FOP and no treatment for HO. Little is known about the HO bone in patients with FOP, and bone biopsies cannot be taken to study HO in FOP patients in detail because bone biopsies can lead to new HO. We explored if HR-pQCT can be used to study the HO bone in patients with FOP. We could visualize and measure the microarchitecture of HO bone and learned how HO bone fuses with the neighboring skeletal bone. These insights may help to improve our knowledge on how to treat HO in FOP. However, we experienced large difficulties with taking HR-pQCT scans in the FOP patients due to the patients’ limited mobility. HR-pQCT scans can also only be taken in the region of the lower arm and hand and of the lower leg and foot, but HO often starts in the back and neck in patients with FOP. Therefore, we recommend to use new high-detail clinical CT- or MRI-scanners in FOP because such scanners have a larger gantry than HR-pQCT scanners. A larger gantry makes it easier to use in case of a limited mobility and enables scanning of all bones and not only of peripheral bones. Although these scanners may not reach the same resolution as we obtained using HR-pQCT, it is expected that their scans can reveal details of cortical and trabecular bone.

In this thesis, we also used HR-pQCT to study the effects of treatment with anti-osteoporosis medications on bone microarchitecture and bone strength, specifically in GIOP (glucocorticoid-induced osteoporosis) and PLO (postpartum- and lactation-associated osteoporosis). GIOP and PLO are both forms of secondary osteoporosis, and DXA does not fully explain the increased fracture risk associated with these two diseases. GIOP is a common form of secondary osteoporosis, and it is caused by treatment with GCs (glucocorticoids) such as prednisone. GC-treatment is prescribed in many diseases to lower inflammation such as inflammatory rheumatoid diseases, but it also worsens bone structure and bone strength. In our study, we compared the effects of a relatively new medication for osteoporosis (denosumab) with the effects of an already longer available medication (risedronate). We showed that denosumab can be beneficial in patients who start with GC-treatment and in patients who continue GC-treatment for a longer period because it maintained bone strength in the GC-starters and improved bone strength in the GC-continuers, while risedronate did not. PLO is a rare form of secondary osteoporosis, in which women have an increased fracture risk due to a poor bone structure and bone strength mostly during the third trimester of pregnancy and the first months after giving birth to their child. The

woman in our study had severe back pain starting during pregnancy and multiple fractures in her spine. She was treated with two anti-osteoporosis medications, and we could monitor the effects of this treatment on her bones using HR-pQCT. HR-pQCT can thus give insights into the specific effects of a medication on the cortical bone and the trabecular bone, which may help in deciding on the best anti-osteoporosis treatment option for specific defects in bone microarchitecture.

Finally, we used HR-pQCT in this thesis to evaluate fractures in two peripheral bones, the first being the distal end of the radius. Distal radius fractures, or wrist fractures, are common fractures, among others in postmenopausal women. They can reduce the functioning of the wrist if they are not healing well. The treatment of a distal radius fracture typically consists of immobilization in a cast, but it is unknown what the optimal duration is to wear the cast. In previous studies in our group, it was found that HR-pQCT can be used to study distal radius fractures in postmenopausal women. In these studies, changes in the fracture region were seen early during the healing process due to the formation of new bone. In this thesis, we developed a new method using HR-pQCT to measure this early bone formation and the effects of this bone formation on the strength of distal radius fractures. This method gives more detailed information about the progression of the fracture healing process than can be obtained using currently available imaging techniques. Such information may improve our knowledge about how to optimally treat a distal radius fracture and may eventually help in deciding how long a cast should be worn. Our method may also be beneficial for other clinical applications, for example to get insights into the effects of anti-osteoporosis medications that form new bone.

The second fracture location that we studied was the scaphoid bone, a small bone in the hand close to the wrist. The application of HR-pQCT to the scaphoid bone and especially to scaphoid fractures was novel. Scaphoid fractures are the most common hand bone fractures, and they are very difficult to diagnose with current diagnostic procedures. A scaphoid fracture that is missed or diagnosed and treated with delay has a high risk of not healing. This can lead to a painful wrist movement and an impaired wrist function on the long term. Therefore, patients get a cast when a scaphoid fracture is suspected and come back to the hospital 1-2 weeks later for a second inspection, even when no scaphoid fracture is seen on the first X-ray. This procedure leads to many unnecessary cast immobilizations. In this thesis, we studied the diagnosis and healing monitoring of scaphoid fractures using HR-pQCT. Because this application was new, we first showed that HR-pQCT can be used in patients with a suspected scaphoid fracture and developed an HR-pQCT protocol for this application. Thereafter, we found that HR-pQCT is much better than standard CT for the diagnosis of scaphoid fractures at the second visit in the hospital. We also studied the complex, cashew-

nut-like shape of the scaphoid bone using HR-pQCT and found that the shape could be associated with the presence of a fracture. Together, our studies showed that HR-pQCT is superior in diagnosing scaphoid fractures. We therefore recommend to standardly use HR-pQCT at the second visit, and future studies should investigate if HR-pQCT can also be used at the first visit. If HR-pQCT is not available, we would recommend to study the use of new high-detail CT- or MRI-scanners because the standard imaging techniques can thus miss scaphoid fractures. Besides that, we showed that HR-pQCT can be used to monitor the healing of scaphoid fractures and that this healing process differs from the healing process of distal radius fractures. These insights may improve our understanding on the optimal treatment for scaphoid fractures, which is not yet known for every type of scaphoid fracture. This may further reduce the risk of non-healing of these fractures.

The studies in this thesis showed the value of HR-pQCT in a clinical setting in addition to current imaging techniques such as DXA, plain radiography, and standard CT. Therefore, we are currently integrating the HR-pQCT scanner in the routine clinical workflow in our hospital (VieCuri Medical Center). This integration makes it possible to assess bone microarchitecture and bone strength in detail in patients with metabolic bone disorders and to collaborate with other top clinical hospitals and academic hospitals in the Netherlands. The cost-effectiveness of HR-pQCT is not yet known, but this should be determined considering the rising healthcare costs. If cost-effective, HR-pQCT or in general high-detail CT and MRI should become available in more hospitals. With that, this thesis gives an impression of what could be possible in future clinical practice when current CT- and MRI-scanners have been further developed to assess bone microarchitecture and bone strength.

DANKWOORD

Wat begon als mijn masterafstudeerproject aan de TU/e is een promotietraject geworden waar ik met veel plezier op terugkijk! Dit dankwoord vormt de afsluiting daarvan. Voor mij het laatste hoofdstuk dat ik schrijf voor dit proefschrift, maar voor vele anderen stiekem het eerste (en soms misschien enige) hoofdstuk dat ze lezen. Het is dan ook zeker geen onbelangrijk hoofdstuk! De hulp en steun van veel mensen hebben eraan bijgedragen dat ik met veel plezier op mijn promotietraject kan terugkijken. In dit hoofdstuk wil ik iedereen daar graag voor bedanken!

Allereerst mijn promotieteam, **Joop**, **Caroline** en **Bert**: bedankt! Een beter promotieteam had ik me niet kunnen wensen. Jullie hulp en begeleiding hebben ervoor gezorgd dat ik me op zowel wetenschappelijk als persoonlijk vlak heb kunnen ontwikkelen. Daarbij wil ik de tijd en moeite die jullie altijd namen voor feedback op teksten en presentaties zeker niet ongenoemd laten! Daarnaast vond ik onze samenwerking altijd laagdrempelig en informeel en met ruimte voor gezelligheid. Ik heb er dan ook veel zin in om de komende jaren met jullie te blijven samenwerken als postdoc onderzoeker in VieCuri en aan de TU/e!

Beste **Joop**, dank voor de mogelijkheid die je hebt geboden om mijn promotieonderzoek in VieCuri te doen. Je vertrouwen en waardering hebben me doen groeien in het onderzoek en ook daarbuiten, net als het doorvragen en stimuleren om concreet te zijn. Het was fijn dat je de ruimte gaf om zelf richting te geven aan mijn proefschrift en tegelijkertijd met een open blik mogelijke richtingen aanreikte. Jouw enthousiasme en visie daarin werkten heel aanstekelijk! Hierdoor heb ik mijn promotieonderzoek een brede insteek kunnen geven en veel van het klinische vak mogen zien en leren. Van jou en ook van artsen en onderzoekers uit jouw netwerk met wie ik kennis heb mogen maken. En toegegeven: ik heb ook wat geleerd van je technische skills (en dat voor iemand die zich ingenieur mag noemen ;)). Ook dank voor het stimuleren om naar de ASBMR in Orlando en Vancouver te gaan. Dat waren geslaagde congressen, mede omdat we hier met een leuk 'VieCuri/Maastricht Studie'-clubje heen gingen! En die lange vliegreizen vielen toch wel mee ;).

Beste **Caroline**, heel fijn dat jij als copromotor mijn dagelijkse begeleider was. Die taak heb je meer dan volbracht! Je nam altijd de tijd om ergens mee te helpen, te kijken of te denken. Ook dacht je altijd mee vooruit en gaf je handige tips, zeker over dingen waaraan ik zelf nog niet had gedacht. Verder kon ik altijd bij je terecht met vragen. Die had ik vooral in de eerste jaren nog wel eens, bijvoorbeeld als ik ergens over twijfelde of iets toch nog even ter controle bij jou wilde nagaan. Je moet er toen af en toe vast mee van zijn geworden, maar toch beantwoordde je mijn vragen altijd

geduldig! Dat heeft mijn zelfverzekerdheid zeker doen groeien. De laatste jaren zijn we als fijne collega's naar elkaar toegegroeid en bellen we elkaar geregeld om 'onze puntjes' te bespreken en meteen even een gezellig praatje te maken. We vullen elkaar goed aan en ik vind het dan ook leuk dat we de komende jaren elkaars collega's zullen blijven!

Beste **Bert**, ook jij bedankt! Onze samenwerking gaat het meest ver terug en begon bij het bacheloreindproject, waarvan jij mijn begeleider was. Dat project was meteen mijn eerste kennismaking met HR-pQCT. Daarna volgde tijdens de master mijn hulp als student-assistent bij jouw vak Mechanica, je mentorschap en het masterafstudeerproject. Daarbij maakte jouw informaliteit, laagdrempeligheid en rustige voorkomen het contact vanaf het begin plezierig. Verder kon ik altijd langslopen of mailen voor technische vragen of een brainstormsessie over een nieuw scriptje om iets te berekenen of te analyseren. Dat waren altijd leuke overleggen, mede vanwege je enthousiasme in het meedenken over die scripts en over onderzoeken. Ik heb veel geleerd van je technische kennis (op software-gebied én op hardware-gebied, al zal dat laatste niet zo snel mijn expertise worden ;)) en van je nuttige en kritische feedback op geschreven stukken. Én van je hulp als er een probleempje was met de scanner of als ik iets niet-standaards op de scanner wilde doen.

Beste **Piet**, u ook hartelijk bedankt. U zat niet in mijn promotieteam maar heeft desondanks een waardevolle bijdrage geleverd aan mijn proefschrift. Ik vond het plezierig, leerzaam en inspirerend om met u te discussiëren en hypothetiseren over studiebevindingen en eerdere onderzoeken. Daarbij was uw interpretatie van resultaten soms wat anders dan de mijne en heel toepassingsgericht, en daardoor heel interessant. Dank ook voor uw enthousiasme tijdens overleggen en voor uw leuke anekdotes en concrete voorbeelden (zoals de walviswervel).

Merle en **Esther**, fijn dat jullie mijn paranimfen wilden zijn! **Merle**, we hebben elkaar in mijn laatste promotiejaar leren kennen toen we samen mochten werken aan een HR-pQCT project (dat alleen niet meer in mijn proefschrift terecht is gekomen). Voor dat project hebben we in korte tijd de nodige uurtjes bij de scanner gezeten, gemaïld, geteamst/gewebext en gebeld. Dat was altijd heel gezellig. Super leuk dat je dan ook voorstelde om na het congres in Vancouver nog een aantal daagjes langer te blijven. Dat waren een paar hele leuke dagen! **Esther**, wij hebben elkaar leren kennen als OPB-collega's van de TU/e, toen we samen met een clubje andere OPB'ers in ongeveer dezelfde periode zijn gestart met onze promotieonderzoeken. We zagen elkaar vooral bij de OPB-activiteiten, wat heel gezellig was en waar we altijd wel iets te kletsen hadden! Jij promoveerde als één van de laatste van de 'oude OPB-garde' voordat ik zou promoveren en had toen handige tips over de verdediging en

bijbehorende - niet onbelangrijke - randzaken. Met jullie hulp als paranimfen kan het niet anders dan een geslaagde dag worden!

Beste leden van de beoordelingscommissie, **Prof. dr. Paul Willems**, **Prof. dr. Annelies Boonen**, **dr. ir. Joost de Jong**, **Prof. dr. Harry van Lenthe**, en **Prof. dr. Edwin Oei**, hartelijk dank voor de tijd en moeite die jullie hebben genomen om mijn proefschrift te lezen en te beoordelen! Dear **Danielle**, thank you for taking the time (and getting up that early!) to discuss my thesis with me as opponent during the defense ceremony!

Mijn klinische AIO-vraagbakens van VieCuri, **Anne** en **Frans**, bedankt voor jullie hulp! **Anne**, we hebben elkaar leren kennen tijdens mijn masterafstudeerproject, waarbij jij een van mijn begeleiders was. Je hielp toen met de data en beantwoordde altijd mijn vragen. Die gingen meestal over de diagnostiek van scaphoïd fractures, welke vrij ingewikkeld te begrijpen bleek voor een niet-arts als ik. Bedankt ook voor je tips en ideeën over het 'boekje' en het verwijzen naar mij bij een technische vraag tijdens jouw verdediging (heb ik die vast kunnen voorbereiden ;)). **Frans**, fijn om met jou te kunnen sparren over de fractuurgenezingsstudie van distale radius breuken en om jouw (klinische) ideeën en inzichten daarover te horen! Dat leverde altijd interessante en leerzame brainstormsessies op.

Team Amsterdam MC, leuk om met elkaar te hebben mogen samenwerken! **Marelise**, dank voor je onophoudelijke en aanstekelijke enthousiasme en interesse. Daardoor hebben we aan een paar leuke casussen kunnen werken, die ook in dit proefschrift staan. **Sanne** en **Esmée**, leuk dat wij samen aan die casussen mochten werken! Die samenwerking was vooral online (op een bezoekje van jullie aan de HR-pQCT scanner in VieCuri na), dus heel leuk om elkaar een aantal jaren later 'offline' te zien en spreken op de DEM. **Silvia**, leuk dat je Sanne en mij toen hebt uitgenodigd om samen een sessie te organiseren! Bedankt ook voor de sportieve ochtendmomentjes in het park tijdens een congres in Sheffield en voor de gezelligheid tijdens congressen daarna. **Sara**, leuk om je te leren kennen. We waren een goed team als voorzitters van een sessie bij de NVCB! Hopelijk tot komende congressen en nieuwe samenwerkingen!

Team Isala, **Arjan**, **Koert**, **Hans** en **Guus**, dank voor de mooie samenwerking die we in de laatste paar jaar van mijn promotietraject zijn gestart! Het was heel leuk en leerzaam om met jullie het project over osteogenesis imperfecta op te zetten, het eerste project dat ik vanaf METC-aanvraag tot publicatie heb mogen uitvoeren. Dank ook voor de mogelijkheden om mijn werk te presenteren bij OI bijeenkomsten en de OI patiëntenvereniging. Zoals wel vaker bij onderzoek leidde elk antwoord weer tot nieuwe vragen en ik heb er zin in om die de komende jaren te gaan onderzoeken!

HR-pQCT ‘operators’, bedankt voor de leuke samenwerking! **Marian, Rudie, Tia, Tiny** en **Annemarie**, door jullie heb ik veel geleerd en een goed beeld gekregen van het maken van HR-pQCT scans in de dagelijkse praktijk. Die praktijkervaring maakt het schrijven van een methode-sectie toch net wat concreter! Ook mochten wij voor een project een tijd lang de week met elkaar afsluiten met metingen en dat was altijd heel gezellig. **Daphne, Judith, Lotte** en **Sanne**, leuk dat jullie als nieuwe HR-pQCT ‘operators’ de groep gaan versterken! Ik heb er zin in om de komende jaren verder met jullie samen te werken.

Daarnaast dank aan vele anderen die op verschillende manieren betrokken zijn geweest bij mijn promotietraject. Aan alle coauteurs voor hun samenwerking en input bij onderzoeken. Leuk om samen te werken met mensen met verschillende achtergronden en expertises. Aan mede-promovendi van het ‘VieCuri/Maastricht Studie’-team voor de gezelligheid tijdens congressen en andere activiteiten. Aan het team van Erasmus MC voor de leuke projecten die we aan het uitvoeren zijn en willen uitvoeren in de komende jaren. Aan de TU/e-studenten voor hun hulp bij HR-pQCT onderzoeken voor hun afstudeerprojecten. En last but not least aan alle studiedeelnemers: zonder jullie interesse en deelname hadden we deze onderzoeken niet uit kunnen voeren. Daarbij was het contact met jullie tijdens metingen en met patiëntenverenigingen heel waardevol en deed dit het belang van de onderzoeken extra leven.

Mede-TU/e-genoten, bedankt voor jullie gezelligheid! Na een paar dagen in het ziekenhuis of thuis te werken was het ook altijd weer leuk om op de TU/e te zijn. **Office 4.10**, thanks for the nice time in the office and during office outings! Misschien vooral het laatste, want op kantoor was ik meestal niet vaker dan één keer per week te vinden ;). Bij de uitjes was ik er meestal wel en dat was altijd leuk! Also everyone of the **OPB-group**, thanks for the nice time in the last four years! Als ‘Viecuriaan’ en iemand die nooit in het cel-lab kwam, moesten we het werk-gerelateerd vooral hebben van de wekelijkse OPB-meeting. Sociaal-gerelateerd waren er de etentjes, OPB-retreats en andere OPB-uitjes en die waren altijd geslaagd! I’m happy to stay around at the office and in the OPB-group in the coming year(s)!

Familie, vrienden en **atletiekmaatjes**, jullie waren niet direct betrokken bij mijn promotietraject maar toch ook een bedankje waard! Dank jullie wel voor alle gezellige theetjes, uitjes, avonden, trainingen en wedstrijden in de afgelopen jaren. Behalve gezellig waren die af en toe ook een fijne afleiding. Zeker de - toch meerdere keren per week terugkerende - trainingen, bij vooral **GAC**. Ook bedankt voor jullie interesse in mijn promotieonderzoek en in alle dingen die daarbij komen kijken (zoals congressen en presentaties). Leuk om jullie nu te kunnen laten zien wat ik allemaal heb gedaan gedurende mijn promotietraject!

Pap, mam en Celine, ik weet dat jullie het niet nodig vinden om hier genoemd te worden, maar toch mogen jullie hier niet ontbreken! Dank jullie wel voor alle steun en toeverlaat en voor het altijd klaar staan. Ook bedankt voor jullie belangstelling in mijn onderzoeken, die alleen maar groter werd naarmate de afronding van mijn proefschrift en de verdediging dichterbij kwamen. Daarbij vond ik het fijn dat jullie af en toe meedachten bij dingen die geregeld moesten worden rondom mijn verdediging, dus ook een dankjewel daarvoor. Leuk om jullie nu mijn werk van de afgelopen jaren te kunnen laten zien!

Melissa

CURRICULUM VITAE

Melissa Bevers was born on December 27, 1995 in Helmond, the Netherlands. After completing secondary education at Commanderij College in Gemert in 2014, she started the bachelor Biomedical Engineering at Eindhoven University of Technology. She obtained her bachelor's degree *cum laude* in 2017, after which she continued her study at Eindhoven University of Technology with the master Medical Engineering. During the master, Melissa did an internship at ETH in Zurich, Switzerland, where she used musculoskeletal modelling to study lower limb moments and knee mechanics during daily life activities. She finalized the master with a graduation project for which she studied the application of high-resolution peripheral quantitative CT (HR-pQCT) to the scaphoid bone in patients with a clinically suspected scaphoid fracture. She obtained her master's degree *cum laude* in 2019 and got the opportunity to continue with her graduation project as a PhD candidate at VieCuri Medical Center Venlo and Maastricht University Medical Center under supervision of prof. Joop van den Bergh PhD, Caroline Wyers PhD, and Bert van Rietbergen PhD. This thesis presents the results of the work done during her PhD research. As of September 2023, Melissa works as a postdoc researcher at VieCuri Medical Center Venlo and Eindhoven University of Technology, continuing and broadening the work she did for her PhD.



Melissa Bevers is geboren op 27 december 1995 in Helmond. Na het afronden van de middelbare school op het Commanderij College in Gemert in 2014 begon ze aan de bachelor Biomedische Technologie aan de Technische Universiteit van Eindhoven. Ze behaalde haar bachelor diploma *cum laude* in 2017, waarna ze haar studie aan de Technische Universiteit van Eindhoven vervolgde met de master Medical Engineering. Tijdens haar master heeft Melissa stage gelopen aan de ETH in Zürich, Zwitserland, waar ze musculoskeletale modellering gebruikte om krachtmomenten in de onderste extremiteit en kniemechanica tijdens dagelijkse activiteiten te bestuderen. Ze rondde de master af met een afstudeerproject waarvoor ze de toepassing van hoge-resolutie perifere kwantitatieve CT (HR-pQCT) op het scaphoïd bot onderzocht bij patiënten met een klinische verdenking op een scaphoïd breuk. Ze behaalde master diploma *cum laude* in 2019 en kreeg de kans om haar afstudeerproject voort te zetten als promovendus aan VieCuri Medisch Center Venlo en Maastricht Universitair Medisch Centrum onder supervisie van prof. dr. Joop van den Bergh, dr. Caroline Wyers en dr. ir. Bert van Rietbergen. Dit proefschrift beschrijft de resultaten van haar promotieonderzoek. Sinds september 2023 werkt Melissa als postdoc onderzoeker in VieCuri Medisch Centrum Venlo en aan de Technische Universiteit van Eindhoven, waar ze het gedane werk tijdens haar promotietraject voortzet en verder uitdiept.

LIST OF PUBLICATIONS

This thesis

Beyers MSAM, Harsevoort AGJ, Gooijer K, *et al.* Bone microarchitecture and strength in adults with osteogenesis imperfecta from HR-pQCT: normative comparison and challenges. *Submitted.*

Beyers MSAM*, Heyer FL*, Wyers CE, *et al.* The contribution of lower-mineralized tissue to the healing of distal radius fracture assessed using HR-pQCT. *Bone.* 2023;175:116859.

Treurniet S*, **Beyers MSAM***, Wyers CE, *et al.* Bone microarchitecture and strength changes during teriparatide and zoledronic acid treatment in a patient with pregnancy and lactation-associated osteoporosis with multiple vertebral fractures. *Calcif Tissue Int.* 2023:1-7.

Geusens PPMM, **Beyers MSAM**, Van Rietbergen B, *et al.* Effect of denosumab compared with risedronate on bone strength in patients initiating or continuing glucocorticoid treatment. *J Bone Miner Res.* 2022;37(6):1136-1146.

Beyers MSAM, Daniels AM, Van Rietbergen B, *et al.* Assessment of the healing of conservatively-treated scaphoid fractures using HR-pQCT. *Bone.* 2021;153:116161.

Beyers MSAM, Wyers CE, Daniels AM, *et al.* Association between bone shape and the presence of a fracture in patients with a clinically suspected scaphoid fracture. *J Biomech.* 2021;128:110726.

Botman E*, **Beyers MSAM***, Wyers CE, *et al.* Microarchitecture of heterotopic ossification in fibrodysplasia ossificans progressiva: an HR-pQCT case series. *Front Cell Dev Biol.* 2021;9.

Daniels AM, **Beyers MSAM**, Sassen S, *et al.* Improved detection of scaphoid fractures with high-resolution peripheral quantitative CT compared with conventional CT. *J Bone Joint Surg.* 2020;102(24):2138-2145.

Beyers MSAM, Daniels AM, Wyers CE, *et al.* The feasibility of high-resolution peripheral quantitative computed tomography (HR-pQCT) in patients with suspected scaphoid fractures. *J Clin Densitom.* 2019;23(3):432-442.

* *These authors have contributed equally to this work and share first authorship.*

Other

Whittier DE, **Beyers MSAM**, Geusens PPMM, Van den Bergh JP, Gabel L. Characterizing bone phenotypes related to skeletal fragility using advanced medical imaging. *Curr Osteoporos Rep.* 2023:1-13.

Arias-Moreno AJ, Hosseini HS, **Beyers MSAM**, Ito K, Zysset P, Van Rietbergen B. Validation of distal radius failure load predictions by homogenized-and micro-finite element analyses based on second-generation high-resolution peripheral quantitative CT images. *Osteoporos Int.* 2019;30(7):1433-1443.

